Indirect Efficiency Determination and Parameter Identification of Permanent-Magnet Synchronous Machines

Vom Fachbereich Elektrotechnik und Informationstechnik
der Technischen Universität Darmstadt
zur Erlangung des akademischen Grades eines
Doktor-Ingenieurs (Dr.-Ing.)
genehmigte Dissertation

von

Dipl.-Ing. Björn Deusinger
geboren am 28. März 1986
in Frankfurt am Main

Referent:	Prof. Dr.-Ing. habil. Dr. h.c. Andreas Binder
Korreferent:	Prof. Dr.-Ing. Martin Doppelbauer
Tag der Einreichung:	16. Juni 2020
Tag der mündlichen Prüfung:	9. November 2020

D 17
Darmstadt 2020

Deusinger, Björn: Indirect Efficiency Determination and Parameter Identification of Permanent-Magnet Synchronous Machines
Darmstadt, Technische Universität Darmstadt
Jahr der Veröffentlichung der Dissertation auf TUprints: 2021
URN: urn:nbn:de:tuda-tuprints-189155
URI: https://tuprints.ulb.tu-darmstadt.de/id/eprint/18915
Tag der mündlichen Prüfung: 09.11.2020

Erklärungen laut Promotionsordnung

§ 8 Abs. 1 lit. c PromO

Ich versichere hiermit, dass die elektronische Version meiner Dissertation mit der schriftlichen Version übereinstimmt.

§ 8 Abs. 1 lit. d PromO

Ich versichere hiermit, dass zu einem vorherigen Zeitpunkt noch keine Promotion versucht wurde.

§ 9 Abs. 1 PromO

Ich versichere hiermit, dass die vorliegende Dissertation selbstständig und nur unter Verwendung der angegebenen Quellen verfasst wurde.

§ 9 Abs. 2 PromO

Die Arbeit hat bisher noch nicht zu Prüfungszwecken gedient.

Vorwort

Die vorliegende Arbeit ist im Rahmen meiner Tätigkeit als wissenschaftlicher Mitarbeiter am *Institut für Elektrische Energiewandlung* der *Technischen Universität Darmstadt* entstanden. Ich möchte mich an dieser Stelle bei allen bedanken, die zum Gelingen meines Promotionsvorhabens beigetragen haben. Hierbei gilt mein Dank in erster Linie meinem Doktorvater Prof. Dr.-Ing. habil. Dr. h.c. Andreas Binder für seine engagierte Betreuung und seine wertvollen fachlichen und methodischen Anregungen. Ebenfalls danke ich Prof. Dr.-Ing. Martin Doppelbauer, dem Inhaber der Professur *Hybridelektrische Fahrzeuge* am *Karlsruher Institut für Technologie (KIT)* für die freundliche Übernahme des Korreferats dieser Arbeit.

Die Untersuchung des vorgestellten Messverfahrens fand in enger Abstimmung mit dem nationalen Normungsgremium DKE/K 311 statt. Ich danke allen beteiligten Mitgliedern für die gute Zusammenarbeit – insbesondere Dr.-Ing. Axel Möhle (*Siemens AG*) und Dr.-Ing. Christian Lehrmann (*Physikalisch-Technische Bundesanstalt Braunschweig*) sowie den Vorsitzenden Prof. Dr.-Ing. Bernd Ponick (*Leibniz Universität Hannover*) und Prof. Dr.-Ing. Martin Doppelbauer (*KIT*). Die zugehörigen Forschungsprojekte wurden vom *Bundesministerium für Wirtschaft und Energie* im Rahmen der Förderprogramme *Innovation mit Normen und Standards (INS)* und *Wissens- und Technologietransfer durch Patente und Normen (WIPANO)* gefördert, wofür ich mich ebenfalls bedanke. Des Weiteren gilt mein Dank allen Firmen, die Testmaschinen zur Verfügung gestellt und mich bei den Messungen unterstützt haben. Besonderer Dank gilt Dr.-Ing. Olaf Körner, Dr.-Ing. Hayder Al-Khafaji und Frederick Claudino (*Siemens Mobility GmbH*) für die erfolgreiche gemeinsame Projektdurchführung.

Ich danke meinen wissenschaftlichen Kolleginnen und Kollegen Jeongki An, Maximilian Clauer, Daniel Dietz, Nicolas Erd, Bogdan Funieru, Yves Gemeinder, Robin Köster, Marcel Lehr, Xing Li, Oliver Magdun, Gael Messager, Alexander Möller, Sascha Neusüs, Kersten Reis, Omid Safdarzadeh, Jinou Wang und Martin Weicker herzlich für die ergiebigen fachlichen Diskussionen, die gute Zusammenarbeit und die stets freundschaftliche Gemeinschaft. Vielen Dank ebenfalls an alle Studenten, die im Rahmen ihrer Abschlussarbeiten bei meinen Forschungstätigkeiten mitgewirkt haben.

Ferner danke ich herzlich allen technischen und administrativen Mitarbeiterinnen und Mitarbeitern am *Institut für Elektrische Energiewandlung*: Klaus Gütlich für die zahllosen elektrischen Installationen und Prüfstandsaufbauten, Herbert Moschko für die Hilfe bei messtechnischen Fragestellungen, Andreas Fehringer und Markus Lohnes für die umfangreichen mechanischen Auf- und Umbauarbeiten an den Testmaschinen und Prüfständen sowie Sabine Waldhaus, Anette Gallinat und Annette Siler für die Unterstützung bei der Projektverwaltung.

Zum Schluss möchte ich mich besonders bei meiner Familie bedanken – vor allem bei meinen Eltern Monika und Alfred Deusinger, die durch die fortwährende Unterstützung und Förderung meiner wissenschaftlichen Ausbildung maßgeblich zum Erreichen meiner beruflichen Ziele beigetragen haben.

Björn Deusinger
im Juni 2021

Abstract

This thesis presents a method for efficiency determination of inverter-fed permanent-magnet synchronous machines by summation of the individual losses. For electrically excited synchronous machines there are already standardized methods, as for high efficiency values the direct procedure of input/output measurement is too inaccurate. With the novel method for machines in the base speed range, the individual losses are determined at the no-load experiment and the removed rotor test and recalculated for rated operation. The prerequisites and the analysis of the experiments are described. To evaluate the procedure, measurement series are performed on five different permanent-magnet synchronous machines with a rated power of 45 kW … 160 kW. The indirect efficiency is compared with a direct measurement. Also for four of the five test machines finite element simulations are carried out to prove the assumptions of the proposed method. The result is, that for four of the test machines a good accordance with deviations below 0.5 % at rated operation is reached. But because of the special design of the fifth test machine the losses and thus the efficiency show deviations of about 1 %. In total, the indirect procedure is usable as an adequate replacement for typical kinds of permanent-magnet synchronous machines with distributed windings and especially for big rated powers, where the direct method is too imprecise. In addition to the efficiency determination the thesis also shows, how to determine the no-load voltage, the short-circuit current, and the synchronous inductance by using the described experiments.

Kurzfassung

Diese Arbeit präsentiert ein Verfahren, um den Wirkungsgrad von umrichtergespeisten Permanentmagnet-Synchronmaschinen im Einzelverlustfahren zu ermitteln. Für elektrisch erregte Synchronmaschinen sind bereits seit langem derartige Verfahren standardisiert, da für sehr hohe Wirkungsgrade die direkte Messung aus Eingangs- und Ausgangsleistung zu ungenau ist. Mit Hilfe des neuartigen Verfahrens für Maschinen im Grunddrehzahlbereich werden die Einzelverluste im Leerlaufversuch sowie im Bohrungsfeldversuch bestimmt und für den Bemessungsbetrieb umgerechnet. Die Anforderungen an die Versuche und deren Auswertung werden beschrieben. Zur Evaluation des Messverfahrens werden Versuchsreihen an fünf unterschiedlichen Permanentmagnet-Synchronmaschinen mit Bemessungsleistungen von 45 kW … 160 kW durchgeführt, wobei letztlich der indirekte Wirkungsgrad mit einer direkten Messung verglichen wird. Außerdem werden für vier der fünf Testmaschinen Finite-Elemente-Simulationen durchgeführt, um die Annahmen, welche für das Verfahren getroffen werden, zu überprüfen. Es zeigt sich, dass für vier der Testmaschinen bei Bemessungsbetrieb eine gute Übereinstimmung mit Abweichungen kleiner als 0.5 % erzielt werden kann. Die fünfte Testmaschine hat aufgrund ihrer Konstruktion ein spezielles Verlustspektrum, sodass hier die Methode Abweichungen von ca. 1 % zeigt. Insgesamt empfiehlt sich die indirekte Methode aber als adäquater Ersatz für die direkte Messung bei typischen Permanentmagnet-Synchronmaschinen mit verteilten Wicklungen und vor allem bei großen Bemessungsleistungen, wo die direkte Methode zu ungenau ist. Neben der Wirkungsgradbestimmung wird gezeigt, wie sich anhand der beschriebenen Versuche zusätzlich die Leerlaufspannung, der Kurzschlussstrom sowie die Synchroninduktivität der Testmaschinen lässt.

Table of contents

Notations and Symbols

Notations

a_o	number of parallel branches per phase	–
a_i	number of parallel sub-conductors	–
a_T	number of horizontal conductors per slot	–
A	area, cross section	m^2
b	width	m
B	magnetic flux density	T
B_R	magnetic remanence flux density	T
d	diameter	m
d_E	penetration depth	m
f	electric frequency	Hz
f_PWM	inverter switching frequency	Hz
h	height	m
I	current	A
k	time harmonic order (inverter)	–
k_R	resistance increase factor (current displacement)	–
k_sc	short-circuit ratio	–
k_V	iron loss increase due to manufacturing	–
k_ϑ	resistance increase factor (temperature)	–
K	total resistance increase factor	–
l	length	m
L	inductance	H
m_s	number of stator phases	–
M	torque	Nm
n	rotational speed	s^{-1}
n	number	–
N_c	number of turns per coil	–

N_s	number of turns per phase	–
P	power	W
q	number of slots per pole and phase	–
Q_s	number of stator slots	–
r	radius	m
R	ohmic resistance	Ω
Re	*Reynolds number*	–
T	electric period $(1\,/\,f)$	s
$u(x_i)$	uncertainty of the value x_i	$[x_i]$
$u_\mathrm{c}(y)$	combined uncertainty of the measurand $y = f(x_1, x_2, \ldots, x_N)$	$[y]$
U	electric voltage	V
V	volume	m^3
X	reactance	Ω
α_e	pole coverage ratio	%
α_{20}	temperature coefficient related to 20 °C	1/K
β^*	current angle	° el.
γ	position angle	° el.
δ	air gap width	m
ε	measured or calculated error	–
η	efficiency	–
ϑ	temperature	°C
$\Delta\vartheta$	temperature rise	K
κ	electric conductivity	$1/(\Omega\mathrm{m})$
μ	space harmonic order (rotor)	–
μ	magnetic permeability	Vs/(Am)
ν	space harmonic order (stator)	–
ν	kinematic viscosity	m^2/s
ξ	reduced conductor height	–
ρ	mass density	kg/m^3
τ_p	pole pitch	m

φ	phase angle	°el.
φ	skin effect factor	–
ψ	proximity effect factor	–
Ψ	magnetic flux linkage amplitude	Vs

Subscripts

0	no-load
1	fundamental
ad	additional
avg	average
b	winding overhang
br	brush
B	bore field, removed rotor
calc	calculated
crit	critical
Cu	copper
d	direct axis
d	dissipative loss
dir	direct
div	division
e	equivalent
ec	eddy current
el	electrical
elem	elements
em	electromagnetic
ex	excess
exc	excitation
ext	external
fr	friction
Fe	iron

Ft	*Foucault*
gen	generator
h	main (voltage)
h	horizontal
Hy	hysteresis
i	inner
in	input
ind	indirect
L	layer
LL	line-to-line
m	mechanical
M	magnet
max	maximum
meas	measured
mot	motor
N	rated
o	outer
out	output
p	pole, back EMF
P	*Potier* (reactance)
q	quadrature axis
Q	slot
r	rotor
R	resistance
s	stator
sc	short-circuit
sh	sheet
sim	simulated
syn	synchronous
T	conductor
U, V, W	phase U, V, W

v	vertical
w	windage
x	reactance
x, y, z	Cartesian coordinates
z	axial direction of cylinder coordinates
δ	air gap
ρ	radial direction of cylinder coordinates
φ	tangential direction of cylinder coordinates
σ	leakage

Abbreviations

AC	alternating current
DC	direct current
DCM	DC machine
DFIG	doubly-fed induction generator
FFT	Fast *Fourier* Transform
PM	permanent magnet
PMSM	permanent-magnet synchronous machine
PWM	pulse width modulation
RMS	root mean square
VSI	voltage source inverter
cond.	conductor
el.	electrical
const.	constant
N. of	number of
p.p.	percentage point
var.	variable
vs.	versus

1. Introduction

Due to the high demand on motor and generator efficiency, permanent magnet synchronous machines are used increasingly in different applications, e.g. big wind generators up to 6 MW rated power, industrial drives with high efficiency class IE4 ([10], [16], [28], [29]), or motors for (hybrid) electric cars. If the machine efficiency is higher than 95 %, the effort for accurate efficiency determination is rather big, as a high measurement accuracy is required. So the experimental validation of the designated machine efficiency values is a big challenge for the machine manufacturers.

The methods of efficiency determination can be classified into two main categories: the *direct* measurement and the *indirect* electrical and mechanical measurement. For the direct method a full-load input/output power measurement is required. The machine efficiency η is calculated via

$$\eta = \frac{P_{\text{out}}}{P_{\text{in}}} \, , \tag{1.1}$$

where P_{out} is the output power and P_{in} the input power.

On the other hand, for indirect efficiency determination, the loss components are determined individually and are summed up to the total losses P_{d}. With these losses the efficiency is calculated via

$$\eta = \frac{P_{\text{out}}}{P_{\text{in}}} = \frac{P_{\text{in}} - P_{\text{d}}}{P_{\text{in}}} \, . \tag{1.2}$$

Besides these two methods there is also the possibility of using a calorimetric measurement according to IEC 60034-2-2 [26], but with even more technical effort (e.g. [1], [14], [34]). Therefore this method is not addressed in this work.

For big electrical machines, an accurate direct efficiency determination is difficult for several reasons. The first problem is the need for a load test with rated power, which requires an adequate load machine with the same power rating. Furthermore, big generators for power plants (mainly electrically excited synchronous machines) with high output power (above several MW) are often finally assembled directly at the plant. So a measurement is only possible there. As the rated efficiency of these machines is usually in the range of 95 % and higher, a high measurement accuracy is very important, as the following example [63] shows.

Example 1 (Direct efficiency determination):
The electrical machine is operated in motor operation at the three-phase sinusoidal grid. The mechanical output power is measured by a speed and torque transducer to

$$P_{\text{out,meas}} = 2\pi \cdot n \cdot M \ , \tag{1.3}$$

where n is the mechanical rotational speed and M is the shaft torque. The electrical input power is measured via

$$P_{\text{in,meas}} = \sqrt{3} \cdot U_{\text{LL}} \cdot I_{\text{s}} \cdot \cos\varphi \ , \tag{1.4}$$

where U_{LL} is the stator line-to-line voltage, I_{s} the stator current and $\cos\varphi$ is the power factor. The *true* machine efficiency η is 95 %, and the measurement accuracy ε is 0.2 %. As a worst-case assumption, the output power is measured due to ε too high and the input power too low:

$$\eta_{\text{meas}} = \frac{P_{\text{out,meas}}}{P_{\text{in,meas}}} = \frac{P_{\text{out}} \cdot (1+\varepsilon)}{P_{\text{in}} \cdot (1-\varepsilon)} = \eta \cdot \frac{1+\varepsilon}{1-\varepsilon} = 0.95 \cdot \frac{1.002}{0.998} = 0.9538 \ .$$

The efficiency η_{meas}/η is determined too high by 0.38 p.p. A comparison of the *true* losses P_{d} and the measured losses $P_{\text{d,meas}}$

$$P_{\text{d}} = \left(\frac{1}{\eta} - 1\right) \cdot P_{\text{out}} = 0.0526 \cdot P_{\text{out}} \ ,$$
$$P_{\text{d,meas}} = \left(\frac{1}{\eta_{\text{meas}}} - 1\right) \cdot P_{\text{out,meas}} = 0.0484 \cdot P_{\text{out,meas}}$$

shows a deviation of $P_{\text{d,meas}}/P_{\text{d}} = 0.92$, i.e. the losses are measured too low by 8 %.

If the same measurement accuracy is applied to the indirect measurement procedure, the error will be reduced significantly, as described in the next example [63].

Example 2 (Indirect efficiency determination):
The input power $P_{\mathrm{in,meas}}$ is measured due to ε too high and the losses $P_{\mathrm{d,meas}}$ are determined too low in worst-case. Then the efficiency is calculated to

$$\eta_{\mathrm{meas}} = \frac{P_{\mathrm{out,meas}}}{P_{\mathrm{in,meas}}} = \frac{P_{\mathrm{in,meas}} - P_{\mathrm{d,meas}}}{P_{\mathrm{in,meas}}} = 1 - \frac{P_{\mathrm{d,meas}}}{P_{\mathrm{in,meas}}} = 1 - \frac{P_{\mathrm{d}}}{P_{\mathrm{in}}} \cdot \frac{1-\varepsilon}{1+\varepsilon}$$

$$= 1 - (1-\eta) \cdot \frac{1-\varepsilon}{1+\varepsilon} = 1 - 0.05 \cdot \frac{0.998}{1.002} = 0.9502 \cong \eta = 0.95$$

The efficiency $\eta_{\mathrm{meas}}/\eta$ is determined too high by 0.02 p.p. In this case the deviation between the *true* and the measured efficiency is with 0.02 p.p. very low. The deviation between $P_{\mathrm{d,meas}}$ and P_{d} is 0.4 %.

Therefore for electrically excited synchronous machines and induction machines there have been standardized indirect efficiency determination methods for many years [35]. If the machine's rated power is higher than 1 MW, the indirect methods are mandatory [14], [25]. As the losses are determined individually, adequate testing procedures and machine models are necessary to calculate the correct efficiency. A brief explanation of these measures for electrically excited synchronous machines is given in Chapter 2. This method is *not* directly applicable for permanent-magnet synchronous machines. The only standardized option is currently a direct efficiency measurement. This thesis presents and evaluates a novel procedure to determine the machine efficiency indirectly without the need of a full-load measurement. Therefore three experiments are presented to calculate the efficiency for sinusoidal operation and inverter operation: The motor no-load test, the generator no-load test, and the removed rotor test. Also the short-circuit test and the reactive current test are explained to identify the synchronous inductance and the short-circuit current of the machine. With help of measurements of five different permanent-magnet synchronous test machines up to a rated power of 160 kW (S1 operation according to IEC 60034-1 [24]) in motor and generator operation the indirect determination procedure is evaluated and compared to analytical and numerical simulation results.

The basic principle of the proposed method was first introduced in [69] and extended in [63], [66]. It was continuously evaluated in cooperation with the national standardization committee DKE/K 311, which is responsible for the standardization process of rotating electrical machines. Since then several publications of the *Physikalisch-Technische Bundesanstalt (PTB) Braunschweig* (the German national metrology institute) also deal with the evaluation and application of the proposed method for motors with a rated power of 7.5 kW [40], [61], [62]. There a good accordance between the indirect method compared with direct measurements is reached. The results are briefly given in Section 7.4.

This thesis explains the proposed method in detail, while the equivalent circuit of the permanent-magnet synchronous machine is used to describe the relevant losses, which are of big impact for industrial drives operated in the base speed range, where no field weakening is applied (Chapter 3 to Chapter 5). The five test machines and the measurement setups for the relevant experiments are described in Chapter 6 and Chapter 7, while Chapter 7 also gives the results of the comparison between measured indirect and direct efficiency. In Chapter 8 finite element simulations are performed on four of the test machines to compare the simulation values with the measurements and to proof the applicability of the proposed method and of the calculation assumptions.

Chapter 4 also describes, how together with further experiments the parameters of the machines are analyzed with respect to no-load voltage, short-circuit current, and synchronous inductance.

2. Efficiency determination of electrically excited synchronous machines

For electrically excited synchronous machines several testing methods for efficiency determination are established and approved by IEC standard 60034-2-1 [25]. This chapter briefly explains the different testing procedures with the focus on the two indirect methods B and C, that are mandatory for bigger synchronous machines.

The three preferred methods that comply to the national energy efficiency regulations are:

Method A – Direct measurement: Input-Output [1],

Method B – Summation of losses with load test ,

Method C – Summation of losses without load test .

In addition, there are four more methods available, that are not compliant to national energy efficiency regulations, but may be used for field testing:

Method D – Dual-supply-back-to-back ,

Method E – Single-supply-back-to-back ,

Method F – Zero power factor with excitation current determined from *Potier*, *ASA*, or *Sweden* diagram [30] ,

Method G – Summation of losses with load test except the additional load losses .

These methods are only mentioned for the sake of completeness and have rather small impact on this work.

It is assumed, that the primary winding is located at the stator. For machine topologies with a rotating primary winding, the terms *stator* and *rotor* have to be exchanged.

---

[1] At the present situation the only applicable method also for permanent-magnet synchronous machines.

2.1. Method A – Direct measurement: Input-Output

For a machine frame size below or equal 180 mm the direct measurement is applied, as the expected efficiency values are low enough to be determined accurately. The full load test requires a second machine of the same power rating and a torque transducer to determine the mechanical power $P_{\mathrm{m}} = 2\pi \cdot n \cdot M$. The electrical power $P_{\mathrm{el}} = \sqrt{3} \cdot U_{\mathrm{LL}} \cdot I_{\mathrm{s}} \cdot \cos\varphi_{\mathrm{s}}$ is measured at the same time.

The direct efficiency in motor operation η_{mot} and in generator operation η_{gen} is calculated via

$$\eta_{\mathrm{mot}} = \frac{P_{\mathrm{m,out}}}{P_{\mathrm{el,in}} + P_{\mathrm{ext}}} \, , \tag{2.1}$$

$$\eta_{\mathrm{gen}} = \frac{P_{\mathrm{el,out}}}{P_{\mathrm{m,in}} + P_{\mathrm{ext}}} \, , \tag{2.2}$$

where P_{ext} are the external losses of the excitation system.

The machine shall be in thermal equilibrium, i.e. the stator winding temperature does not change by more than 2 K in one hour.

This procedure is at the present situation the only method, that may also be applied for permanent-magnet synchronous machines. Therefore in this work, the direct measurement is conducted to compare the results to the proposed indirect efficiency determination. The procedure is slightly different, as no excitation losses occur and the permanent-magnet synchronous machine is usually operated at inverter operation. The exact procedure is explained in Section 4.4.

2.2. Method B – Summation of losses with load test

For machines with a frame size above 180 mm and a rated power up to 1 MW this indirect efficiency determination procedure is applied. Again a drive equipment for full load is required to determine the excitation losses at rated operation.

The total losses of the synchronous machine can be divided into three major groups:

- No-load losses: Iron losses P_{Fe} and friction and windage losses $P_{\mathrm{fr+w}}$

- Load-dependent losses: Stator copper losses $P_{\mathrm{Cu=}}$ and additional load losses P_{ad}
- Excitation losses P_{exc}

2.2.1. No-load losses

To determine the no-load losses, a no-load test is performed. The machine is driven at constant rated speed either by an auxiliary drive at open terminals (generator no-load) or uncoupled (motor no-load). By variation of the excitation current I_{f}, the characteristics $U_{\mathrm{s0}}(I_{\mathrm{f}})$, $I_{\mathrm{s0}}(I_{\mathrm{f}})$ in case of motor no-load, and $P_0(I_{\mathrm{f}})$ are obtained. The no-load power P_0 is determined as the mechanical input power in case of generator no-load. A minimum number of seven different voltage values between $30\,\% \dots 110\,\%$ of the rated stator voltage U_{sN} is required.

With knowledge of the stator winding resistance R_{s} per phase (m_{s} phases) at the correct stator winding temperature ϑ_{Cu} the iron losses and friction and windage losses $P_{\mathrm{Fe+fw}}$ are calculated together as

$$P_{\mathrm{Fe+fw}} = P_0 - m_{\mathrm{s}} \cdot R_{\mathrm{s}} \cdot I_{\mathrm{s0}}^2 - P_{\mathrm{exc0}} \; . \tag{2.3}$$

The excitation losses P_{exc0} depend on the excitation system and are discussed below. By plotting the iron losses and friction and windage losses over the square of the stator voltage, the extrapolated value of the curve $P_{\mathrm{Fe+fw}}(U_{\mathrm{s0}}^2)$ for $U_{\mathrm{s0}}^2 = 0$ shows the constant amount of friction and windage losses $P_{\mathrm{fr+w}}$. The variable part of the curve is associated with the iron losses P_{Fe}, which are therefore known at rated stator voltage (Figure 2.1).

2.2.2. Load-dependent losses

At first a full load test of the machine is performed at rated excitation, and rated stator voltage and current. The measurement shall start after the machine is in thermal equilibrium (machine over-temperatures $\Delta\vartheta \leq 2\,\mathrm{K}$ in one hour). After the electrical measurement the stator winding resistance $R_{\mathrm{s=}}$ at DC operation and thus the stator winding temperature ϑ_{Cu} is determined, when compared to $R_{\mathrm{s=}}$ at cold machine.

The stator copper losses are calculated via

$$P_{\mathrm{Cu=}} = m_{\mathrm{s}} \cdot R_{\mathrm{s=}} \cdot I_{\mathrm{sN}}^2 \; . \tag{2.4}$$

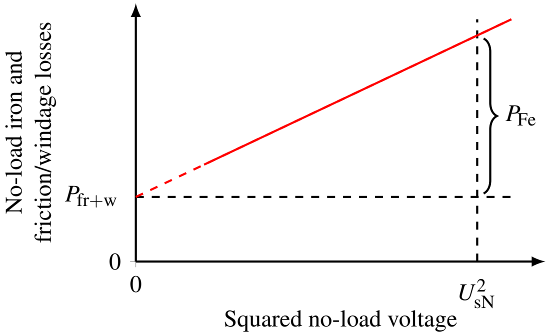

Figure 2.1.: Exemplary curve of the no-load loss separation of an electrically excited synchronous machine

Afterwards the steady-state short-circuit test is carried out to determine the additional load losses. Therefore, like at the no-load test, the machine is driven by the auxiliary drive for different excitation states, but now with all terminals short-circuited. The mechanical input power $P_{\mathrm{m,sc}} = 2\pi \cdot n \cdot M_{\mathrm{sc}}$ is measured by a torque transducer, while the excitation current is adjusted to let the rated stator current I_{sN} flow as short-circuit current in the stator winding.

The rated additional load losses $P_{\mathrm{ad,N}}$ are calculated as the difference between the measured mechanical power and the stator copper losses $P_{\mathrm{Cu=}}$, friction and windage losses $P_{\mathrm{fr+w}}$ and excitation losses P_{exc}:

$$P_{\mathrm{ad,N}} = P_{\mathrm{m,sc}} - P_{\mathrm{Cu=}} - P_{\mathrm{fr+w}} - P_{\mathrm{exc}} \ . \tag{2.5}$$

As the additional load losses (e.g. due to current displacement) are depending on the square of the current, the loss value for different operation points is calculated via

$$P_{\mathrm{ad}} = P_{\mathrm{ad,N}} \cdot \left(\frac{I_{\mathrm{s}}}{I_{\mathrm{sN}}} \right)^2 \ . \tag{2.6}$$

2.2.3. Excitation losses

The excitation losses of synchronous machines depend on the excitation system, that is used to supply the required DC excitation. Several different options are available, like shaft driven or external exciters with slip-rings or brushless excitation with a rotating diode bridge. Therefore the excitation losses P_{exc} may include:

- Losses in the field winding P_{f}
- Losses in the brushes P_{br} of the slip-ring system
- External losses in the excitation system P_{ext}

The required DC field excitation current at rated conditions is determined during the full load test at thermal equilibrium with Method B. Extended calculation examples are given in IEC 60034-2-1 [25], but are not addressed here.

2.2.4. Efficiency calculation

Finally the total losses P_{d} are summed up to

$$P_{\mathrm{d}} = P_{\mathrm{Fe}} + P_{\mathrm{fr+w}} + P_{\mathrm{Cu=}} + P_{\mathrm{ad}} + P_{\mathrm{exc}} \ . \tag{2.7}$$

The indirect efficiency is then determined according to (1.2)

2.2.5. Distinction to permanent-magnet synchronous machines

The described procedures of no-load and short-circuit measurement both require a variable excitation to adjust the magnetic flux to a) rated flux in no-load operation and b) minimum flux (mainly stray flux) in short-circuit operation. This is not possible due to the constant permanent-magnet excitation. On the other hand, no excitation losses occur in permanent-magnet synchronous machines.

Therefore, in order to perform an indirect efficiency determination also for permanent-magnet synchronous machines, adequate alternative testing procedures have to be found to measure and separate the load-independent and load-dependent losses.

2.2.6. Determination of the synchronous inductance

According to IEC 60034-4 [30], the synchronous inductance L_{d} can be calculated using the no-load and short-circuit characteristic. Therefore the short-circuit ratio k_{sc} is determined according to Figure 2.2 via

$$k_{\mathrm{sc}} = \frac{I_{\mathrm{s,sc}}(I_{\mathrm{f0}})}{I_{\mathrm{sN}}} = \frac{I_{\mathrm{f0}}}{I_{\mathrm{f,sc}}} . \tag{2.8}$$

From this, the synchronous inductance L_{d} results as

$$L_{\mathrm{d}} = \frac{1}{\omega_{\mathrm{s}}} \frac{Z_{\mathrm{N}}}{k_{\mathrm{sc}}} = \frac{1}{\omega_{\mathrm{s}}} \frac{U_{\mathrm{sN}}}{I_{\mathrm{s,sc}}(I_{\mathrm{f0}})} , \tag{2.9}$$

where $Z_{\mathrm{N}} = U_{\mathrm{sN}}/I_{\mathrm{sN}}$ is the nominal impedance of the synchronous machine.

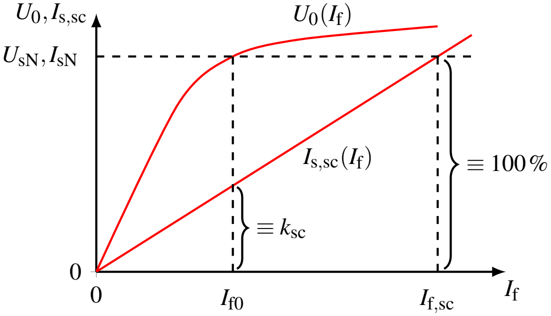

Figure 2.2.: No-load and short-circuit characteristic of an electrically excited synchronous machine

2.3. Method C – Summation of losses without load test

For even bigger machines with a rated power above 1 MW the previous method is not longer applicable due to the too complicated full load test. Instead of determining the rated excitation current from measurement at rated conditions, now I_{fN} is calculated using the no-load and short-circuit characteristic. Additionally an over-excitation test at zero power factor has to be carried out: The machines is operated either as motor with zero active power or as generator with zero mechanical shaft power, while the excitation is increased further, until the rated stator current is reached. With this excitation current, the *Potier* reactance X_{P} is determined according to IEC 60034-4 [30]. The *Potier* reactance is considered as an artificially increased leakage reactance to represent the increased voltage drop due to maximum saturation of the excitation poles.

To determine the rated excitation current I_{fN}, three geometrical construction methods exist: *Potier* diagram, *ASA* diagram, and *Sweden* diagram. The details of the construction are not addressed here, but are described in IEC 60034-4 [30].

With knowledge of the rated excitation current, the excitation losses P_{exc} are calculated. For the other loss components, the procedure is equivalent to the previously described Method B.

2.4. Method D + E – Back-to-back test

Both methods D and E require two identical machine units. One machine is operated as motor, the other one as generator at rated stator voltage and current. For the efficiency determination of the tested machines 50 % of the total measured losses are taken into account. At Method D each machine is fed separately, while at Method E both machines are coupled electrically and fed by one single source.

2.5. Method F – Zero power factor test

This Method F approximates the load losses with help of the zero power factor test at motor operation and the calculated excitation losses like at Method C. To adjust the stator current to rated current a variable voltage source is required at the stator side. Again, the efficiency is determined by summation of the individual losses, while the input power is calculated from the rated values of stator voltage, current, and power factor.

2.6. Method G – Summation of losses except the additional load losses

In this procedure the short-circuit test is omitted. Therefore, the additional load losses cannot be determined, and the resulting efficiency values are less accurate. The calculation itself is performed like explained above for Method B.

2.7. Inverter-fed machines

The previously mentioned methods are only usable for machines operated at sinusoidal voltage sources. As nowadays variable-speed drives are increasingly utilized, the additional losses at inverter-feeding and the efficiency in more operation points than only at rated speed and torque are addressed. Here IEC 60034-2-3 [27] describes interpolation procedures to determine the efficiency of AC drives for a wider operation range by measurement of seven fixed operation points P1 … P7 (Table 2.1), see also [15].

Table 2.1.: Operation points according to IEC 60034-2-3 [27]

	n/n_N	M/M_N	P/P_N
P1	0.9	1	0.9
P2	0.5	1	0.5
P3	0.25	1	0.25
P4	0.9	0.5	0.45
P5	0.5	0.5	0.25
P6	0.5	0.25	0.125
P7	0.25	0.25	0.0625

Again for these seven operation points, the direct measurement from input and output power is presently applied for permanent-magnet synchronous machines.

3. The permanent-magnet synchronous machine (PMSM)

The permanent-magnet synchronous machine is widely used in industrial, energy or traction applications, where a high efficiency is needed. Several stator and rotor designs are established, while two main types have to be mentioned: Surface-mounted magnets and buried magnets (Figure 3.1). With surface-mounted magnets usually the magnetic reluctance in d-axis and q-axis is equal, whereas for buried magnets it is possible to significantly increase this difference by the specific magnet arrangement and the use of flux barriers.

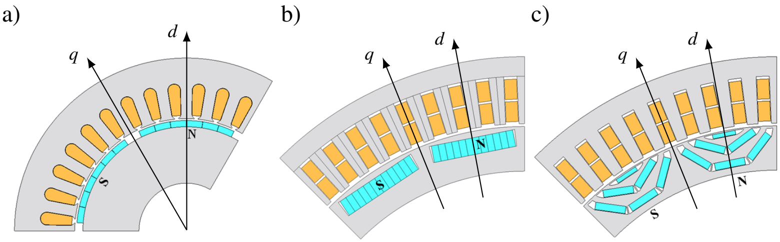

Figure 3.1.: Different section examples of permanent-magnet synchronous machines: a) Surface-mounted rotor magnets, b) buried rotor magnets, c) buried rotor magnets with increased reluctance difference L_q/L_d [65]

3.1. Parameters and equivalent circuit

The presented indirect method for efficiency determination is mainly based on the electrical equivalent circuit per phase of a permanent-magnet synchronous machine. There are already standardized procedures for induction machines, based on the equivalent circuit. The idea of calculating the efficiency this way is therefore well-accepted. Figure 3.2 shows the equivalent circuit of a permanent-magnet synchronous machine without reluctance difference in d- and q-axis for constant speed n. The parameters are explained in Table 3.1.

The inner air gap power P_δ is built up by the stator current I_s the back EMF U_p. According

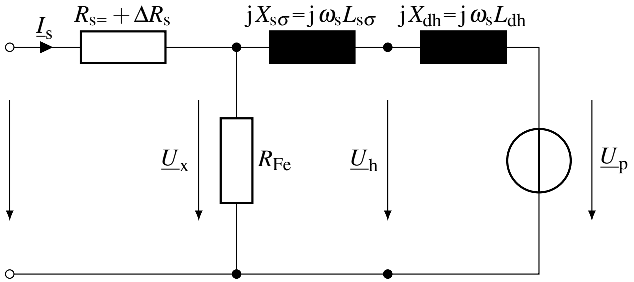

Figure 3.2.: Equivalent circuit per phase of a permanent-magnet synchronous machine without reluctance difference in d- and q-axis ($X_{dh} \cong X_{qh}$)

to the electromagnetic energy conversion the electromagnetic torque M_{em} is created. Due to the rotor rotation several rotor losses occur: the mechanical friction and windage losses P_{fr+w} (Section 3.2), the eddy current and hysteresis losses in the rotor lamination due to sub- and super-harmonic field waves $P_{Fe,r}$ (Section 3.3), and the eddy current losses in the rotor magnets P_M (Section 3.4). If e.g. motor operation is assumed, the shaft torque will be:

$$M = M_{em} - \left(P_{fr+w} + P_{Fe,r} + P_M\right) / \left(2\pi \cdot n\right) \ . \tag{3.1}$$

In this case the rotor losses are not present in the equivalent circuit at first. They may be but are approximated by calculating the equivalent iron resistance R_{Fe} from the stator iron losses $P_{Fe,s}$ (Section 3.3) *and* the rotor iron losses $P_{Fe,r} + P_M$. Then the calculated shaft torque is $M = M_{em}$.

The electromagnetic torque of the machine at q-current operation ($I_s = I_{sq}, I_{sd} = 0$) (Figure 3.3) is calculated via [5]

$$M_{em} = m_s \cdot p \cdot \frac{\Psi_p}{\sqrt{2}} \cdot I_s \ , \tag{3.2}$$

where m_s is the number of stator phases [2], p is the number of pole pairs and Ψ_p is the magnetic flux linkage amplitude due to the rotor permanent-magnet excitation.

The AC resistance $R_{s\sim}$ represents both the DC copper losses $P_{Cu=}$ and the additional eddy

---

[2] In the most common case of three-phase machines $m_s = 3$.

Table 3.1.: Electrical parameters per phase of a permanent-magnet synchronous machine according to Figure 3.2

U_s	Stator phase voltage
U_x	Reactance voltage
U_h	Induced voltage in the stator winding due to the resulting air gap field as sum of stator and rotor fundamental field wave (main voltage)
U_p	Induced voltage in the stator winding due to the magnetized rotor (back EMF)
I_s	Stator phase current
$R_{\mathrm{s}\sim} = R_{\mathrm{s}=} + \Delta R_\mathrm{s}$	AC winding resistance per phase (as sum of the DC resistance $R_{\mathrm{s}=}$ and additional losses due to current displacement ΔR_s)
R_Fe	Equivalent iron resistance to take the stator iron losses into account
$X_{\mathrm{s}\sigma} = 2\pi f_\mathrm{s} \cdot L_{\mathrm{s}\sigma}$	Stator leakage reactance (f_s: Stator frequency, $L_{\mathrm{s}\sigma}$: Stator leakage inductance)
$X_\mathrm{dh} = 2\pi f_\mathrm{s} \cdot L_\mathrm{dh}$	Main reactance of d-axis (L_dh: Main inductance of d-axis)

current losses in the stator winding ΔP_Cu due to the induction effect of the AC stray slot field ($f = f_\mathrm{s}$, Section 3.2). For the calculation of the equivalent iron resistance R_Fe from measurements it is assumed that the main flux as well as the stator stray flux contribute to the stator iron losses. In the stator yoke this assumption is more or less correct, in the teeth it is less accurate, as the main flux passes the teeth in normal direction whereas the stray flux is crossing perpendicularly with linear increasing intensity along the tooth axis towards the bottom of the slots. For the small stray flux at the winding overhang the flux path is even more complex. Nevertheless also the stray flux has an impact on the stator iron losses due to the induced eddy currents. Therefore the equivalent iron resistance R_Fe is arranged like in Figure 3.2 and not between the main reactance X_dh and the leakage reactance $X_{\mathrm{s}\sigma}$ [41].

The equivalent circuit is valid for sinusoidal voltages and currents and $L_\mathrm{d} = L_\mathrm{q}$. If the machines is fed by a voltage source inverter, the stator voltage U_s is replaced by $U_{\mathrm{s},k}$ (k-th

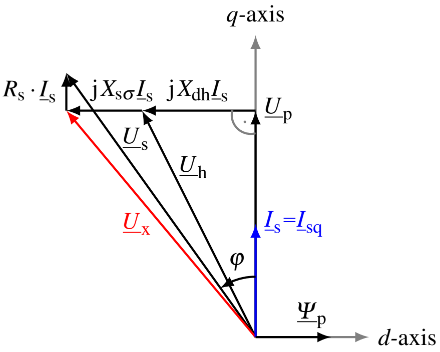

Figure 3.3.: Phasor diagram per phase of a permanent-magnet synchronous machine at load with q-current operation ($X_{qh} = X_{dh}$)

voltage harmonic of the inverter output voltage, frequency $f_{s,k} = k \cdot f_s$), while U_p is zero ($\forall k \neq 1$). This leads to harmonic stator currents $I_{s,k}$ and additional losses due to inverter feeding (Section 3.6).

For machines with reluctance difference in d-axis and q-axis (Figure 3.4) the torque calculation in (3.2) extends to

$$M_{em} = m_s \cdot p \cdot \left(\frac{\Psi_p}{\sqrt{2}} \cdot I_{sq} + (L_d - L_q) \cdot I_{sd} \cdot I_{sq} \right) , \tag{3.3}$$

where $(L_d - L_q) \cdot I_{sd} \cdot I_{sq}$ is the amount of reluctance torque. In case that the inductance $L_q = L_{qh} + L_{s\sigma}$ in q-axis is smaller than L_d in d-axis, a negative d-current I_d has to be set for positive torque M_{em} and the current angle β^* (Figure 3.4) is positive between $0° \ldots 90°$ el. in motor operation and between $180° \ldots 90°$ el. in generator operation. The phasor diagram (Figure 3.4) shows, that this operation is already a kind of field weakening due to $I_{sd} < 0$, although the machine is operated in the base speed range.

The following subsections give a brief overview of the loss components, that are relevant for this work. A deeper view into the nature of losses and their calculation is given e.g. in [5], [43], [48].

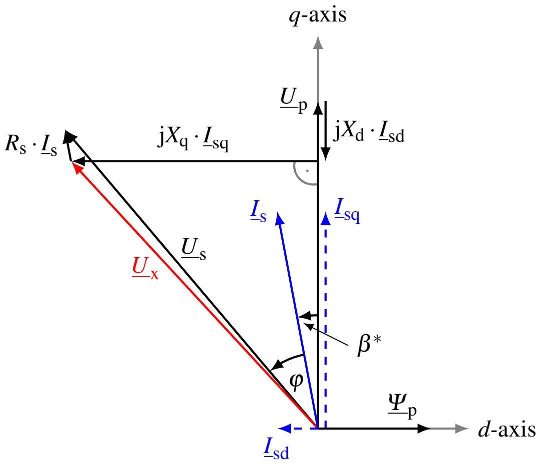

Figure 3.4.: Phasor diagram per phase of a permanent-magnet synchronous machine at load with positive current angle $\beta^* = 10\,^\circ\mathrm{el.}$

3.2. Losses in the stator winding

For slow turning permanent-magnet synchronous machineswith a high number of poles and a high rated torque usually the copper losses [3] in the stator winding are the dominant loss component. For AC machines these losses have to be divided into two major components: The *DC* copper losses $P_{\mathrm{Cu}=}$, which are independent from the frequency of the stator current and the additional stator losses ΔP_Cu, which strongly depend on the stator frequency f_s. Both components together are expressed as $P_{\mathrm{Cu}\sim}$, where

$$P_{\mathrm{Cu}\sim} = P_{\mathrm{Cu}=} + \Delta P_\mathrm{Cu} \, . \tag{3.4}$$

In general the stator copper losses depend on the stator winding resistance. With the number of stator phases m_s the losses are calculated as

$$P_{\mathrm{Cu}\sim} = m_\mathrm{s} \cdot R_{\mathrm{s}\sim} \cdot I_\mathrm{s}^2 = m_\mathrm{s} \cdot (R_{\mathrm{s}=} + \Delta R_\mathrm{s}) \cdot I_\mathrm{s}^2 \, , \tag{3.5}$$

where, like in (3.4), also the stator winding resistance is split into a *DC* component $R_{\mathrm{s}=}$ and an amount of increased resistance ΔR_s due to the additional stator copper losses. Both

---

[3] The term *copper losses* and the subscript Cu is used for each kind of conductor material.

components of the stator resistance also depend on the stator winding temperature θ in different manners, which will be described in the following sections. Usually a reference temperature of 20 °C is assumed and therefore defined by the subscript *cold*, while the (variable) winding temperature under load is much higher and is defined as *warm*.

3.2.1. Frequency-independent losses

The *DC* component of the cold stator resistance depends on the material conductivity and the conductor geometry and is calculated via

$$R_{\mathrm{s=,cold}} = \frac{N_{\mathrm{s}} \cdot l_{\mathrm{Cu}}}{\kappa_{20\,^{\circ}\mathrm{C}} \cdot A_{\mathrm{Cu}} \cdot a_{\mathrm{o}} \cdot a_{\mathrm{i}}} \;, \tag{3.6}$$

with the number of turns per phase N_{s}, the total conductor length per turn (stack length plus winding overhang) l_{Cu}, the number of parallel branches per phase a_{o} and parallel strands per turn a_{i}, the electric conductivity $\kappa_{20\,^{\circ}\mathrm{C}}$ at 20 °C [4], and the conductor cross section per strand A_{Cu}. In the typical temperature range of electrical machines, the electric conductivity changes linearly with the conductor temperature ϑ_{Cu}. Therefore the warm resistance is calculated via

$$R_{\mathrm{s=,warm}} = [1 + \alpha_{\mathrm{Cu}} \cdot (\vartheta_{\mathrm{Cu}} - 20\,^{\circ}\mathrm{C})] \cdot R_{\mathrm{s=,cold}} = k_{\vartheta} \cdot R_{\mathrm{s=,cold}} \;, \tag{3.7}$$

where α_{Cu} is the linear temperature coefficient [5], and k_{ϑ} is defined here as the linear *DC* resistance increase factor. The linear resistance increase of copper windings is shown in Figure 3.5.

3.2.2. Frequency-dependent losses

At AC feeding additional losses due to current displacement occur in the stator winding. This effect is considered by the corresponding increase of stator resistance and is described as follows.

---

[4] For copper windings a conductivity of $\kappa_{20\,^{\circ}\mathrm{C}} = 56\,\mathrm{MS/m}$ is typical.

[5] $\alpha_{\mathrm{Cu}} = 0.392\,\%/\mathrm{K}$

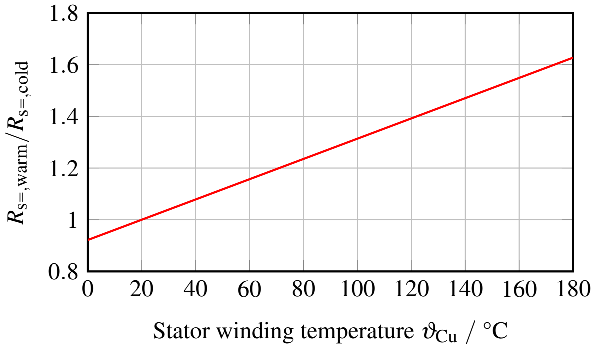

Figure 3.5.: Linear temperature dependency of the electrical resistance of copper

Second order current displacement

The slot leakage flux crosses the slot perpendicularly. If an AC current with frequency f_{s} is flowing in the stator winding, circulating eddy currents in axial direction are induced in the conductors. According to Lenz's rule, these currents must flow in the specific direction to create an additional magnetic field, which partially compensates the original inducing leakage field [5]. As a result, the eddy currents add up with the original impressed stator current in the upper part of the conductor, while they cancel out in the lower conductor part. Therefore the resulting current flows in a smaller area at the top side of the conductor (skin effect). This effect is called *second order* current displacement. Also an interference between the magnetic field of adjacent conductors occurs leads to additional current displacement in the conductor area (proximity effect). As the conducting area reduces, the conductor resistance is increased.

The current density decreases exponentially along the conductor cross-section in slot axis direction, while the penetration depth

$$d_{\mathrm{E}} \propto \sqrt{\frac{1}{\pi f \mu \kappa}} \tag{3.8}$$

depends on the current frequency f, the conductor material permeability μ, and the material conductivity κ. The permeability is usually near to μ_0 as well for copper (diamagnetic material) as aluminum (paramagnetic material). The electric conductivity strongly depends on the conductor temperature ϑ_{Cu}, which leads to a decreasing current displacement for rising temperature.

For calculation, the concepts of *Field* and *Emde* [19], [20] are applied, which are used e.g. in [3], [36], [41].

At first, an artificial slot geometry is considered, where the conductors are equally distributed (Figure 3.6b). Conductors with round cross section are transformed to equivalent rectangular conductors with the width b_{T} and the height h_{T}. The number of vertical conductor layers is called m_{T}, while the number of conductors side by side is a_{T}.

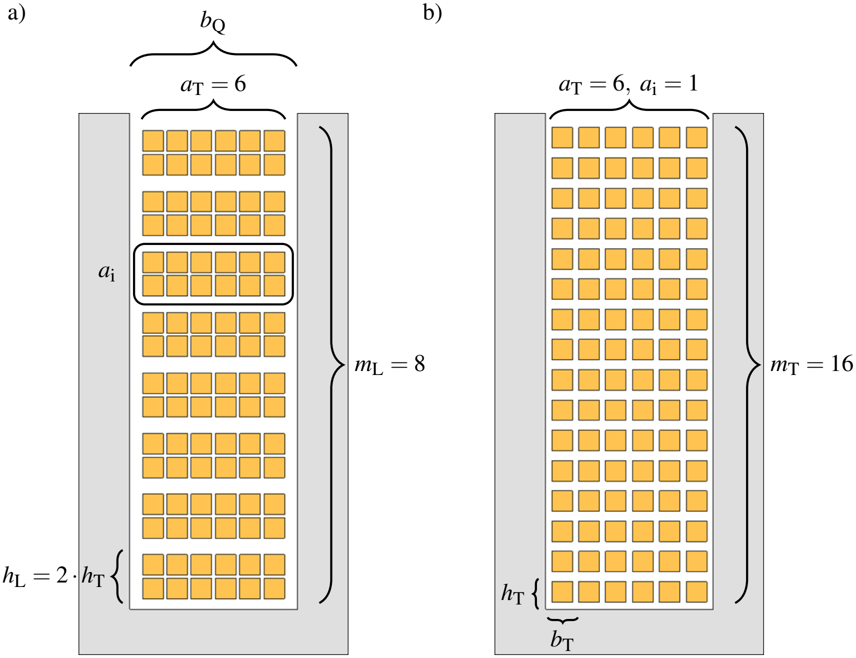

Figure 3.6.: Simplified exemplary slot model for the determination of current displacement: a) first and second order current displacement effect: 8 turns per slot with 12 parallel strands per turn, b) only second order current displacement effect: 16 turns per slot with one strand per turn

With the *reduced conductor height* ξ for this geometry

$$\xi = \frac{h_\mathrm{T}}{d_\mathrm{E}} = h_\mathrm{T} \cdot \sqrt{\pi \cdot f \cdot \mu_0 \cdot \kappa_\mathrm{Cu}(\vartheta) \cdot \frac{a_\mathrm{T} \cdot b_\mathrm{T}}{b_\mathrm{Q}}} \tag{3.9}$$

the second order current displacement factors are determined:

$$\varphi(\xi) = \xi \cdot \frac{\sinh(2\xi) + \sin(2\xi)}{\cosh(2\xi) - \cos(2\xi)} \; , \tag{3.10}$$

$$\psi(\xi) = 2\xi \cdot \frac{\sinh(2\xi) - \sin(2\xi)}{\cosh(2\xi) + \cos(2\xi)} \; , \tag{3.11}$$

where $\varphi(\xi)$ describes the influence of the skin effect and $\psi(\xi)$ the influence of the proximity effect between adjacent conductors. In (3.9) $a_\mathrm{T} \cdot b_\mathrm{T}$ is the total width of conductors, which is evaluated in relation to the slot width b_Q.

With (3.10) and (3.11) the resistance increase factor

$$k_\mathrm{R2} = \varphi(\xi) + \frac{m_\mathrm{T}^2 - 1}{3} \cdot \psi(\xi) \tag{3.12}$$

is determined. The current displacement is assumed to occur only in the axial machine section with the iron length l_Fe due to the AC slot stray flux, whereas the flux density in the winding overhang is much smaller. Therefore (nearly) no resistance increase occurs in the winding overhang (length l_b), and the increase factor k_R2 reduces to

$$\bar{k}_\mathrm{R2} = \frac{k_\mathrm{R2} \cdot l_\mathrm{Fe} + l_\mathrm{b}}{l_\mathrm{Fe} + l_\mathrm{b}} \; . \tag{3.13}$$

First order current displacement

In order to reduce second order current displacement, the conductor height has to be reduced. Therefore a_i parallel sub-conductors per turn are introduced (Figure 3.6a). The actual arrangement especially of round conductors is usually not exactly known, so that assumptions about the location of the conductors in the slot are necessary for calculation.

If no further measures are applied, the AC slot leakage flux again induces eddy currents in the parallel connection of the a_i sub-conductors, which leads to equalizing currents between the parallel sub-conductors. So the resistance is also increased, as if the bundle was one "big" conductor with the accumulated cross section $A_{\mathrm{Cu}} = a_{\mathrm{i}} \cdot b_{\mathrm{T}} \cdot h_{\mathrm{T}}$. But the equalizing currents have to flow along the total length per sub-conductor to the electric parallel connection point, so these losses are smaller than in one "big" conductor. This increase of losses is called *first order* current displacement. In order to effectively reduce these circulating equalizing currents, the sub-conductors, also called conductor strands, have to be transposed along the machine's axial length in one slot or between different slots. If all possible permutations of transpositions were applied, the resulting induced eddy currents as equalizing currents would cancel out to zero. For big machines this is done by using *Roebel* bars. However, for round wires usually a random unpredictable transposition is present, which in most cases is rather ineffective.

Therefore in the following formulas do not consider any transpositions. These calculations are only valid, if the sub-conductor cross-section is small enough, so that no excessive second order current displacement occurs.

Again the reduced conductor height is calculated, but now the height of the total conductor layer h_{L} per turn is taken into account, and the length between two connection points of the a_{i} parallel sub-conductors is – in worst case – only one turn length $2 \cdot (l_{\mathrm{Fe}} + l_{\mathrm{b}})$:

$$\xi = \frac{h_{\mathrm{L}}}{d_{\mathrm{E}}} = h_{\mathrm{L}} \cdot \sqrt{\pi \cdot f \cdot \mu_0 \cdot \kappa_{\mathrm{Cu}}(\vartheta) \cdot \frac{l_{\mathrm{Fe}}}{l_{\mathrm{Fe}} + l_{\mathrm{b}}} \cdot \frac{a_{\mathrm{T}} \cdot b_{\mathrm{T}}}{b_{\mathrm{Q}}}} \; . \tag{3.14}$$

With the current displacement factors (3.10) and (3.11), applied to the circulating equalizing current effect, in combination with (3.14) the first order current displacement increase factor of the resistance is determined:

$$k_{\mathrm{R1}} = \varphi(\xi) + \frac{m_{\mathrm{L}}^2 - 1}{4} \cdot \psi(\xi) \; . \tag{3.15}$$

AC resistance increase

Both first order and second order resistance increase factors (3.13, 3.15) are combined to the resulting AC resistance increase factor k_{R}. Thus the AC resistance $R_{\mathrm{s}\sim}$ is determined via

$$R_{\mathrm{s}\sim}(\vartheta) = k_{\mathrm{R}}(\vartheta) \cdot R_{\mathrm{s}=}(\vartheta) = \big(k_{\mathrm{R1}}(\vartheta) + \bar{k}_{\mathrm{R2}}(\vartheta) - 1\big) \cdot R_{\mathrm{s}=}(\vartheta) \; . \tag{3.16}$$

The factor $k_{\mathrm{R}}(\vartheta)$ decreases with increasing conductor temperature due to the decreasing $\kappa_{\mathrm{Cu}}(\vartheta)$.

3.2.3. Total losses and temperature dependency

By combining the DC and AC resistance factors k_ϑ and $k_{\mathrm{R}}(\vartheta)$ to

$$K = k_\vartheta \cdot k_{\mathrm{R}}(\vartheta) = k_\vartheta \cdot \left(k_{\mathrm{R1}}(\vartheta) + \bar{k}_{\mathrm{R2}}(\vartheta) - 1\right) \ , \tag{3.17}$$

the AC resistance $R_{\mathrm{s=,warm}}$ at a given conductor temperature ϑ_{Cu} is determined. The total losses $P_{\mathrm{Cu}\sim}$ are hence

$$P_{\mathrm{Cu}\sim} = m_{\mathrm{s}} \cdot k_{\mathrm{R}} \cdot R_{\mathrm{s=,warm}} \cdot I_{\mathrm{s}}^2 = m_{\mathrm{s}} \cdot K \cdot R_{\mathrm{s=,cold}} \cdot I_{\mathrm{s}}^2 \ . \tag{3.18}$$

As the conductivity κ_{Cu} decreases with rising temperature ϑ, the DC component of the stator resistance is increased (Figure 3.5), while the AC component is decreased according to increased penetration depth (3.8). For rather small $k_{\mathrm{R}}(\vartheta = 20\,°\mathrm{C}) < 2$, the increasing trend of the DC component is dominant (Figure 3.7) – exemplary shown for test machine M2 (see Chapter 6) at rated stator frequency $f_{\mathrm{sN}} = 133.3\,\mathrm{Hz}$.

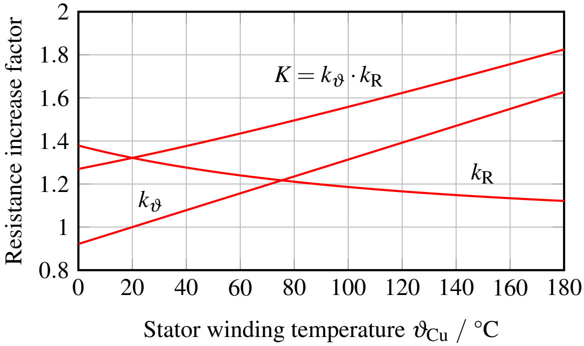

Figure 3.7.: Calculated AC resistance increase. Example: Test machine M2 at rated stator frequency $f_{\mathrm{sN}} = 133.3\,\mathrm{Hz}$

For higher $k_{\mathrm{R}}(\vartheta = 20\,°\mathrm{C}) > 2$, a loss minimum occurs at temperatures $\vartheta_{\mathrm{Cu}} > 20\,°\mathrm{C}$ (Figure 3.8) – exemplary shown for test machine M2 at increased stator frequency $f_{\mathrm{s}} = 2.5 \cdot f_{\mathrm{sN}} = 333.3\,\mathrm{Hz}$.

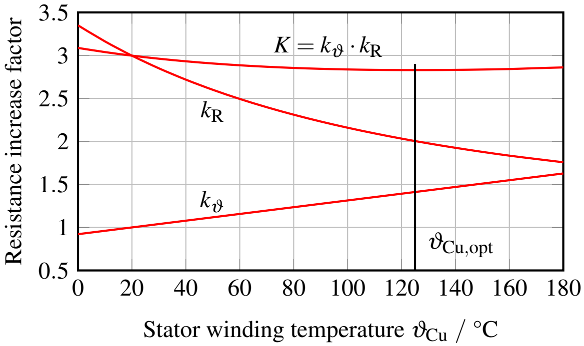

Figure 3.8.: Calculated AC resistance increase. Example: Test machine M2 at the stator frequency $f_{\mathrm{s}} = 2.5 \cdot f_{\mathrm{sN}} = 333.3\,\mathrm{Hz}$. Minimum of AC stator resistance at $\vartheta_{\mathrm{Cu,opt}} = 125\,°\mathrm{C}$

3.3. Losses in the motor lamination

Due to the operation principle of electromagnetic machines, high-permeable ferromagnetic iron is necessary to guide the magnetic flux. If the varying electromagnetic fields of the electrical machine enter the iron, losses due to induced eddy currents and changing magnetization with corresponding hysteresis losses occur. In order to reduce the eddy currents, the magnetically active iron parts are made of electrically insulated laminated stacks.

Classical empirical calculation approaches like Steinmetz [55] or Bertotti [4] usually divide the total iron losses P_{Fe} into up to three loss groups: hysteresis losses $P_{\mathrm{Fe,Hy}} \propto f \cdot B^2$, classical eddy current losses $P_{\mathrm{Fe,ec}} \propto f^2 \cdot B^2$, and excess losses $P_{\mathrm{Fe,ex}} \propto f^{3/2} \cdot B^{3/2}$, which are identified with anomalous eddy current losses. For each component loss coefficients are determined by measurement e.g. with a standardized Epstein frame or single sheet tester.

Several extended semi-analytic or analytic loss models, like [21], [22], [33], [54], exist, that allow a loss calculation especially for high-speed machines, where due to the high frequencies the iron losses are the main loss component.

The manufacturers of steel sheets for electrical machines often provide iron loss coefficients at defined testing parameters, but do not give the parameters of each of the three above noted individual loss groups.

For non-grain-oriented steel sheets, which are mainly used in electrical machines, the excess losses are usually less then 10 % of P_{Fe}. Hence, only hysteresis and classical eddy current losses are used as approximation of the total iron losses as

$$P_{\mathrm{Fe}} = k_{\mathrm{V}} \cdot \left(P_{\mathrm{Fe,Hy}} + P_{\mathrm{Fe,Ft}}\right) \ . \tag{3.19}$$

Each loss group depends with a limit of $B < 2.3\,\mathrm{T}$ roughly on the square of the magnetic flux density B. Here the *Foucault* losses $P_{\mathrm{Fe,Ft}} \propto f^2 \cdot B^2$ are the approximation of the total eddy current losses. The eddy current reaction field is for $f < 1\,\mathrm{kHz}$ usually neglected, giving the dependency $\propto f^2$.

By using finite element software, a separation into these two loss groups (3.19) is possible, if no detailed separate loss coefficients are available.

The processes of punching or laser cutting, stacking, and welding lead to increased hysteresis losses, to decreased magnetic permeability and increased eddy current losses due to an increased effective electrical conductivity of the iron stack. This results e.g. from crystal changes, low-resistive bridges between sheets at the cutting edges and welding spots, or local surface damages [37], [38], [47], [59], [60]. The loss increase is considered by the post-processing factor k_{V} in (3.19) and may differ for the individual sections of the motor. In this work the factor will be determined from the difference of measured and simulated no-load iron losses as one separate parameter for each section.

At the permanent-magnet synchronous machine the air gap flux density B_δ correlates via the magnetic flux density $B \propto B_\delta$ in the iron with the reactance voltage U_{x}. Therefore a square dependency $P_{\mathrm{Fe}} \propto U_{\mathrm{x}}^2$ is assumed in the following chapters.

For the stator and the rotor of a permanent-magnet synchronous machine different traveling and pulsating field waves are responsible for the iron losses in the steel sheets.

The stator lamination is mainly induced by the fundamental rotating traveling field wave, through the combination of the stator field and the first order rotor field $\mu = 1$ at synchronous speed and to a small amount by higher harmonics $\mu > 1$.

The rotor is rotating synchronously with the stator field. Therefore the fundamental stator field wave $\nu = 1$ cannot induce the rotor. But due to harmonic effects other field waves

$\nu \neq 1$ may enter the rotor and produce losses like (3.19).

At generator no-load operation, when the stator field is zero, the rotor can only be induced by the modulation effect of the rotor field due to the stator slot openings. The frequency f_{Q} of the inducing field wave due to this effect with the order μ_{Q} in the rotor is determined by

$$f_{\mathrm{Q}} = Q_{\mathrm{s}} \cdot n = Q_{\mathrm{s}} \cdot \frac{f_{\mathrm{s}}}{p} = \frac{Q_{\mathrm{s}}}{p} \cdot f_{\mathrm{s}} \,, \tag{3.20}$$

with the number of stator slots Q_{s}, the mechanical rotor speed n, the number of pole pairs p, and the fundamental electrical stator frequency f_{s} of stator voltage (and current). The rotor frequencies f_{Q} are also caused by the slot harmonic field waves ν_{Q} of the stator at load.

So, if the stator current system I_{s} excites the stator field, further harmonics $\nu \neq 1$ and especially the slot harmonics ν_{Q} can induce the rotor. The rotor frequencies f_{r} depend on the harmonics ν of the stator field wave by:

$$f_{\mathrm{r}} = |1 - \nu| \cdot f_{\mathrm{s}} \,. \tag{3.21}$$

For integer-slot windings and the double-layer tooth-coil winding with $q = 1/2$, which all have no sub-harmonic field waves, the lowest value is $\nu = 1$. For all other fractional slot windings there exist long-wave-length sub-harmonic fields $|\nu| < 1$, e.g. for $q = 1/4$ one sub-harmonic with $\nu = -1/2$.

3.4. Losses in the permanent magnets

Like the rotor iron, also rotor magnets are induced by harmonic air gap field components, e.g. due to the pulsating field changes at the stator slot openings. This leads to eddy current losses P_{M} in the magnet volume. Several publications (e.g. [6], [8], [13], [23], [42], [44], [46], [49]) deal with analytical calculation approaches to determine these magnet losses. Some of these method are based on planar representations of the cylindrical field problem, where a stator current sheet with variable amplitude and frequency is applied, or on extended equivalent circuit models for higher harmonics. On the other hand three-dimensional, or less accurate two-dimensional, numerical simulations are possible to determine the magnet losses.

The eddy currents can effectively be reduced by using magnet segments instead of massive magnets per pole ([18], [53]). This is especially true for surface-mounted rotor magnets. For buried magnets, the surrounding rotor iron guides the magnetic flux around the magnets due to the much higher magnetic iron permeability ($\mu_{\mathrm{Fe}} \gg \mu_{\mathrm{M}}$), so that the magnet losses are small, if the rotor iron is not saturated too much. But then the iron losses in the rotor iron surface are increased.

The machines, that are investigated in this work, do all have segmented rotor magnets (Chapter 6). Also the rotational speed n is rather low. Therefore the magnet losses are considered to be rather small compared to the total machine losses and are not calculated analytically here. At the numerical simulations (Chapter 8) they are of course considered.

3.5. Friction and windage losses

In each rotating machine friction and windage losses occur due to a) the dominating air movement inside the machine as air friction and fan losses (in case of shaft-mounted fans) and b) the much smaller inner friction in the mechanical bearings. These losses strongly depend on the machine's mechanical speed n and therefore have a big impact on high-speed machines. The friction and windage losses are mainly load-independent (apart from a load-dependent component of the bearing friction losses) and are already fully present at no-load operation.

In order to calculate the air friction and fan losses in detail, complex non-linear fluid dynamics simulations are required, but there exist also empirical formulas to approximate the losses. In this work, due to the rather low speeds ($\leq 3000\,\mathrm{min}^{-1}$), small shaft diameter, and grease-lubricated high-quality low-friction ball bearings, the bearing friction losses are small and therefore neglected.

For a cylindrical rotor the surface is usually very smooth and the air friction losses at low speed are of small magnitude. The losses are roughly estimated [11], [41] via:

$$P_{\mathrm{fr+w,air}} = c_{\mathrm{f}} \cdot \pi \cdot \rho_{\mathrm{air}} \cdot (2\pi \cdot n)^3 \cdot r_{\mathrm{ro}}^4 \cdot l_{\mathrm{Fe}} \tag{3.22}$$

with use of

$$c_{\mathrm{f}} = 0.035 \cdot Re^{-0.15} \tag{3.23}$$

and

$$Re = 2\pi \cdot n \cdot r_{\mathrm{ro}} \cdot \frac{\delta}{\nu_{\mathrm{air}}} \ , \tag{3.24}$$

where ρ_{air} is the temperature-dependent air mass density, r_{ro} is the rotor outer radius, l_{Fe} the active iron length, δ is the mechanical air gap, ν_{air} is the kinematic viscosity of air, and Re is the dimensionless *Reynolds number*. These formulas hold true for turbulent air flow $Re > Re_{\mathrm{crit}}$, with $Re_{\mathrm{crit}} \cong 1000$.

If a shaft-mounted fan is used to cool the machine, the fan power has to be provided internally by the electrical motor power. The fan power leads to increased friction and windage losses. Like before, an empirical formula is used to estimate the fan losses at turbulent air flow [50]:

$$P_{\mathrm{fr+w,fan}} = 20 \cdot r_{\mathrm{ro}} \cdot (l_{\mathrm{Fe}} + 0.15) \cdot (2\pi \cdot r_{\mathrm{ro}} \cdot n)^2 \ . \tag{3.25}$$

In (3.25), $P_{\mathrm{fr+w,fan}}$ is in [W], r_{ro} is in [m], l_{Fe} is in [m], and n is in $[1/\mathrm{s}]$.

The shaft-mounted fan losses – if present – usually exceed the air friction losses significantly.

3.6. Additional losses due to inverter supply

At voltage source inverter operation the feeding voltage is not longer sinusoidal. Depending on the modulation procedure higher harmonics with ordinal number k and RMS values $U_{\mathrm{s},k}$ of the stator voltage occur, while $U_{\mathrm{s},1}$ is the fundamental voltage. The voltage harmonics lead to stator current harmonics $I_{\mathrm{s},k}$ with the frequency $f_{\mathrm{s},k} = k \cdot f_{\mathrm{s}} = \omega_{\mathrm{s},k}/(2\pi)$.

The equivalent circuit (Figure 3.9) differs from Figure 3.2 as the back EMF U_{p} is considered zero for all voltage harmonics $k > 1$. Considering a three-phase stator winding system, harmonics of ordinal number k, that generate fundamental field waves $\nu = 1$, that rotate in the same direction as $\nu = 1$ for $k = 1$, are of positive order $k > 0$. Those, that rotate into opposite direction, can be denoted by negative k. Hence, we get $|k| > 1$ and $k > 0$ or $k < 0$.

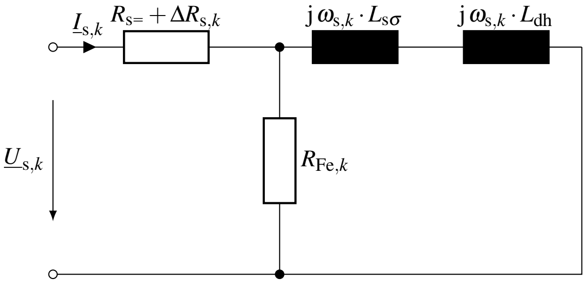

Figure 3.9.: Equivalent circuit per phase of a permanent-magnet synchronous machine at inverter feeding for $k>1$ and $L_{dh}\cong L_{qh}$, $L_{s\sigma d}\cong L_{s\sigma q}=L_{s\sigma}$. $R_{Fe,k}\gg\omega_{s,k}(L_{s\sigma}+L_{dh})=\omega_{s,k}L_d$ and $\omega_{s,k}=|k|\omega_s$

The harmonic current $I_{s,k}$ is approximately calculated [5] via

$$I_{s,k}\cong\frac{U_{s,k}}{\sqrt{R_{s\sim,k}^2+(k\omega_s)^2\cdot L_d^2}}\cong\frac{U_{s,k}}{|k|\omega_s\cdot L_d}\ , \tag{3.26}$$

with $R_{s,k}=R_{s=}+\Delta R_{s,k}$.

As, in contrast to induction machines, at synchronous machines the total synchronous inductance is limiting the harmonic components and not only the small stray inductance $L_{s\sigma}$, the values $I_{s,k}$ are small, and the stator current is nearly sinusoidal even for moderate switching frequencies f_{PWM} of the feeding voltage source inverter. The difference between the RMS value of the total current I_s and the RMS value of the fundamental current $I_{s,1}$ should therefore be small with respect to the rated current I_{sN}.

Nevertheless the harmonic currents $I_{s,k}$ (RMS values) lead to a) additional losses in the stator winding with rather high frequencies, described by $\Delta R_{s,k}\cdot I_{s,k}^2$, b) additional fast rotating fundamental air gap field waves ($\nu=1$) with positive or negative speed $n_{syn,k}=k\cdot f_s/p$. These field harmonics induce the stator and rotor and cause additional iron losses and magnet losses, described by $R_{Fe,k}$ [7], [46], [58].

According to Figure 3.9 the values $I_{s,k},|k|\neq 1$, are independent of the machine power proportional to $U_p\cdot I_{s,1}\cdot\cos\varphi_i$ with $\cos\varphi_i=\angle(\underline{U}_p,\underline{I}_{s,1})$. Hence, the sum of additional losses is nearly load-independent and depends only on the amount of voltage harmonics and thus on the modulation degree m_a of the voltage source inverter:

$$m_\mathrm{a} = \frac{\hat{U}_{\mathrm{LL},1}}{(\sqrt{3}/2) \cdot U_\mathrm{DC}}, \quad 0 \leq m_\mathrm{a} \leq 1 \,, \tag{3.27}$$

where $\hat{U}_{\mathrm{LL},1}$ is the amplitude of the fundamental line-to-line inverter output voltage and U_DC is the DC link voltage of the inverter. Figure 3.10 [41] shows an exemplary calculated *Fourier* spectrum of the most dominant voltage harmonics for synchronous pulse width modulation with a ratio of switching frequency vs. fundamental frequency $f_\mathrm{PWM}/f_\mathrm{s} = 15$. The maximum harmonic content and therefore the maximum additional losses are expected at a modulation degree between 0.5 ... 0.75.

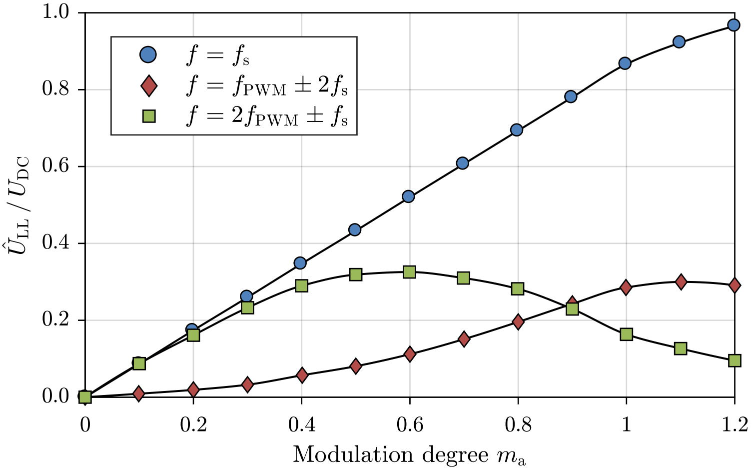

Figure 3.10.: Calculated fundamental and harmonic voltage amplitudes of the inverter output voltage at PWM with $f_\mathrm{PWM}/f_\mathrm{s} = 15$ in dependence of the modulation degree m_a [41]

4. Experiments

This chapter describes the experiments for the indirect efficiency determination: The generator and motor no-load tests, and the removed rotor test. Furthermore the direct efficiency determination method is explained for comparison. In addition, the short-circuit test and the reactive current test may be used for parameter identification of the equivalent circuit.

Each experiment requires specific testing equipment, which is listed at the beginning of each section. The measurement setup for the electrical stator parameters *voltage*, *current*, and *power factor* is considered obligatory for each experiment.

4.1. Generator no-load test

REQUIREMENTS:	Auxiliary drive, torque transducer
VARIABLE:	Mechanical stator speed n
MEASUREMENT:	Stator voltage U_s, shaft torque M

Like for electrically excited synchronous machines, at the generator no-load test the machine is operated with open stator winding terminals and the rotor is driven by an auxiliary drive. But now there is no variable excitation but a variable speed operation. Both machines are coupled by a torque-transducer to measure the no-load shaft torque M_0. The measurement setup is visualized in Figure B.1a.

The stator voltage at the open stator winding terminals represents the no-load load voltage U_0, which itself is nearly equal to the back EMF ($U_\mathrm{s} = U_0 \cong U_\mathrm{p}$, Figure 4.1) as the stator current I_s is zero and the equivalent iron resistance R_Fe is much bigger then the synchronous reactance $X_\mathrm{d} = X_\mathrm{dh} + X_{\mathrm{s}\sigma} = \omega_\mathrm{s} \cdot L_\mathrm{d}$. Due to the proportionality between the RMS value of the back EMF U_p and the corresponding frequency f_s and thus the mechanical speed n, the no-load voltage U_0 rises linearly with n (Figure 4.2). The value of the voltage at a given speed can be used as an indicator for the correct magnet temperature, as the no-load voltage depends linear on the air gap flux density and therefore on the magnet

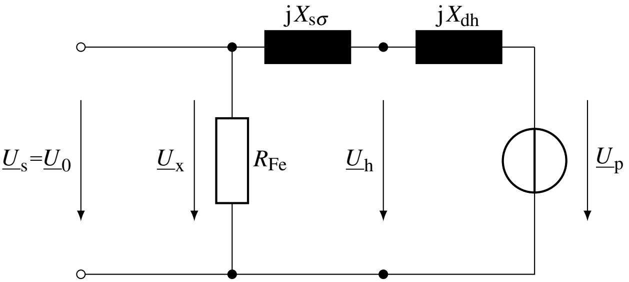

Figure 4.1.: Equivalent circuit per phase at the generator no-load test ($X_{\mathrm{dh}} \cong X_{\mathrm{qh}} \ll R_{\mathrm{Fe}}$)

remanence, which depends on the magnet temperature (Chapter 3). Hence, the experiment should be carried out for the *warm* machine at temperatures similar to the steady-state load condition.

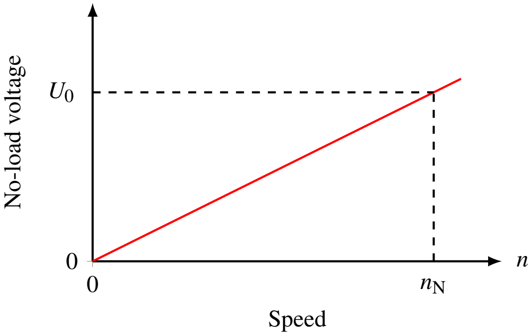

Figure 4.2.: Exemplary curve of generator no-load voltage over speed

With help of the torque transducer the mechanical input power from the auxiliary drive is determined to:

$$P_{\mathrm{m,in,0}} = 2\pi \cdot n \cdot M_0 \ . \tag{4.1}$$

This is performed for different rotor speeds n. The mechanical input power covers the friction and windage losses $P_{\mathrm{fr+w}}$ as well as the no-load iron losses $P_{\mathrm{Fe,0}}$ in stator and rotor and the eddy current magnet losses $P_{\mathrm{M,0}}$. As a result the no-load losses depend on the rotor speed n with $P_{\mathrm{m,in,0}} \propto n^x, x = 2\ldots3$, (Figure 4.3).

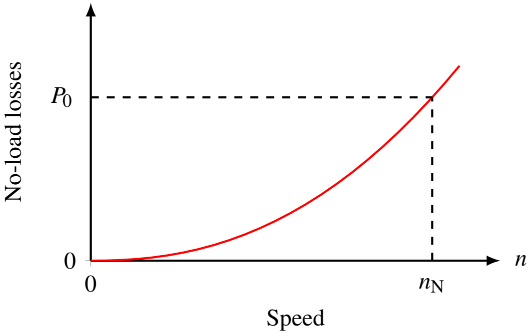

Figure 4.3.: Exemplary curve of generator no-load losses over speed (subscript "m,in" suppressed for readability)

For the further calculations the iron losses are required separately, but a clear separation of $P_{\mathrm{m,in,0}}$ between the mechanical losses and the electromagnetic losses is only possible if the experiment is carried out additionally with a non-magnetized rotor. This might be done during the production process of the machine. If no non-magnetized rotor is available, the friction and windage losses have to be approximated analytically as shown in Section 3.5. As long as these losses are small compared to the total losses, the influence of the approximation on the efficiency value is small.

The generator no-load experiments require a high precision torque measurement of typically a) small torque range $0 \leq M \leq M_{0,\mathrm{max}} \ll M_{\mathrm{N}}$ and b) small measurement error of below $0.5\,\%$. To overcome offset errors of the torque transducer, the test should be performed both in clockwise and counterclockwise rotation direction. The respective measured losses are then to be averaged to the final no-load losses. This procedure is only possible, when no shaft-mounted fan is applied, which has a direction-dependent loss characteristic. Fans with simply radial fan blades allow this test procedure.

4.2. Motor no-load test

REQUIREMENTS:	Inverter-fed variable drive
VARIABLE:	Mechanical rotor speed n
MEASUREMENT:	Fundamental and harmonic stator voltage $U_{\mathrm{s},1}, U_{\mathrm{s},k}$, current $I_{\mathrm{s},1}, I_{\mathrm{s},k}$, and power factor $\cos\varphi_{\mathrm{s},1}, \cos\varphi_{\mathrm{s},k}$

For machines with inverter feeding the variable speed under motor no-load is possible. Again the no-load losses are to be determined for different rotor speed values n. To achieve this, the machine is operated uncoupled, hence without a load machine, at the feeding voltage source inverter. The electrical input power of the machine $P_{\mathrm{el,in,0}}$ is measured by a poly-phase power analyzer at the motor stator winding terminals with the ability to separate the fundamental losses $P_{\mathrm{el,in,0,1}}(k=1)$ from the total no-load losses (sum over all k-values). At the measurement of the total losses no inverter output filter shall be applied to cover all relevant signal frequencies of order k [2]. By doing this, the additional losses due to inverter feeding $P_{\mathrm{el,in,0,ad}}$ are determined (Figure 4.4):

$$P_{\mathrm{el,in,0,ad}} = P_{\mathrm{el,in,0}} - P_{\mathrm{el,in,0,1}} \ . \tag{4.2}$$

The fundamental no-load losses $P_{\mathrm{el,in,0,1}}(k=1)$ contain – like for the generator case – the no-load iron losses $P_{\mathrm{Fe,0}}$ and friction and windage losses $P_{\mathrm{fr+w}}$ as well the $\mathrm{I}^2\mathrm{R}$ losses $P_{\mathrm{Cu,0}}$ due to the fundamental no-load current $I_{\mathrm{s,0,1}}$. Therefore, if a separation of the fundamental and harmonic losses is not possible by the power analyzer, the additional losses due to inverter supply might be calculated via:

$$P_{\mathrm{el,in,0,ad}} = P_{\mathrm{el,in,0}} - m_{\mathrm{s}} \cdot R_{\mathrm{s}\sim} \cdot I^2_{\mathrm{s,0,1}} - P_{\mathrm{m,in,0}} \ , \tag{4.3}$$

where $P_{\mathrm{Cu,0}} = m_{\mathrm{s}} \cdot R_{\mathrm{s}\sim} \cdot I^2_{\mathrm{s,0,1}}$ are the copper losses in the stator resistance at the actual stator winding temperature.

A similar procedure is mentioned in IEC 60034-2-3 [27]. Here the additional losses shall be determined by subtracting the total losses, obtained by feeding the test motor by a true sinusoidal voltage source, such as a special synchronous generator.

The measured fundamental voltage at the motor terminals is the no-load voltage $U_{\mathrm{s},1} = U_0$, which is almost as big as the back EMF U_{p}, because the stator current $I_{\mathrm{s},1} = I_{\mathrm{sq}}$ to over-

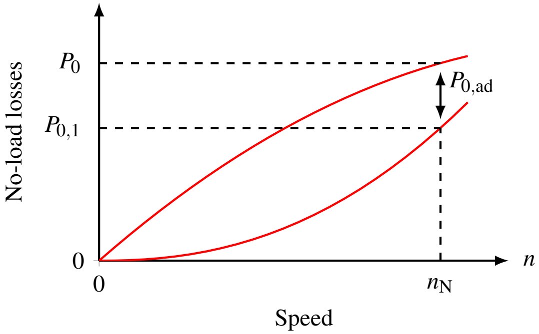

Figure 4.4.: Exemplary curve of fundamental and total motor no-load losses over speed (subscript "el,in" suppressed for readability)

come the no-load losses and thus the voltage drop $X_\mathrm{q} \cdot I_\mathrm{sq}$ is very small. The no-load voltage U_0 depends linearly on the rotor speed n. This allows a definition of the additional losses due to inverter feeding over to the voltage (Figure 4.5). As explained in Section 3.6, the maximum of the additional losses is located between $m_\mathrm{a} = 0.5 \ldots 0.75$, hence roughly between 50 % and 75 % of the maximum inverter output voltage at $m_\mathrm{a} = 1$, if no overmodulation is used. As the total stator inductance L_d or L_q is smoothing the stator current, the current waveform is nearly sinusoidal. The difference between the total and the fundamental stator current I_s and $I_{\mathrm{s},1}$ is rather small for machines with a big stator inductance, e.g. for tooth-coil windings. This difference directly influences the amount of additional losses due to inverter feeding $P_{\mathrm{el,in,0,ad}}$.

4.3. Removed rotor test

REQUIREMENTS:	Variable sinusoidal poly-phase AC source
VARIABLE:	Amplitude and frequency of stator current I_s
MEASUREMENT:	Stator voltage U_s and stator power factor $\cos \varphi_\mathrm{s}$, stator winding temperature ϑ

At the removed rotor test, the current-depending $\mathrm{I}^2\mathrm{R}$ losses in the stator winding are to be determined. These losses include the frequency-independent DC losses $P_{\mathrm{Cu=}}$ as well as the frequency-dependent AC losses ΔP_Cu (Section 3.2). Therefore an AC feeding of the

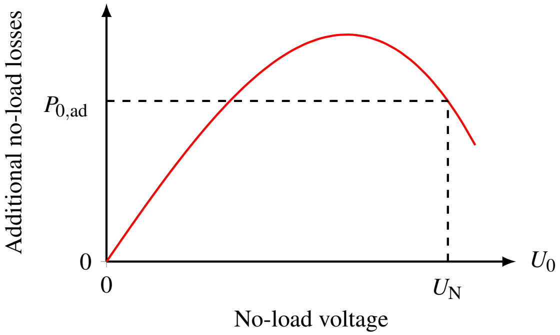

Figure 4.5.: Exemplary curve of the additional no-load losses due to voltage source inverter feeding over the no-load voltage (subscript "el,in" suppressed for readability)

stator winding is necessary. As the additional losses due to voltage source inverter feeding are already determined during the motor no-load test, the fed currents and voltages have to be sinusoidal. This can be achieved by a variable sinusoidal poly-phase AC source, e.g. a rotating converter (Section 7.1.2) or a well filtered static converter. Since the (average) temperature of the stator winding has a big impact on each kind of I^2R loss (Section 3.2), the winding temperature has to be monitored or determined right after the measurement and should fit to the designated winding temperature at load operation.

The removed rotor test is already included in IEC 60034-4 [30] for determination of the leakage inductance and has been used for measuring the stray-load losses in poly-phase inductions machines in [3].

When the rotor of a permanent-magnet synchronous machine is removed, the air gap increases to the whole stator inner diameter. This significantly reduces the main reactance X_dh to the bore field reactance X_sB (Figure 4.6). Nevertheless the resulting magnetic field is not zero, i.e. also iron losses $P_\mathrm{Fe,B}$ in the motor lamination and eddy current losses in massive metal parts may occur. Therefore the end shields of the motor have to be remounted after the rotor removal to cover also all loss components there. Like before, the iron losses are represented by R_Fe in the equivalent circuit.

With the measured electrical input power $P_\mathrm{el,in,B}$ during the removed rotor test at different

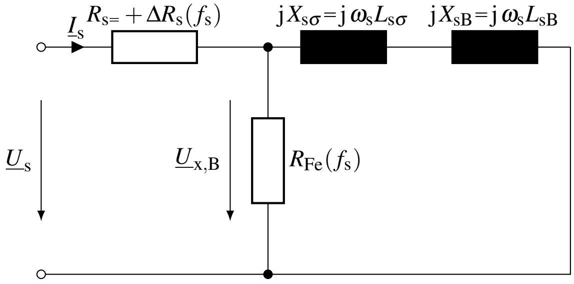

Figure 4.6.: Equivalent circuit per phase at the removed rotor test at frequency f_s ($X_\mathrm{sB} \ll X_\mathrm{dh}$: bore field reactance)

stator frequencies f_s the loss balance is:

$$P_\mathrm{el,in,B} = P_{\mathrm{Cu}=} + \Delta P_\mathrm{Cu} + P_\mathrm{Fe,B} \ . \tag{4.4}$$

To calculate the current-depending losses, the iron losses $P_\mathrm{Fe,B}$ have to be subtracted from the electrical input power $P_\mathrm{el,in,B}$:

$$P_{\mathrm{Cu}=} + \Delta P_\mathrm{Cu} = P_\mathrm{el,in,B} - P_\mathrm{Fe,B} \ . \tag{4.5}$$

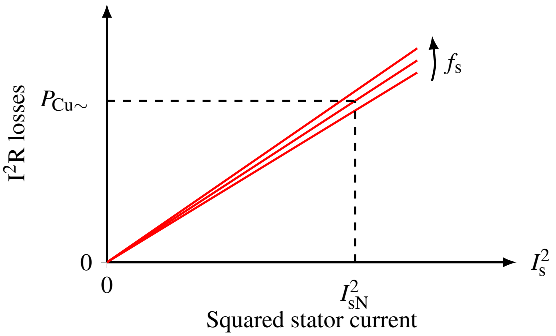

Figure 4.7.: Exemplary curve of current-depending losses over squared stator current for different stator frequencies at removed rotor test

Especially for machines with big leakage inductance (like tooth-coil windings with several sub- and super-harmonic field waves) the iron losses at the removed rotor test are not negligible. The calculation method for estimating the iron losses is presented in Chapter 5.

As the current-depending I^{2}R losses $P_{\mathrm{Cu}\sim} = P_{\mathrm{Cu}=} + \Delta P_{\mathrm{Cu}}$ for different stator frequencies f_s depend on the square of the stator current I_s, the family of curves $P_{\mathrm{Cu}\sim} = f\left(I_\mathrm{s}^2, f_\mathrm{s}\right)$ is linear with I_s^2 (Figure 4.7) for constant stator winding temperatures ϑ_{Cu}.

4.4. Full load test

REQUIREMENTS:	Inverter-fed variable drive, auxiliary drive as brake for up to 150 % of the rated power, torque transducer
VARIABLE:	Mechanical speed n, torque M
MEASUREMENT:	Fundamental and harmonic stator voltage $U_{\mathrm{s},1}, U_{\mathrm{s},k}$, current $I_{\mathrm{s},1}, I_{\mathrm{s},k}$, and power factor $\cos\varphi_{\mathrm{s},1}, \cos\varphi_{\mathrm{s},k}$

To perform a direct efficiency determination a full load test is required. The tested machine is coupled with a braking or driving device, which is usually a second electrical machine with the same power and torque rating. As the mechanical output power in motor operation and the mechanical input power in generator operation is needed to calculate the direct efficiency, a torque transducer is, if possible, utilized for speed and torque sensing. Otherwise a separate speed measurement is needed, or the speed is calculated from the fundamental electrical stator frequency f_s) . For big electrical machines, like generators for wind or water power plants, the demand of a second machine of the same size may lead to logistical problems, as the machine is often mounted only on-site and not in the manufacturer halls. So on-site there is no load machine available. Besides the mechanical measurement also the electrical parameters *voltage*, *current*, and *power factor* are needed to calculate the electrical in-/output power. Here usually a three-phase power analyzer is used.

In this work, the full load test is performed to compare the calculated direct and indirect efficiency values for different torque and speed values in motor and generator operation.

The full-load test covers all explained loss components of the permanent-magnet synchronous machine (Chapter 3), but requires a high measurement accuracy of less than 0.5 % of the electrical power P_el and the mechanical power $P_\mathrm{m} = 2\pi \cdot n \cdot M$. For increased accuracy several measurements of different load M/M_N are performed to allow an averaging of the measurement values.

The direct efficiency in motor operation η_mot and in generator operation η_gen is calculated similar to (2.1) and (2.2) via

$$\eta_\mathrm{mot} = \frac{P_\mathrm{m,out}}{P_\mathrm{el,in}} \,, \tag{4.6}$$

$$\eta_\mathrm{gen} = \frac{P_\mathrm{el,out}}{P_\mathrm{m,in}} \,. \tag{4.7}$$

With the fundamental values of the stator voltage $U_\mathrm{s,1}$, the stator current $I_\mathrm{s,1}$, and the power factor $\cos\varphi_\mathrm{s,1}$ also the direct efficiency value for *sinusoidal operation* is calculated via

$$\eta_\mathrm{mot,1} = \frac{P_\mathrm{m,out}}{P_\mathrm{el,in,1}} = \frac{P_\mathrm{m,out}}{m_\mathrm{s} \cdot U_\mathrm{s,1} \cdot I_\mathrm{s,1} \cdot \cos\varphi_\mathrm{s,1}} \,, \tag{4.8}$$

$$\eta_\mathrm{gen,1} = \frac{P_\mathrm{el,out,1}}{P_\mathrm{m,in}} = \frac{m_\mathrm{s} \cdot U_\mathrm{s,1} \cdot I_\mathrm{s,1} \cdot \cos\varphi_\mathrm{s,1}}{P_\mathrm{m,in}} \,, \tag{4.9}$$

where $\cos\varphi_\mathrm{s,1} \in [-1\ldots0)$ in generator operation and $\cos\varphi_\mathrm{s,1} \in (0\ldots1]$ in motor operation.

4.5. Generator short-circuit test

REQUIREMENTS:	Auxiliary drive, torque transducer
VARIABLE:	Mechanical rotor speed n
MEASUREMENT:	Stator current I_s, shaft torque M

At the generator short-circuit test the machine is driven by an auxiliary drive like at the generator no-load test, but with all stator terminals short-circuited. Therefore the stator voltage U_s is zero. The setup is similar to the generator short-circuit test of the electrically excited synchronous machine (Section 2.2.2), but here not the excitation current but the mechanical speed n is variable to change the current values of the machine. The back EMF U_p is changing linearly with the speed, as shown at the no-load test. As the equivalent iron resistance R_Fe is usually much bigger than the stator resistance $R_\mathrm{Fe} \gg R_\mathrm{s=} + \Delta R_\mathrm{s} = R_\mathrm{s\sim}$, the sinusoidal stator short-circuit current $I_\mathrm{s,sc}$ is mainly limited by the stator winding re-

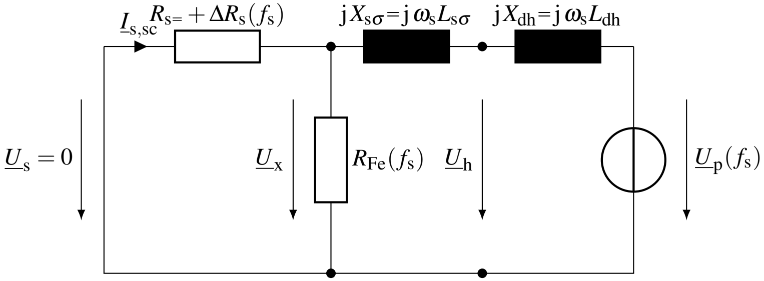

Figure 4.8.: Equivalent circuit per phase at the generator short-circuit test ($X_{dh} \cong X_{qh}$)

sistance $R_{s\sim}$ and the synchronous reactance X_d (Figure 4.8). The stator current is thus calculated via

$$\underline{I}_{s,sc} \cong -\frac{\underline{U}_p}{R_{s\sim}+jX_d} \;, \tag{4.10}$$

$$I_{s,sc} = |\underline{I}_{s,sc}| = \frac{U_p}{\sqrt{R_{s\sim}^2+X_d^2}} \;. \tag{4.11}$$

At low speed values the synchronous reactance $X_d = \omega_s L_d$ is rather small, leading to a fast linear rise of the stator short-circuit current with increasing speed n, while for higher speeds, and thus higher angular frequencies $\omega_s = 2\pi f_s$ the influence of the stator resistance descends. Then the stator short-circuit current is constant:

$$I_{s,sc} = I_{sc} \cong \frac{U_p}{X_d} = \frac{1}{\sqrt{2}}\frac{\omega_s \cdot \Psi_p}{\omega_s \cdot L_d} = \frac{1}{\sqrt{2}}\frac{\Psi_p}{L_d} \;. \tag{4.12}$$

Therefore, for $\omega_s L_d \gg R_{s\sim}(f_s)$, the synchronous inductance can be calculated via

$$L_d \cong \frac{U_p}{\omega_s \cdot I_{sc}} \;. \tag{4.13}$$

With the decomposition of the stator short-circuit current $\underline{I}_{s,sc} = I_{sd,sc} + j I_{sq,sc}$ according to [5] into

$$I_{sd,sc} = \frac{\omega_s L_q \cdot U_p}{R_{s\sim}^2 + \omega_s L_d \cdot \omega_s L_q} \;, \quad I_{sq,sc} = \frac{R_{s\sim} \cdot U_p}{R_{s\sim}^2 + \omega_s L_d \cdot \omega_s L_q} \;, \tag{4.14}$$

a comparison of measured and calculated short-circuit current is possible. This allows the determination of the inductances via curve fitting.

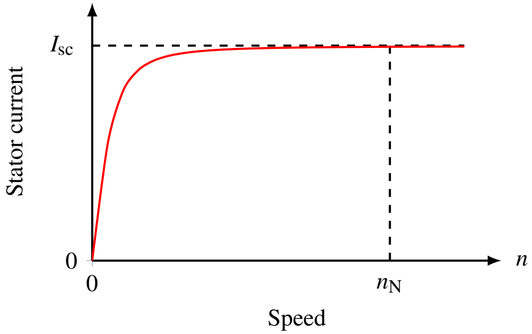

Figure 4.9.: Exemplary curve of the short-circuit stator current over speed at the generator short-circuit test

The short-circuit torque

$$M_{sc} = \frac{3 \cdot U_p^2}{2\pi \cdot n} \cdot \frac{R_{s\sim}}{R_{s\sim}^2 + X_d^2} \tag{4.15}$$

rises approximately linearly with n for low speeds until, like before, the increasing synchronous reactance X_d leads to a hyperbolic descending torque curve again [5] (Figure 4.10). For machines with different d- and q-axis inductance ($L_d \neq L_q$), the short-circuit torque depends on the d-axis reactance $X_d = \omega_s L_d$ and on the q-axis reactance $X_q = \omega_s L_q$ via

$$M_{sc} = \frac{3 \cdot U_p^2}{2\pi \cdot n} \cdot \frac{R_{s\sim} \cdot (R_{s\sim}^2 + X_q^2)}{(R_{s\sim}^2 + X_d X_q)^2} \ . \tag{4.16}$$

The maximum short-circuit torque can exceed the rated torque by far, so that the short-circuit experiment has to be carried out with adequate torque measurement devices of a torque range $0 \leq M \leq \hat{M}_{sc}$.

If the short-circuit test cannot be performed due to the high short-circuit torque or the lack of an auxiliary drive, the reactive current test can be used to determine the synchronous inductance of the permanent-magnet synchronous machine.

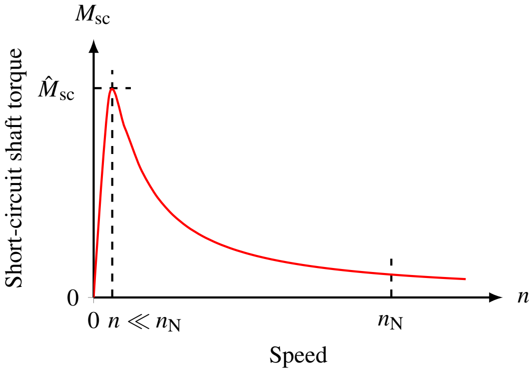

Figure 4.10.: Exemplary curve of the torque over speed at the generator short-circuit test

4.6. Reactive current test

REQUIREMENTS:	Inverter-fed variable drive
VARIABLE:	Stator current angle φ_s, Mechanical rotor speed n
MEASUREMENT:	Fundamental stator voltage $U_{s,1}$, stator current $I_{s,1}$, and stator power factor $\cos\varphi_{s,1}$

When the permanent-magnet synchronous machine is driven by a voltage source inverter, the synchronous inductance L_d can be determined instead of (4.13) by the reactive current test. The initial setup is the same as for the motor no-load operation (Section 4.2). The machine is driven without any coupled load, while the speed n is variable by the inverter output voltage. The stator current angle φ_s is defined as $\angle(\underline{U}_s, \underline{I}_{s,1})$. Again the fundamental stator terminal voltage $U_{s,1}$ is the no-load voltage U_0. By increasing the current angle φ_s to nearly $-90\,°$el., an additional negative d-current can be impressed by the inverter, which leads to field weakening. The small q-current remains constant, as the torque requirements do not change at constant speed. Therefore an additional voltage drop $\mathrm{j}X_d \cdot I_{sd}$ occurs, reducing the stator voltage $U_{s,1}$. Of course the stator voltage cannot be reduced to zero in motor operation, but the extrapolation of the nearly linear graph $I_{s,1} = f(U_{s,1})$ to $U_{s,1} = 0$ yields to the maximum current, which is approximately the short-circuit current I_{sc} (Figure 4.11). The inclination of the linear curve changes for different speeds, as the no-load voltage changes proportionally, but all curves have the same final value I_{sc}. The stator current cannot be increased any further than I_{sc}.

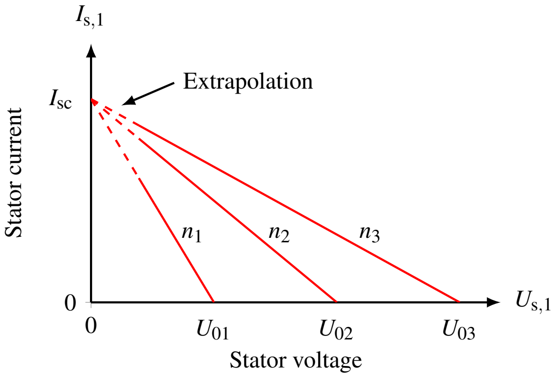

Figure 4.11.: Exemplary curve at $n = const.$ for different speeds $n_1 < n_2 < n_3$ of the stator current $I_{s,1}$ over the stator voltage $U_{s,1}$ at the reactive current test

Figure 4.12 compares the circuit diagrams of the mentioned experiments. In a) the small motor no-load current I_{sq} is omitted for readability. With rising d-current I_{sd} the stator voltage $U_{s,1}$ gets smaller (b). At zero voltage theoretically the short-circuit case (c) is obtained. Therefore the reactive current experiment might also be called the *motor short-circuit* experiment.

With the no-load voltage U_0 at $I_{sd} = 0$ the synchronous inductance is determined at fixed n and ω_s via

$$L_d \cong \frac{1}{\omega_s} \frac{\Delta U_s}{\Delta I_s} \cong \frac{U_0}{\omega_s \cdot I_{sc}} \ . \tag{4.17}$$

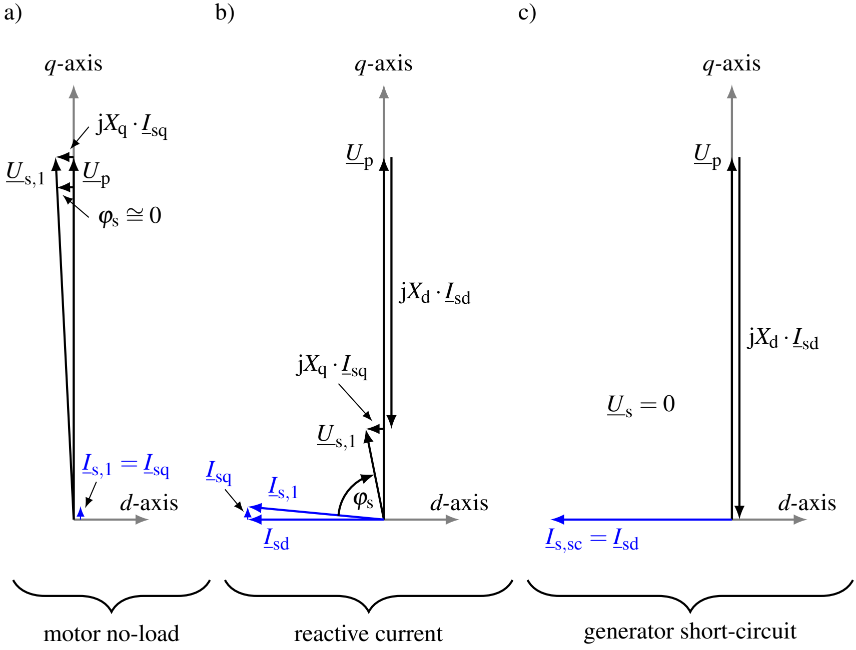

Figure 4.12.: Comparison of phasor diagrams at $R_\mathrm{s} \cong 0$ of a) motor no-load ($I_{\mathrm{s},1} = I_\mathrm{sq} \ll I_\mathrm{N}$), b) reactive current ($\varphi_\mathrm{s} \cong -90\,^\circ$el.), c) generator short-circuit experiment

5. Indirect efficiency determination of PMSMs

This chapter describes the procedure, how to determine the efficiency of permanent-magnet synchronous machines by summation of losses. This method shall be used for machines operated in the base speed range, where a *d*-*q*-current operation may be used to utilize also the reluctance torque component. Investigations concerning the field weakening range are not part of this thesis. Similar to method B for electrically excited synchronous machines (Section 2.2) the machine losses are divided into three groups:

- Voltage-depending losses
  - Iron losses $P_{\mathrm{Fe},0}$ and additional no-load losses $P_{\mathrm{ad},0} \cong P_{\mathrm{M},0}$ at sine wave voltage operation
  - Additional losses due to inverter feeding $P_{\mathrm{el,in,0,ad}}$
- Current-depending losses $P_{\mathrm{Cu}\sim}$ at sinusoidal current supply
  - Stator DC copper losses $P_{\mathrm{Cu=}}$
  - Additional stator losses due to current displacement $\Delta P_{\mathrm{Cu}} = P_{\mathrm{ad,1,s}}$
- Friction and windage losses $P_{\mathrm{fr+w}}$

The current-depending additional rotor losses $P_{\mathrm{ad,1,r}}$ are neglected. The individual loss groups are determined with help of the previously described experiments: Motor and generator no-load test and removed rotor test.

For a given (rated) load operation point with the fundamental stator voltage $U_{\mathrm{s},1}$, the fundamental stator current $I_{\mathrm{s},1}$, the fundamental power factor $\cos\varphi_{\mathrm{s},1}$, and thus the electrical power $P_{\mathrm{el}} = m_{\mathrm{s}} U_{\mathrm{s},1} I_{\mathrm{s},1} \cos\varphi_{\mathrm{s},1}$, the efficiency is calculated as follows.

5.1. Method description

Step I: Iron losses at load

Depending on which no-load experiment was carried out to determine the fundamental no-load losses (either motor or generator no-load test), the sum of iron and friction and windage losses at no-load as $f(n)$ are determined for generator no-load operation as

$$P_{\mathrm{Fe},0}+P_{\mathrm{ad},0}+P_{\mathrm{fr+w}} \cong P_{\mathrm{Fe+M},0}+P_{\mathrm{fr+w}}=P_{\mathrm{m,in},0} \tag{5.1}$$

and for motor no-load operation as

$$P_{\mathrm{Fe},0}+P_{\mathrm{ad},0}+P_{\mathrm{fr+w}} \cong P_{\mathrm{Fe+M},0}+P_{\mathrm{fr+w}}=P_{\mathrm{el,in},0}-m_{\mathrm{s}} \cdot R_{\mathrm{s}\sim} \cdot I_{\mathrm{s},0,1}^{2} \; . \tag{5.2}$$

After subtracting the friction and windage losses $P_{\mathrm{fr+w}}$, the no-load iron losses $P_{\mathrm{Fe},0}+P_{\mathrm{ad},0} \cong P_{\mathrm{Fe+M},0}=f(n)$ are determined.

At load operation the stator field superimposes to the no-load field of the rotor magnets. This typically leads to increased iron losses P_{Fe}. As shown in Section 3.3, these losses depend on the square of the total magnetic flux and thus on the square of the resulting induced reactance voltage U_{x} in the stator winding. According to Figure 3.2 this voltage is determined via

$$\underline{U}_{\mathrm{x}}=\underline{U}_{\mathrm{s}}-R_{\mathrm{s}\sim} \cdot \underline{I}_{\mathrm{s}} \; . \tag{5.3}$$

Therefore the iron losses P_{Fe} at load operation are calculated from the no-load iron losses as

$$P_{\mathrm{Fe}}=P_{\mathrm{Fe,s}}+P_{\mathrm{Fe,r+M}} \cong P_{\mathrm{Fe+M},0} \cdot\left(\frac{U_{\mathrm{x}}}{U_{0}}\right)^{2} \; . \tag{5.4}$$

For this calculation the value of the stator winding resistance per phase $R_{\mathrm{s},\sim}$ has to be known at the actual stator winding temperature. For machines with a small amount of additional stator I^{2}R losses ΔP_{Cu} (see below), the DC value of the stator resistance $R_{\mathrm{s=,warm}}$, which may be determined by a resistance measurement according to IEC 60034-4 [30], or by using an appropriate temperature sensor to measure the average stator winding temperature ϑ_{Cu}, can be used. If the resistance change due to current displacement is significant, the exact value of $R_{\mathrm{s}\sim,\mathrm{warm}}$ should be used at this step. However, usually the total voltage drop at the stator winding resistance is rather small compared to the reactance voltage U_x.

From a critical point of view (5.4) is only an approximation of the total iron losses. At load operation the sub- or super-harmonic components of the stator field lead to increased rotor iron losses and magnet losses $P_{\mathrm{ad,1,r}} = P_{\mathrm{Fe,r+M}}$, but these losses are not included in $P_{\mathrm{Fe+M,0}}$. This means, the total iron and magnet losses at load and sine wave stator current may be underestimated. Another inaccuracy occurs, if the friction and windage losses are not known from a measurement with a non-magnetized rotor, and if their calculation is omitted, assuming that these losses are small. Then in (5.1) and (5.2) the losses $P_{\mathrm{Fe,0}}$ are overestimated. This systematic error is small, if the reactance voltage U_x at load is not differing much from the no-load voltage U_0.

Step II: Current-depending losses at load

According to (4.5) the current-depending losses at the removed rotor test with a stator sine wave current system are determined by subtracting the iron losses $P_{\mathrm{Fe,B}}$ from the measured electrical input power. These iron losses are determined in the same manner as shown before for load operation. Therefore again the reactance voltage $U_{\mathrm{x,B}}$ (Figure 4.6) has to be calculated via (5.3). As the amount of current displacement effect is not known yet, hence $R_{\mathrm{s}\sim}$ is not known, an iterative calculation process of $R_{\mathrm{s}\sim}$ might be necessary at this step. Afterwards the iron losses are calculated via

$$P_{\mathrm{Fe,B}} \cong P_{\mathrm{Fe+M,0}} \cdot \left(\frac{U_{\mathrm{x,B}}}{U_0}\right)^2 . \tag{5.5}$$

As the no-load losses $P_{\mathrm{Fe+M,0}}$ also cover the rotor losses $P_{\mathrm{Fe,r+M,0}}$ at no-load, which are of course missing during the removed rotor test, the iron losses $P_{\mathrm{Fe,B}}$ may be overestimated. Due to the big "equivalent" air gap $\delta = d_{\mathrm{si}}/2$ the reactance voltage $U_{\mathrm{x,B}}$ and thus the iron losses $P_{\mathrm{Fe,B}}$ are depending on the stator leakage reactance per phase.

After the iron losses $P_{\mathrm{Fe,B}}$ are subtracted from $P_{\mathrm{el,in,B}}$, the current-depending losses at sine wave load $P_{\mathrm{Cu}\sim} = f(I_\mathrm{s}^2, f_\mathrm{s})$ are determined:

$$P_{\mathrm{Cu}\sim} = P_{\mathrm{el,in,B}} - P_{\mathrm{Fe,B}} . \tag{5.6}$$

Step III: Friction and windage losses at load

Due to the nature of the mechanical friction and windage losses, the losses $P_\mathrm{w} = P_\mathrm{w}(n)$ are load-independent and vary only with different rotor speed values n for fixed machine geometry parameters. The bearing friction losses P_fr may also depend to a certain extend on the load torque M. Usually the bearing friction losses are much smaller than the windage losses, especially for rotors with shaft-mounted fan. Hence $P_\mathrm{fr} + P_\mathrm{w} = P_\mathrm{fr+w} = P_\mathrm{fr+w}(n)$ are assumed also load-independent. Therefore the same calculations (Section 3.5) – or measurement results with non-magnetized rotor – like at no-load operation are applied.

Step IV: Efficiency at sine wave operation

The previously described three loss components are already present at sinusoidal voltage and current operation. Therefore the efficiency at sine wave operation is given by (5.7) for motor operation and (5.8) for generator operation:

$$\eta_\mathrm{mot,1} = \frac{m_\mathrm{s} U_\mathrm{s,1} I_\mathrm{s,1} \cos\varphi_\mathrm{s,1} - P_\mathrm{Fe} - P_\mathrm{Cu\sim} - P_\mathrm{fr+w}}{m_\mathrm{s} U_\mathrm{s,1} I_\mathrm{s,1} \cos\varphi_\mathrm{s,1}} , \tag{5.7}$$

$$\eta_\mathrm{gen,1} = \frac{m_\mathrm{s} U_\mathrm{s,1} I_\mathrm{s,1} \cos\varphi_\mathrm{s,1}}{m_\mathrm{s} U_\mathrm{s,1} I_\mathrm{s,1} \cos\varphi_\mathrm{s,1} + P_\mathrm{Fe} + P_\mathrm{Cu\sim} + P_\mathrm{fr+w}} . \tag{5.8}$$

In both equations

$$P_\mathrm{Fe} + P_\mathrm{Cu\sim} + P_\mathrm{fr+w} = P_\mathrm{d,1} \tag{5.9}$$

is corresponding to the sum of the losses at fundamental voltage and current at inverter supply.

As the permanent-magnet synchronous machine is usually inverter driven, the additional losses due to inverter operation $P_\mathrm{el,in,0,ad}$ have to be considered to calculate the total efficiency at inverter operation.

Step V: Additional losses due to inverter feeding

Here only voltage source inverters are investigated, which form the major part of feeding inverters for permanent-magnet synchronous machines. During the motor no-load test the additional losses due to inverter feeding $P_\mathrm{el,in,0,ad} = f(U_0)$ are determined via (4.2). These losses are nearly load-independent for sufficient high switching frequencies f_{PWM} of the inverter and depend only on the modulation degree m_{a} of the inverter output voltage. Therefore for a given load point at the fundamental stator voltage $U_{\mathrm{s},1}$, the losses are determined via $P_{\mathrm{el,in,0,ad}}(U_{\mathrm{s},1})$.

Step VI: Efficiency at inverter operation

Taking the additional losses due to inverter operation into account, (5.7) and (5.8) are extended by $P_{\mathrm{el,in,0,ad}}$. Finally the total efficiency at voltage source inverter operation is given by (5.10) for motor operation and (5.11) for generator operation:

$$\eta_{\mathrm{mot}} = \frac{m_{\mathrm{s}} U_{\mathrm{s},1} I_{\mathrm{s},1} \cos\varphi_{\mathrm{s},1} - P_{\mathrm{Fe}} - P_{\mathrm{Cu}\sim} - P_{\mathrm{fr+w}}}{m_{\mathrm{s}} U_{\mathrm{s},1} I_{\mathrm{s},1} \cos\varphi_{\mathrm{s},1} + P_{\mathrm{el,in,0,ad}}} , \tag{5.10}$$

$$\eta_{\mathrm{gen}} = \frac{m_{\mathrm{s}} U_{\mathrm{s},1} I_{\mathrm{s},1} \cos\varphi_{\mathrm{s},1}}{m_{\mathrm{s}} U_{\mathrm{s},1} I_{\mathrm{s},1} \cos\varphi_{\mathrm{s},1} + P_{\mathrm{Fe}} + P_{\mathrm{Cu}\sim} + P_{\mathrm{fr+w}} + P_{\mathrm{el,in,0,ad}}} , \tag{5.11}$$

with the total losses P_{d} at inverter operation:

$$P_{\mathrm{Fe}} + P_{\mathrm{Cu}\sim} + P_{\mathrm{fr+w}} + P_{\mathrm{el,in,0,ad}} = P_{\mathrm{d},1} + P_{\mathrm{el,in,0,ad}} = P_{\mathrm{d}} . \tag{5.12}$$

The process of efficiency determination is visualized in Figure 5.1.

5.2. Drawbacks

The load-dependent rotor losses $P_{\mathrm{Fe,r+M}}$ at sine wave current operation are neglected by the proposed method. Therefore the calculated efficiency will be fitting better to the direct efficiency value for machines with a small amount of stator winding sub- and super-harmonic field components.

According to Step I, if the friction and windage losses are unknown or calculated imprecise, the iron loss prediction at load is inaccurate. This holds true especially for machines with shaft-mounted fan, where the losses $P_{\mathrm{fr+w}}$ are relatively big. For external cooling systems the air friction losses are usually small except for special high-speed drives, and thus the error is also small.

The assumption $P_{\mathrm{Fe}} \propto U_{\mathrm{x}}^2$ is also influencing the efficiency calculation. Whereas in in-

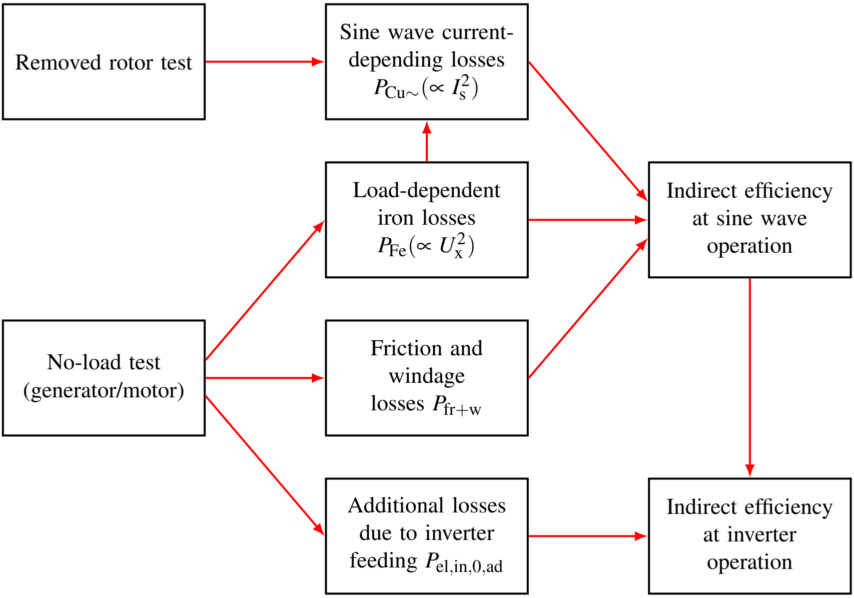

Figure 5.1.: Block diagram of the indirect efficiency determination of sine wave and voltage source inverter operated permanent-magnet synchronous machines [66]

duction machines the main field reactance is by 20 . . . 30 bigger than the stator leakage reactance, this ratio is much smaller with permanent-magnet synchronous machines, especially with surface-mounted rotor magnets. Hence the stray flux contribution to the iron losses is considered. The influence of field harmonics of higher rotor order μ than the fundamental $\mu = 1$ and the influence of variable iron saturation especially at load will disturb the assumption $P_{\mathrm{Fe}} \propto U_{\mathrm{x}}^2$ to a certain extend.

Of course the resulting air gap field at load as the interaction of the stator and rotor field with its additional load-dependent iron saturation will not be the same like at no-load and removed rotor operation. This effect also occurs for electrically excited synchronous machines, where the no-load and short-circuit test is used to determine the efficiency indirectly. Also here this influence cannot be considered. So, especially for machines with high magnetic utilization, the load-dependent saturation will lead to higher deviations from $P_{\mathrm{Fe}} \propto U_{\mathrm{x}}^2$.

The rotor removal of an already completed permanent-magnet synchronous machine is rather difficult due to the rotor permanent magnet forces especially for bigger machines. Therefore this method is primarily useful for the manufacturer, where the test equipment is available and the test can be performed during the production process before the machine is completed.

In the same way the generator no-load test with a non-magnetized rotor is typically only possible during the manufacturing process.

6. Tested machines

The goal of the thesis is the validation of the proposed method for different types of permanent-magnet synchronous machines in the power range $\leq 200\,\mathrm{kW}$, fitting to our laboratory conditions. Therefore five three-phase permanent-magnet synchronous machines with quite different stator and rotor design have been chosen – each of them with a maximum efficiency of approximately 95 %, where also a direct efficiency determination is still possible with sufficient accuracy. This allows a direct efficiency determination as comparison. The first two test machines M1, M2 have a fractional-slot tooth-coil winding, a higher number of 16 poles, a rather low rated speed of $1000\,\mathrm{min}^{-1}$, and high rated torque of 430 Nm. The two test machines M3, M4 have a distributed integer-slot single-layer winding, a smaller number of 6…8 poles, and a lower rated torque of about 300 Nm. Test machine M5 has a fractional-slot distributed stator winding, a medium number of 12 poles, a rather high rated torque of 1019 Nm, and a rated speed of $1500\,\mathrm{min}^{-1}$. The rated power of the investigated test machines is in the range of 45 kW…160 kW. Each machine has a three-phase stator winding, NdFeB rotor magnets, and is designed to be driven by a conventional two-level voltage source inverter without any filter, with a field-oriented d-q-control, and with a rated DC link voltage of 560 V for test machines M1 …M4 and a rated DC link voltage of 650 V for test machine M5. The summarized data of the five evaluated permanent-magnet synchronous machines is to be found in Appendix A.

In the following sections the stator air gap field harmonics are calculated by means of the matrix analysis of *Štěpina* [56] to illustrate the influence of stator space harmonics.

6.1. Fractional-slot tooth-coil winding

The non-skewed tooth-coil test machines M1 and M2 were designed and constructed in a former research project at the *Institute of Electrical Energy Conversion, TU Darmstadt* [11]. Each of them has a rated power of $P_\mathrm{N} = 45\,\mathrm{kW}$, a rated speed of $n_\mathrm{N} = 1000\,\mathrm{min}^{-1}$, and a rated torque of $M_\mathrm{N} = 430\,\mathrm{Nm}$.

The stator inner diameter is $d_\mathrm{si} = 181\,\mathrm{mm}$ and the active iron length is $l_\mathrm{Fe} = 180\,\mathrm{mm}$. While the outer dimensions and the power ratings are equal, the stator and rotor design of both machines differs strongly.

Both machines are equipped with a water jacket stator cooling system with a rated coolant flow rate of $6\,\ell/\text{min}$.

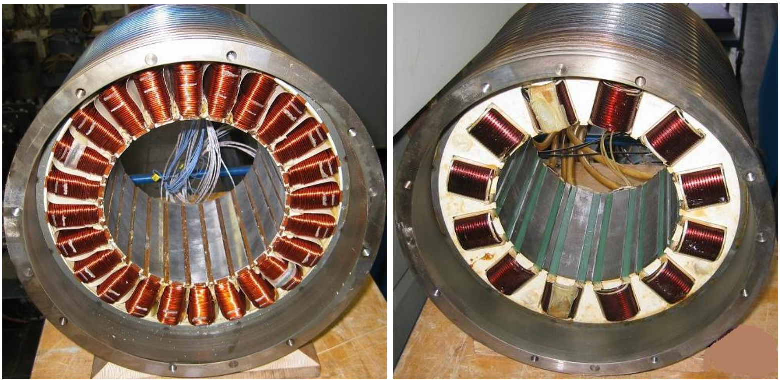

(a) Test machine M1

(b) Test machine M2

Figure 6.1.: Stators of the two test machines M1, M2 with fractional-slot tooth-coil winding with $q = 1/2$ slots per pole and phase: a) machine M1 with double-layer winding, b) machine M2 with single-layer winding [11], [12]

6.1.1. Test machine M1

Test machine M1 has a double-layer tooth-coil winding with a number of slots per pole and phase of $q = 1/2$, parallel teeth sides, and semi-closed stator slots (Figure 6.1a). With this winding configuration the winding factor is $k_{\mathrm{ws},\nu} = 0.866$ for each existing stator harmonic field wave with the harmonic order ν. Therefore, neglecting the slot opening influence and the iron saturation, with

$$\hat{B}_{\delta,\nu} \propto \frac{k_{\mathrm{ws},\nu}}{\nu} \,, \tag{6.1}$$

the amplitudes of the stator air gap flux density harmonics are decaying only by $1/\nu$ (Figure 6.2). The big harmonic content leads to a high harmonic leakage inductance $L_{\mathrm{s}\sigma\mathrm{o}}$ and thus to a big ratio of leakage vs. main inductance per phase $L_{\mathrm{s}\sigma}/L_{\mathrm{dh}} > 1$. Due to $q = 1/2$ and double-layer winding, for the fractional-slot tooth-coil winding the fundamental air gap field wave $\nu = 1$ is dominant like in integer-slot windings, and no sub-harmonic field waves exist [5].

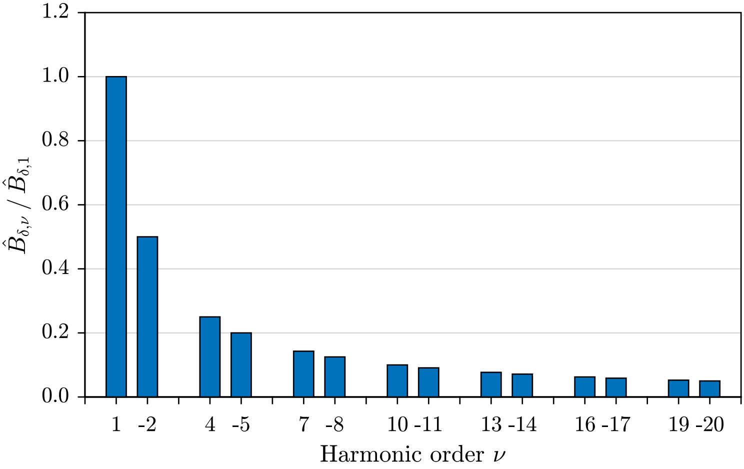

Figure 6.2.: Calculated space harmonic amplitudes of the stator air gap field of test machine M1 without influence of slot opening and iron saturation

The NdFeB rotor magnets of test machine M1 are surface-mounted with a rotor magnet pole coverage ratio of $\alpha_e = 0.77$. To suppress most of the occurring eddy currents, the magnets are segmented in axial and tangential direction. The combination of the mechanical air gap width δ, the carbon fiber magnet bandage thickness d_B, and the magnet height h_M leads to a rather big resulting magnetic equivalent air gap width of $\delta_e = \delta + d_B + h_M = 6.1\,\mathrm{mm}$ for the stator field waves, which reduces the effect of asynchronous entering of the stator harmonic field waves into the rotor. Thus the rotor iron and magnet losses $P_{\mathrm{Fe,r+M}}$ at load are small. Their neglect has minor influence on the efficiency.

The stator winding is designed as a random-wound round wire winding with a high number of turns per coil $N_c = 96$. No parallel sub-conductors per turn exist: $a_i = 1$. Hence no equalizing currents between parallel strands occur to reduce additional copper losses due to their first order current displacement effect as part of ΔP_{Cu}. The second order skin and proximity eddy current losses are small due to the small round wire diameters of 1.6 mm and a maximum fundamental frequency of 133.3 Hz.

6.1.2. Test machine M2

Test machine M2 also has $q = 1/2$ slots per pole and phase, but is designed as single-layer winding with inter teeth between adjacent coil sides per slot and open stator slots. This allows an optimum coil and teeth width, yielding a high winding factor of $k_{\mathrm{ws},2} \cong 0.98$. But also a strong sub-harmonic field wave with $\nu = -1/2$ exists, while $\nu = 1$ is the working field wave (Figure 6.3). Especially the sub-harmonic field $\nu = -1/2$ increases $L_{\mathrm{s}\sigma}$ strongly. So, like before, the ratio of leakage vs. main inductance per phase $L_{\mathrm{s}\sigma}/L_{\mathrm{dh}} > 1$ is rather big due to the high amount of stator field harmonics.

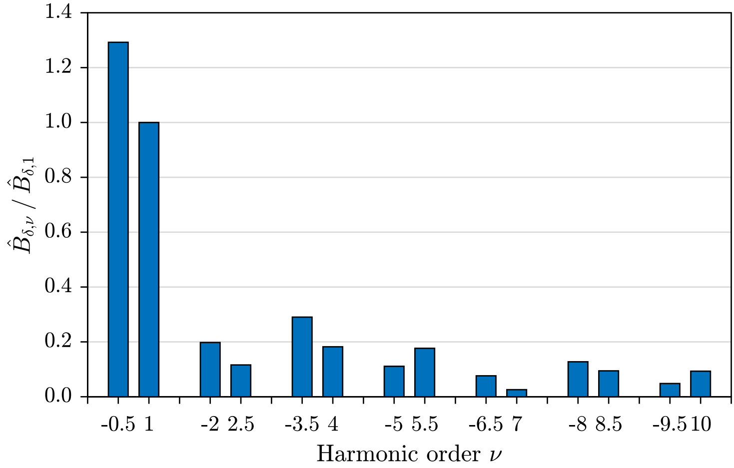

Figure 6.3.: Calculated space harmonic amplitudes of the stator air gap field of test machine M2. The slot opening effect is neglected, so the amplitudes are smaller than in reality, as the machine open slot effect accounts for increased harmonic amplitudes.

In contrast to test machine M1, now the segmented NdFeB rotor magnets are buried by rotor bridges. This leads to higher rotor iron losses $P_{\mathrm{Fe,r}}$ especially in the iron bridges on top of the magnets. Although the magnets are shielded by these iron bridges, again an axial and tangential segmentation is applied to reduce the eddy current losses P_{M}. Especially the sub-harmonic stator field $\nu = -1/2$ with its double wave length (compared to the fundamental field $\nu = 1$) penetrates deep into the rotor, causing considerable load-dependent losses $P_{\mathrm{Fe,r+M}}$. As these losses are neglected during indirect efficiency measurement, their influence on the efficiency can be underrated. The rotor magnet pole coverage ratio is again $\alpha_\mathrm{e} = 0.77$ to minimize the torque ripple of the non-skewed machine.

The stator winding consists of prefabricated coils with rectangular wires, which due to their increased conductor height of 2.5 mm lead to higher additional losses ΔP_Cu due to second order current displacement as sum of skin and proximity effect at maximum frequency of 133.3 Hz. Like for test machine M1 no parallel sub-conductors per turn exist to avoid losses of first order current displacement.

The influence of the additional rotor losses at load became visible during former experiments with test machine M2 at $5000\,\mathrm{min}^{-1}$ at field weakening operation. The subharmonic $\nu = -1/2$ induced the rotor with 1000 Hz and heated up the magnets and especially the rotor iron bridges above 200 °C. So the rotor magnets got partially demagnetized and lost 15 % of their initial remanence flux density. Therefore the remaining back EMF is 85 % of the original value [11] and is used for the tests.

6.2. Integer-slot distributed winding

Besides the two rather special tooth-coil machines, two standard commercially-built permanent-magnet synchronous machines are evaluated. These two test machines M3, M4 with distributed winding both have a quite similar design. The stators have $q = 2$ slots per pole and phase, which contain the single-layer distributed random-wound round wire stator winding. The slots are semi-closed and of oval shape (Figure 6.4). In contrast to the test machines M1 and M2 the harmonic content $|\nu| > 1$ of the stator air gap flux density field waves is rather low. Thus is the stator harmonic leakage inductance $L_{\mathrm{s}\sigma\mathrm{o}}$. The winding factor of the fundamental field wave is $k_{\mathrm{ws},1} = 0.966$, while the strongest super-harmonic field waves are the slot harmonics $\nu = -11$ and $\nu = 13$ (Figure 6.5).

On the rotor the NdFeB magnets are surface-mounted and fixed by a glass-fiber rotor bandage. This magnet arrangement leads to a rather low main inductance L_dh, yielding a ratio $L_{\mathrm{s}\sigma}/L_\mathrm{dh} \cong 0.4$.

Both test machines have many parallel wires per turn (M3: $a_\mathrm{i} = 21$, M4: $a_\mathrm{i} = 16$), so an influence of first order current displacement on ΔP_Cu is expected (Appendix A).

The differences between both machines are explained in the following sections.

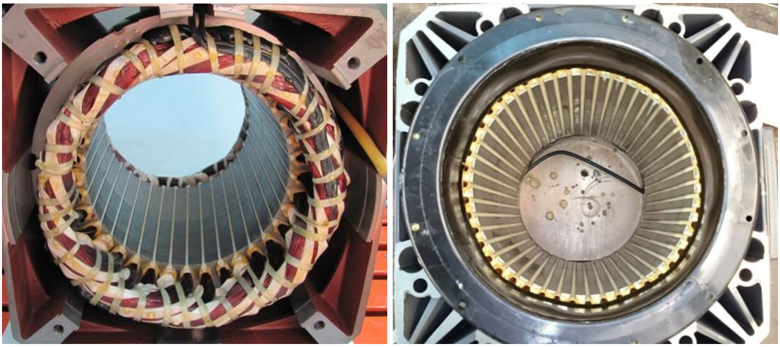

(a) Test machine M3

(b) Test machine M4

Figure 6.4.: Stators of the two test machines M3, M4 with integer-slot distributed single-layer winding with $q = 2$ slots per pole and phase: a) 6-pole machine M3, b) 8-pole machine M4

6.2.1. Test machine M3

The 6-pole test Machine M3 has a rated power of $P_{\mathrm{N}} = 90\,\mathrm{kW}$, a rated speed of $n_{\mathrm{N}} = 3000\,\mathrm{min}^{-1}$, and a rated torque of $M_{\mathrm{N}} = 286\,\mathrm{Nm}$.

The stator inner diameter is $d_{\mathrm{si}} = 188\,\mathrm{mm}$ and the active length is $l_{\mathrm{Fe}} = 210\,\mathrm{mm}$. The $a_{\mathrm{i}} = 21$ parallel wires per stator winding turn have a diameter of 0.75 mm. No rotor magnet skewing is applied.

As the cooling system consists of a shaft-mounted fan, the friction and windage losses of test machine M3 are more relevant compared to the other machines.

6.2.2. Test machine M4

Test machine M4 has the same stator topology as machine M3, but 8 instead of 6 poles. The rated power is $P_{\mathrm{N}} = 84\,\mathrm{kW}$ at the rated speed of $n_{\mathrm{N}} = 2500\,\mathrm{min}^{-1}$ and the rated torque of $M_{\mathrm{N}} = 320\,\mathrm{Nm}$.

The stator inner diameter $d_{\mathrm{si}} = 190\,\mathrm{mm}$ is nearly equal to machine M3, while the active length $l_{\mathrm{Fe}} = 310\,\mathrm{mm}$ is about 50 % bigger. The wires of the stator winding have a diameter of 1.0 mm and are connected as $a_{\mathrm{i}} = 16$ parallel wires per turn. In order to reduce the

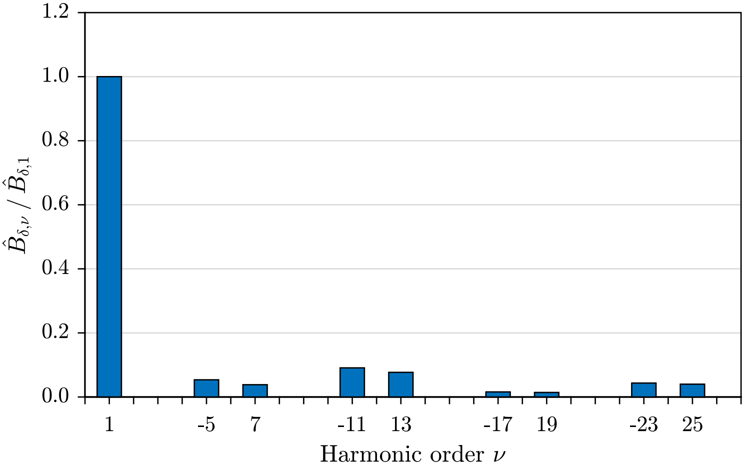

Figure 6.5.: Calculated space harmonic amplitudes of the stator air gap field of test machine M3 and M4 without influence of slot opening and iron saturation

torque ripple, the rotor magnets of test machine M4 are skewed by one slot pitch.

Due to an external cooling fan in the machine no fan losses occur. The external fan losses will not be considered during the efficiency calculation.

6.3. Fractional-slot distributed winding

6.3.1. Test machine M5

The 12-pole test machine M5 (rated power $P_\mathrm{N} = 160\,\mathrm{kW}$, rated speed $n_\mathrm{N} = 1500\,\mathrm{min}^{-1}$, rated torque $M_\mathrm{N} = 1019\,\mathrm{Nm}$) is also a commercially-built permanent-magnet synchronous machine with distributed stator winding. In contrast to test machines M3 and M4, the stator winding has a fractional number of slots per pole and phase $q = 3/2$. Therefore also super-harmonic stator field waves with even ordinal numbers $|\nu| > 1$ exist (Figure 6.6). The strongest super-harmonic field waves are the slot harmonics $\nu = -8$ and $\nu = 10$, which have the same winding factor as the fundamental field wave $k_{\mathrm{ws},1} = 0.945$.

The stator has $Q_\mathrm{s} = 54$ semi-closed slots of oval shape. The stator inner diameter is $d_\mathrm{si} = 324\,\mathrm{mm}$ and the active length is $l_\mathrm{Fe} = 250\,\mathrm{mm}$. The round wires of the stator winding have a diameter of $d_{\mathrm{Cu}} = 1.4\,\mathrm{mm}$ and are connected as $a_{\mathrm{i}} = 7$ parallel conductors per turn. Therefore first order current displacement will occur. Like for test machines M1 and M2 a water jacket cooling is used.

The segmented NdFeB rotor magnets are buried in the rotor iron sheets, leading to a reluctance difference between d- and q-axis.

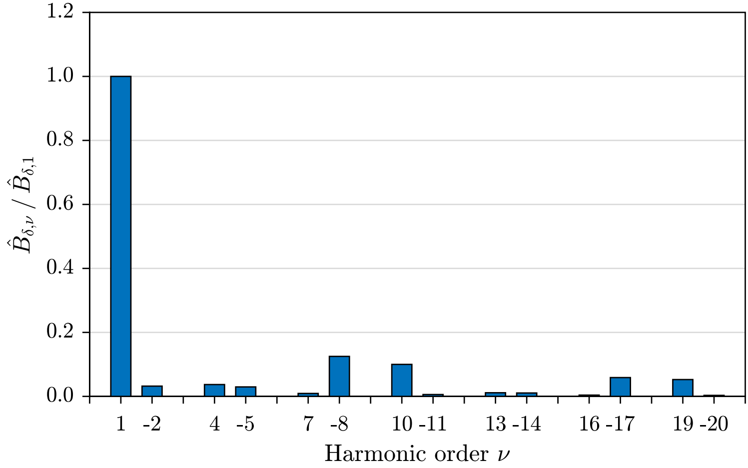

Figure 6.6.: Calculated space harmonic amplitudes of the stator air gap field of test machine M5 without influence of slot opening and iron saturation

7. Measurements

The experiments for indirect and direct efficiency determination as described in Chapter 4 are carried out with slightly different test setups. This chapter first explains the different measurement setups at the test bench in the laboratory of the *Institute of Electrical Energy Conversion, TU Darmstadt* and afterwards the measurement results of the five different permanent-magnet synchronous test machines (Chapter 6).

7.1. Test bench

In order to carry out the different experiments, several parts of the measurement setup are reusable. This setup is termed as the *conventional* setup, while for the removed rotor test a special layout is necessary.

7.1.1. Conventional setup

Nearly all experiments share an overall setup: the *conventional setup* (Figure 7.1). The examined tes machine "M" and the driving or loading machine "Load" are individually fed by a voltage source inverter ("VSI") and mechanically coupled via a torque transducer.

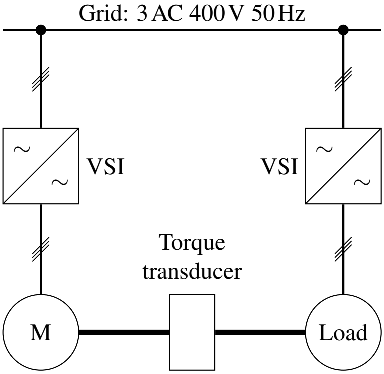

Figure 7.1.: Conventional measurement setup

By optionally disconnecting or short-circuiting the supply voltage both the generator no-load and generator short-circuit test can be carried out. For motor no-load operation and reactive current operation the torque transducer and thus the load machine have to be disconnected. A more detailed view on the options of the conventional setup is given in Appendix B (Figure B.1).

Test machines M1 and M2

For the first two test machines with tooth-coil winding a back-to-back arrangement is chosen, as the machines M1 and M2 have the same rated data and thus are acting as load machines for each other (Figure 7.2). Each machine is fed by a four-quadrant inverter (*Siemens Simodrive 611*, DC link voltage: 560 V, switching frequency: 3.2 kHz, Appendix B, Table B.3). The inverter *Simodrive 611* has a rated power of 120 kW and has the option to feed the power back into the grid due to the possible four-quadrant operation. Each machine is equipped with a forced water cooling system with a volume flow of 6 ℓ/min to allow full-load operation for the direct efficiency measurement, which is used as benchmark for the indirect efficiency test.

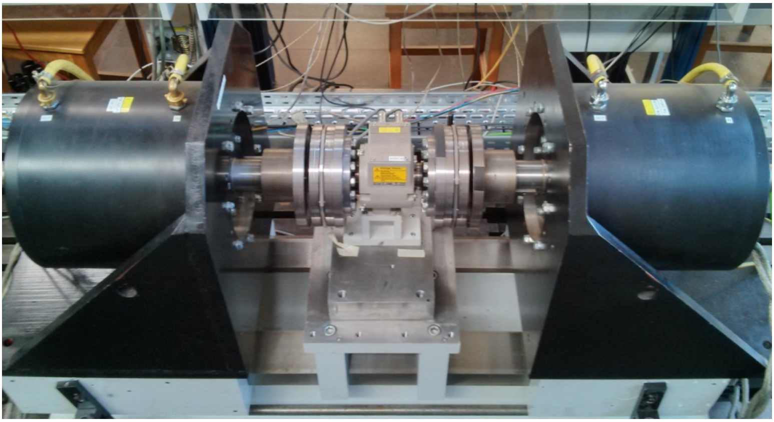

Figure 7.2.: Test bench with the test machines M1 (left) and M2 (right) in back-to-back arrangement with removed shaft protection at the *Institute of Electrical Energy Conversion, TU Darmstadt* [63]

Test machine M3

Test machine M3 is fed by a two-quadrant two-level voltage source inverter with a rated power of 55 kW at a switching frequency of 4 kHz (Appendix B, Table B.4). Due to the power limit of the inverter the maximum torque during the load test has to be reduced to 75 % of the rated torque. As the inverter is not able to feed the power back into the grid, an artificial generator operation is realized as a braking chopper operation with help of a braking resistor at the DC link, but only in the low power range. Therefore only small currents are possible. With these limitations test machine M1 was adequate for use as load machine for test machine M3.

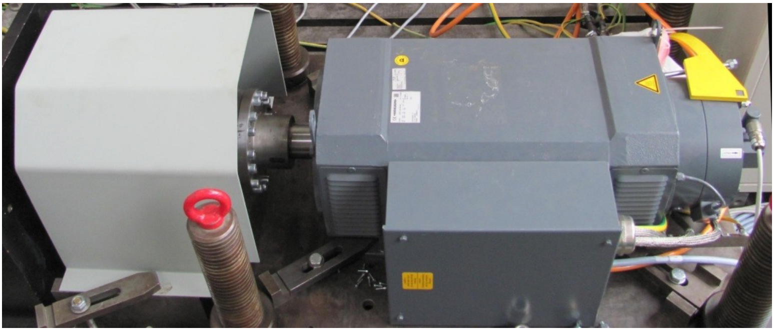

Figure 7.3.: Test bench with test machine M3 (right) and test machine M1 (left, hidden) as load machine at the *Institute of Electrical Energy Conversion, TU Darmstadt* [63]

Test machine M4

Due to the limitations of the inverter for test machine M3, the measurements are also carried out with the quite similar test machine M4. Here the full torque range can be used, as this machine is again fed by the four-quadrant *Simodrive 611* inverter – now at a switching frequency of 4 kHz. Here a DC machine is used as a load machine (data see Appendix B, Table B.6). The external cooling fan is operated at constant speed for each experiment.

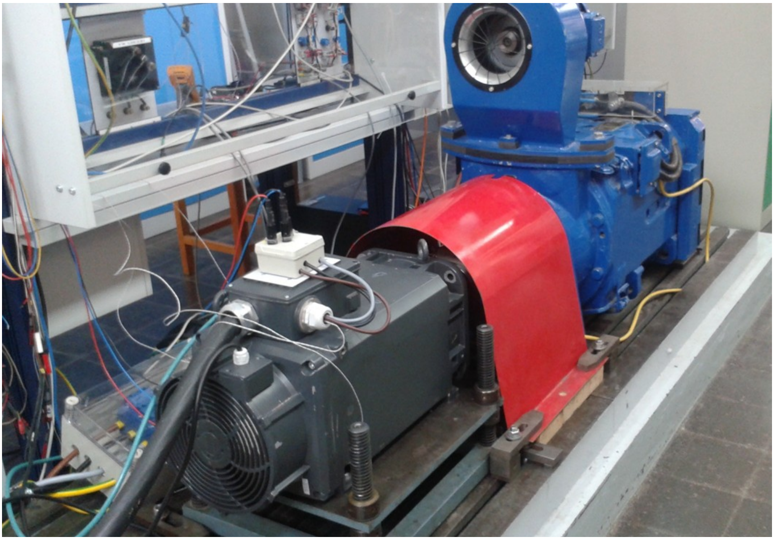

Figure 7.4.: Test bench with test machine M4 (front) and a DC load machine (back) at the *Institute of Electrical Energy Conversion, TU Darmstadt* [66]

Test machine M5

Test machine M5 is operated at a higher DC link voltage of 650 V at a switching frequency of 6 kHz (inverter data see Appendix B, Table B.5). The same DC load machine (Appendix B, Table B.6) as for test machine M4 is used. To reach the rated torque of 1019 Nm at load operation, no field weakening of the DC load machine is applied. Therefore the speed at the load measurements is limited to 67 % of the rated speed, i.e. $n_{\mathrm{max}} = 1000\,\mathrm{min}^{-1}$. The forced water cooling system for test machine M5 has a coolant volume flow of $30\,\ell/\mathrm{min}$.

7.1.2. Removed rotor setup

For the removed rotor test a totally different setup is necessary. Each stator of the five machines is fed by a rotational converter with sinusoidal voltage and current output at variable frequency. The converter consist of a 10-pole doubly-fed induction generator (DFIG) with the synchronous speed $n_{\mathrm{syn,DFIG}} = 600\,\mathrm{min}^{-1}$, connected to speed-controlled variable speed DC drive (DCM). The stator of the rotational converter is fed by a three-phase voltage system from a variable voltage transformer at $f_{\text{DFIG}} = 50\,\text{Hz}$. By varying the rotor speed n_{DFIG}, a sinusoidal voltage with variable amplitude (via the transformer) at the variable frequency

$$f_{\text{s}} = s \cdot f_{\text{DFIG}} = \frac{n_{\text{syn,DFIG}} - n_{\text{DFIG}}}{n_{\text{syn,DFIG}}} \cdot f_{\text{DFIG}} \tag{7.1}$$

is achieved at the rotor-side clamps and thus at the stator of the permanent-magnet synchronous machine. With the speed limit of the rotating converter

$$n_{\text{DFIG}} \in [600\,\text{min}^{-1} \ldots -1800\,\text{min}^{-1}], \quad s \in [0 \ldots 4]$$

a variable frequency of $f_{\text{s}} \in [0\,\text{Hz} \ldots 200\,\text{Hz}]$ is achieved. As the current-limiting impedance of the stator winding of the test machines is rather low at the removed rotor test especially for low frequencies, the experiment has to be carried out at low stator voltage U_{s} to avoid extensive stator currents.

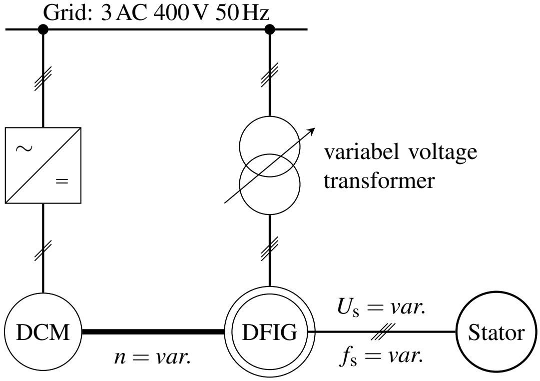

Figure 7.5.: Measurement setup during the removed rotor test

7.2. Methodology

The measurement values of each test are determined by an automatized measurement system based on a *LabVIEW* environment. With this the electrical values are measured by the three-phase power analyzer *Fluke NORMA 5000* (Appendix B, Table B.1) with help of an AC current clamp with a maximum current limit of 1000 A. The torque is determined by a statically calibrated torque transducer (*HBM T30 FNA*, Appendix B, Table B.2). The complete parameters of the measurement devices is listed in Appendix B.

For temperature determination and monitoring, several thermocouples are applied at the stator winding and at the cooling in- and outflow. Also the rotor (magnet) temperature can be monitored by a slip-ring based measurement system.

All different quantities are measured synchronously during the same averaging time. The FFT separation of the fundamental values requires a stable operation along several fundamental electrical periods. Therefore a minimum averaging time during measurement T_{meas} of 2 s is used, which leads to a sequence of at least 10 electrical periods at frequencies above 20 Hz. For higher fundamental frequencies more electrical periods are covered. Therefore the amount of averaged measurement values is rather high.

During the measurements also the measurement uncertainty $u(x_i)$ of each measurement quantity x_i has to be taken into account. The measurement uncertainties are determined according to the *Guide to the Expression of Uncertainty in Measurement (GUM)* [31] by using the specifications and error limits of the measurement devices (*Type B* evaluation, see Table B.1, Table B.2). For each measurand y, that is not directly measured but determined from N other quantities $x_1, x_2, \ldots, x_N$ through a functional relationship $y = f(x_1, x_2, \ldots, x_N)$, the combined uncertainty $u_{\text{c}}(y)$ is calculated with the law of propagation of uncertainties [9], [31]

$$u_{\text{c}}(y) = \sqrt{\sum_{i=1}^{N} \left(\frac{\partial f(x_{\text{i}})}{\partial x_{\text{i}}} \right)^2 \cdot u^2(x_{\text{i}})} \ . \tag{7.2}$$

An example of the uncertainty determination and propagation is given in Appendix D.

In the case of the correlated electrical quantities U, I, φ of the three-phase power analyzer the uncertainty of the power measurement is calculated via

$$\frac{u_{\text{c}}(P)}{P} = \frac{2}{\sqrt{3}} \sqrt{\left(\frac{u(U)}{U} \right)^2 + \left(\frac{u(I)}{I} \right)^2 + \left(\frac{u(\cos\varphi)}{\cos\varphi} \right)^2} \tag{7.3}$$

instead of (7.2), where $u(U)$, $u(I)$, and $u(\cos\varphi)$ are the uncertainties of the voltage U, current I, and the power factor $\cos\varphi$ [45].

For the calculation of the mechanical power $P_\mathrm{m} = 2\pi \cdot n \cdot M$ during generator no-load, generator short-circuit, and load operation, the mechanical speed $n = f_\mathrm{s}/p$ is determined by electrical measurement of the fundamental stator frequency f_s.

The measurement uncertainties are shown by error bars within the graphs. If the uncertainty is smaller than the marker symbol, the error bars are omitted.

7.3. Measurement results

7.3.1. Generator no-load test

The generator no-load test is carried out for all five warmed-up test machines M1 … M5 in the speed range up to 3000 min^{-1} shortly after the load tests, which are described below. Therefore the machine temperatures and so the PM remanence flux density and thus the no-load voltage and power are close to the rated conditions. As the test machines are driven by an auxiliary drive (the "Load" machine), no inverter voltage limitations have to be considered.

The induced no-load voltage U_0 rises linear with the speed n, while the actual amplitudes are varying for each machine due to different magnet material and stator winding topologies. At rated speed conditions, stator no-load RMS voltages per phase between 122 V … 195 V occur for test machines M1 … M4 (Table 7.1), while for test machine M5 the RMS no-load voltage $U_0 = 210\,\mathrm{V}$ is higher, already at 67 % of the rated speed. The rather low value of test machine M2 can be explained by the partial irreversible demagnetization of the rotor that occurred in an earlier test [11] (see Chapter 6).

With

$$\Psi_\mathrm{p} = \frac{\hat{U}_\mathrm{p}}{\omega_\mathrm{s}} \tag{7.4}$$

the magnetic PM flux linkage amplitude Ψ_p of each test machine stator winding per phase is determined (Table 7.1). The flux linkage amplitude is in the range of 0.21 Vs … 0.32 Vs. In (7.4) the assumption $U_0 \cong U_\mathrm{p}$ is valid, as the equivalent iron resistance

$$R_\mathrm{Fe} = 3 \cdot \frac{U_0^2}{P_\mathrm{Fe+M,0}} \tag{7.5}$$

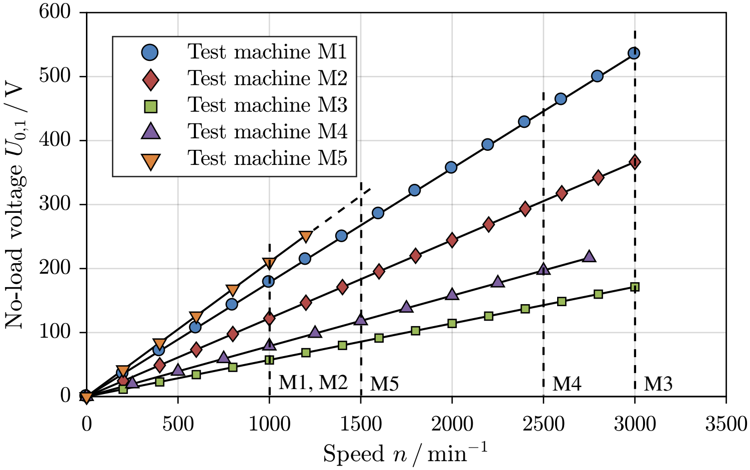

Figure 7.6.: Measured RMS no-load voltage U_0 per phase during the generator no-load test over speed n (rated speed marked, test machine M5 extrapolated, error bars omitted)

is actually much bigger than the synchronous reactance X_d. For the calculation of $X_\mathrm{d} = \omega_\mathrm{s} \cdot L_\mathrm{d}$ the value of the synchronous inductance L_d is taken from the short-circuit test (Section 7.3.5).

The no-load losses $P_\mathrm{m,in,0} = P_\mathrm{Fe+M,0} + P_\mathrm{fr+w}$ (Figure 7.7) also depend on the mechanical speed as expected. The losses rise over-proportional with increasing speed for each machine, while the biggest absolute values occur for test machines M1 and M3. As test machines M1 and M2 share the same rated data and the same type of steel lamination material, the big difference of the much smaller no-load losses for M2 is again explained by the previous demagnetization of the permanent magnets of test machine M2. Each shown curve is an offset-less cubic interpolation of the mean value of the loss measurements at clockwise and counter-clockwise rotation to compensate offset errors during the torque measurement.

Test machine M3 has noticeable friction and windage losses due to the shaft-mounted fan (Table 7.1). These losses are calculated to 573 W at a rated speed of 3000 min^{-1} according to (3.25), as a no-load test without rotor magnetization to separate the fan friction losses from the total no-load losses is not possible. This holds true also for test machines M1,

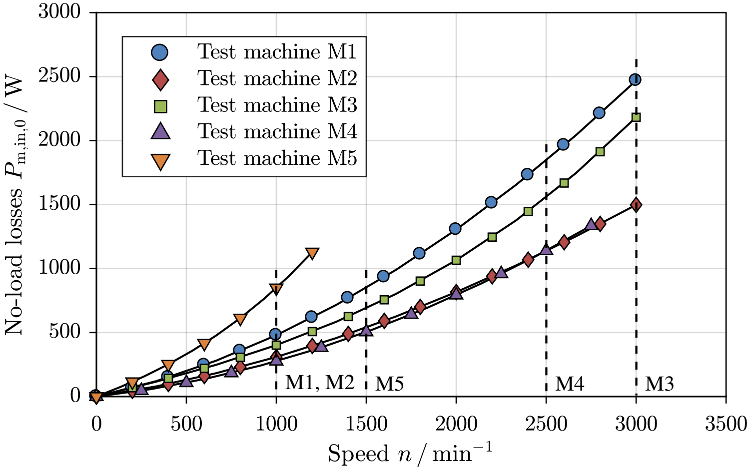

Figure 7.7.: Measured no-load losses $P_{\mathrm{m,in,0}}$ at the generator no-load test over speed (rated speed marked, error bars omitted but shown in Figure C.2 to Figure C.6)

M2, and M4, but here the air friction and windage losses are determined via (3.22) and are of quite low impact on the total no-load losses (Table 7.1).

For test machine M5 the generator no-load test was carried out with a non-magnetized rotor by the manufacturer. Therefore no analytical calculation is necessary to determine the friction and windage losses $P_{\mathrm{fr+w}}$. The loss values are averaged and interpolated from clockwise and counter-clockwise measurement.

In Figure C.7 the friction and windage losses $P_{\mathrm{fr+w}}$ are compared for each test machine. The error bars of the measured losses of test machine M5 show the difference between clockwise and counter-clockwise measurement.

As the generator no-load measurement is carried out right after the load operation, the torque transducer is over-sized. Therefore the measurement uncertainty is quite high. The large error bars are shown at the comparison of the generator and the motor no-load experiment for each machine in Figure C.2 to Figure C.6. For the sake of readability the error limits are omitted in Figure 7.7.

Table 7.1.: Measurement and calculation results of the generator and motor no-load test at rated speed for test machines M1 … M4 and at 67 % of the rated speed for test machine M5

	Unit	M1	M2	M3	M4	M5
Operation conditions						
Speed n **	min^{-1}	1000	1000	3000	2500	1000
Stator frequency f_s **	Hz	133.3	133.3	150.0	166.7	100.0
Switching frequency f_PWM	kHz	3.2	3.2	4.0	4.0	6.0
Stator winding temperature ϑ_Cu	°C	60	60	50	85	55
Measured values at the generator no-load test						
No-load RMS voltage U_0 *	V	178.5	122.2	171.4	197.9	209.7
No-load losses $P_\mathrm{m,in,0}$	W	480	310	2199	1139	854
Friction and windage losses $P_\mathrm{fr+w}$	W	–	–	–	–	292
Calculated value from theory						
Friction and windage losses $P_\mathrm{fr+w}$	W	1	1	573	16	–
Calculated values from generator no-load measurement						
PM flux linkage amplitude Ψ_p *	Vs	0.301	0.206	0.257	0.267	0.315
Iron resistance R_Fe *	Ω	199.5	145.0	54.2	104.6	260.7
Synchronous reactance X_d * (as reference, see Table 7.3)	Ω	2.37	2.08	0.51	0.46	1.19
Measured values at the motor no-load test						
No-load RMS voltage $U_{0,1}$ *	V	177.6	121.3	169.7	195.2	210.8
No-load RMS current $I_{\mathrm{s},0,1}$ *	A	1.0	0.9	4.7	1.8	1.8
Total losses $P_\mathrm{el,in,0}$	W	652	436	3123	1806	1041
Fundamental losses $P_\mathrm{el,in,0,1}$ (at inverter operation)	W	477	305	2466	1050	874
Calculated values from motor no-load measurement						
$\mathrm{I}^2\mathrm{R}$ losses $P_\mathrm{Cu,0}$	W	<1	<1	1	<1	<1
Iron losses $P_\mathrm{Fe+M,0}$	W	476	304	1892	1034	525
Additional losses $P_\mathrm{el,in,0,ad}$ (due to inverter operation)	W	175	131	657	756	167

* per phase, ** rated values, except for test machine M5

7.3.2. Motor no-load test

In order to determine the additional losses due to inverter feeding, the motor no-load test is performed on each of the five test machines M1 … M5. The measurements are carried out up to the voltage limit of the feeding speed-controlled inverter. After that point field weakening would be applied and the no-load operation is no longer valid. With help of the three-phase power analyzer (data see Appendix B) the total and fundamental values of the stator voltage, current, and electrical power are measured, while the stator frequency is changed to adjust the mechanical speed to the set-up value.

Like the generator no-load test, the motor no-load test is carried out just after load operation to have the rotor temperature nearly the rated value, which influences the no-load voltage and losses. The rotor temperature decrease is rather slow in comparison to the short thermal time constant of the stator winding, but it is uncertain to reach exactly the same temperature as at the generator no-load test. Therefore the fundamental no-load voltage $U_{0,1}$ is slightly different between motor and generator test, but is in the range of $\pm 1\ \%$ deviation (Table 7.1). The curves of the fundamental RMS voltage per phase over speed for each of the five test machines at motor no-load test are similar to Figure 7.6 except of the inverter voltage limit at approximately 230 V. The curves are shown in Appendix C, Figure C.1.

Due to the low fundamental stator no-load current $I_{\mathrm{s},0,1}$ in combination with the small stator winding resistance of the test machines, the $\mathrm{I}^2\mathrm{R}$ losses $P_{\mathrm{Cu},0} = 3 \cdot R_{\mathrm{s}} \cdot I_{\mathrm{s},0,1}^2$ at motor no-load test are negligible (Table 7.1).

The fundamental no-load power $P_{\mathrm{el,in},0,1} = U_{0,1} \cdot I_{\mathrm{s},0,1} \cdot \cos\varphi_{\mathrm{s},1}$ covers all losses, which are already present at sinusoidal feeding and should be equal to the mechanical no-load power $P_{\mathrm{m,in},0}$ from the generator no-load experiment. For test machines M1 and M2 this holds exactly true in the operating area up to the inverter voltage limit (see Figure C.2 and Figure C.3). After this point no further comparison is possible due to field weakening. The losses of test machine M3 (Figure C.4) show bigger deviations, but if the error limits of the used big-rated torque transducer are considered, the concordance is reasonable. Tesr machine M4 and M5 has also some smaller deviations within the error limits (Figure C.5).

For the further loss calculations the fundamental motor no-losses are applied, as the accuracy of the electrical measurement is higher than the mechanical measurement at the generator no-load test, because the torque transducer is utilized only up to 2 % of the

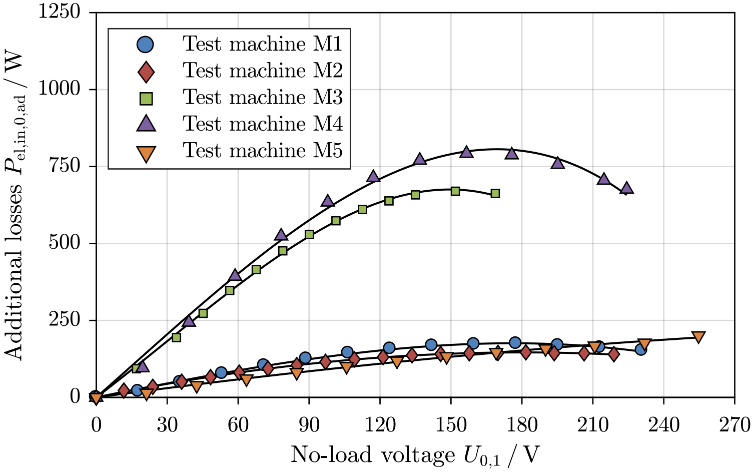

Figure 7.8.: Measured additional losses due to inverter feeding $P_{\mathrm{el,in,0,ad}}$ over the fundamental RMS no-load voltage $U_{0,1}$ per phase [63], [66] (error bars omitted)

torque limit.

According to (5.2) the no-load iron losses $P_{\mathrm{Fe+M,0}}$ are calculated, while the friction and windage losses $P_{\mathrm{fr+w}}$ are determined in the same way as explained in Section 7.3.1. The no-load iron losses will be used to calculate the iron losses at the removed rotor test and at load operation in the following subsections.

In each of the previous mentioned no-load figures also the total no-load input power $P_{\mathrm{el,in,0}}$ is shown. This power is always higher than the fundamental power $P_{\mathrm{el,in,0,1}}$, as it covers also the additional losses due to inverter feeding $P_{\mathrm{el,in,0,ad}}$. The difference between the total and fundamental input power is shown in Figure 7.8 over the RMS no-load voltage per phase $U_{0,1}$. It is noticeable, that for test machines M1 … M4 an expected maximum of the additional losses occurs at approximately 150 V, hence at medium modulation degree of the PWM voltage, like predicted in Section 3.6. For test machine M5 the maximum of $P_{\mathrm{el,in,0,ad}}$ is not yet reached due to the higher DC link voltage of the feeding voltage source inverter.

The absolute values of the additional losses $P_{\mathrm{el,in,0,ad}}$ of the two test machines with integer-slot distributed winding M3 and M4 are about four times higher than the values of the test machines M1 and M2 with tooth-coil winding. This approves the reciprocal dependency of the additional harmonic losses on the synchronous reactance X_d, which is also about four times bigger due to the high harmonic leakage inductance of the tooth-coil machines (Table 7.1). Therefore the harmonic currents are suppressed stronger and the additional losses decrease. A further reason might be the first order current displacement effect in M3, M4, especially at the high switching frequencies, which does not occur in M1, M2. This effect was not mathematically considered in Chapter 8. The additional losses of test machine M5 are also rather low at the switching frequency of 6 kHz.

The additional losses $P_\mathrm{el,in,0,ad} = f(U_\mathrm{s})$ are assumed to be load-independent and are therefore added up to the sinusoidal losses in Section 7.3.4.

7.3.3. Removed rotor test

In order to determine the current-depending losses $P_{\mathrm{Cu}\sim}$, including the current displacement, the rotor of each test machine is removed according to Section 4.3. The remaining stator is fed by a rotating converter with a three-phase sinusoidal voltage as explained in Section 7.1.2. By varying the stator voltage U_s the stator current I_s is adjusted, which is mainly limited by the stator winding resistance $R_{\mathrm{s}\sim}$ and the stator leakage reactance $X_{\mathrm{s}\sigma}$. The experiment is carried out for different stator frequencies f_s to visualize the effect of changing current displacement. The machine's cooling systems are not active during the removed rotor test. Therefore the current is only applied for short time. As a result, the stator winding temperature ϑ_Cu is rather low (Table 7.2). With a more sophisticated cooling system it would be possible to reach the rated stator winding temperature better, giving more accurate loss results closer to rated conditions, as the current displacement effect changes nonlinear with the temperature (Section 3.2.3).

With (5.5) the stator iron losses $P_\mathrm{Fe,B}$ are determined from the no-load iron losses $P_\mathrm{Fe+M,0}$ with help of the reactance voltage $U_\mathrm{x,B}$, which is – due to the small stator resistance – nearly equal to the stator voltage U_s (Table 7.2). The calculated stator iron losses of the test machines with tooth-coil winding and high leakage reactance M1 and M2 are at rated conditions about 20 % of the total losses $P_\mathrm{el,in,B}$, while for the test machines M3, M4, and M5 only about 2 % … 6 % iron losses are present.

The current-depending stator copper losses $P_{\mathrm{Cu}\sim} = f(I_\mathrm{s}, f_\mathrm{s})$ are calculated by subtracting

Table 7.2.: Measurement and calculation results of the removed rotor test at rated frequency

	Unit	M1	M2	M3	M4	M5
Operation conditions						
Stator frequency $f_\mathrm{s} = f_\mathrm{sN}$	Hz	133.3	133.3	150.0	166.7	150.0
Stator winding temperature ϑ_Cu	°C	31	49	41	27	104
Measured values at the removed rotor test						
Stator current I_s *	A	102	120	150	154	158
Stator voltage U_s *	V	197.3	137.1	34.3	38.2	110.2
Total losses $P_\mathrm{el,in,B}$	W	2635	2709	1353	1337	4171
Calculated values from removed rotor measurement						
Reactance voltage $U_\mathrm{x,B}$ *	V	197.2	136.9	34.2	38.1	109.8
Iron losses $P_\mathrm{Fe,B}$	W	590	386	78	40	97
Copper losses $P_\mathrm{Cu\sim}$	W	2045	2323	1275	1297	4074
Ratio $P_\mathrm{Cu\sim}/P_\mathrm{el,in,B}$	%	78	86	94	97	98

* RMS, per phase

the iron losses $P_\mathrm{Fe,B}$ from the total losses $P_\mathrm{Fe,in,B}$ for different stator current RMS values I_s and frequencies f_s. For a better comparison each loss value is recalculated to the reference stator winding temperature of 20 °C and plotted over the square of the stator current (see exemplary Figure 7.9 for test machine M1). As expected in Section 4.3, the loss curves are straight lines, and the values increase with rising stator frequency due to increased current displacement. This holds true also for the other test machines M2 (Figure C.8), M3 (Figure C.9), M4 (Figure C.10), and M5 (Figure C.11). For test machines M3 and M5 the removed rotor experiment is carried out only up to the maximum stator current, that is applied during the load tests (Section 7.3.4).

With its biggest number of $a_\mathrm{i} = 21$ parallel strands per turn the first order current displacement effect is expected to be biggest for test machine M3, which seems to be confirmed by the biggest increase of ΔP_Cu with frequency f_s.

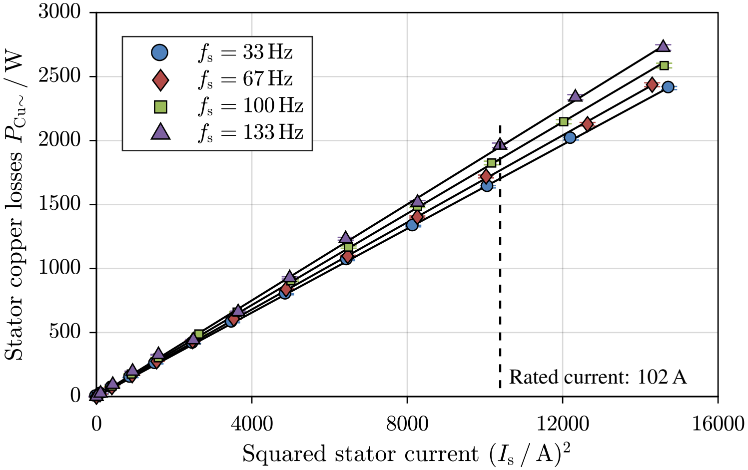

Figure 7.9.: Measured stator copper losses $P_{\mathrm{Cu}\sim}$ during the removed rotor test over squared RMS stator current I_s^2 for test machine M1 at 20 °C [63]

7.3.4. Load operation and efficiency test

In order to validate the method for indirect efficiency determination, several load test are carried out in motor and generator operation mode for each test machine at warm operation temperature. The torque transducer (Section 7.1.1) is used to determine via the torque and speed measurement the direct efficiency by means of (4.6) to (4.9), while both the total electrical power P_{el} and the fundamental power $P_{\mathrm{el},1}$ for *sinusoidal operation* is measured electrically. The fundamental power is determined by the three-phase power analyzer. Like at the motor no-load test the minimum averaging time for this measurement is $T_{\mathrm{meas}} = 2\,\mathrm{s}$. Of course also a *true* sinusoidal operation would be possible, but with much more effort to apply the correct current angle and without any d-q-field oriented control. In Chapter 8 simulations for the losses are carried out. There also a sinusoidal current feeding is used.

For each load measurement 25 %, 50 %, 75 %, and 100 % of the rated speed n_{N} is analyzed, but due to machine and inverter limitations the rated power P_{N} cannot be evaluated for each test machine. As test machine M2 is partially demagnetized [11] (as described in Chapter 6), the load experiments of both tooth-coil machines back-to-back are limited to about $0.85 \cdot P_{\mathrm{N}}$. Also the small inverter rating of test machine M3 prevents a full-load measurement. With test machine M4 a load of $1.25 \cdot M_\mathrm{N}$ is possible. Test machine M5 is operated up to 67 % of the rated speed due to load machine limitations. In the following comparisons, the focus is set to the operation at 100 % (M5: 67 %) and 50 % of the rated speed.

The current angle β^* is set via the inverter to 15 °el. in motor operation and 165 °el. in generator operation at rated current in the inverter firmware to use the additional reluctance torque of the test machines M1 and M2 according to [11]. At lower torque values the current angle is automatically adjusted by the inverter. The test machines M3 and M4 are driven in q-current operation, as the reluctance torque is negligible due to the surface-mounted rotor magnets. The inverter of test machine M5 does not allow an adaption of the current angle by the end user.

As the torque transducer is designed for at least the rated torque of the machines, the direct values at low torque measurements are associated with rather big error bars.

For the indirect efficiency determination with (5.7) to (5.11) the sum of individual losses at sinusoidal operation $P_\mathrm{d,1}$ and at inverter operation $P_\mathrm{d} = P_\mathrm{d,1} + P_\mathrm{el,in,0,ad}$ are required. These losses are taken from the previous subsections and are recalculated for load operation according to Chapter 5. For the current-depending $\mathrm{I}^2\mathrm{R}$ losses $P_{\mathrm{Cu}\sim}$ it is important to operated at the same stator winding temperature ϑ_Cu as at the corresponding load operation. The iron losses P_Fe are determined with (5.4) by using the no-load iron losses $P_\mathrm{Fe,0}$ from the motor no-load test again at warmed-up test machine.

In order to visualize the indirect efficiency values in dependence of the shaft torque, the indirect shaft torque value M is calculated for motor operation (7.6) and generator operation (7.7) by

$$M_\mathrm{mot} = \frac{P_\mathrm{el} - P_\mathrm{d}}{2\pi \cdot n} \ , \tag{7.6}$$

$$M_\mathrm{gen} = \frac{P_\mathrm{el} + P_\mathrm{d}}{2\pi \cdot n} \ , \tag{7.7}$$

while for sinusoidal operation the fundamental values $P_\mathrm{el,1}$ and $P_\mathrm{d,1}$ are used instead of the total values P_el and P_d.

The comparison of the directly and indirectly measured efficiency of test machine M1 is shown in Figure 7.10 for rated speed and in Appendix C in Figure C.12 for 50 % of the rated speed. For both speed values the indirect efficiency graph is very similar in motor and generator operation, while the direct efficiency deviates by about 1 p.p. near the rated torque. In motor operation the direct efficiency is higher than the indirect values and in generator operation the curves are vice versa. By taking the error limits into account, the deviations are tolerable. This holds already true for the fundamental efficiency. The rather big error bars for the direct efficiency values in comparison to the small error bars for the indirect efficiency values prove the superiority of the latter method for machines with an efficiency above 95 %.

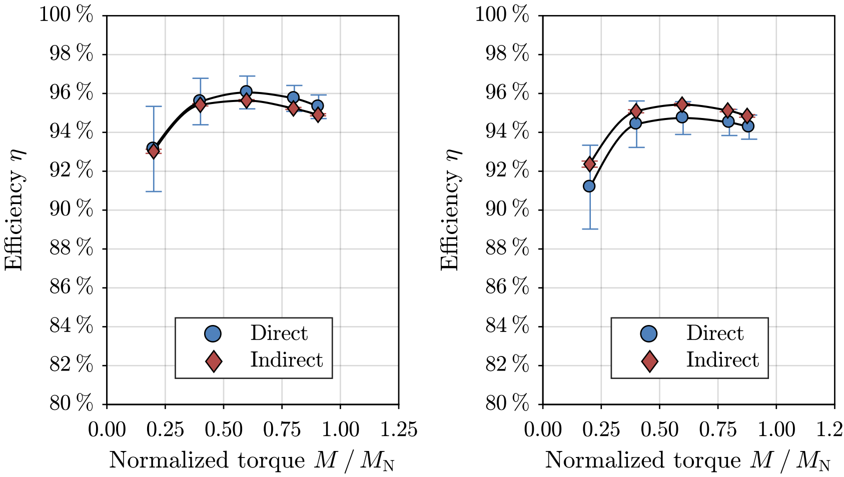

(a) Motor operation (b) Generator operation

Figure 7.10.: Comparison of direct and indirect measured efficiency for test machine M1 at inverter-operation at rated speed ($n_\mathrm{N} = 1000\,\mathrm{min}^{-1}$)

Test machine M2 shows bigger deviations between indirect and direct efficiency at low loads, especially in motor operation. Again the indirect efficiency is nearly equal in motor and generator operation, while the direct efficiency differs. At half rated torque and power the efficiency is comparable to test machine M1, but it shows a stronger drop at rated conditions due to the partial demagnetization, which requires a higher current to reach the torque requirement (Figure C.13). At 50 % of the rated speed the efficiency is again considerably lower than for test machine M1 (Figure C.14). Again, a more or less tolerable accordance between the direct and indirect efficiency within the error limits is shown.

Due to the already described inverter limitations of test machine M3, the efficiency can only be determined up to $0.5 \cdot M_\mathrm{N}$ in generator operation and in motor operation at rated speed (Figure C.15). At lower speeds in motor operation $0.75 \cdot M_\mathrm{N}$ is achieved (Figure C.16). The direct and indirect values show in principle a good accordance except for generator operation at 50 % of the rated speed, where a slightly bigger difference occurs. At fundamental value evaluation operation the accordance between the direct and indirect efficiency is even better, so we conclude that the additional losses due to inverter feeding, which are higher for the two test machines M3, M4 with distributed winding, might be slightly underestimated at low voltage and hence low degree of inverter modulation.

As test machine M4 is constructed very similar to test machine M3, except for the different cooling system, the consistent results of M3 are also valid for M4 at the complete speed and torque range up to rated power. Again a very good accordance between the direct and indirect efficiency occurs at rated speed (Figure 7.11) as well as at 50 % of the rated speed (Figure C.17) in motor and generator operation.

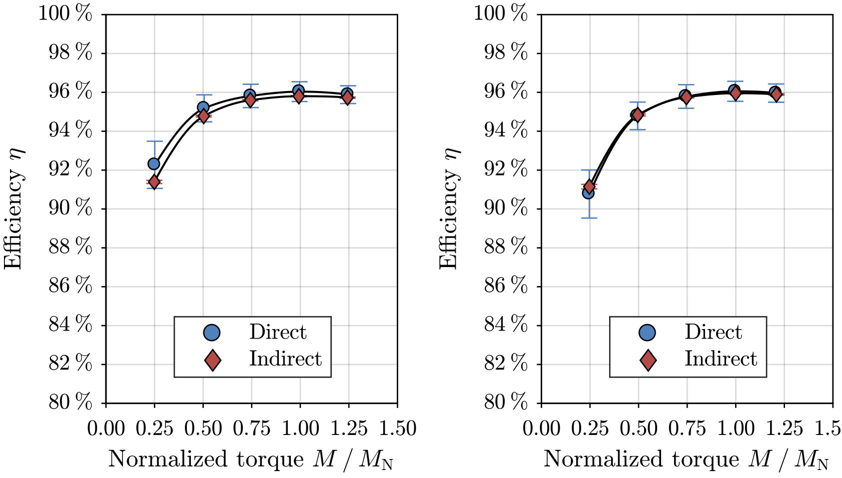

(a) Motor operation

(b) Generator operation

Figure 7.11.: Like Figure 7.10, but for test machine M4 ($n_\mathrm{N} = 2500\,\mathrm{min}^{-1}$) [66]

The deviations between directly and indirectly determined efficiency of test machine M5 are also rather small for 67 % of the rated speed (Figure C.19) and slightly higher for

50 % of the rated speed (Figure C.18). This tendency allows the prediction, that at rated conditions, like for test machines M3 and M4, the accuracy of the indirect method is rather good.

The loss separation of each test machine at rated speed (M5: 67 % of rated speed) in motor operation is shown in Figure C.20 to Figure C.24. The I^2R losses are taken from the removed rotor measurement, the iron losses and the additional losses due to inverter feeding are taken from the motor no-load measurement, and the friction and windage losses are taken from theoretically calculated values. The loss separation in generator operation is very close to the shown motor loss separation. Therefore it is not given in this thesis.

For test machine M1 at low torque the iron losses P_{Fe} are dominant and do not change much with increased load, as the stator fundamental voltage is nearly constant with variable load. Also the additional losses due to inverter feeding $P_{\mathrm{el,in,0,ad}}$ are assumed to be independent of load and are rather small for this test machine. The current-depending losses $P_{\mathrm{Cu}\sim}$ rise with increased torque demand and are the dominant loss component at rated operation. The analytically calculated friction and windage losses $P_{\mathrm{fr+w}}$ are with 1 W very small and therefore neglected.

For test machine M2 the additional losses $P_{\mathrm{el,in,0,ad}}$ are also rather small, while the iron losses P_{Fe} have a much higher increase with rising current due to increased U_{x}. Considering the natural increase of the losses $P_{\mathrm{Cu}\sim}$ also with rising current, at $0.8 \cdot M_{\mathrm{N}}$ the share between iron and copper losses is nearly equal. Like before, the friction and windage losses $P_{\mathrm{fr+w}}$ are calculated to 1 W and therefore negligibly small.

As test machine M3 is only loaded up to $0.5 \cdot M_{\mathrm{N}}$, the current-depending losses $P_{\mathrm{Cu}\sim}$ are with 5 % … 14 % of P_{d} rather low. The dominant loss component are the iron losses P_{Fe} with about 58 % of P_{d}, which do not change much with load due to the small investigated torque range of 25 % … 50 % of M_{N}. Test machine M3 shows significant calculated friction and windage losses $P_{\mathrm{fr+w}}$ according to (3.25) due to the shaft-mounted fan. These losses are nearly equal to the additional losses $P_{\mathrm{el,in,0,ad}}$, which are also increased due to the larger current ripple, caused by the smaller harmonic leakage and hence smaller synchronous inductance of the machines with distributed winding.

Like test machine M3 also test machine M4 has nearly constant iron losses P_{Fe} and assumed constant additional losses $P_{\mathrm{el,in,0,ad}}$ over the whole torque range. The calculated friction and windage losses $P_{\mathrm{fr+w}}$ are negligible. At rated torque and current the current-depending losses are 46 % of the total losses P_{d}.

For test machine M5 at 67 % of the rated speed, again the current-depending losses $P_{\mathrm{Cu}\sim}$ are dominant with 74 % of P_{d} at rated torque, while the iron losses P_{Fe} are about 15 % of P_{d}. The measured friction and windage losses $P_{\mathrm{fr+w}}$ are with about 5 % of P_{d} in the same order of magnitude as the additional losses due to inverter feeding $P_{\mathrm{el,in,0,ad}}$.

The torque over stator current characteristics (Figure 7.12) are measured for M1… M5 at very low speed to have very small speed-dependent losses P_{Fe}, $P_{\mathrm{fr+w}}$, and $P_{\mathrm{ad,1}}$. The investigated operation points for test machines M3, M4, and M5 are within the linear current range. The rated torque $M_{\mathrm{N}} = 320\,\mathrm{Nm}$ of test machine M4 is reached at approximately the rated current of $I_{\mathrm{sN}} = 148\,\mathrm{A}$. Also the rated torque $M_{\mathrm{N}} = 1019\,\mathrm{Nm}$ of test machine M5 is already reached at about 82 % of the rated current of $I_{\mathrm{sN}} = 176\,\mathrm{A}$ for low speed.

For machine M3 the tests are stopped at the inverter current limit of approximately 130 A and the rated torque cannot be reached. Noticeable load-dependent saturation occurs for test machine M2 at about 100 A. The torque over current curve of test machine M1 shows the influence of saturation above the rated current 80 A and the inclination of the characteristic is higher due to the different number of turns per phase. Here also the effect of partial demagnetization of test machine M2, and thus less magnet flux linkage, is visible – like already remarked during the efficiency calculations.

Overall, the load measurements suggest, that the method of indirect efficiency determination has reasonable accordance with the direct efficiency determination within the considered error limits of the measurement devices.

The calculated phasor diagrams of test machine M1 (Figure C.25), M2 (Figure C.26), M4 (Figure C.27), and M5 (Figure C.28) for rated speed (M5: 67 % of the rated speed) and approximately rated torque is shown in Appendix C at the same voltage scale of 35 V/cm but different current scale. The back EMF at load U_{p} is approximated by the no-load voltage U_0. For both tooth-coil test machines M1 and M2, a current angle of $\beta^* = 15\,^\circ\mathrm{el.}$ is used for calculation. Due to the lower stator winding magnetic flux linkage per phase of test machine M2, the phase angle φ is larger compared to test machine M1. Test machine M4 is operated at q-current operation, so that I_{sd} is zero. As test machine M3 is not operated in the relevant torque range, no phasor diagram is shown, but it is similar to test machine M4. For test machine M5 a current angle of $\beta^* = 35\,^\circ\mathrm{el.}$ is used. With

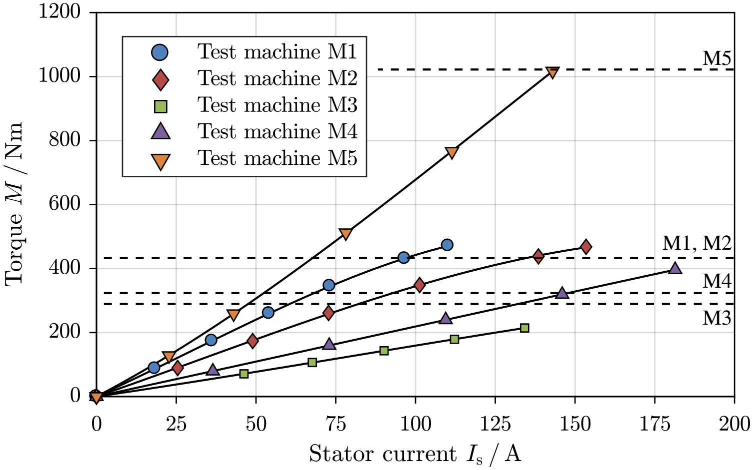

Figure 7.12.: Measured torque M over stator current I_s (rated torque marked, error bars omitted)

the used assumptions the values of the d- and q-axis inductances L_d and L_q are roughly approximated (Table 7.3).

7.3.5. Generator short circuit test

The synchronous inductance L_d is a very important parameter of the permanent-magnet synchronous machine. It is determined with the short-circuit experiment in combination with the no-load results as explained in Section 4.5. Each machine is driven by an external speed-controlled drive, while the stator terminals are shorted. The short-circuit torque M_{sc} and the stator current $I_{s,sc}$ is measured.

As exemplary shown for test machine M4 (Figure 7.13), the torque M_{sc} rises very fast to its maximum $\hat{M}_{sc} = 489\,\mathrm{Nm}$ and decreases as expected. On the other hand the stator current $I_{s,sc}$ rises to its maximum – the short-circuit current $I_{sc} = 426\,\mathrm{A}$. With (4.13) the synchronous inductance is determined at the maximum speed to $L_d = 0.44\,\mathrm{mH}$.

For test machine M3 the procedure is stopped at about $200\,\mathrm{min}^{-1}$ and $150\,\%$ of the rated current (Figure C.31) to prevent the stator winding from overheating due to the lack of adequate cooling at low speed. But with (4.11) the synchronous inductance can still be

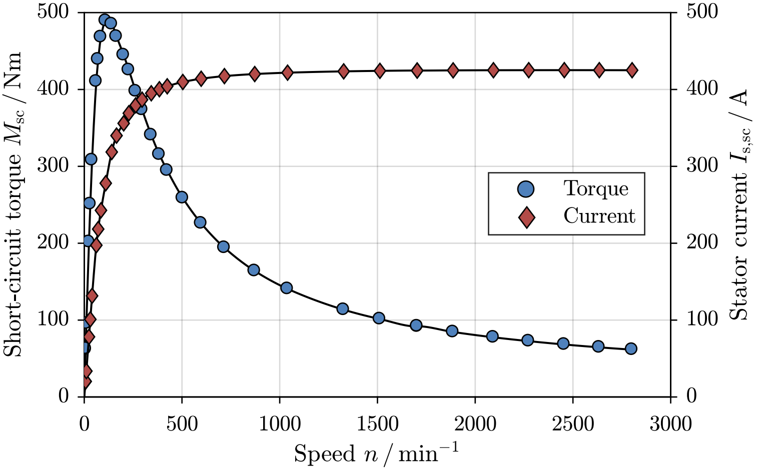

Figure 7.13.: Torque M_{sc} and current I_{sc} over speed at the short-circuit test for test machine M4 (error bars omitted)

determined to $L_{\mathrm{d}} = 0.53\,\mathrm{mH}$. This value is close to the one of test machine M4, which is reasonable, as both machine share a similar design. The magnetically effective air gap δ_{e} of test machine M3 is only about 10 % smaller (Table A.3). Therefore the inductance is slightly higher (Table 7.3). With the no-load voltage at rated speed the stationary short-circuit current $I_{\mathrm{sc}} = 334.6\,\mathrm{A}$ is calculated for M3.

For both test machines M1 and M2 the maximum of the short-circuit torque $\hat{M}_{\mathrm{sc}}$ occurs at a very low speed of $n = 20\,\mathrm{min}^{-1}$, where the speed controller resolution of the driving machine is giving a possible speed deviation of about 10 % (Figure C.29, Figure C.30). Therefore the true torque maximum might be of a slightly higher amplitude, located slightly beside the given set-point speed of $n = 20\,\mathrm{min}^{-1}$ (Table 7.3). The stationary short-circuit current I_{sc} is much lower than for the previous machines M3 and M4, as the harmonic leakage inductance $L_{\mathrm{s}\sigma\mathrm{o}}$ is much bigger for this kind of fractional-slot tooth-coil windings due to the high harmonic content (see Chapter 6). The synchronous inductance is calculated to $L_{\mathrm{d}} = 2.83\,\mathrm{mH}$ for test machine M1 and $L_{\mathrm{d}} = 2.48\,\mathrm{mH}$ for test machine M2. These values are close to the values measured at the previous research project on these machine [11] (M1: $L_{\mathrm{d}} = 2.78\,\mathrm{mH}$, M2: $L_{\mathrm{d}} = 2.45\,\mathrm{mH}$).

For test machine M5 only few values above a speed of $n = 100\,\mathrm{min}^{-1}$ could be obtained due to limitations of the driving load machine. Therefore the torque and current curves are only roughly approximated for higher speed values. Due to the small deviation of the stator current, the last value of $I_{\mathrm{s,sc}} = 266\,\mathrm{A}$ is assumed to approximate the stationary short-circuit current I_{sc}. With this value the synchronous inductance is calculated to 1.26 mH.

Besides the calculation of the synchronous inductance via (4.13), also a curve fitting of the short-circuit current or torque is possible to estimate the inductance values. The results of the curve fitting method are also given in Table 7.3.

7.3.6. Reactive current test

Like explained in Section 4.6, the reactive current experiment can replace the generator short-circuit test, if it is not possible to perform this test. To prove this, the reactive current experiment is carried out for test machines M1, M2, and M5. Each test machine is driven uncoupled in motor no-load operation via the inverter, when the amplitude of the field weakening current I_{d} is increased with the current angle $\beta^* > 0$ for different speed values. The fundamental values of the stator current $I_{\mathrm{s},1}$ over the stator voltage $U_{\mathrm{s},1}$ are straight lines (Figure 7.14, Figure C.33, Figure C.34). The experiment is stopped at a minimum fundamental stator voltage per phase of 70 V to keep the stator counter field on the rotor magnets within reasonable limits. At the extrapolated value of $U_{\mathrm{s},1} = 0$ each of the curves points to the *motor short-circuit current* I_{sc}. The measured values are within 5 % of the values from the generator short-circuit test. Therefore also the synchronous inductance, calculated with (4.13), is close to the calculated values of Section 7.3.5 (Table 7.3). This shows, that the reactive current is also usable to determine the synchronous inductance for inverter-driven permanent-magnet synchronous machine.

As a side effect, the impressed stator current without mechanical load may be used to heat up the stator winding and the whole machine for further experiments, like the no-load tests, if the short-circuit current is high enough to exceed the rated current of the machine, like seen for test machines M3 ($I_{\mathrm{sc}}/I_{\mathrm{N}} = 1.7$), M4 ($I_{\mathrm{sc}}/I_{\mathrm{N}} = 2.9$), and M5 ($I_{\mathrm{sc}}/I_{\mathrm{N}} = 1.5$). Due to the higher stator inductance of test machines M1 ($I_{\mathrm{sc}}/I_{\mathrm{N}} = 0.7$) and M2 ($I_{\mathrm{sc}}/I_{\mathrm{N}} = 0.5$), the short-circuit current is lower than the rated current. These machines have a wider operation range for field weakening (five times the rated speed in [11]), but here the reactive current test is not suitable for an adequate current impression to heat up the machine.

Table 7.3.: Measurement and calculation results of the short-circuit and reactive current test

	Unit	M1	M2	M3	M4	M5
Measured values at the generator short-circuit test						
Stator current $I_{\mathrm{s,sc}}$ *	A	75.0	58.4	306.9	425.0	265.9
at speed n	min^{-1}	1400	1400	197	2803	508
Short-circuit torque $\hat{M}_{\mathrm{sc}}$	Nm	*195*	*103*	295	489	993
at speed n	min^{-1}	*20*	*20*	90	110	48
Calculated values from motor no-load and generator short-circuit measurement						
Voltage ratio U_0/f_s	V/Hz	1.33	0.91	1.13	1.17	2.11
Stationary short-circuit current I_{sc} *	A	75.0	58.4	334.6	425.0	265.9
d-axis inductance L_d * (unsaturated, calculated with (4.13))	mH	2.83	2.48	0.53	0.44	1.26
Calculated values from generator short-circuit measurement via curve fitting						
d-axis inductance L_d * (unsaturated, calculated from current via (4.14))	mH	2.83	2.49	0.57	0.44	1.27
q-axis inductance L_q * (unsaturated, calculated from current via (4.14))	mH	2.83	2.49	0.57	0.44	3.39
d-axis inductance L_d * (unsaturated, calculated from torque via (4.16))	mH	2.93	2.36	0.49	0.42	1.30
q-axis inductance L_q * (unsaturated, calculated from torque via (4.16))	mH	2.35	2.36	0.49	0.42	3.88
Calculated values from reactive current measurement						
Voltage ratio $U_{0,1}/f_\mathrm{s}$	V/Hz	1.36	0.94	–	–	2.17
Stationary short-circuit current I_{sc} *	A	76.0	57.4	–	–	253.3
d-axis inductance L_d * (unsaturated, calculated with (4.17))	mH	2.85	2.61	–	–	1.36
Calculated values from phasor diagram of motor load measurement						
d-axis inductance L_d *	mH	2.96	2.37	–	0.63	0.92
q-axis inductance L_q *	mH	2.35	2.64	–	0.63	2.31

* per phase

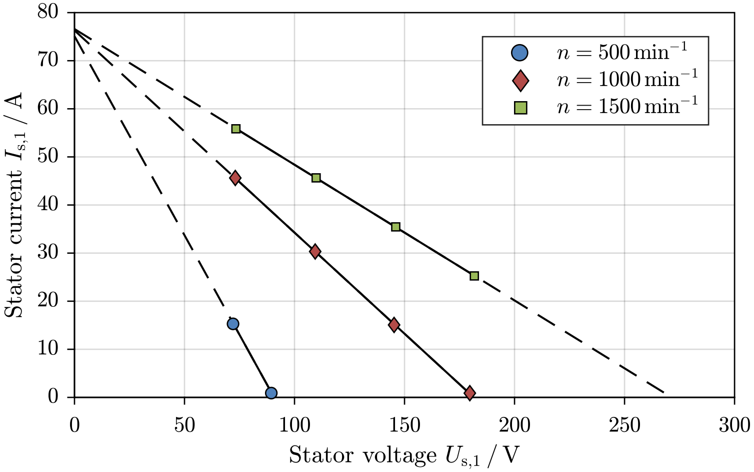

Figure 7.14.: Measured stator current $I_{s,1}$ over stator voltage $U_{s,1}$ at the reactive current test for different speeds n of test machine M1 [69] (error bars omitted)

7.4. Results of other authors

The proposed method for indirect efficiency determination has also been evaluated by the *PTB Braunschweig* in [40], [61]. There a permanent-magnet synchronous machine with a smaller rated power of 7.5 kW was used. The test machine (here denoted as test machine M6) had a distributed integer-slot stator winding and surface-mounted rotor magnets.

Like in this thesis, the efficiency was determined directly and indirectly for different rotor speeds n. For the indirect efficiency determination, the friction and windage losses $P_{\mathrm{fr+w}}$ were measured at the generator no-load experiment with a non-magnetized rotor.

The measured indirect and direct efficiency values show a good agreement in a wide speed range with deviations below 0.5 p.p., as shown for rated speed $n_{\mathrm{N}} = 1500\,\mathrm{min}^{-1}$ in Figure 7.15 and for 67 % of the rated speed in Figure 7.16. Also the measurement uncertainty of the indirect efficiency is lower than the measurement uncertainty of the direct efficiency.

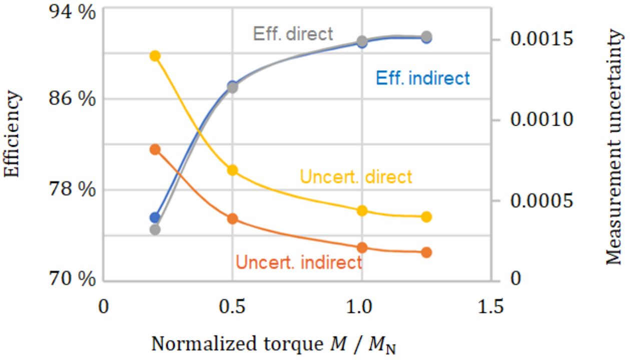

Figure 7.15.: Comparison of direct and indirect measured efficiency and measurement uncertainty for test machine M6 by the *PTB Braunschweig* at inverter-operation at rated speed ($n_\mathrm{N} = 1500\,\mathrm{min}^{-1}$) [61]

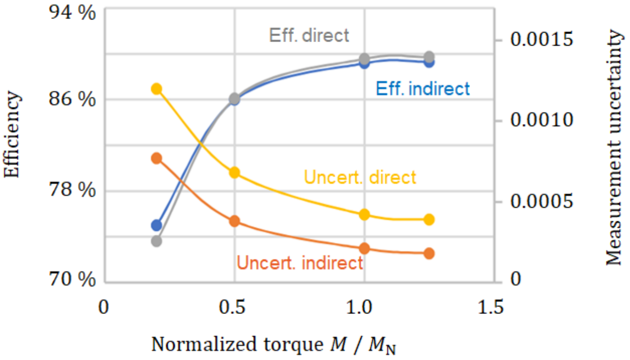

Figure 7.16.: Like Figure 7.15, but for 67 % of the rated speed ($n = 1000\,\mathrm{min}^{-1}$) [61]

8. Finite element simulations

The proposed measurement routines in Chapter 4 are based on several assumptions concerning the voltage- and current-depending losses. To validate these assumptions, finite element (FE) simulations at sine-wave voltage and current are performed. The inverter PWM operation is not simulated. As the machine behavior strongly depends on the nonlinear material properties of e.g. the magnets and the steel sheets, fixed-step transient simulations are chosen with a time step e.g. like in Table 8.1. For each experiment setup the FE software *JMAG* is used in a two-dimensional package.

The following sections describe the FE models of all four investigated test machines, which depend on the particular requirements of the individual experiments: In the no-load and load case usually one pole pair is needed, while for the removed rotor experiment for the eddy current losses in the stator winding for simplicity one stator slot is sufficient. In general *JMAG* offers the required simulation options, like circuit modeling, iron loss post-processing and the consideration of eddy currents. The simulations concentrate on the losses at sinusoidal current feeding. The inverter PWM operation is not simulated. Therefore the calculated efficiency of Section 8.5 is comparable with the measured fundamental efficiency values of Chapter 7.

8.1. Methodology

The simulation process consist of three major stages: model design, transient analysis, and post-processing.

In the design stage (first stage) the geometry of the two-dimensional machine model is created. By using the rotational periodic symmetry of the machines, the size of the final models can be reduced drastically, which leads to less finite elements and less simulation time. The individual parts – like stator and rotor iron, copper conductors, and magnets – are modeled separately to assign different material properties. Each iron part is assigned to a specific steel sheet type, which includes the respective magnetic flux density over field strength curve $B(H)$ and the specific iron losses. The copper conductivity is set according to the material temperature. For the magnets the magnetization direction is set to create north or south poles. Also the remanence flux density, coercive field strength, and conductivity is set according to material data.

In order to impress stator currents into the model, an electrical equivalent circuit is used to link the FE field quantities to outer parameters. Here also approximations of the three-dimensional winding overhang are modeled by resistance and leakage reactance parameters.

In the next step the finite element mesh is created. The size and thus the amount of elements strongly influences the precision of the analysis and the simulation time. So here a trade-off has to be found. Nevertheless in regions with large field gradients, like for eddy current calculation, the element size has to be at least three times smaller than the penetration depth of the highest considered frequency. Overall the (triangular) shape of the elements shall be as regular is possible. In the air gap, between the fixed stator and the moving rotor, rectangular elements are used. The air gap is automatically remeshed for each time step. The amount of tangential divisions shall correspond to the amount of time steps, so that the mesh shape does not change during the rotation of the rotor. The number of time steps per electrical period corresponds to the frequency of the highest investigated air gap field harmonic, i.e. for a higher time resolution also a higher element resolution in the air gap is necessary. The number of radial divisions is chosen afterwards according to the requirement of regular element shapes (see Figure 8.2).

The transient analysis (second stage) uses a non-linear Newton-Raphson solver to calculate the electromagnetic quantities at each step. The step time interval has a fixed size $T_{\mathrm{step}} = T_{\mathrm{s}}/n_{\mathrm{div}}$, where T_{s} is the electrical period and n_{div} is the number of time divisions. The overall number of steps n_{step} is higher than the number of division, as at the beginning some steps are omitted until the transient solution has reached steady-state.

In order to analyze different operation states of the machines, parametric *case studies* are applied to easily change parameters like e.g. simulation end time, rotational speed, and current amplitude.

After the transient simulation the results of the electromagnetic quantities are gathered and further analyzed by means of e.g. averaging calculation or *Fourier* analysis. Also graphical field plots of e.g. the magnetic flux density or current density are created. In this stage all results except the iron losses are being determined.

The iron losses in the stator and rotor lamination are determined in the third stage. Here the results of the transient simulation are used to calculate the amount of iron losses by using a loss table for each considered frequency of the magnetic flux density. The fundamental frequency of the harmonic analysis shall correspond to the rotational speed of the transient simulation. Here also parametric studies are utilized to link the post-processing calculation to the correct case of the transient simulation.

Further details of the individual model settings for each simulation are given at the beginning of the following sections.

8.2. Generator no-load operation

At the generator no-load simulation the no-load flux density, the stator no-load voltage (as back EMF) and the no-load losses are analyzed. This requires a mechanical rotor movement, while the stator current is zero. The rotor speed is varied in the base speed range according to Table 8.1.

Table 8.1.: Parameters of the generator no-load simulations for the four test machines M1 … M4

	Unit	M1	M2	M3	M4
Rated speed	min^{-1}	1000	1000	3000	2500
Minimum speed	min^{-1}	250	250	500	625
Maximum speed	min^{-1}	1500	1500	3000	3125
Rated frequency	Hz	133.3	133.3	150.0	166.7
Minimum frequency	Hz	33.3	33.3	25.0	41.7
Maximum frequency	Hz	200.0	200.0	150.0	208.3
Number of simulated cases	–	5	5	6	5
Time step	s	$\frac{1}{90} \cdot T_\text{s}$	$\frac{1}{120} \cdot T_\text{s}$	$\frac{1}{60} \cdot T_\text{s}$	$\frac{1}{60} \cdot T_\text{s}$

8.2.1. Model description

Test machine M1

Due to symmetry reasons it is sufficient to model only one pole pair of the machine in cylindrical coordinates ($\rho - \varphi - z$). Therefore the model (Figure 8.1) consists of 45° of the stator and rotor circumference.

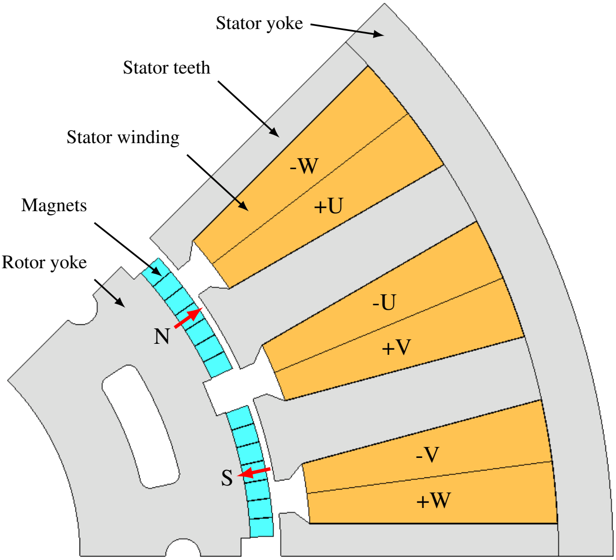

Figure 8.1.: FE model of basic stator winding scheme (= one pole pair) of test machine M1 for generator no-load operation

The stator is divided into the stator yoke and the stator teeth, so that the yoke and teeth iron losses in the lamination can be separated, and can be considered individually. In the rotor only one iron section exists: the rotor yoke. The material properties of the iron sections are defined in *JMAG* from exemplary manufacturers data sheets. Here mainly the $B(H)$-curve without hysteresis influence and the loss coefficients (Section 3.3) are important. For test machine M1 the steel sheet material 400-50AP is used in the stator and rotor lamination sections [11]. All iron losses are calculated via post-processing with the results of the time-step simulation with the formulas and the evaluation method of *JMAG*, which is shortly described in Appendix F.

The stator winding is simplified to a so called *FEM coil* condition. Here *JMAG* applies the stator currents, which are zero in generator no-load, using an external circuit without any eddy current calculation. Therefore the conductor may be modeled by a solid section inside the slot, carrying the total ampere-turns per coil, while the conducting cross-section is not important. The phase order of the double-layer tooth-coil winding in the model is +U, +V, +W. As no eddy current calculation is used, the electric conductivity of the copper material is not relevant.

For the rotor magnets, the magnetic properties are known from previous works (Vacodym 655 HR [11]). With the rotor temperature set to fit with the measurements (60 °C, Chapter 7), the remanence flux density is $B_{\mathrm{R}} = 1.207\,\mathrm{T}$. The magnets are tangentially divided into seven segments per pole. The axial segmentation is approximated by reducing the electric conductivity of the magnets according to (8.3). With this equivalent conductivity the eddy currents in z-axis due to harmonics of the electromagnetic air gap field are calculated during the time-step simulation.

In the air gap a *sliding mesh* is applied. The mesh consists of (here five) layers, where the half of the layers is assigned to the stator (blue) and the other half is rotating with the rotor (purple). By choosing the appropriate numbers of tangential divisions, rectangular mesh elements are achieved, that do not change their position and shape during the rotor movement, leading to an accurately calculated air gap flux density. The rotor carbon fiber bandage is modeled as air.

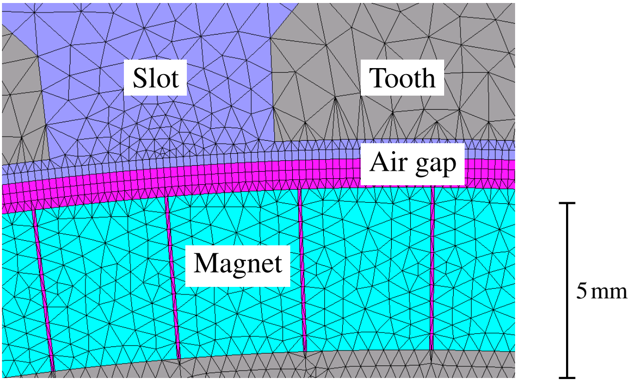

Figure 8.2.: Detail of air gap sliding mesh of test machine M1

Test machine M2

For test machine M2 two pole pairs have to be simulated according to the single-layer tooth-coil winding. Again, by using the symmetry, only 90° of the complete machine need to be modeled.

The stator lamination is divided into the yoke, the stator teeth and the inter-teeth (Figure 8.3). In the rotor, beside the yoke, iron bridges are necessary to cover the magnets. Like test machine M1 each of the iron components is assigned to the steel sheet material 400-50AP [11].

The magnet material Vacodym 655 HR is basically equal to test machine M1, but due to irreversible demagnetization in earlier experiments [11], the magnets lost 15 % of their remanence flux density ($B_\mathrm{R} = 1.026\,\mathrm{T}$ instead of $B_\mathrm{R} = 1.207\,\mathrm{T}$ at 60 °C).

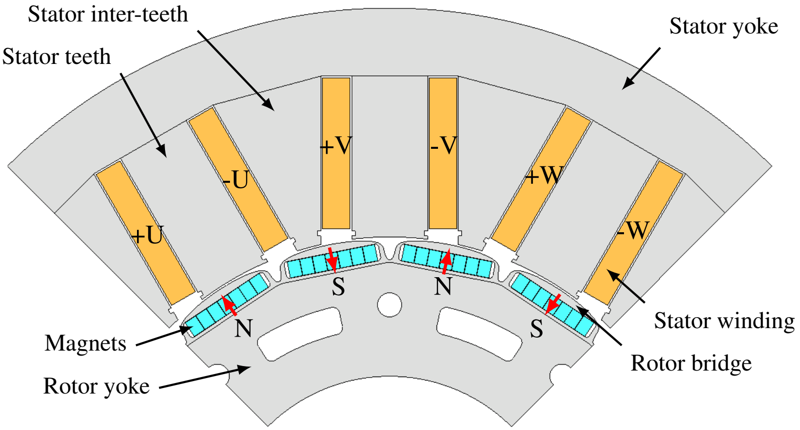

Figure 8.3.: FE model of one basic stator winding scheme (4 poles) of test machine M2 for generator no-load operation

Test machine M3

As test machine M3 has an integer-slot winding, only one pole, hence one sixth (60° of the machine circumference is necessary to model with anti-symmetric boundary condition for generator no-load operation. Here one pole pair was simulated. The distributed integer-slot winding with $q = 2$ slots per pole and phase is again simplified as FEM coils (Figure 8.4).

The material of the iron sections (stator yoke and teeth, rotor yoke) is assigned to M470-50A from information of the manufacturer. The rotor magnets are segmented in tangential and axial direction. The segmentation has been evaluated by visual inspection of the rotor. As no magnet material data was given for this machine, a comparable magnet material is chosen with the remanence flux density of $B_\mathrm{R} = 1.03\,\mathrm{T}$ to fit the calculated generator no-load voltage to the measurements of the warm machine.

As for the previous machines, a sliding mesh condition is used in the air gap, where again the rotor carbon fiber bandage is replaced by air.

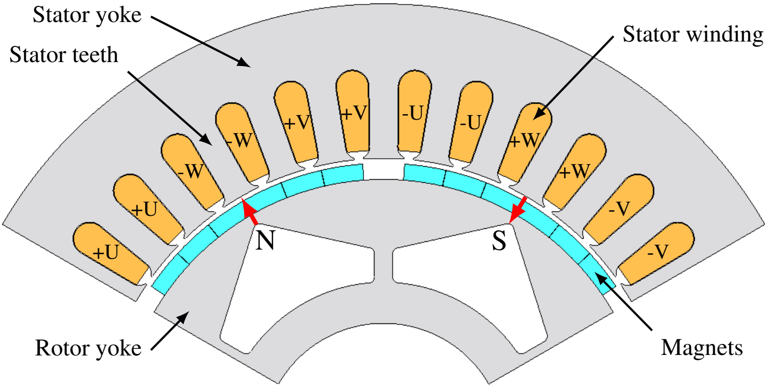

Figure 8.4.: FE model of one pole pair of test machine M3 for no-load operation

Test machine M4

Test machine M4 is very similar to test machine M3. The model differs mainly in the slot opening geometry, the number of poles ($2p = 8$), and the amount of magnet segments per pole in circumference direction. As no rotor iron cross-section was given for this test machine, no axial cooling ducts are considered and the rotor inner diameter is estimated.

The material of the iron sections is M530-50A. Like for test machine M3 the magnet properties have to be chosen in respect to the measured no-load voltage of the warm rotor. The resulting remanence flux density is $B_R = 1.15\,\mathrm{T}$.

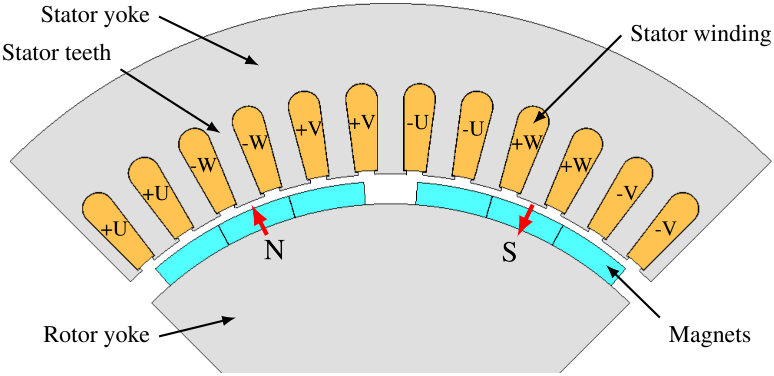

Figure 8.5.: FE model of one pole pair of test machine M4 for no-load operation

8.2.2. Generator no-load flux density and voltage

For each of the four test machines the magnetic no-load flux density is analyzed during the transient time-step simulations. Therefore a probe is placed in the center of the mechanical air gap, which covers at least one pole pair in tangential direction ($0\ldots360°$ el.). The magnetic flux-density at a given time-step consists mainly of a radial component. This component is shown in Appendix E together with the sinusoidal fundamental flux density (Figure E.2 to Figure E.5). The three test machines with surface-mount magnets (M1, M3, and M4) have a rather flat-top radial flux density component with some flux density drop due to the stator slot openings, while for test machine M2 this impact due to the rectangular open slots is even higher. The results for test machines M1 and M2 are comparable to the simulations in [11], if the partial demagnetization of test machine M2 is taken there also into account. The fundamental amplitudes of all test machines are in the range of $0.79\,\mathrm{T}\ldots0.91\,\mathrm{T}$ (Table 8.2).

The generator no-load phase voltage of test machine M1 is nearly sinusoidal (Figure E.13). This shows up also in the amplitude spectrum (Figure E.14), where nearly only the fundamental occurs. The RMS value of the fundamental no-load voltage $U_{0,1} = 178.9\,\mathrm{V}$ fits to the measured no-load voltage (Table 7.1).

Table 8.2.: Calculated generator no-load magnetic flux density and voltage at rated speed for the four test machines M1 … M4

	Unit	M1	M2	M3	M4
Rated speed	min^{-1}	1000	1000	3000	2500
Radial flux density $B_{\delta,1}$	T	0.91	0.79	0.84	0.79
Magnet temperature ϑ_{M}	°C	60	60	–	–
Fundamental voltage $U_{0,1}$ (RMS, per phase)	V	178.9	121.6	169.9	196.7

For test machine M2 more harmonics are present in the no-load phase voltage spectrum (Figure E.16). The voltage has a flat-top shape (Figure E.15) with an RMS value of the fundamental $U_{0,1} = 121.6\,\mathrm{V}$, which also matches the measured value.

Due to the similar motor design of the test machines M3 and M4 the spectral amplitude distribution of the generator no-load voltage is also similar (Figure E.18, Figure E.20). The influence of the stator slot harmonic effect of the stator winding factor, which amplifies the corresponding rotor field harmonic induction, on the phase voltage is clearly visible at the flat-top curves in Figure E.17 and Figure E.19.

Like before, the fundamental no-load RMS values (M3: $U_{0,1} = 169.9\,\mathrm{V}$, M4: $U_{0,1} = 196.7\,\mathrm{V}$) coincide with the measurement. Note, that the line-to-line voltages do not contain any harmonics of order multiple of three.

The plots of the flux lines during no-load operation are given in Appendix E (Figure E.6 to Figure E.9).

8.2.3. Iron losses

The iron losses are calculated via post processing with help of the result table of the electromagnetic simulations. The material loss coefficients of the manufacturer data is used to calculate the specific losses. An FFT analysis is used to determine the harmonic components of the magnetic flux density B in each element, which is explained in Appendix F. The loss coefficients for frequencies, that are not implemented, are extrapolated by *JMAG*. The basic frequency of the analysis corresponds to the first harmonic $\nu = 1$ of the stator field according to the simulation period. For each given frequency f the amount of iron loss is determined as

$$P_{\mathrm{Fe}} = k_{\mathrm{V}} \cdot \left(P_{\mathrm{Fe,Hy}} + P_{\mathrm{Fe,Ft}}\right) \ . \tag{8.1}$$

The hysteresis losses $P_{\mathrm{Fe,Hy}}$ and the *Foucault* losses $P_{\mathrm{Fe,Ft}}$ are determined separately for each element. The separation into the two loss mechanisms is done by the FE software according to Appendix F. In the following results, at first, no loss increase due to manufacturing is considered ($k_{\mathrm{V}} = 1$).

Starting with test machine M1, Figure 8.6 shows the simulated iron losses with the separation into hysteresis losses and *Foucault* losses. The hysteresis component has as linear dependency on the mechanical rotor speed and thus on the frequency of the magnetic flux density due to the used loss formula. The *Foucault* losses depend, according to the loss formula for thin sheets ($b_{\mathrm{sh}} \ll d_{\mathrm{E}}$) on the square of the frequency. At the speed of approximately $n = 850\,\mathrm{min}^{-1}$ both components are of equal size.

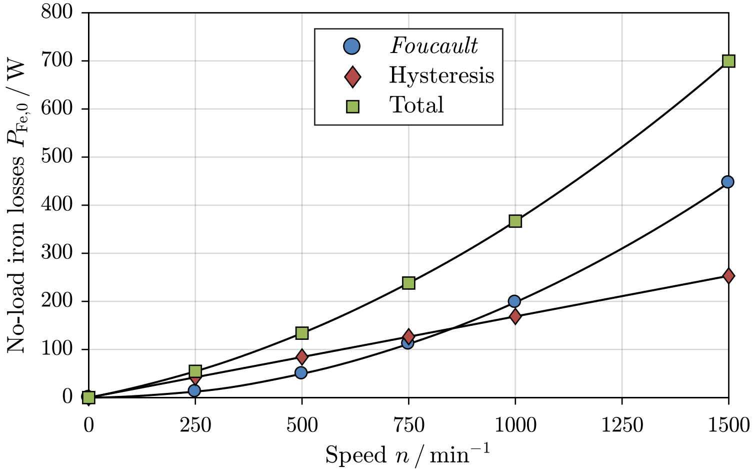

Figure 8.6.: Simulated iron losses as sum of hysteresis losses and *Foucault* losses at generator no-load operation of test machine M1 ($n_{\mathrm{N}} = 1000\,\mathrm{min}^{-1}, k_{\mathrm{V}} = 1$)

Due to the separation of individual iron regions, also the difference between stator and rotor iron losses may be analyzed. For test machine M1 the rotor iron losses are nearly zero, as the magnetically effective air gap is big enough to decrease the influence of the stator openings. This effect is clearly visible at the distribution of the respective iron loss density (Figure 8.7). The plot colors indicate a nearly homogeneously distributed loss density P_{Fe}/V in $\mathrm{W/m^3}$ in the stator yoke and the stator teeth as well, with slightly increased values at the tooth tips.

At test machine M2 the rotor bridges are located much closer to the stator tooth tips, where the modulation of the flux density due to the stator slot openings with slot frequency $n \cdot Q_{\mathrm{s}}$ has an increased influence on the rotor iron losses as tooth pulsation losses. The largest values of the iron loss density (Figure 8.8) are therefore located in the smaller bridge regions, and are approximately five times higher than the maximum values of test machine M1.

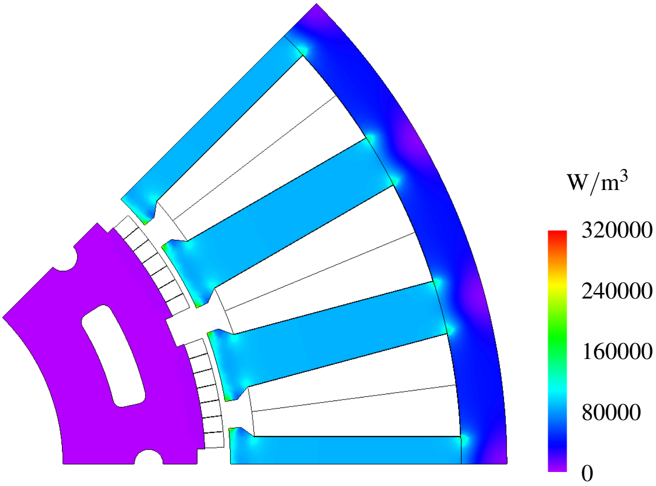

Figure 8.7.: Simulated iron loss density at generator no-load operation of test machine M1 at rated speed $n_{\mathrm{N}} = 1000\,\mathrm{min}^{-1} (k_{\mathrm{V}} = 1)$

After weighting the iron loss densities with the respective iron areas, the integral iron losses are smaller than for test machine M1, as the amplitude of the magnetic flux density is smaller due to the partial demagnetization of the rotor magnets. The comparison of the iron losses for different rotor speed (Figure E.22) shows that the amount of rotor iron losses is significant with approximately one third of the total iron losses at generator no-

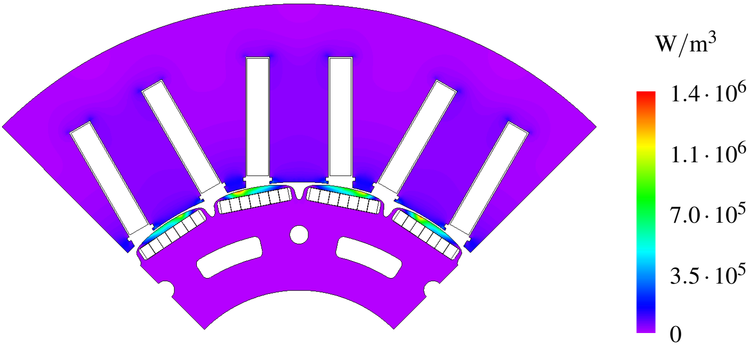

Figure 8.8.: Simulated iron loss density at generator no-load operation of test machine M2 at rated speed $n_\mathrm{N} = 1000\,\mathrm{min}^{-1}$ ($k_\mathrm{V} = 1$)

load operation.

For both test machines M3 and M4 nearly no rotor iron losses occur, as the magnetically effective air gap is rather big and the slot openings are small due to the semi-closed slots. The iron loss density (M3: Figure E.25, M4: Figure E.26) as well as the separation of the iron losses into *Foucault* and hysteresis losses (M3: Figure E.23, M4: Figure E.24) is shown in Appendix E.

Table 8.3.: Comparison of measured and simulated no-load iron losses at rated speed

	Unit	M1	M2	M3	M4
Rated speed n_N	min^{-1}	1000	1000	3000	2500
Rated frequency f_sN	Hz	133.3	133.3	150.0	166.7
No-load iron losses $P_\mathrm{Fe,0}$ (measured)	W	476	304	1892	1034
No-load iron losses $P_\mathrm{Fe,0}$ (simulated)	W	367	234	996	977
Iron loss factor k_V (calculated)	–	1.3	1.3	1.9	1.1

The comparison of the simulated total no-load iron losses with the measured values is shown in Table 8.3. By dividing both values, the iron loss increase factor k_V at rated speed and frequency is determined:

$$k_{\mathrm{V}} = \frac{P_{\mathrm{Fe,0,sim}}}{P_{\mathrm{Fe,0,meas}}} \; . \tag{8.2}$$

The loss increase factor is nearly unity for test machine M4 ($k_{\mathrm{V}} = 1.1$) and relatively high for test machine M3 ($k_{\mathrm{V}} = 1.9$).

8.2.4. PM losses

The surface-mounted rotor magnets of test machines M1, M3, and M4 are located much closer to the stator than the rotor iron. Therefore a pulsating magnetic field due to the stator slot openings already at no-load and increased at sinusoidal stator load current, but also stator field waves due to stator current harmonics, will enter the magnet material and induce eddy currents, causing ohmic losses P_{M} in the magnets. To determine the amount of magnet losses P_{M}, in each magnet segment the eddy current condition, i.e. that the sum of current density per cross-section is zero, and the PM material conductivity κ_{M} has to be set in *JMAG*. The three-dimensional end effect and the effect of axial magnet segmentation is considered roughly by the effective conductivity [52]

$$\kappa_{\mathrm{M,eff}} = \frac{\kappa_{\mathrm{M}}}{1 + b_{\mathrm{M}}/l_{\mathrm{M}}} \; , \tag{8.3}$$

like in [6], [39], [51], where κ_{M} is the original magnet conductivity and b_{M} and l_{M} are the magnet segment width and length. Of course this is just an approximation, but this way a three-dimensional FE simulation can be avoided. The magnet losses P_{M} are not the dominating loss group anyway due to the working principle of the permanent-magnet synchronous machine, i.e. of a stationary stator fundamental field wave with respect to the rotor.

For each test machine the eddy current loss density in the magnets first at generator no-load is analyzed. As example it is shown for test machine M3 in Figure 8.9, that the maximum loss density occurs below the stator slot openings due to the modulated pulsating rotor air gap field at the slot openings. This is also the case for test machine M1 (Figure E.27) and test machine M4 (Figure E.29). The high-permeable rotor iron bridges of test machine M2 guide the magnetic flux around the magnets. Therefore the loss density in the magnets is very low (Figure E.28). On the other hand, the iron losses in the laminated rotor iron bridges on top of the magnets are increased.

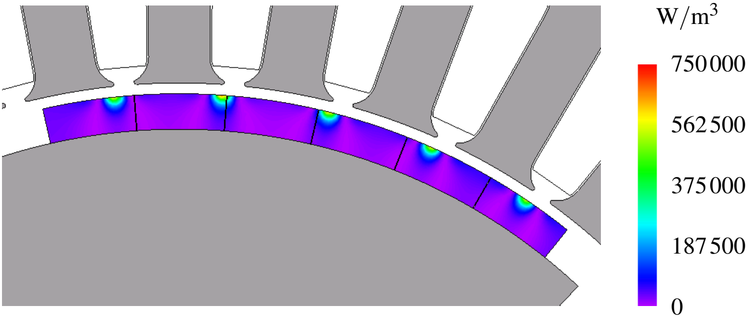

Figure 8.9.: Simulated magnet eddy current loss density at generator no-load operation of test machine M3 at rated speed ($n_N = 3000\,\text{min}^{-1}$)

The calculated integral no-load magnet losses $P_{M,0}$ of all magnets at rated speed and frequency is given in Table 8.4. Test machine M4 has less magnet segments and therefore bigger magnets with thus the biggest losses, while for the other test machines the no-load magnet losses are rather low (less than 0.5 % of the total rated losses).

The frequencies of the induced eddy currents in the rotor magnets is also analyzed by the FE software. Due to the stator slot frequency $f_Q = n \cdot Q_s$, multiples of the slot frequency f_Q occur (Table 8.4), where the component with f_Q dominates.

Table 8.4.: Simulated no-load magnet losses at rated speed

	Unit	M1	M2	M3	M4
Rated speed n_N	min^{-1}	1000	1000	3000	2500
Rated frequency f_{sN}	Hz	133.3	133.3	150.0	166.7
Number of stator slots Q_s	–	24	24	36	48
Effective conductivity $\kappa_{M,eff}$	MS/m	0.56	0.56	0.19	0.33
No-load magnet losses $P_{M,0}$	W	10	<1	19	89
Rotor frequency f_Q	Hz	400	400	1800	2000

Similar to the rotor iron losses of test machine M2, rotor magnet losses are a part of the measured losses at the no-load loss measurement hence they can't be separated for the recalculation of stator iron losses at the removed rotor test and at load operation like described in Chapter 5.

8.3. Removed rotor operation

With the loss simulation at removed rotor operation the current-depending losses $P_{\mathrm{Cu}\sim} = P_{\mathrm{Cu=}} + \Delta P_{\mathrm{Cu}}$ in the stator winding and the stator iron losses $P_{\mathrm{Fe,B}}$ are determined.

Table 8.5.: Parameters of the removed rotor simulations

Parameter	Unit	M1	M2	M3	M4
Rated frequency	Hz	133.3	133.3	150.0	166.7
Minimum frequency	Hz	5.0	6.7	5.0	5.0
Maximum frequency	Hz	133.3	400.0	150.0	166.7
Minimum temperature	°C	0	0	0	0
Maximum temperature	°C	140	140	140	120
Number of simulated cases	–	40	56	48	40
Time step	s	$\frac{1}{90} \cdot T_{\mathrm{s}}$	$\frac{1}{120} \cdot T_{\mathrm{s}}$	$\frac{1}{60} \cdot T_{\mathrm{s}}$	$\frac{1}{60} \cdot T_{\mathrm{s}}$

8.3.1. Model description

For this simulation the rotor of the FE models is removed completely. For the determination of the current-depending losses $P_{\mathrm{Cu}\sim}$ in the stator winding, the no-load FE models have to be extended by a detailed conductor model. As due to the AC slot stray field current displacement occurs in the stator winding conductors, the winding has to be modeled with single conductors, and has to be placed in the stator slot according to the real geometry (Figure 8.10). In the easiest case of test machine M2 the placement of each rectangular single conductor is known from the manufacturing and can be modeled accurately. For the other test machines with round wires the actual placement of the conductors is not

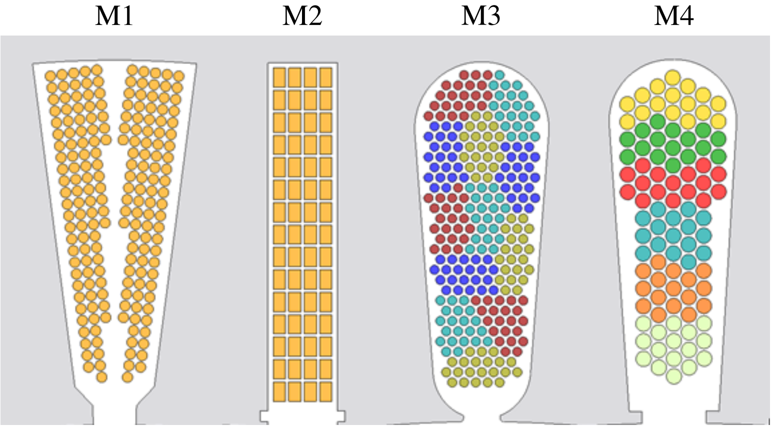

Figure 8.10.: Single conductor models of one stator slot (different scale)

well-defined and random transpositions due to the manufacturing process from slot to slot are possible. If parallel sub-conductors are present per turn ($a_\mathrm{i} > 1$), the first order current displacement with unequal current distribution per sub-conductor may dominate. Then the conductor positions significantly influence the losses. This is the case for test machines M3 ($a_\mathrm{i} = 21$) and M4 ($a_\mathrm{i} = 16$). Here a positioning with a conductor bundle height h_L as small as possible for lower first order current displacement is chosen. The conductor arrangement does not change in different stator slots, i.e. no transpositions of the sub-conductors occurs. The colors in Figure 8.10 indicate adjacent parallel conductor bundles, which define each turn per slot and layer. In reality there will be random transpositions from slot to slot, but in order to keep the two-dimensional FE model as simple as possible, this is not considered here. Test machine M1 does not have any parallel sub-conductors. Here only second order current displacement, i.e. eddy currents per sub-conductor, occurs.

Each single sub-conductor or conductor is assigned to a *FEM conductor* condition in *JMAG*. This allows circulating eddy currents per conductor cross-section during the transient time-step simulations. It is assumed that in the winding overhang no current-displacement is present due to the small stray field there, but of course the conductor current has to close over the winding overhang. This leads to an additional damping of the eddy currents in case of first order current displacement. To approximate this three-dimensional effect, additional static impedances are applied in the external circuit in series with the FEM conductors. Also the parallel connection of the sub-conductors is completed in the external circuit. Each conductor conductivity κ_{Cu} and winding overhang resistance is set depending on a given variable stator winding temperature. With these models the total resistance increase due to temperature and current displacement $K = k_{\vartheta} \cdot k_{\mathrm{R}}$ is determined for different fundamental frequencies f_{s} of the stator current and for different winding temperatures ϑ_{Cu} according to Table 8.5. The calculation is done only for sinusoidal currents, neglecting the influence of PWM current ripple. The finite element length in the conductor cross section is chosen roughly less than one third of penetration depth $d_{\mathrm{E}} \propto 1/\sqrt{f_{\mathrm{s}}}$ for the highest considered frequency f_{s}. This allows a rather accurate second order current displacement simulation. The sinusoidal current is impressed by ideal current sources per phase.

8.3.2. Current-depending losses

The effect of second order current displacement inside the single conductors is clearly visible with the rectangular cross-section of conductor wires of test machine M2 with relatively big conductor height h_{Cu}. In Figure 8.11 the slot stray field lines and the resulting total current density J_{z} is shown. The color gradient from red (high density) to blue (low density) indicates, that inside the upper conductors the current displacement is strong due to the large slot stray field, while in the lower conductors the current density is homogeneously distributed.

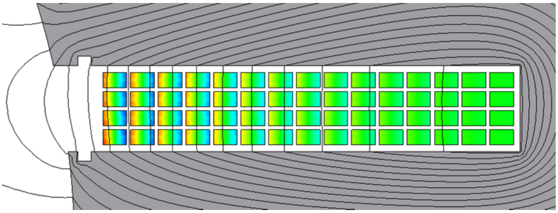

Figure 8.11.: Simulated current density J_{z} of test machine M2 with removed rotor ($f_{\mathrm{sN}} = 133.3\,\mathrm{Hz}$)

The big resulting conductor bundles per turn of test machines M3 and M4 due to the inner parallel connection of sub-conductors per turn leads to visible first order current displacement. Like before, the color gradient shows the bigger current density due to the unequal current share between parallel sub-conductors per turn towards the slot opening inside each bundle (Figure 8.12).

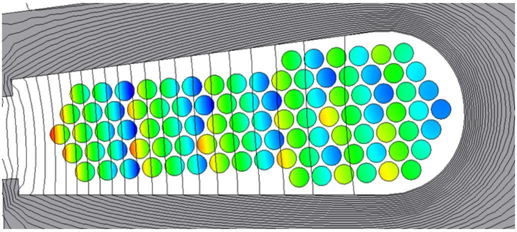

Figure 8.12.: Like Figure 8.11, but for test machine M4 ($f_{sN} = 166.7\,\mathrm{Hz}$)

The equivalent resistance increase of the stator winding due to the additional losses ΔP_{Cu} is also calculated analytically according to Section 3.2. Here the round wires are approximated by equivalent rectangular conductors (Table 8.6). Also the overall slot geometry is assumed to be rectangular instead of oval by using an average slot width $b_{Q,avg}$. For the test machines M3 and M4 the conductor bundle positions and dimensions are estimated by average values of the bundle position coordinates.

The comparison of simulated and analytical resistance increase k_R is shown for example for test machine M2 at rated frequency in Figure 8.13. The increased conductor temperature ϑ_{Cu} reduces κ_{Cu}, thus increasing the penetration depth $d_E \propto 1/\sqrt{\kappa_{Cu}}$, so k_R decreases at constant frequency f_s with increased ϑ_{Cu}. The analytical calculation meets the simulated values quite well. For this machine about 20 % loss increase $P_{Cu\sim}/P_{Cu=}$ at rated operation conditions occurs.

The small round wire dimensions h_T of the other test machines M1, M3, and M4 lead to a smaller ratio h_T/d_E, hence to less eddy currents and so to less resistance increase due to current displacement at rated frequency. Here also the analytical calculation is in accordance with the simulated values (Figure E.31 to Figure E.33).

As mentioned in Table 8.5, the removed rotor simulations are carried out for a wide range of stator frequencies and winding temperatures. These results are used for the indirect efficiency calculation as well. The calculated loss curves look quite similar to the presented ones at rated frequency and are therefore omitted here. Of course, at lower frequencies the loss increase is also lower due to a reduced ratio $h_T/d_E \propto \sqrt{f_s}$ and the graph of $k_R(\vartheta)$

Table 8.6.: Parameters for the analytical calculations of first and second order current displacement

	Unit	M1	M2	M3	M4
Rated frequency f_s	Hz	133.3	133.3	150.0	166.7
Conductor height h_T	mm	1.4	2.5	0.7	0.9
Conductor width b_T	mm	1.4	1.6	0.7	0.9
Slot width $b_{Q,avg}$	mm	18.8	9.0	9.5	7.2
Calculation of first order current displacement according to (3.14)					
N. of horizontal wires a_T	–	–	–	9	6
N. of vertical layers m_L	–	–	–	6	6
Layer height h_L / h_T	–	–	–	6	3
Calculation of second order current displacement according to (3.9)					
N. of horizontal wires a_T	–	4	4	9	6
N. of vertical wires m_T	–	24	15	28	16

becomes more and more linear like the graph of $k_\vartheta(\vartheta)$.

8.3.3. Iron losses

At removed rotor operation also a small amount of stator iron losses $P_{Fe,B}$ is present due to the induced magnetic field. These losses result from the stator slot stray field and, due to the big resulting air gap $\delta = d_{si}$, the small bore field. The calculated two-dimensional flux distribution is shown for example in Figure E.30 for test machine M2. Mainly the slot stray flux is visible, while in the air gap only few flux lines are present, showing the much smaller bore field. In the proposed method for efficiency determination, the iron losses P_{Fe} are calculated from the no-load iron losses $P_{Fe,0}$ and have to be subtracted from the total electrical input power to get the current-depending I^{2}R losses $P_{Cu\sim}$. Therefore a calculation error leads to wrong current-depending losses. Such a systematic error is the inclusion of $P_{M,0}$ in the losses $P_{Fe,0}$, which do not occur during the removed rotor test. A second systematic error is the slightly different field distribution in the stator at removed

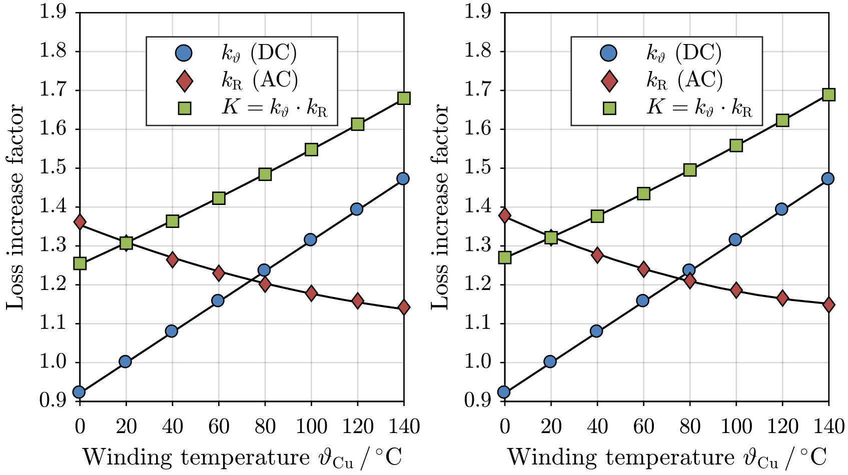

(a) simulated (b) analytical

Figure 8.13.: Calculated resistance increase k_R, k_ϑ, and K over conductor temperature at rated frequency $f_{\mathrm{sN}} = 133.3\,\mathrm{Hz}$ and rated current $I_{\mathrm{sN}} = 120\,\mathrm{A}$ of test machine M2

rotor in comparison to the generator no-load. To verify the method, the iron losses $P_{\mathrm{Fe,B}}$ are determined with two approaches:

a) Directly from the results of the transient simulations via post-processing: $P_{\mathrm{Fe,B,sim}}$

b) Indirectly calculated from the simulated no-load losses, as it is done in the proposed method for efficiency determination:
$P_{\mathrm{Fe,B,calc}} = P_{\mathrm{Fe,0}} \cdot \left(U_{\mathrm{x,B}}/U_0\right)^2$

For both cases, the hysteresis and *Foucault* losses are considered separately by post processing. The *Bertotti* anomalous eddy current losses are small in iron sheets without grain orientation and are therefore neglected.

The comparison of both calculations is analyzed for each test machine for different stator frequencies f_s of the stator sine wave currents. The PWM influence is not considered, as it is already done at the motor no-load test.

For test machine M1 a good accordance is achieved in the whole frequency range. Both the hysteresis and *Foucault* loss ratio do not change over frequency and are within the range of 5 % deviation (Figure 8.14a).

Test machine M2 has a relative high amount of rotor iron losses in the rotor iron bridges. Therefore, as expected, the deviation between $P_{\mathrm{Fe,B,sim}}$ and $P_{\mathrm{Fe,B,calc}}$ is higher, because the rotor losses are included in $P_{\mathrm{Fe,B,calc}}$, as at removed rotor operation only stator iron losses occur. The calculated values of the total iron losses $P_{\mathrm{Fe,B,calc}}$ are on average 50 % higher than the directly calculated values $P_{\mathrm{Fe,B,sim}}$. The hysteresis loss ratio is hereby more or less constant, while the *Foucault* loss ratio has a minimum at 50 % of the rated frequency (Figure 8.14b).

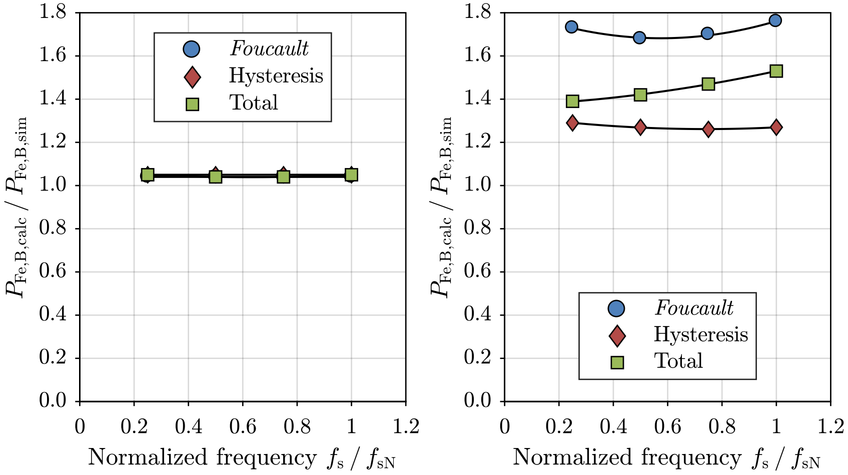

(a) Test machine M1 (b) Test machine M2

Figure 8.14.: Ratio between calculated and simulated iron losses at the removed rotor simulation of test machines M1 and M2

For test machine M3 with $P_{\mathrm{Fe,B,calc}}$ an average underestimation of the iron losses of about 10 % is visible. Again the hysteresis loss ratio is constant. The *Foucault* loss ratio has a maximum deviation at 50 % of the rated frequency, and thus has the total iron loss ratio $P_{\mathrm{Fe,B,calc}}/P_{\mathrm{Fe,B,sim}}$ (Figure 8.15a).

The hysteresis loss ratio for test machine M4 is constantly rather low, while the *Foucault* loss ratio is overestimated by $P_{\mathrm{Fe,B,calc}}$ and changes over frequency. In total, an average underestimation of the iron losses of 25 % occurs (Figure 8.15b).

For each of the previous analyses the stator has been fed with rated sinusoidal stator current I_{sN}. At lower current values the described deviations are higher than at rated current feeding. Therefore the removed rotor test should be carried out at higher currents – preferably with rated current. Also the amount of iron losses $P_{\mathrm{Fe,B}}$ in relation to the total losses $P_{\mathrm{el,in,B}}$ is reduced with rising stator current amplitudes.

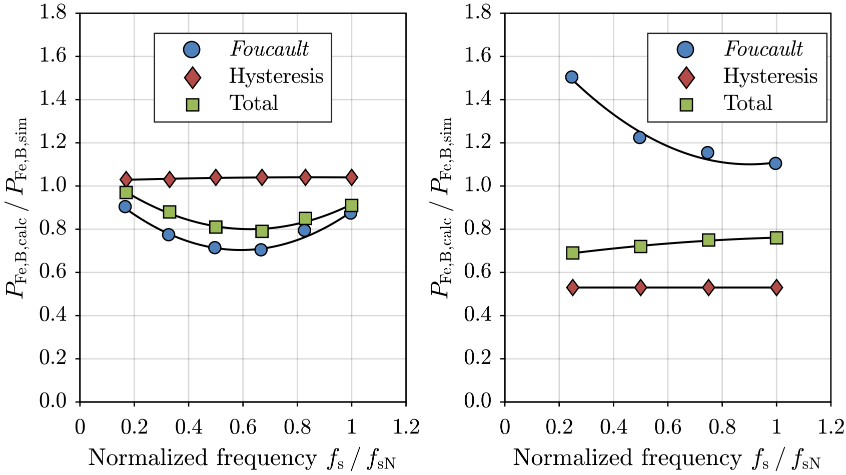

(a) Test machine M3

(b) Test machine M4

Figure 8.15.: Ratio between calculated and simulated iron losses at the removed rotor simulation of test machines M3 and M4

To quantify the influence of the stator iron losses $P_{\mathrm{Fe,B,calc}}$ on the total losses $P_{\mathrm{el,in,B}}$, the relative error

$$\varepsilon = k_{\mathrm{V}} \cdot \frac{|\Delta P_{\mathrm{Fe,B}}|}{P_{\mathrm{Cu\sim}}} \tag{8.4}$$

is evaluated with $\Delta P_{\mathrm{Fe,B}} = P_{\mathrm{Fe,B,calc}} - P_{\mathrm{Fe,B,sim}}$ for rated current feeding. Here the iron loss increase factor k_{V} is chosen according to the calculated values at the no-load simulations (Table 8.3).

Table 8.7 summarizes the results of the error calculation at the removed rotor simulations. The amount of iron losses $P_{\mathrm{Fe,B}}$ with respect to $P_{\mathrm{el,in,B}}$ is high for test machine M1 with

Table 8.7.: Error calculation for iron loss determination at the removed rotor simulation

Parameter	Unit	M1	M2	M3	M4
Frequency $f_\mathrm{s}/f_\mathrm{sN}$	–	$0.3\ldots1.0$	$0.3\ldots1.0$	$0.2\ldots1.0$	$0.3\ldots1.0$
Loss increase k_V	–	1.3	1.3	1.9	1.1
$P_\mathrm{Fe,B,sim}/P_\mathrm{el,in,B}$	%	$4\ldots21$	$2\ldots9$	$0.4\ldots5$	$0.3\ldots2$
Error ε	%	$0.2\ldots1.3$	$0.6\ldots5.3$	$0\ldots0.5$	$0.1\ldots0.4$

up to 21 %, but due to the small deviations $\Delta P_\mathrm{Fe,B}$ the error ε is low. For test machine M2, which has less iron loss ratio $P_\mathrm{Fe,B}/P_\mathrm{el,in,B}$, the bigger deviations $\Delta P_\mathrm{Fe,B}$ lead to an error up to 5 %. Test machines M3 and M4 show a rather small amount of iron losses $P_\mathrm{Fe,B}/P_\mathrm{el,in,B}$, so that the described underestimations $\Delta P_\mathrm{Fe,B} < 0$ do not lead to big errors ε. The simulated amount of iron losses is in rather good accordance to the measured/calculated values at the removed rotor test (Table 7.2).

Overall only for test machine M2 significant errors ε are present by the method for $P_\mathrm{Fe,B,calc}$ at feeding with rated current. Therefore overall, under these conditions the removed rotor experiment is suitable for the determination of the current-depending losses $P_\mathrm{Cu\sim}$.

8.4. Load operation

For the simulations of the four permanent-magnet synchronous machines at load, the operation points have to be set to cover a broad torque and speed area. For each test machine at least four different speed values, below and up to rated speed, are considered. (Table 8.8). No field-weakening is considered here, hence no speed $n > n_\mathrm{N}$ is simulated. To vary the machine torque, the stator current is varied from low values to a bit more than rated current. As the tooth-coil test machines M1 and M2 have a different reluctance in *d*- and *q*-axis [11], the electrical angle of the impressed stator current is varied from 0 °el. to 15 °el. and 20 °el. respectively. This procedure is used also for generator operation – starting from 180 °el. For both test machines with distributed winding and surface-mounted magnets (M3 and M4), the current angle is fixed as *d*- and *q*-axis stator inductances are similar. Only sinusoidal current is simulated, as the PWM influence is already considered at motor no-load operation.

Table 8.8.: Parameters for loss determination via load simulations

	Unit	M1	M2	M3	M4
Rated speed	min^{-1}	1000	1000	3000	2500
Minimum speed	min^{-1}	250	250	500	625
Maximum speed	min^{-1}	1000	1500	3000	3125
Rated frequency	Hz	133.3	133.3	150.0	166.7
Minimum freq.	Hz	33.3	33.3	25.0	41.7
Maximum freq.	Hz	133.3	200.0	150.0	208.3
Rated current	A	102	120	200	148
Minimum current	A	18	35	39	35
Maximum current	A	124	141	233	177
Current angle (mot.)	°el.	$0\ldots15$	$0\ldots30$	0	0
Current angle (gen.)	°el.	$180\ldots165$	$180\ldots150$	180	180
Number of sim. cases	–	280	336	72	40
Time step	s	$\frac{1}{90}\cdot T_\mathrm{s}$	$\frac{1}{120}\cdot T_\mathrm{s}$	$\frac{1}{60}\cdot T_\mathrm{s}$	$\frac{1}{60}\cdot T_\mathrm{s}$

8.4.1. Model description

For load operation all previously considered loss components are relevant. Therefore the FE models have to be adjusted to allow the calculation of eddy currents in the rotor magnets and in the stator winding conductors, i.e. a combination of the generator no-load models section with single conductor models of the removed rotor simulation. The temperature of the stator winding and of the rotor magnets is set according to the values of the measurements.

8.4.2. Current-depending losses

The current-depending losses in the stator winding at load are simulated in the same manner as at the removed rotor simulations. Now also the rotating air gap field is present via non-linear transient time-step simulation. If the conductors are located near the slot openings, the radial component of the rotor air gap field will enter the conductors, which lead to additional eddy current losses in the top conductors, so in total to different losses in the conductors than without rotor. The simulations show, that for the considered test machines, this influence is small.

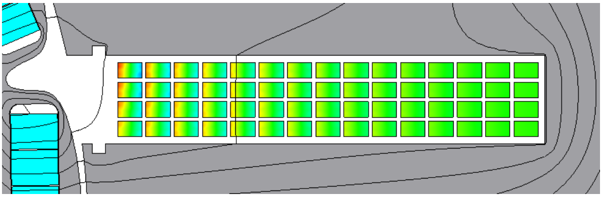

Figure 8.16.: Simulated total current density J_z of test machine M2 at load ($f_{sN} = 133.3\,\mathrm{Hz}$)

The biggest influence occurs for test machine M2 due to the open slots, where in worst case the total copper losses differ by up to 4 % with respect to the removed rotor simulation. In most of the cases the difference is smaller. In Figure 8.16 the rotor flux lines are shown, that enter the slot. The effect of additional current displacement is only visible at the upper conductor rows and covers only a small area.

For the other test machines the difference between the simulated total copper losses at load and at removed rotor operation is always below 2 %. Of course, other machine designs with open slots and non-segmented stator top conductors may lead to bigger eddy current losses, but with the here considered machines the removed rotor test is suitable to determine the current-depending losses accurately.

8.4.3. Iron losses

In the same way as shown at the removed rotor simulations, the iron losses at load P_{Fe} are determined by two methods:

a) Directly from the results of the transient simulations via post-processing: $P_{Fe,sim}$

b) Indirectly calculated from the simulated no-load losses: $P_{\mathrm{Fe,calc}} = P_{\mathrm{Fe,0}} \cdot (U_{\mathrm{x}}/U_0)^2$

At the test machines with tooth-coil winding M1 and M2 the total electromagnetic torque is increased by using the reluctance torque at negative d-current operation I_{sd}, in addition to the q-current operation I_{sq}. Due to the higher current angle β^* ($I_{\mathrm{sd}} = I_{\mathrm{s}} \sin\beta^*, I_{\mathrm{sq}} = I_{\mathrm{s}} \cos\beta^*$) the electromagnetic field inside the machines gets an additional negative flux in the magnet axis. This effect is also analyzed here for motor and generator operation. For test machines M3 and M4 this kind of field weakening is not considered, as no reluctance difference in d- and q-axis is present. So β^* is zero.

For test machine M1 a good accordance between $P_{\mathrm{Fe,calc}}$ and $P_{\mathrm{Fe,sim}}$, especially at rated frequency, is reached. This holds true for q-current operation with $\beta^* \in \{\text{motor } 0\,^\circ\text{el.}, \text{generator } 180\,^\circ\text{el.}\}$ (Figure E.34) as well as for increased d-current by $\beta^* \in \{\text{motor } 15\,^\circ\text{el.}, \text{generator } 165\,^\circ\text{el.}\}$ (Figure E.35).

Test machine M2 shows bigger deviations between $P_{\mathrm{Fe,calc}}$ and $P_{\mathrm{Fe,sim}}$, as like at the removed rotor test, the electromagnetic field differs from the no-load field. The deviations occur in motor operation as well as in generator operation with an average of about 25 % at q-current operation (Figure 8.17). At the relative highly current angle $\beta^* \in \{\text{motor } 30\,^\circ\text{el.}, \text{generator } 150\,^\circ\text{el.}\}$ the overestimation $P_{\mathrm{Fe,calc}} > P_{\mathrm{Fe,sim}}$ is slightly smaller (Figure E.36). As the amount of iron losses increases with rising frequency (see below), the constant overestimation is problematic for the final efficiency determination.

Test machine M3 with its distributed winding also shows a more or less constant overestimation of the iron losses $P_{\mathrm{Fe,calc}} > P_{\mathrm{Fe,sim}}$ of about 20 % in motor and generator operation (Figure 8.18).

Despite the similar motor construction, the deviation between the calculated and the simulated iron losses of test machine M4 is lower than 10 % at rated frequency, i.e. in that frequency region, where the iron losses are most relevant. At lower frequencies the iron losses are slightly more overestimated in motor operation and underestimated in generator operation (Figure E.37).

In total, for all test machines except for test machine M2 the best approximation of the iron losses by $P_{\mathrm{Fe,calc}}$ is possible at rated frequency f_{sN}, hence where usually the efficiency is determined. A detailed analysis of the overestimated iron losses at load of test machines M2 and M3 is given in Appendix G.

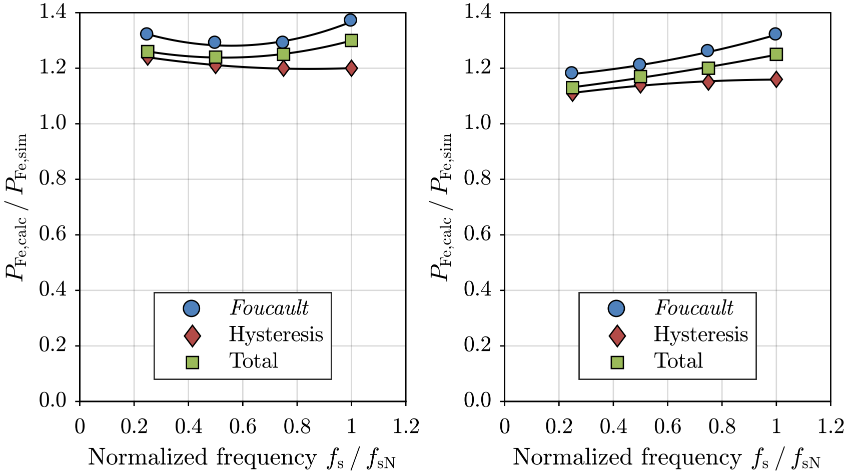

(a) Motor ($\beta^* = 0\,°$el.)

(b) Generator ($\beta^* = 180\,°$el.)

Figure 8.17.: Ratio between calculated and simulated iron losses $P_{\mathrm{Fe,calc}}$ and $P_{\mathrm{Fe,sim}}$ at rated stator current ($I_{\mathrm{sN}} = 120\,\mathrm{A}$) and q-current operation of test machine M2

8.4.4. PM losses

At load the eddy current losses in the rotor magnets are usually increased, as the space harmonics of the stator air gap field already at sinusoidal current enter the rotor and induce additional eddy currents and related losses P_{M}. Based on the no-load magnet losses $P_{\mathrm{M,0}}$ the loss increase is analyzed for each test machine at different stator frequencies and speeds. The stator current is increased up to $1.2 \cdot I_{\mathrm{sN}}$ at q-current motor and generator operation. Here no distinction of different current angles β^* apart from $0\,°$el. (motor) and $180\,°$el. (generator) is regarded. As expected, the magnet losses at generator operation are nearly identical to the magnet losses in motor operation. Therefore only the motor operation is shown here.

The PM losses of test machine M1 rise moderately until about $0.4 \cdot I_{\mathrm{sN}}$, when the inclination increases and continues linearly up to $1.2 \cdot I_{\mathrm{sN}}$ for each speed and stator frequency (Figure 8.19). The losses at rated current and speed are approximately three times higher than at no-load, but still rather small with only about 1 % of the total losses.

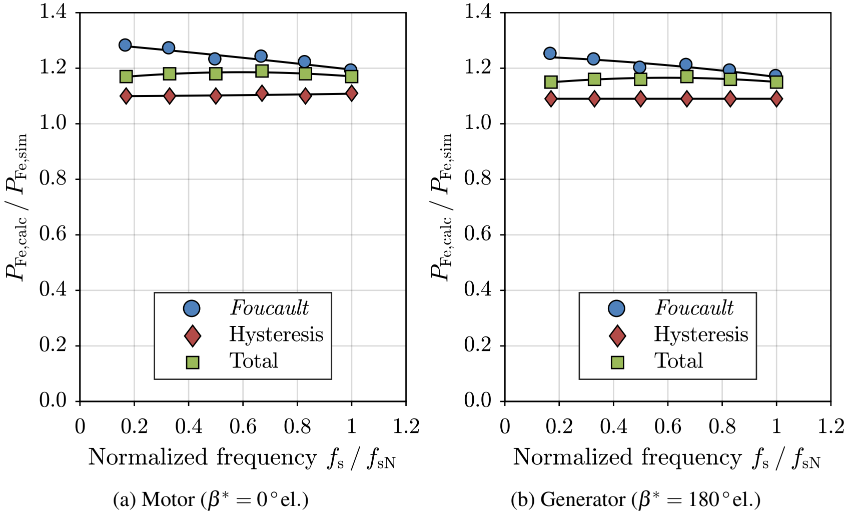

(a) Motor ($\beta^* = 0\,°$el.) (b) Generator ($\beta^* = 180\,°$el.)

Figure 8.18.: Like Figure 8.17, but for test machine M3 ($I_{\mathrm{sN}} = 200\,\mathrm{A}$)

The PM loss curves of test machine M2 start at zero losses due to the nearly ideal shielding effect of the rotor iron bridges at no-load. When the stator field rises, the iron bridges saturate and space harmonic field components (especially the sub-harmonic, but also slot harmonics) enter the magnets. Therefore the PM losses are increased (Figure E.38) and end up at approximately at the same level as for test machine M1. This is reasonable, as the magnet dimensions and their segmentation is similar.

Test machines M3 and M4 show, like test machine M1, significant magnet losses already at no-load as they also have surface-mounted magnets. The magnet losses at rated speed and current are about four times higher than at no-load for test machine M3 (Figure E.39) and about two times higher for test machine M4.

The frequencies of the magnet eddy currents and therefore the related magnet losses P_{M} fit to the predicted rotor frequencies f_{Q} in Chapter 3 for test machines M1, M3, and M4. This is due to the stator slot harmonic field waves with ordinal number $\nu_{\mathrm{Q}} = 1 \pm Q_{\mathrm{s}}/p$, which cause the rotor frequencies $n \cdot Q_{\mathrm{s}}$. In test machine M2 the stator sub-harmonic field wave with a wave length $4\tau_{\mathrm{p}}$ penetrates the rotor deeply, inducing eddy currents with $1.5 \cdot f_{\mathrm{s}}$.

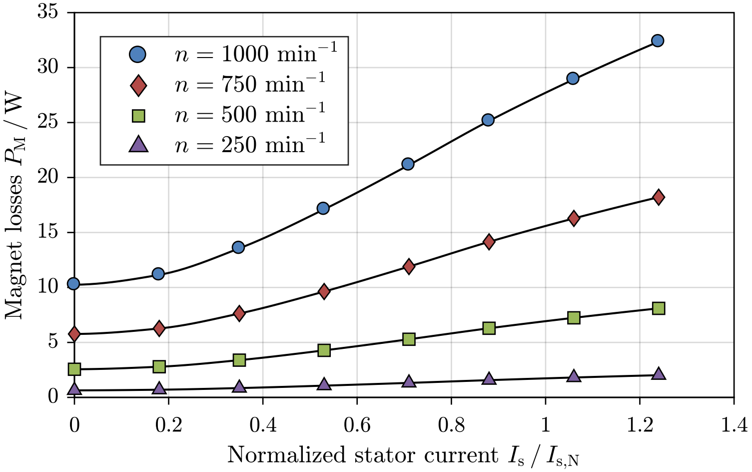

Figure 8.19.: Simulated magnet losses P_M for different rotor speed n and stator currents I_s for test machine M1

8.4.5. Total losses

The loss distribution at load is different for each test machine. Remarkably high are the rotor iron losses of test machine M2 due to the iron bridges and the stator sub-harmonic field wave, and the friction and windage losses of test machine M3 due to the shaft-mounted fan. The latter are calculated analytically according to Table 7.1, as no results with a non-magnetized rotor are available. The total copper losses $P_{\mathrm{Cu}\sim}$ have a big impact on the total losses, especially at lower speed. Clearly visible is the strong dependency of the stator iron losses $P_\mathrm{Fe,s}$ on the speed and stator fundamental frequency, as well as the rotor iron losses $P_\mathrm{Fe,r}$, the friction and windage losses $P_\mathrm{fr+w}$, and even of the small magnet losses P_M.

The loss distribution for motor operation at rated speed and 50 % of the rated speed is shown in Appendix E (Figure E.41 to Figure E.48). Although the measurements, especially for test machine M3, are available at lower torque values than rated torque, the loss graphs over torque show comparable results to the fundamental measured/calculated losses in Figure C.20 to Figure C.23.

8.5. Efficiency calculation

With the results of the no-load, of the removed rotor, and of the load simulations the machine efficiency is calculated in two manners:

a) *Directly* from the results of the transient and post-processing simulations at load operation: η_{dir}

b) *Indirectly* calculated by means of Chapter 5 according to the proposed method for indirect efficiency determination: η_{ind}

Of course, the *direct* calculation is also of summation of losses, but only by simulation, and it does not use any results of the no-load or removed rotor simulations.

The direct efficiency is determined in motor (8.5) and generator (8.6) operation via

$$\eta_{\mathrm{mot,dir}} = \frac{P_{\mathrm{m}}}{P_{\mathrm{el,mot}}} = \frac{P_\delta - P_{\mathrm{Fe,r}} - P_{\mathrm{fr+w}}}{P_\delta + P_{\mathrm{Cu\sim}} + P_{\mathrm{Fe,s}} + P_{\mathrm{M}}} , \tag{8.5}$$

$$\eta_{\mathrm{gen,dir}} = \frac{P_{\mathrm{el,gen}}}{P_{\mathrm{m}}} = \frac{P_\delta - P_{\mathrm{Cu\sim}} - P_{\mathrm{Fe,s}} - P_{\mathrm{M}}}{P_\delta + P_{\mathrm{Fe,r}} + P_{\mathrm{fr+w}}} , \tag{8.6}$$

with the air gap power $P_\delta = 2\pi \cdot n \cdot M_\delta$, where M_δ is calculated from the Maxwell stress tensor in *JMAG*.

On the other hand the indirect efficiency is calculated in motor (8.7) and generator (8.8) operation via

$$\eta_{\mathrm{mot,ind}} = \frac{P_{\mathrm{m}}}{P_{\mathrm{el,mot}}} = \frac{P_{\mathrm{el,mot}} - P_{\mathrm{d,ind}}}{P_{\mathrm{el,mot}}} , \tag{8.7}$$

$$\eta_{\mathrm{gen,ind}} = \frac{P_{\mathrm{el,gen}}}{P_{\mathrm{m}}} = \frac{P_{\mathrm{el,gen}}}{P_{\mathrm{el,gen}} + P_{\mathrm{d,ind}}} , \tag{8.8}$$

where $P_{\mathrm{d,ind}} = P_{\mathrm{Cu\sim}}\left(I_{\mathrm{s}}^2, f_{\mathrm{s}}\right) + P_{\mathrm{Fe}}\left(U_{\mathrm{x}}^2\right) + P_{\mathrm{fr+w}}$ are the total indirect losses.

The magnet losses P_{M} are not addressed by the proposed method, but are included in $P_{\mathrm{Fe+M,0}}$ and so in $P_{\mathrm{Fe}}(U_{\mathrm{x}}^2)$ as in reality. The friction and windage losses $P_{\mathrm{fr+w}}$ are again calculated analytically.

The here calculated efficiency values at sinusoidal current are compared to the sine wave current measurement efficiency values according to Chapter 7.

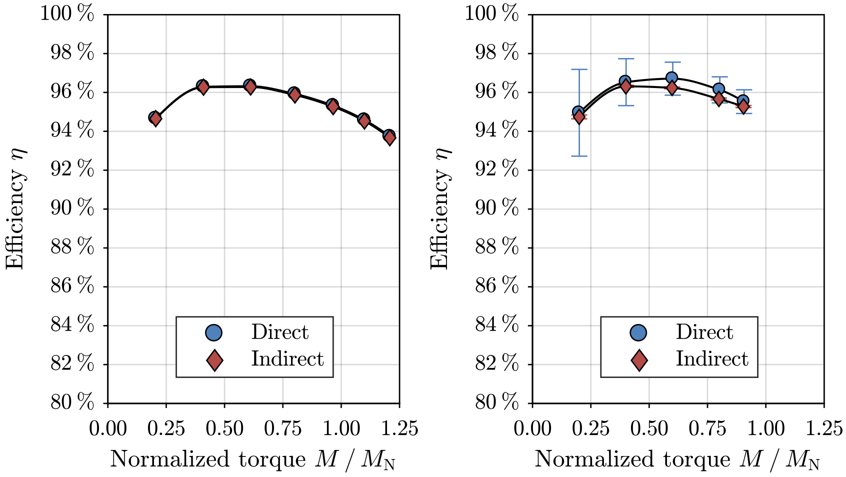

(a) Simulation ($\beta^* = 15\,°$el.)

(b) Measurement

Figure 8.20.: Comparison of the simulated and measured efficiency at sinusoidal current operation of test machine M1 at motor operation and rated speed ($n_N = 1000\,\text{min}^{-1}$)

For test machine M1 the simulated direct and indirect efficiency are nearly identical in motor operation ($\beta^* = 15\,°$el., Figure 8.20) as well as in generator operation ($\beta^* = 165\,°$el., Figure E.49) over the whole torque range, proving the well-defined methodology for the individual determination via the removed rotor and no-load test. The measurement results at sinusoidal current cover a smaller torque range up to about $0.85 \cdot M_N$, but a good accordance between the simulated and the indirectly measured efficiency is reached up to that value $0.85 \cdot M_N$. As already discussed for the efficiency including the PWM effects at inverter operation in Section 7.3.4, also the fundamental current directly measured efficiency differs from the indirect efficiency slightly, but stays within the error tolerances due to the measurement uncertainty according to Appendix D.

Test machine M2 also shows deviations of the measured fundamental current direct and indirect efficiency in motor (Figure 8.21) and generator (Figure E.50) operation. For test machine M2 already the simulated values for η_{dir} and η_{ind} with $\beta^* = 15\,°$el. (motor) and $\beta^* = 165\,°$el. (generator) differ due to the considerable rotor iron losses at load, caused by the sub-harmonic field wave and the open stator slots. The deviation is about 0.3 p.p.

higher in motor operation. The differences result also from the discussed overestimation of the iron losses, that are the highest for test machine M2. At q-current operation (the results are not shown here) even higher differences occur (by about 0.2 p.p.). When comparing simulation and measurement, the indirectly measured efficiency is closer to the simulated ones and nearly identical for motor and generator operation. The simulated efficiency values are slightly higher. Besides model uncertainties, maybe the current angle β^* during measurement was not exactly identical to the simulated values. The influence of β^* on the efficiency is shown in Figure 8.22.

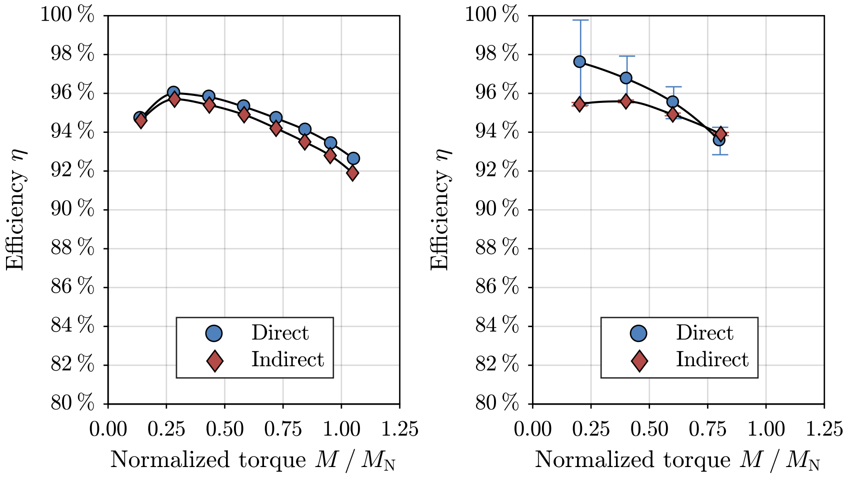

(a) Simulation ($\beta^* = 15\,°$el.)

(b) Measurement

Figure 8.21.: Like Figure 8.20, but for test machine M2 ($n_N = 1000\,\text{min}^{-1}$)

Test machine M3 shows only minor deviations of the simulated efficiency values η_{dir} and η_{ind}. At rated torque M_N the losses at sinusoidal current are by 6 % slightly overestimated by the indirect procedure. An additional uncertainty for this machine is present due to the analytical calculation of the friction and windage losses, which are dominated by the shaft-mounted fan. As the measurements are only carried out up to $0.5 \cdot M_N$ due to the current limit of the feeding inverter, a comparison is only possible in this torque range. Again, both the measured and simulated indirect efficiency values show a good accordance. In motor operation (Figure E.51) also the directly measured efficiency is identical. In generator operation (Figure E.52) the directly measured values are by 0.5 p.p. slightly higher, but again within the error tolerances due to the measurement uncertainty according to Appendix D.

For test machine M4 a very good accordance between the directly and indirectly simulated efficiency is reached over the whole torque range up to $1.25 \cdot M_\mathrm{N}$. At the sinusoidal current measurements the measured generator efficiency (Figure E.54) also fits quite well to the calculation, while the directly measured motor efficiency is increased by 1 p.p. for low torque values, but is nearly the same as the indirectly measured efficiency at rated torque (Figure E.53).

At lower speeds $n < n_\mathrm{N}$, comparable results are achieved like at rated speed operation. Due to the lower frequencies the iron loss calculation errors are less relevant there.

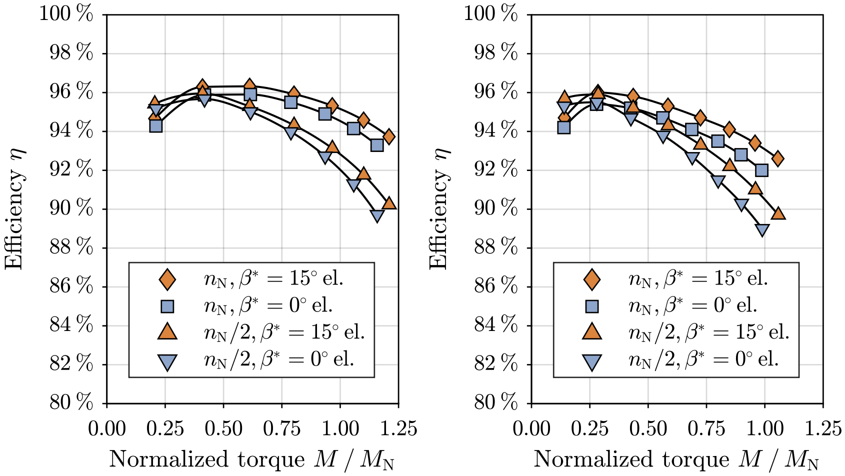

(a) Test machine M1

(b) Test machine M2

Figure 8.22.: Influence of the current angle β^* on the simulated direct efficiency

Finally the influence of the changing current angle β^* on the simulated direct efficiency for test machines M1 and M2 is analyzed numerically in motor operation. Due to the higher torque by means of the additional reluctance torque, thus higher output power, in combination with the lower iron losses due to field weakening, the efficiency is significantly increased at the current angle of $\beta^* = 15\,^\circ$el. for both test machines M1 and M2 (Figure 8.22). This holds also true for the simulated indirect efficiency (Figure 8.23).

As a result, for typical permanent-magnet synchronous machines like test machines M3 and M4 with distributed stator winding and semi-closed slots the proposed indirect method via no-load and removed rotor test is adequate for efficiency determination. Also for test machine M1 with its tooth-coil winding without sub-harmonic fields rather good results with small deviation between η_{ind} and η_{dir} are achieved. Due to the relatively high rotor losses of test machine M2 with its sub-harmonic stator field wave and big slot openings the indirect method determines the efficiency with a bigger deviation of typically 0.5 . . . 1 p.p. from η_{dir}. If these deviations are tolerable, as no other procedure is possible especially for big machines with high efficiency $> 95\,\%$, the method is also usable for rather special machines like test machine M2.

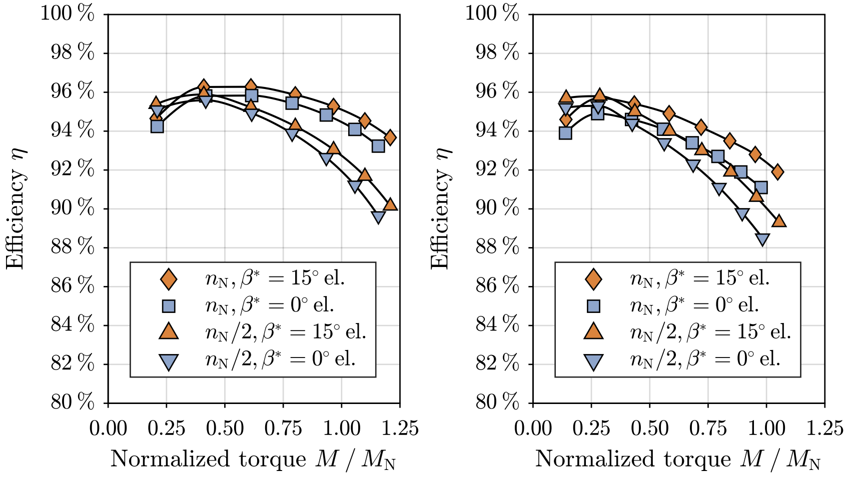

(a) Test machine M1

(b) Test machine M2

Figure 8.23.: Influence of the current angle β^* on the simulated indirect efficiency

9. Conclusion

By the analysis of the measurement and simulation data, the usefulness of the proposed method for indirect efficiency determination of permanent-magnet synchronous machine by summation of losses from no-load and removed rotor test has been proven for the six examined machines (five by the author, one by the *PTB Braunschweig*). Especially the four test machines with distributed winding (M3 … M5, M6: *PTB* test machine) show a good accordance to the direct measurements and simulations, which were carried out for comparison. The test machine with double-layer fractional-slot tooth-coil winding (M1) without sub-harmonic stator field waves also has a good accordance between the indirect and direct efficiency. Although some deviations occurred during the measurements, with consideration of the error limits of the measurement devices, the indirect measurement gives satisfying results. As a drawback of the proposed method, the no-load stator and rotor losses cannot be separated, so a high amount of rotor losses may result in miscalculations of these losses at load, as shown for the test machine with single-layer fractional-slot tooth-coil winding (M2). Here the indirect method gives about 1 p.p. difference to the direct efficiency. This was shown as before by simulation and measurement.

The recalculation of the no-load iron losses with the square of the reactance voltage to get the load iron losses is plausible for five of the six test machines. The dominating loss component at rated load of these investigated machines are the current-depending $\mathrm{I}^2\mathrm{R}$ losses. Hence the overestimation of the iron losses at load is less relevant. From the comparison of simulated and measured no-load iron losses, very different loss increase factors from $k_\mathrm{V} = 1.1$ to $k_\mathrm{V} = 1.9$ were found due to the manufacturing influence in comparison to the Epstein frame loss values. This implies, that the iron losses are still hard to predict by simulation only without precise knowledge of the iron sheet material data after the manufacturing process.

At the removed rotor test, the amount of iron losses is usually small and the current-depending losses are dominant. Hence, the removed rotor test is suitable for an accurate determination of the $\mathrm{I}^2\mathrm{R}$ losses at load. The best results for small difference between η_dir and η_ind can be reached at high stator currents $I_\mathrm{s}/I_\mathrm{sN}$.

The additional losses due to inverter feeding were not analyzed by simulation, but per sinusoidal current simulation and measurement were compared in detail. By the comparison of the measured efficiency at inverter operation with total and fundamental current wave losses it was shown, that these additional inverter-caused losses are almost independent of the load.

As a no-load experiment with non-magnetized rotor was not possible with test machines M1 … M4, the determination of the friction and windage losses for the recalculation of the iron losses by calculation, which was done, may be inaccurate. But these losses are usually small, and their value is only needed for the recalculation. In the summation of losses they are included anyway. These losses are only relevant for test machine M3 in this thesis due to the larger power of the shaft-mounted fan. Here also a good accordance between the simulated and measured efficiency is achieved. For the test machines M5 and M6 the accurate friction and windage losses were measured with non-magnetized rotors.

The magnet losses are rather small for the examined machines. With the FFT analysis at the simulations the frequencies of the induced eddy currents in the magnets due to air gap field harmonic and slot pulsations were correctly determined.

For test machines M1 and M2 it is shown, that the change of the current angle β^* is also covered by the proposed indirect efficiency determination method. The absolute efficiency values are strongly influenced by the increased torque due to the additional reluctance torque from the d- and q-axis inductance difference.

The proposed indirect measurement method for efficiency determination is preferably suitable for the machine manufacturers, where the experiments can be carried out on unfinished machines like:

1. Perform the removed rotor test prior to the completion of the machine.
2. Perform the generator no-load test without rotor magnets at a prototype.
3. Perform the generator no-load test with magnetized rotor.
4. Perform the motor no-load test with magnetized rotor at inverter feeding.
5. Determine from 1 … 4 the efficiency by calculation.

Here the fundamental values of the stator voltage, current, and from that the derived power factor have to be known for precise loss calculations for step 5, which is also a preferred task for the manufacturer in the test bay. Modern poly-phase electrical power analyzers give these values with big accuracy. In step 3 and step 4 the machine should be in warm conditions. The reactive current experiment is suitable to heat the machine to a certain extent, if no load machine is available.

Besides the efficiency calculation, like for the electrically excited synchronous machine, the machine parameters "no-load voltage", "short-circuit current", and "synchronous inductance" can be determined by the no-load and short-circuit experiment. If the generator short-circuit experiment is not possible to be performed, the reactive current test at inverter feeding also delivers the values of the short-circuit current and thus of the synchronous inductance as well.

List of Tables

List of Figures

Bibliography

Literature

[1] L. Aarniovuori, H. Kärkkäinen, A. Kosonen, J. Pyrhönen, Z. Liu, and W. Cao, "Overview of calorimetric systems used in loss determination of electric motors and drives", in *IECON 2017 – 43rd Annu. Conf. IEEE Ind. Electron. Soc.*, Oct. 2017, pp. 2110–2115. DOI: `10.1109/IECON.2017.8216354`.

[2] E. B. Agamloh, "On Efficiency Measurement of Motor-Drive Systems", in *10th Int. Conf. Energy Efficiency Motor Driven Syst. (EEMODS)*, Mar. 2017, 14 pages.

[3] M. Aoulkadi, A. Binder, and G. Joksimovic, "Additional losses in high-speed induction machine – removed rotor test", in *2005 Eur. Conf. Power Electron. Appl.*, Sep. 2005, 10 pp.–P.10. DOI: `10.1109/EPE.2005.219567`.

[4] G. Bertotti, "General properties of power losses in soft ferromagnetic materials", *IEEE Trans. Magn.*, vol. 24, no. 1, pp. 621–630, Jan. 1988. DOI: `10.1109/20.43994`.

[5] A. Binder, *Elektrische Maschinen und Antriebe - Grundlagen, Betriebsverhalten*, 2nd ed. Berlin, Heidelberg, Germany: Springer Vieweg, 2017, [German].

[6] A. Binder, "Analytical Calculation of Eddy-Current Losses in Massive Rotor Parts of High-Speed Permanent Magnet Machines", in *Symp. Power Electron., Elect. Drives, Automation Motion (SPEEDAM)*, Jan. 2000, C2–1–C2–6.

[7] A. Boehm and I. Hahn, "Influence of pulse width modulation (PWM) on the iron losses of electrical steel", in *2014 Int. Power Electron. Conf. (IPEC-Hiroshima 2014 - ECCE ASIA)*, 2014, pp. 283–288. DOI: `10.1109/IPEC.2014.6869594`.

[8] O. Bottauscio, G. Pellegrino, P. Guglielmi, M. Chiampi, and A. Vagati, "Rotor loss estimation in permanent magnet machines with concentrated windings", *IEEE Trans. Magn.*, vol. 41, no. 10, pp. 3913–3915, Oct. 2005. DOI: `10.1109/TMAG.2005.854969`.

[9] G. Bucci, F. Ciancetta, E. Fiorucci, and A. Ometto, “Uncertainty Issues in Direct and Indirect Efficiency Determination for Three-Phase Induction Motors: Remarks About the IEC 60034-2-1 Standard”, *IEEE Trans. Instrum. Meas.*, vol. 65, no. 12, pp. 2701–2716, 2016.

[10] A. T. De Almeida, F. J. T. E. T. E. Ferreira, and J. A. C. Fong, “Standards for Efficiency of Electric Motors”, *IEEE Ind. Appl. Mag.*, vol. 17, no. 1, pp. 12–19, Jan. 2011. DOI: `10.1109/MIAS.2010.939427`.

[11] C. Deák, “Modular Permanent-Magnet Synchronous Motors with high Electromagnetic Utilization”, Ph.D. dissertation, Technical University of Darmstadt, 2011.

[12] C. Deák and A. Binder, “Design of compact permanent-magnet synchronous motors with concentrated windings”, *Rev. Roum. Sci. Techn. – Électrotechn. et Énerg.*, vol. 52, pp. 183–197, Apr. 2007.

[13] K. Dempewolf and B. Ponick, “Modelling of permanent magnet synchronous machines for simulations of transient phenomena”, in *2007 Europ. Conf. Power Electron. Appl.*, 2007, pp. 1–10. DOI: `10.1109/EPE.2007.4417622`.

[14] DKE Komitee 311, *Drehende elektrische Maschinen - Erläuterungen zu DIN EN 60034 (VDE 530)*, 7th ed. Berlin, Offenbach, Germany: VDE Verlag, 2004, [German].

[15] M. Doppelbauer, “Interpolation Procedures for the Determination of Losses and Energy Efficiency of Electrical Machines”, in *9th Int. Conf. Energy Efficiency Motor Driven Syst. (EEMODS)*, 2015, 13 pages.

[16] M. Doppelbauer, “Update on IEC motor and converter standards”, *6th Int. Motor Summit for Energy Efficiency powered by Impact Energy*, 2016.

[17] P. Dück and B. Ponick, “A novel iron-loss-model for permanent magnet synchronous machines in traction applications”, in *2016 Int. Conf. Elect. Sys. Aircraft, Railway, Ship Propulsion Road Vehicles – Int. Transp. Electrific. Conf. (ESARS-ITEC)*, 2016, pp. 1–6. DOI: `10.1109/ESARS-ITEC.2016.7841432`.

[18] J. D. Ede, K. Atallah, G. W. Jewell, J. B. Wang, and D. Howe, “Effect of Axial Segmentation of Permanent Magnets on Rotor Loss in Modular Permanent-Magnet Brushless Machines”, *IEEE Trans. Ind. Appl.*, vol. 43, no. 5, pp. 1207–1213, Sep. 2007. DOI: `10.1109/TIA.2007.904397`.

[19] F. Emde, “Einseitige Stromverdrängung in Ankernuten”, *Elektrotechnik und Maschinenbau*, no. 26, pp. 703–707, 726–731, 1908, [German].

[20] A. B. Field, “Eddy Currents in Large Slot-Wound Conductors”, *Trans. Amer. Inst. Elect. Eng.*, vol. XXIV, pp. 761–788, Jan. 1905. DOI: `10.1109/T-AIEE.1905.4764567`.

[21] Y. Gao, Y. Matsuo, and K. Muramatsu, “Investigation on Simple Numeric Modeling of Anomalous Eddy Current Loss in Steel Plate Using Modified Conductivity”, *IEEE Trans. Magn.*, vol. 48, no. 2, pp. 635–638, 2012. DOI: `10.1109/TMAG.2011.2174624`.

[22] W. Guan, D. Zhang, Y. Zhu, Y. Gao, and K. Muramatsu, “Numerical Modeling of Iron Loss Considering Laminated Structure and Excess Loss”, *IEEE Trans. Magn.*, vol. 54, no. 11, pp. 1–4, 2018. DOI: `10.1109/TMAG.2018.2850851`.

[23] K. Hruska and J. Laksar, “A comprehensive approach to calculation of permanent magnet losses”, in *2019 21st Eur. Conf. Power Electron. Appl. (EPE ’19 ECCE Europe)*, Sep. 2019, P.1–P.9. DOI: `10.23919/EPE.2019.8915493`.

[24] *IEC 60034-1:2010. Rotating electrical machines – Part 1: Rating and performance*, 2010.

[25] *IEC 60034-2-1:2014. Rotating electrical machines – Part 2-1: Standard methods for determining losses and efficiency from tests (excluding machines for traction vehicles)*, 2014.

[26] *IEC 60034-2-2:2010. Rotating electrical machines – Part 2-2: Specific methods for determining separate losses of large machines from tests*, 2010.

[27] *IEC 60034-2-3:2020. Rotating electrical machines – Part 2-3: Specific test methods for determining losses and efficiency of converter-fed AC motors*, 2020.

[28] *IEC 60034-30-1:2014. Rotating electrical machines – Part 30-1: Efficiency Classes of Line Operated AC Motors (IE code)*, 2014.

[29] *IEC 60034-30-2:2016. Rotating electrical machines – Part 30-2: Efficiency classes of variable speed AC motors (IE code)*, 2016.

[30] *IEC 60034-4:2008. Rotating electrical machines – Part 4: Methods for determining synchronous machine quantities from tests*, 2008.

[31] *JCGM 100:2008 Evaluation of measurement data – Guide to the expression of uncertainty in measurement*, Geneva, Switzerland, 2010.

[32] *JMAG User's Manual*, Tokyo, Japan: JSOL Corporation, 2019. [Online]. Available: `https://www.jmag-international.com/`.

[33] J. Juergens, B. Ponick, O. Winter, and A. Fricassè, "Influences of iron loss coefficients estimation on the prediction of iron losses for variable speed motors", in *2015 IEEE Int. Elect. Mach. Drives Conf. (IEMDC)*, 2015, pp. 1254–1259. DOI: `10.1109/IEMDC.2015.7409222`.

[34] R. Kanchan, L. Aarniovuori, M. Niemelä, R. Chitroju, and F. Gyllensten, "Loss measurements analysis of VSD motors using both direct input-output and calorimetric methods", in *9th Int. Conf. Energy Efficiency Motor Driven Syst. (EEMODS)*, 2015, 17 pages.

[35] H. Karkkainen, L. Aarniovuori, M. Niemela, and J. Pyrhönen, "Converter-Fed Induction Motor Efficiency: Practical Applicability of IEC Methods", *IEEE Ind. Electron. Mag.*, vol. 11, no. 2, pp. 45–57, Jun. 2017. DOI: `10.1109/MIE.2017.2693421`.

[36] M. Klohr, "Entwicklung und Konstruktion einer umrichtergespeisten magnetgelagerten Permanentmagnet-Synchronmaschine für 40 kW / 40000/min", Ph.D. dissertation, Technical University of Darmstadt, 2007, [German].

[37] E. Lamprecht and R. Gräf, "Fundamental investigations of eddy current losses in laminated stator cores created through the impact of manufacturing processes", in *2011 1st Int. Elect. Driv. Prod. Conf.*, 2011, pp. 29–35. DOI: `10.1109/EDPC.2011.6085544`.

[38] E. Lamprecht, M. Hömme, and T. Albrecht, "Investigations of eddy current losses in laminated cores due to the impact of various stacking processes", in *2012 2nd Int. Elect. Driv. Prod. Conf. (EDPC)*, 2012, pp. 1–8. DOI: `10.1109/EDPC.2012.6425097`.

[39] M. Lehr, "Auslegung und Bewertung elektrischer Maschinen mit Permanentmagneten im Stator für hohe Drehmomentdichten", Ph.D. dissertation, Technical University of Darmstadt, 2020, [German].

[40] C. Lehrmann, "Wirkungsgradmessung permanentmagneterregter Synchronmaschinen – Ein Überblick unter den Aspekten der Messunsicherheit", *17. Techn. Tag der VEM-Gruppe*, 2019, [German].

[41] T. Lu, "Weiterentwicklung von hochtourigen permanenterregten Drehstromantrieben mit Hilfe von Finite-Elemente-Berechnungen und experimentellen Untersuchungen", Ph.D. dissertation, Technical University of Darmstadt, 2004, [German].

[42] M. Mirzaei, A. Binder, B. Funieru, and M. Sušić, "Analytical Calculations of Induced Eddy Currents Losses in the Magnets of Surface Mounted PM Machines With Consideration of Circumferential and Axial Segmentation Effects", *IEEE Trans. Magn.*, vol. 48, no. 12, pp. 4831–4841, Dec. 2012. DOI: 10.1109/TMAG.2012.2203607.

[43] G. Müller, K. Vogt, and B. Ponick, *Berechnung elektrischer Maschinen*, 6. Auflage. Weinheim: Wiley-VCH, 2008, [German].

[44] G. Narjes and B. Ponick, "Novel Method for the Determination of Eddy Current Losses in the Permanent Magnets of a High-Speed Synchronous Machine", in *2018 XIII Int. Conf. Elect. Mach. (ICEM)*, 2018, pp. 1285–1290. DOI: 10.1109/ICELMACH.2018.8506813.

[45] *NORMA 4000/5000 Power Analyzer, Operators Manual*, Washington, USA: Fluke Corporation, 1999.

[46] J. Ou, Y. Liu, D. Liang, and M. Doppelbauer, "Investigation of PM Eddy Current Losses in Surface-Mounted PM Motors Caused by PWM", *IEEE Trans. Power Electron.*, vol. 34, no. 11, pp. 11 253–11 263, 2019. DOI: 10.1109/TPEL.2019.2895679.

[47] R. Pliquett, "Nichtkornorientierte Elektrobleche für drehende elektrische Maschinen", *16. Techn. Tag der VEM-Gruppe*, 2017, [German].

[48] J. Pyrhönen, T. Jokinen, and V. Hrabovcová, *Design of rotation electrical machines*. Chichester, United Kingdom: John Wiley & Sons, 2011.

[49] J. Pyrhönen, H. Jussila, Y. Alexandrova, P. Rafajdus, and J. Nerg, "Harmonic Loss Calculation in Rotor Surface Permanent Magnets – New Analytic Approach", *IEEE Trans. Magn.*, vol. 48, no. 8, pp. 2358–2366, 2012. DOI: 10.1109/TMAG.2012.2190518.

[50] A. Rastogi, “Berechnung von doppelgespeisten Asynchronmaschinen und permanenterregten Synchronmaschinen als Windgeneratoren und Industrieantriebe”, Ph.D. dissertation, Technical University of Darmstadt, 2010, [German].

[51] K. Reis, “Hochausgenutzte kompakte E-Maschinen zum Einsatz in Radnabenantrieben”, Ph.D. dissertation, Technical University of Darmstadt, Nov. 2017, ISBN: 978-3-8440-5571-9, [German].

[52] R. L. Russell and K. H. Norsworthy, “Eddy currents and wall losses in screened-rotor induction motors”, *Proc. IEE – Part A: Power Eng.*, vol. 105, no. 20, pp. 163–175, 1958. DOI: `10.1049/pi-a.1958.0036`.

[53] P. Sergeant and A. Van den Bossche, “Segmentation of Magnets to Reduce Losses in Permanent-Magnet Synchronous Machines”, *IEEE Trans. Magn.*, vol. 44, no. 11, pp. 4409–4412, Nov. 2008. DOI: `10.1109/TMAG.2008.2001347`.

[54] S. Steentjes, G. von Pfingsten, M. Hombitzer, and K. Hameyer, “Iron-Loss Model With Consideration of Minor Loops Applied to FE-Simulations of Electrical Machines”, *IEEE Trans. Magn.*, vol. 49, no. 7, pp. 3945–3948, 2013. DOI: `10.1109/TMAG.2013.2244072`.

[55] C. P. Steinmetz, “On the Law of Hysteresis”, *Trans. Amer. Inst. Elect. Eng.*, vol. IX, no. 1, pp. 1–64, Jan. 1892. DOI: `10.1109/T-AIEE.1892.5570437`.

[56] J. Štěpina, “Matrix analysis of space harmonics of asymmetrical stator windings”, *IEE Proc. B – Elect. Power Appl.*, vol. 134, no. 4, pp. 207–210, Jul. 1987. DOI: `10.1049/ip-b.1987.0035`.

[57] *Technische Daten T30 FNA*, Darmstadt, Germany: Hottinger Baldwin Messtechnik. [Online]. Available: `https://www.hbm.com`.

[58] M. van der Geest, H. Polinder, and J. A. Ferreira, “Influence of PWM switching frequency on the losses in PM machines”, in *2014 Int. Conf. Elect. Mach. (ICEM)*, 2014, pp. 1243–1247. DOI: `10.1109/ICELMACH.2014.6960341`.

[59] L. Vandenbossche, S. Jacobs, X. Jannot, M. McClelland, J. Saint-Michel, and E. Attrazic, “Iron loss modelling which includes the impact of punching, applied to high-efficiency induction machines”, in *2013 3rd Int. Elect. Drives Prod. Conf. (EDPC)*, Oct. 2013, pp. 1–10. DOI: `10.1109/EDPC.2013.6689720`.

[60] M. Veigel, A. Krämer, G. Lanza, and M. Doppelbauer, “Investigation of the impact of production processes on iron losses of laminated stator cores for electric machines”, in *2016 IEEE Energy Convers. Congr. Expo. (ECCE)*, Sep. 2016, pp. 1–5. DOI: 10.1109/ECCE.2016.7855220.

[61] N. Yogal, C. Lehrmann, and M. Henke, “Determination of the Measurement Uncertainty of Direct and Indirect Efficiency Measurement Methods in Permanent Magnet Synchronous Machines”, in *2018 XIII Int. Conf. Elect. Mach. (ICEM)*, Sep. 2018, pp. 1149–1156. DOI: 10.1109/ICELMACH.2018.8506857.

[62] N. Yogal, C. Lehrmann, and M. Henke, “Magnetic loss measurement of surface-mounted permanent magnet synchronous machines used in explosive environments”, *J. Eng.*, vol. 2019, no. 17, pp. 3760–3765, 2019. DOI: 10.1049/joe.2018.8224.

Publications of the author

[63] B. Deusinger and A. Binder, “Indirect efficiency determination of permanent magnet synchronous machines for sine wave and inverter operation”, in *9th Int. Conf. Energy Efficiency Motor Driven Syst. (EEMODS)*, 2015, 14 pages.

[64] B. Deusinger and A. Binder, “Bestimmung des Wirkungsgrads von permanentmagneterregten Synchronmaschinen im Einzelverlustverfahren”, *16. Techn. Tag der VEM-Gruppe*, 2017, [German].

[65] B. Deusinger and A. Binder, “Different rotor geometry concepts for high pole count permanent magnet machines with buried magnets”, in *24th Int. Workshop Rare-Earth Future Permanent Magnets Appl. (REPM)*, Jan. 2017, 6 pages.

[66] B. Deusinger and A. Binder, “Quantitative Analysis and Finite Element Modeling for Indirect Efficiency Determination of Permanent Magnet Machines”, in *10th Int. Conf. Energy Efficiency Motor Driven Syst. (EEMODS)*, Mar. 2017, 13 pages.

[67] B. Deusinger and A. Binder, “Indirekte Wirkungsgradbestimmung von Permanentmagnet-Synchronmaschinen”, *ECPE – Cluster Leistungselektronik: Seminar – Echtzeitanalyse und Leistungsmessung von elektrischen Maschinen und Stromrichtern*, 2018, [German].

[68] B. Deusinger and A. Binder, “Update on the indirect efficiency determination of permanent-magnet synchronous machines”, *10th Int. Motor Summit for Energy Efficiency powered by Impact Energy*, 2020.

[69] B. Deusinger, M. Lehr, and A. Binder, “Determination of efficiency of permanent magnet synchronous machines from summation of losses”, in *2014 Int. Symp. Power Electron., Elect. Driv., Automation Motion (SPEEDAM)*, Jun. 2014, pp. 619–624. DOI: `10.1109/SPEEDAM.2014.6871917`.

Supervised student theses

[70] T. Becker, “Entwurf und Implementierung von Regelungen für Permanentmagnet-Synchronmotoren mit Doppelwicklung”, Master thesis, Technical University of Darmstadt, 2014.

[71] Y. K. Bhagat, “Measurement of the material-specific parameters of soft magnetic materials under controlled magnetization conditions”, Master thesis, Technical University of Darmstadt, 2015.

[72] T. Djoukwe, “Finite-Elemente-Modellierung und Wirkungsgradbestimmung unterschiedlicher Permanentmagnet-Industrieantriebe im Grunddrehzahlbereich”, Master thesis, Technical University of Darmstadt, 2017.

[73] P. P. Fehn, “Auslegung eines synchronen Reluktanzmotors für die Serienfertigung unter Ausnutzung veränderter Symmetrieeigenschaften der Rotorgeometrie”, Master thesis, Technical University of Darmstadt, 2021.

[74] M. K. Flößer, “Entwurf der Leistungsversorgung eines Hochdrehzahl-Traktionsantriebs-Prüfstands mit DC-Bus und Isolationsüberwachung”, Bachelor thesis, Technical University of Darmstadt, 2019.

[75] L. Kniedel, “Energieautarker und sensorloser Fahrradcomputer”, Bachelor thesis, Technical University of Darmstadt, 2019.

[76] S. Neusüs, T. Plößer, and P. Schneider, “Automatisierte Messsungen zur Wirkungsgradbestimmung von PM-Synchronmaschinen”, Project seminar, Technical University of Darmstadt, 2014.

[77] M. Schwebach, “Indirekte Wirkungsgradbestimmung von Permanentmagnet-Synchronmaschinen im Feldschwächbereich am Beispiel zweier 16-poliger Zahnspulenmaschinen”, Master thesis, Technical University of Darmstadt, 2021.

A. Test machine data

Table A.1.: Machine parameters I

	Unit	M1	M2	M3	M4	M5
Rated power P_{N}	kW	45	45	90	84	160
Rated speed n_{N}	min^{-1}	1000	1000	3000	2500	1500
Rated torque M_{N}	Nm	430	430	286	320	1019
Rated stator voltage U_{sN}	V	230	230	230	230	323
Rated stator current I_{sN}	A	102	120	200	148	176
Rated stator frequency f_{N}	Hz	133.3	133.3	150.0	166.7	150.0
No-load voltage $U_0(n = n_{\mathrm{N}})$ *	V	177.6	121.3	169.7	195.2	316.2
Stationary short-circuit current I_{sc} *	A	75.0	58.4	334.6	425.5	365.9
Synchronous inductance L_{d} *	mH	2.83	2.48	0.53	0.44	1.26
Stator resistance $R_{\mathrm{cold,=}}$ *	mΩ	48	32	12	16	37

* per phase

Table A.2.: Machine parameters II

	M1	M2	M3	M4	M5
Stator winding	DL, FS, TC	SL, FS, TC	SL, IS, DW	SL, IS, DW	DL, FS, DW
Slot opening	semi-closed	open	semi-closed	semi-closed	semi-closed
Slot design	oval	parallel	oval	oval	oval
Rotor magnets	surface	buried	surface	surface	buried
Cooling system	water jacket	water jacket	shaft-mounted fan	external fan	water jacket
Skewing	none	none	none	rotor	none

DL/SL: double-layer/single-layer

FS/IS: fractional-slot/integer-slot

TC/DW: tooth-coil/distributed winding

Table A.3.: Machine parameters III

	Unit	M1	M2	M3	M4	M5
Number of stator phases m	–	3	3	3	3	3
Number of stator slots Q_s	–	24	24	36	48	54
Number of rotor poles $2p$	–	16	16	6	8	12
Slots per pole and phase q	–	$1/2$	$1/2$	2	2	$3/2$
Number of turns per coil N_c	–	96	60	12	6	6
N. of parallel branches a_o	–	8	4	3	2	2
N. of sub-conductors a_i	–	1	1	21	16	7
N. of turns per phase N_s	–	96	60	24	24	54
Axial length l_Fe	mm	180	180	210	310	250
Stator inner diameter d_si	mm	181	181	188	190	324
Pole pitch τ_p	mm	35.5	35.5	98.6	74.6	84.8
Mechanical air gap δ	mm	0.7	0.7	1.1	1.0	1.5
Bandage thickness d_B	mm	0.7	–	0.5	0.9	–
Magnet height h_M	mm	4.7	4.7	5.3	5.8	10.0
Pole coverage ratio α_e	%	77	77	86	82	–
Cond. diameter d_Cu	mm	1.6	–	0.75	1.0	1.4
Cond. dimensions $b_\mathrm{Cu} \mid h_\mathrm{Cu}$	mm	–	1.6 | 2.5	–	–	–

B. Measurement setup and device data

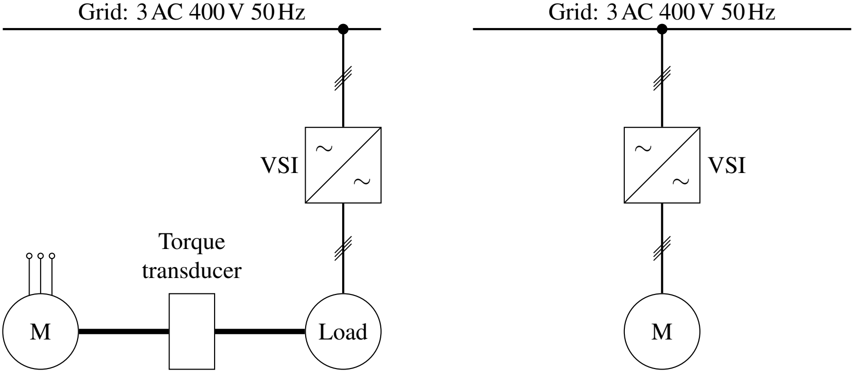

(a) Generator no-load test (b) Motor no-load and reactive current test

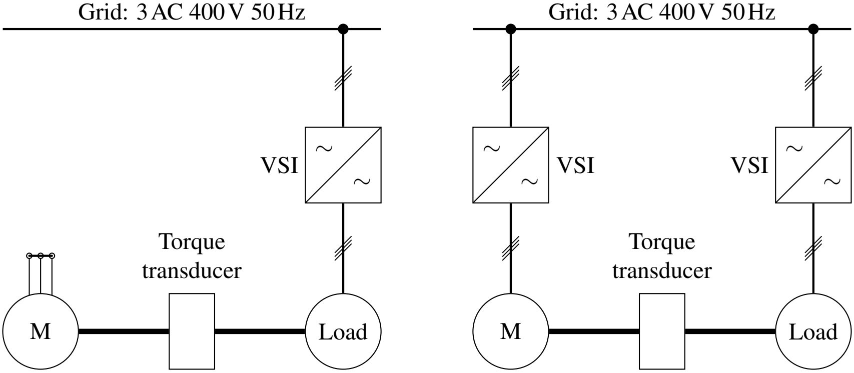

(c) Short-circuit test (d) Full load test

Figure B.1.: Different options of the conventional measurement setup

For the removed rotor test setup see Figure 7.5.

VSI:	voltage source inverter
M:	tested machine
Load:	load machine (brake) or auxiliary driving machine

Table B.1.: Parameters of the power analyzer *Fluke NORMA 5000* [45]

Input module	PP50
Current probe	61C1
Bandwidth	10 MHz
Sampling rate	1024 kHz
Maximum input voltage	1000 V
Maximum input current (internal)	10 A
Maximum input current (current probe)	1000 A
Error limit (voltage)	0.05 % FS + 0.05 % RD
Error limit (current)	0.2 % RD
Error limit (phase angle)	0.005° + 0.005°/kHz
Error limit (frequency)	0.01 % RD

FS = full scale, RD = reading

Table B.2.: Parameters of the two torque transducers type *HBM T30 FNA* [57]

Rated torque	
a) Transducer 1: test machines M1, M2, M5	1000 Nm
b) Transducer 2: test machines M3, M4	500 Nm
Error limit (torque)	0.2 % FS
Amplifier	*HBM MGCPLUS / ML60*

FS = full scale

Table B.3.: Parameters of the *Siemens Simodrive 611* inverter

Rated power	120 kW
Maximum power	175 kW
Rated current	200 A
Maximum current	257 A
Rated switching frequency	3.2 kHz
Input voltage	3 AC 400 V
Output voltage	0…430 V

Table B.4.: Parameters of the inverter for test machine M3

Input voltage	3 AC 400 V
Rated power	55 kW
Rated current	90 A
Rated switching frequency	4 kHz

Table B.5.: Parameters of the inverter for test machine M5

Input voltage	3 AC 480 V
DC link voltage	650 V
Rated current	250 A
Rated switching frequency	6 kHz

Table B.6.: Parameters of the DC load machine for test machines M4 and M5

Rated power	150 kW
Rated voltage	600 V
Rated current	274 A
Rated speed	$1275\,\mathrm{min}^{-1}$
Rated torque	1123 Nm
Maximum speed	$3600\,\mathrm{min}^{-1}$

C. Measurement results

No-load operation

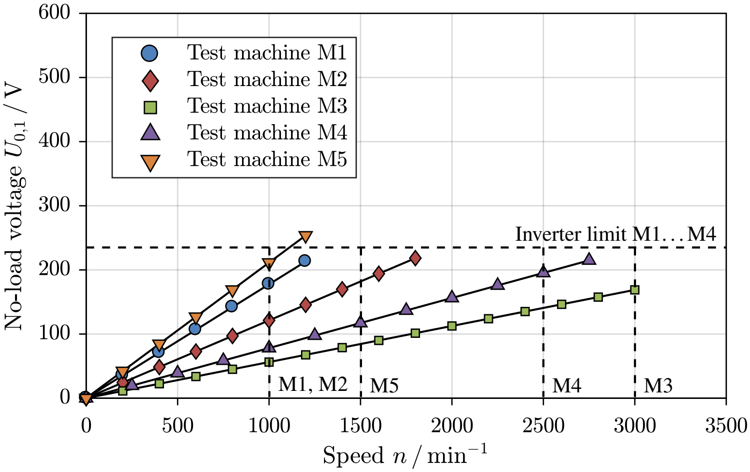

Figure C.1.: Measured fundamental RMS no-load voltage per phase $U_0 = U_{s,1}$ at the motor no-load test over speed (rated speed marked, error bars omitted)

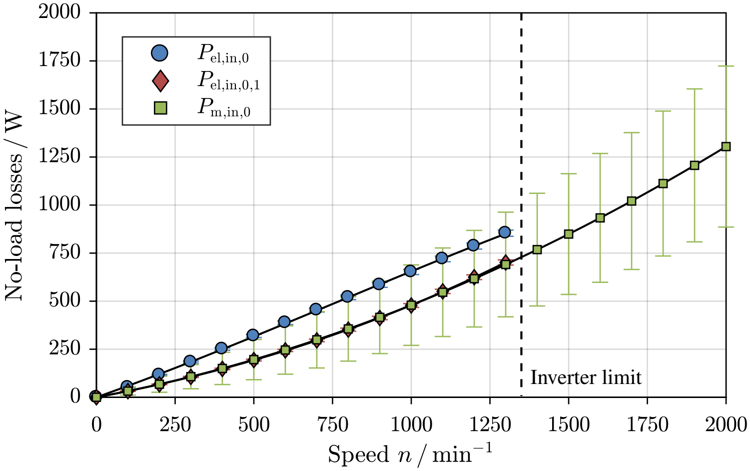

Figure C.2.: Comparison of the measured no-load losses at the no-load test (motor: $P_{\mathrm{el,in,0}}$, generator: $P_{\mathrm{m,in,0}}$) for test machine M1 ($n_{\mathrm{N}} = 1000\,\mathrm{min}^{-1}$) [63]

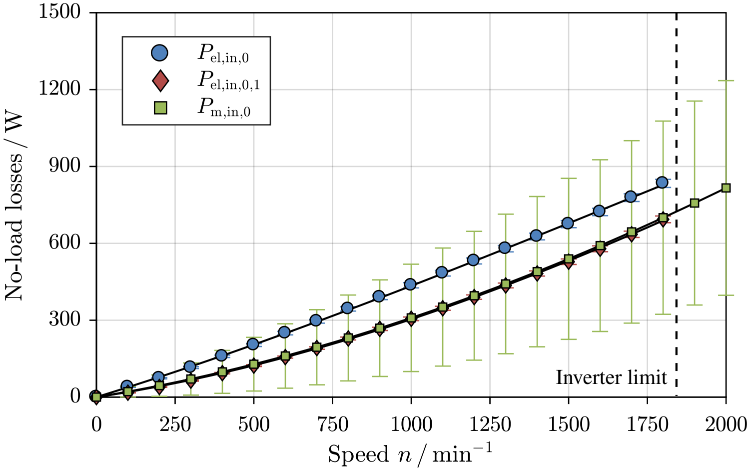

Figure C.3.: Like Figure C.2, but for test machine M2 ($n_{\mathrm{N}} = 1000\,\mathrm{min}^{-1}$) [63]

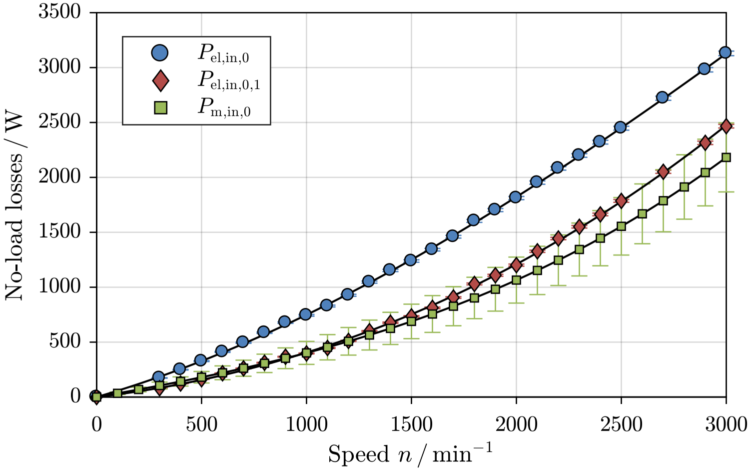

Figure C.4.: Like Figure C.2, but for test machine M3 ($n_{\mathrm{N}} = 3000\,\mathrm{min}^{-1}$) [63]

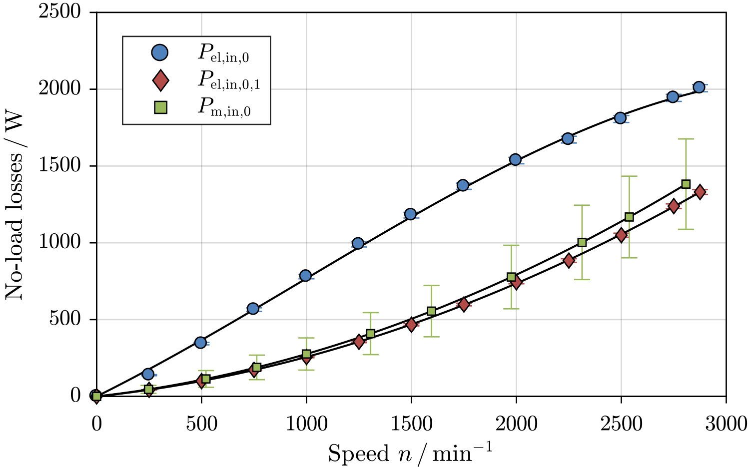

Figure C.5.: Like Figure C.2, but for test machine M4 ($n_{\mathrm{N}} = 2500\,\mathrm{min}^{-1}$) [66]

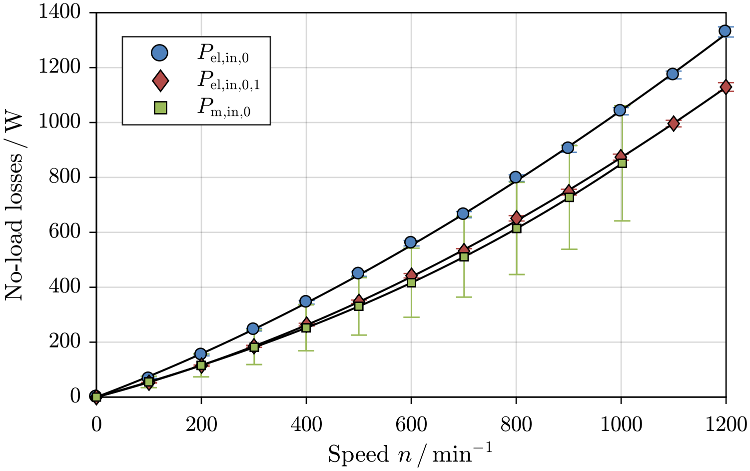

Figure C.6.: Like Figure C.2, but for test machine M5 ($n_{\mathrm{N}} = 1500\,\mathrm{min}^{-1}$)

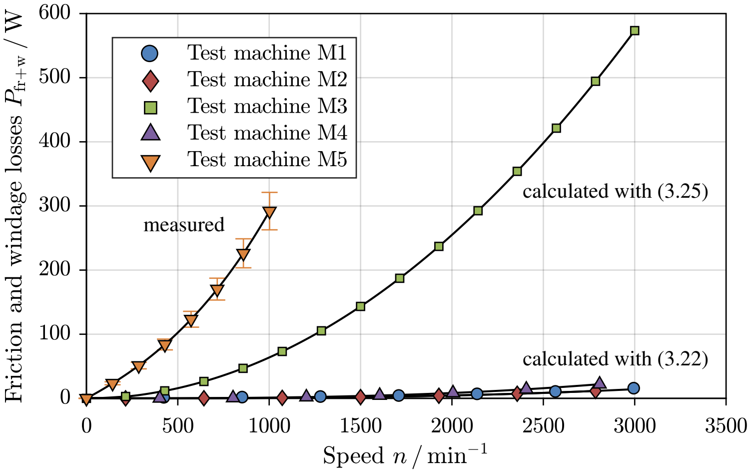

Figure C.7.: Calculated and measured friction and windage losses $P_{\mathrm{fr+w}}$ of each test machine

Removed rotor test

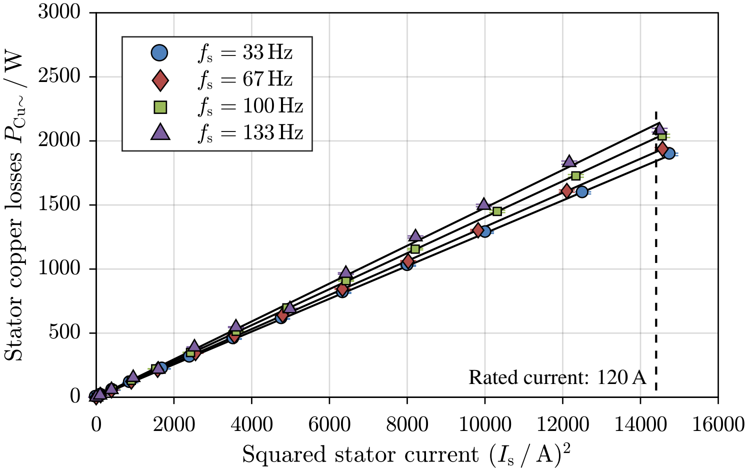

Figure C.8.: Measured stator copper losses $P_{\mathrm{Cu}\sim}$ during the removed rotor test over squared stator current I_s^2 for test machine M2 at 20 °C [63]

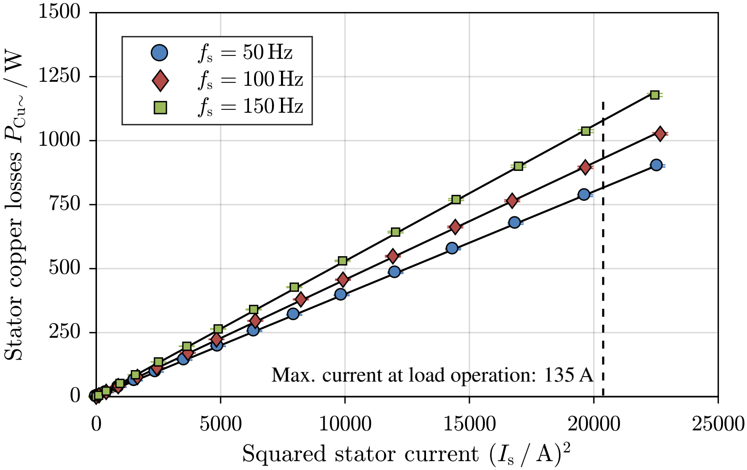

Figure C.9.: Like Figure C.8, but for test machine M3 [63]

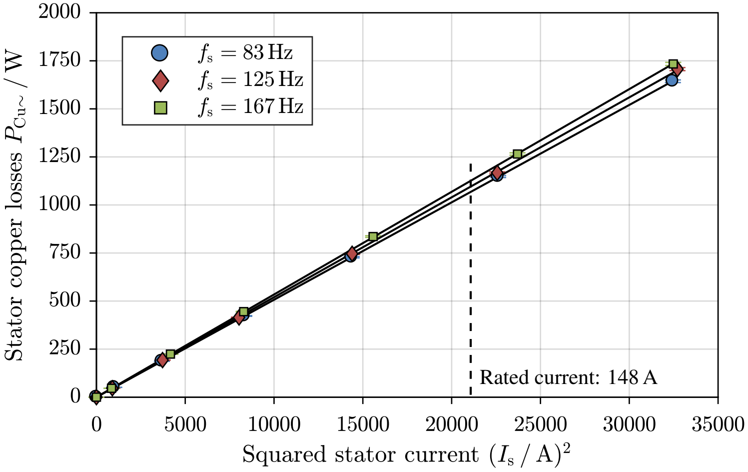

Figure C.10.: Like Figure C.8, but for test machine M4 [66]

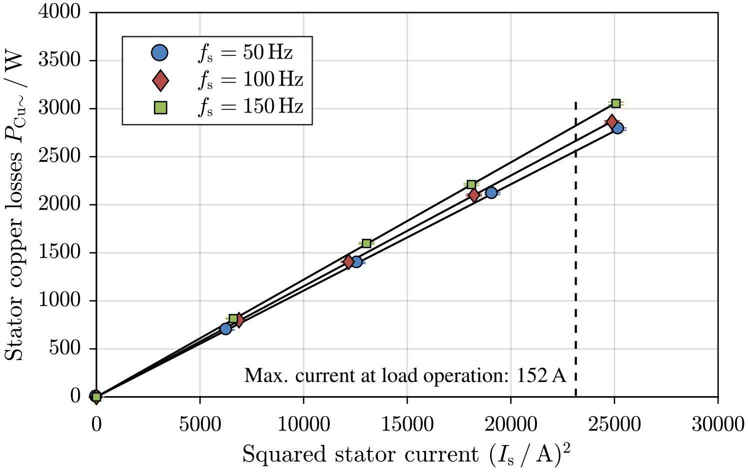

Figure C.11.: Like Figure C.8, but for test machine M5

Load operation

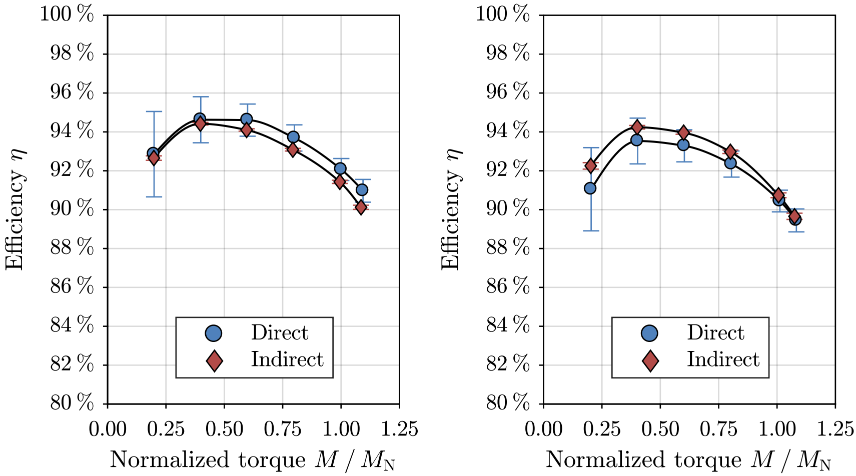

(a) Motor operation (b) Generator operation

Figure C.12.: Comparison of direct and indirect measured efficiency for test machine M1 at 50 % of the rated speed ($n = 500\,\mathrm{min}^{-1}$)

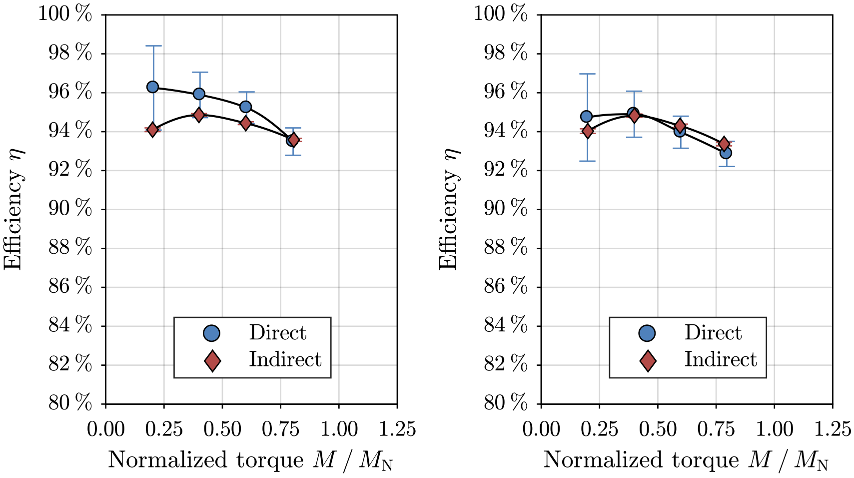

(a) Motor operation

(b) Generator operation

Figure C.13.: Like Figure C.12, but for test machine M2 at rated speed ($n_\mathrm{N} = 1000\,\mathrm{min}^{-1}$)

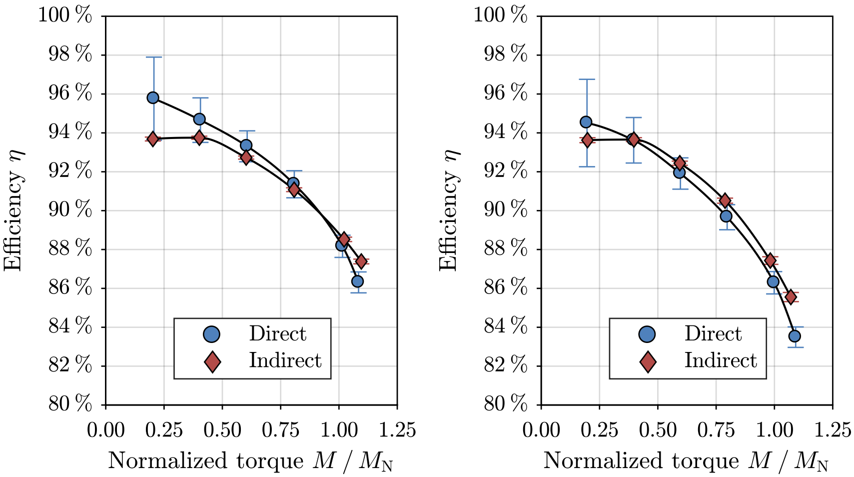

(a) Motor operation

(b) Generator operation

Figure C.14.: Like Figure C.12, but for test machine M2 at 50 % of the rated speed ($n = 500\,\mathrm{min}^{-1}$)

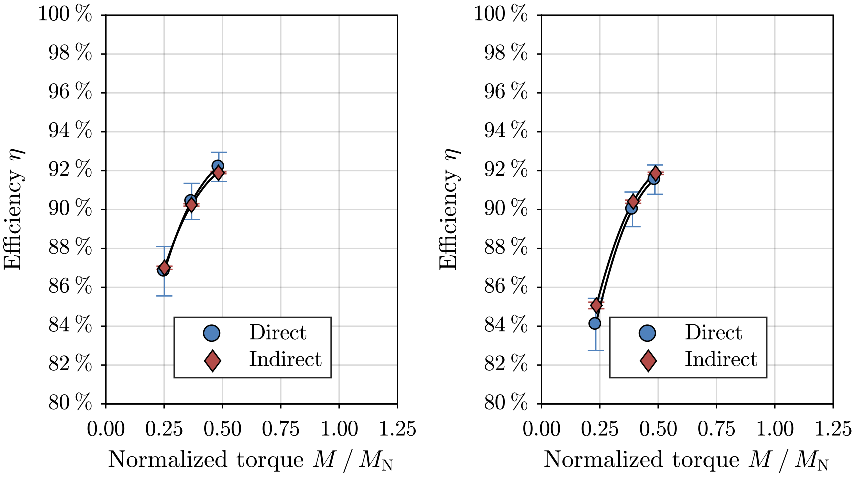

(a) Motor operation

(b) Generator operation

Figure C.15.: Like Figure C.12, but for test machine M3 at rated speed ($n_{\mathrm{N}} = 3000\,\mathrm{min}^{-1}$)

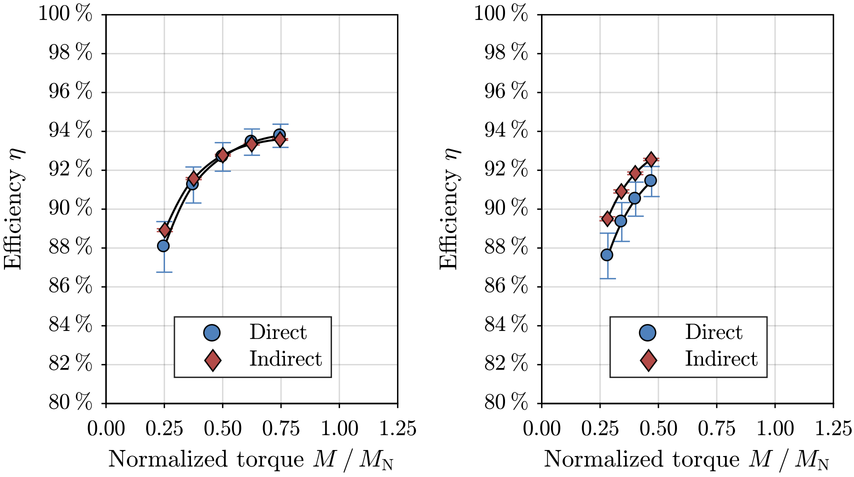

(a) Motor operation

(b) Generator operation

Figure C.16.: Like Figure C.12, but for test machine M3 at 50 % of the rated speed ($n = 1500\,\mathrm{min}^{-1}$)

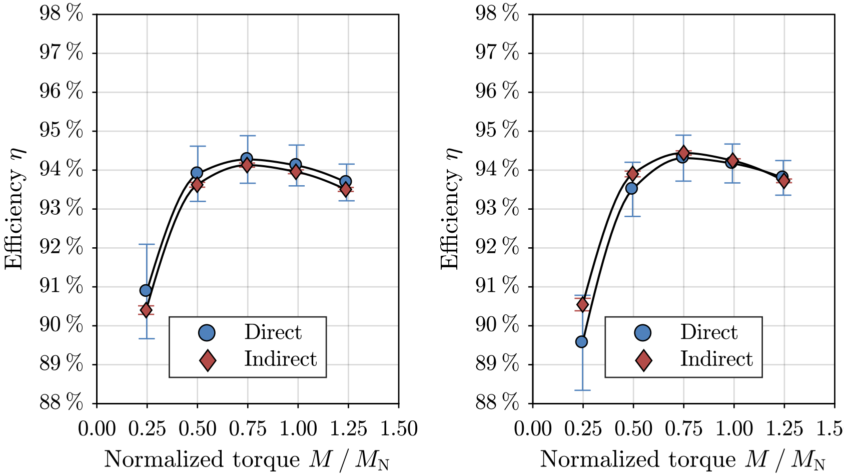

(a) Motor operation (b) Generator operation

Figure C.17.: Like Figure C.12, but for test machine M4 at 50 % of the rated speed ($n = 1250\,\mathrm{min}^{-1}$) [66]

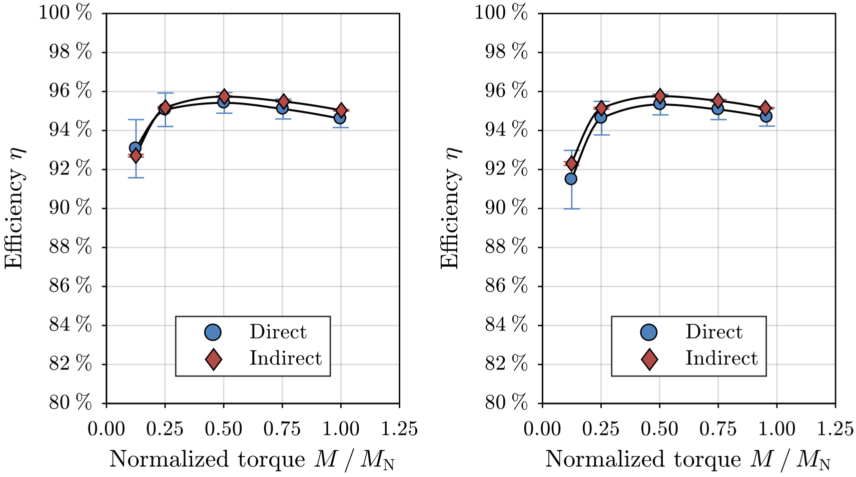

(a) Motor operation (b) Generator operation

Figure C.18.: Like Figure C.12, but for test machine M5 at 50 % of the rated speed ($n = 750\,\mathrm{min}^{-1}$)

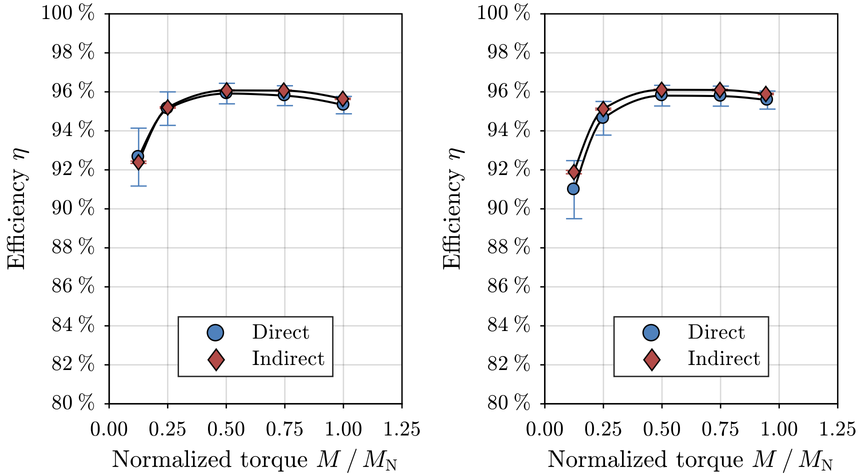

(a) Motor operation

(b) Generator operation

Figure C.19.: Like Figure C.12, but for test machine M5 at 67 % of the rated speed ($n = 1000\,\mathrm{min}^{-1}$)

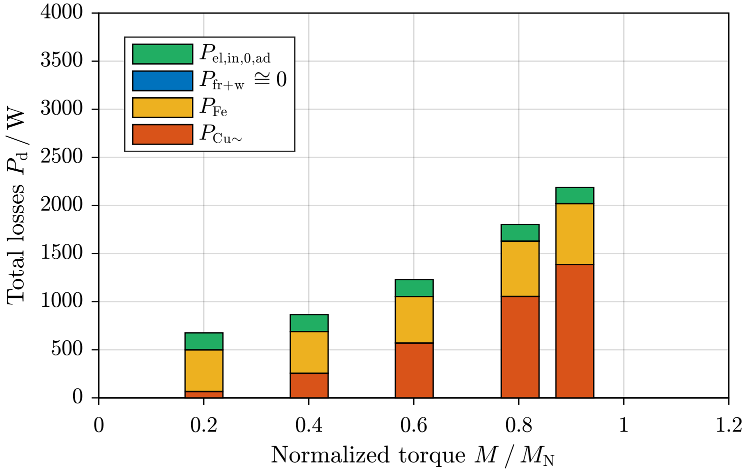

Figure C.20.: Separation of total losses P_d by the indirect efficiency measurement over torque M for test machine M1 as inverter-fed motor at rated speed ($n_\mathrm{N} = 1000\,\mathrm{min}^{-1}$)
Equations: $P_\mathrm{el,in,0,ad}$ (4.2), $P_\mathrm{fr+w}$ (3.22), P_Fe (5.2), $P_\mathrm{Cu\sim}$ (5.6)

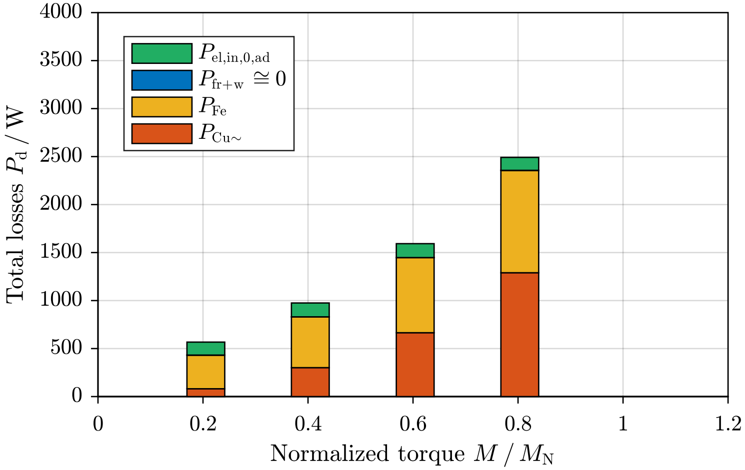

Figure C.21.: Like Figure C.20, but for test machine M2 ($n_{\mathrm{N}} = 1000\,\mathrm{min}^{-1}$)
Equations: $P_{\mathrm{el,in,0,ad}}$ (4.2), $P_{\mathrm{fr+w}}$ (3.22), P_{Fe} (5.2), $P_{\mathrm{Cu}\sim}$ (5.6)

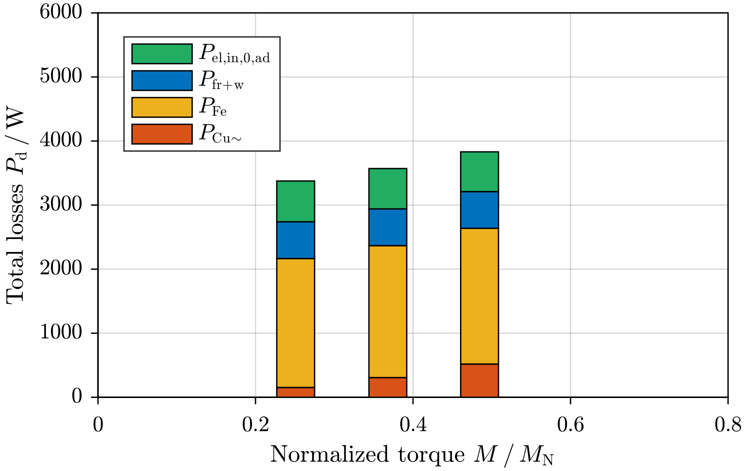

Figure C.22.: Like Figure C.20, but for test machine M3 ($n_{\mathrm{N}} = 3000\,\mathrm{min}^{-1}$)
Equations: $P_{\mathrm{el,in,0,ad}}$ (4.2), $P_{\mathrm{fr+w}}$ (3.25), P_{Fe} (5.2), $P_{\mathrm{Cu}\sim}$ (5.6)

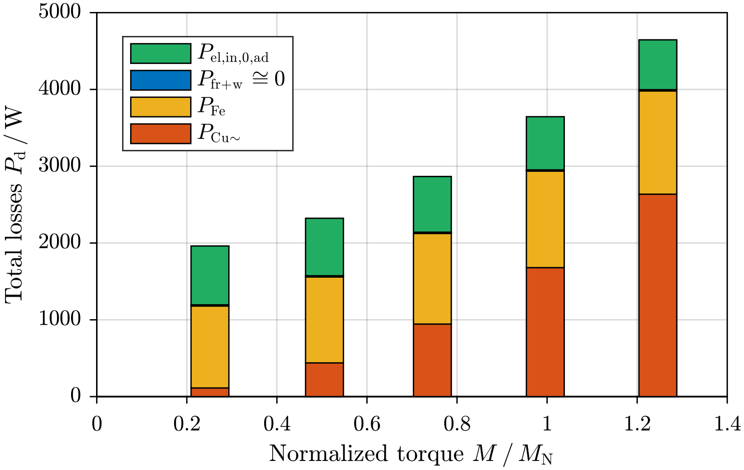

Figure C.23.: Like Figure C.20, but for test machine M4 ($n_\mathrm{N} = 2500\,\mathrm{min}^{-1}$)
Equations: $P_\mathrm{el,in,0,ad}$ (4.2), $P_\mathrm{fr+w}$ (3.22), P_Fe (5.2), $P_\mathrm{Cu\sim}$ (5.6)

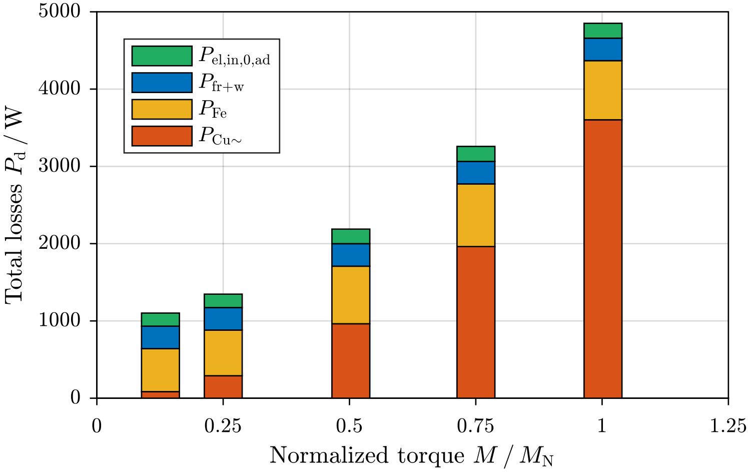

Figure C.24.: Like Figure C.20, but for test machine M5 at 67 % of the rated speed ($n = 1000\,\mathrm{min}^{-1}$)
Equations: $P_\mathrm{el,in,0,ad}$ (4.2), $P_\mathrm{fr+w}$ (measured), P_Fe (5.2), $P_\mathrm{Cu\sim}$ (5.6)

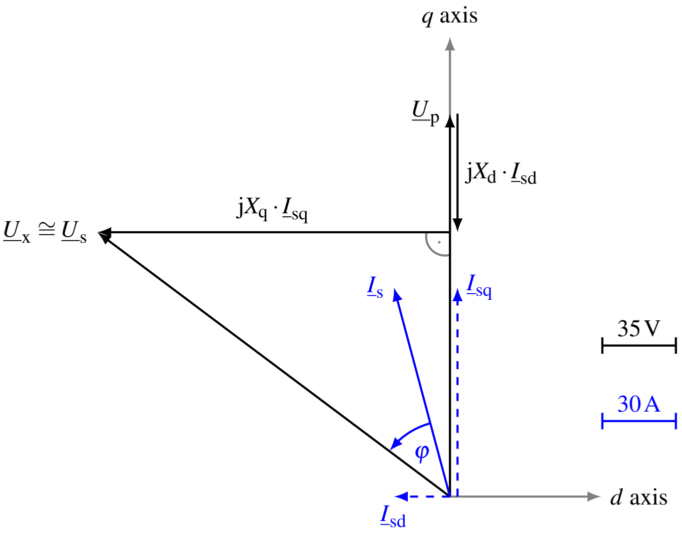

Figure C.25.: Phasor diagram of test machine M1 from measurement at motor operation ($n = n_{\mathrm{N}}, M = 0.9 \cdot M_{\mathrm{N}}$)

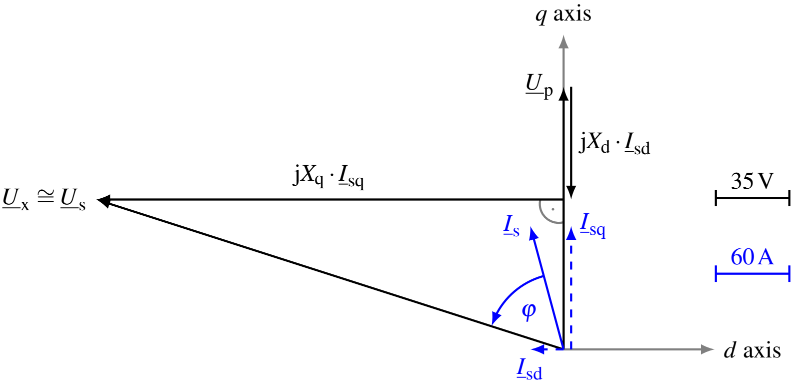

Figure C.26.: Like Figure C.25, but for test machine M2 ($n = n_{\mathrm{N}}, M = 0.8 \cdot M_{\mathrm{N}}$)

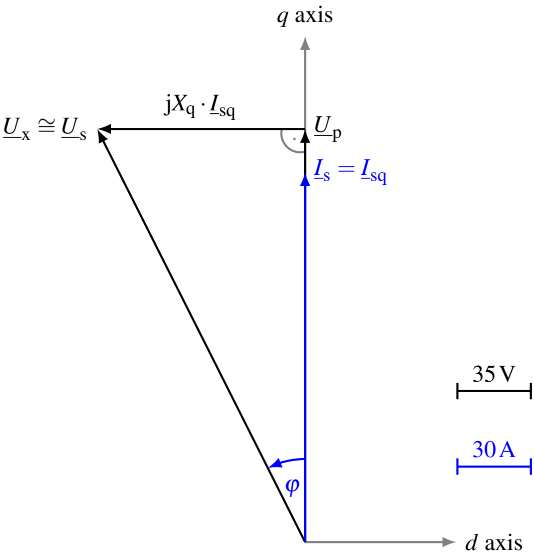

Figure C.27.: Like Figure C.25, but for test machine M4 ($n = n_N, M = M_N$)

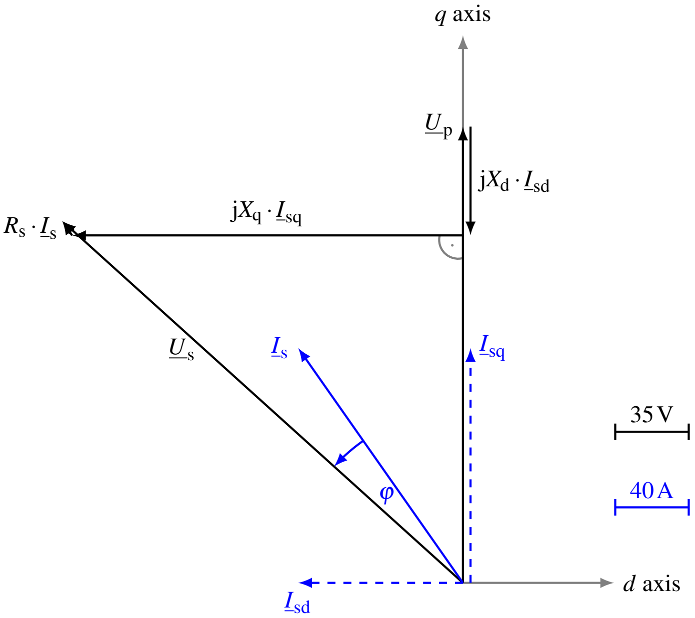

Figure C.28.: Like Figure C.25, but for test machine M5 ($n = 0.67 \cdot n_\mathrm{N}, M = M_\mathrm{N}$)

Short-circuit test

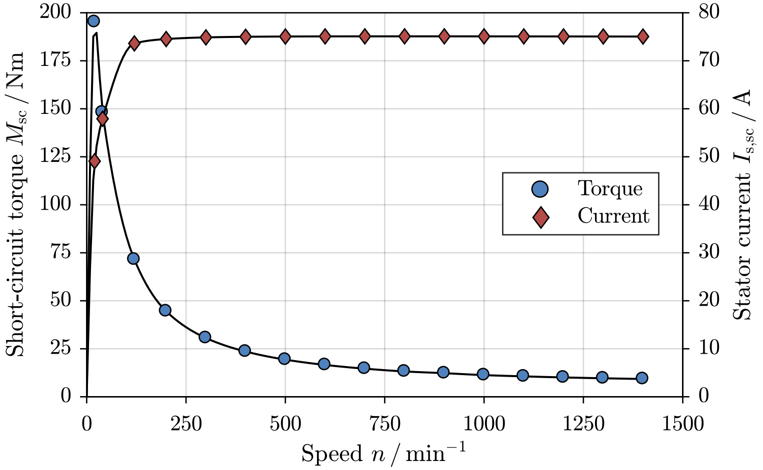

Figure C.29.: Measured torque M_{sc} and current I_{sc} over speed at the short-circuit test for test machine M1 (error bars omitted)

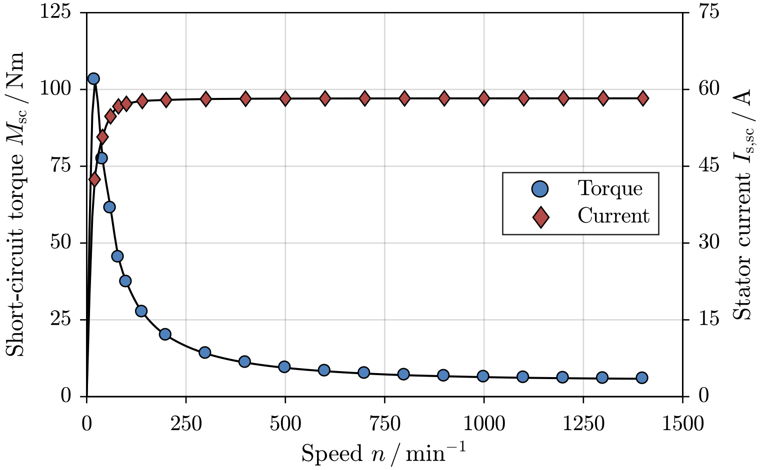

Figure C.30.: Like Figure C.29, but for test machine M2

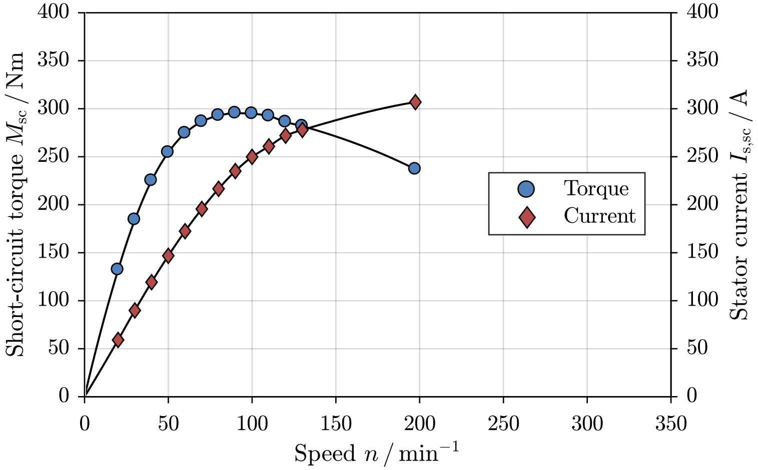

Figure C.31.: Like Figure C.29, but for test machine M3

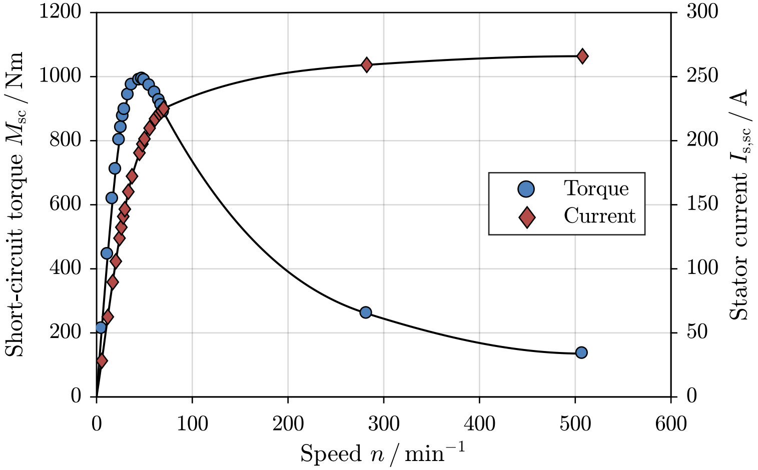

Figure C.32.: Like Figure C.29, but for test machine M5

Reactive current test

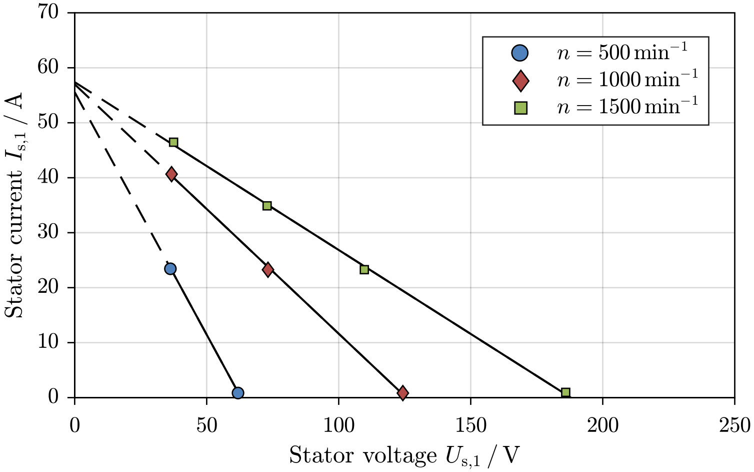

Figure C.33.: Measured stator current $I_{s,1}$ over stator voltage $U_{s,1}$ at the reactive current test for different speeds n of test machine M2 [69] (error bars omitted)

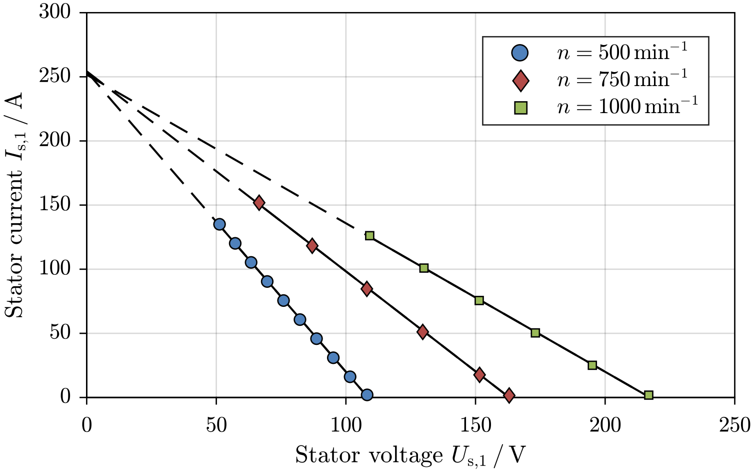

Figure C.34.: Like Figure C.33, but for test machine M5 (error bars omitted)

D. Calculation of measurement uncertainty

General calculation of combined uncertainty:

$$y = f(x_1, x_2, \ldots, x_N) \quad \rightarrow \quad u_\mathrm{c}(y) = \sqrt{\sum_{i=1}^{N} \left(\frac{\partial f(x_\mathrm{i})}{\partial x_\mathrm{i}} \right)^2 \cdot u^2(x_\mathrm{i})} \tag{D.1}$$

Simplifications:

$$y = x_1 + x_2 - x_3 \quad \rightarrow \quad u_\mathrm{c}(y) = \sqrt{u^2(x_1) + u^2(x_2) + u^2(x_3)} \tag{D.2}$$

$$y = x_1 \cdot x_2 \,/\, x_3 \quad \rightarrow \quad \frac{u_\mathrm{c}(y)}{y} = \sqrt{\left(\frac{u(x_1)}{x_1} \right)^2 + \left(\frac{u(x_2)}{x_2} \right)^2 + \left(\frac{u(x_3)}{x_3} \right)^2} \tag{D.3}$$

The error limits of the measurement devices, which were used in the following examples, are given in Appendix B

Example 1: Motor operation
Test machine M4, inverter feeding, rated speed and torque

a) Direct efficiency determination

Efficiency in motor operation:

$$\eta_\mathrm{mot} = \frac{P_\mathrm{m,out}}{P_\mathrm{el,in}}$$

Combined measurement uncertainty:

$$u_\mathrm{c}(\eta_\mathrm{mot}) = \sqrt{\left(\frac{\partial \eta_\mathrm{mot}}{\partial P_\mathrm{m,out}} \right)^2 \cdot u^2(P_\mathrm{m,out}) + \left(\frac{\partial \eta_\mathrm{mot}}{\partial P_\mathrm{el,in}} \right)^2 \cdot u^2(P_\mathrm{el,in})}\ ,$$

with the partial derivatives:

$$\frac{\partial \eta_\mathrm{mot}}{\partial P_\mathrm{m,out}} = \frac{1}{P_\mathrm{el,in}}\ , \quad \frac{\partial \eta_\mathrm{mot}}{\partial P_\mathrm{el,in}} = -\frac{P_\mathrm{m,out}}{\left(P_\mathrm{el,in}\right)^2}$$

b) Indirect efficiency determination

Efficiency in motor operation:

$$\eta_{\mathrm{mot}} = \frac{P_{\mathrm{el,in,1}} - P_{\mathrm{d,1}}}{P_{\mathrm{el,1}} + P_{\mathrm{el,in,0,ad}}}$$

Combined measurement uncertainty:

$$\begin{aligned} u_{\mathrm{c}}(\eta_{\mathrm{mot}}) = \Bigg(& \left(\frac{\partial \eta_{\mathrm{mot}}}{\partial P_{\mathrm{el,in,1}}}\right)^2 \cdot u^2(P_{\mathrm{el,in,1}}) \\ & + \left(\frac{\partial \eta_{\mathrm{mot}}}{\partial P_{\mathrm{d,1}}}\right)^2 \cdot u^2(P_{\mathrm{d,1}}) \\ & + \left(\frac{\partial \eta_{\mathrm{mot}}}{\partial P_{\mathrm{el,in,0,ad}}}\right)^2 \cdot u^2(P_{\mathrm{el,in,0,ad}}) \Bigg)^{1/2} , \end{aligned}$$

with the partial derivatives:

$$\begin{aligned} \frac{\partial \eta_{\mathrm{mot}}}{\partial P_{\mathrm{el,in,1}}} &= \frac{P_{\mathrm{d,1}} + P_{\mathrm{el,in,0,ad}}}{\left(P_{\mathrm{el,1}} + P_{\mathrm{el,in,0,ad}}\right)^2} , \\ \frac{\partial \eta_{\mathrm{mot}}}{\partial P_{\mathrm{d,1}}} &= -\frac{1}{P_{\mathrm{el,in,1}} + P_{\mathrm{el,in,0,ad}}} , \\ \frac{\partial \eta_{\mathrm{mot}}}{\partial P_{\mathrm{el,in,0,ad}}} &= \frac{P_{\mathrm{d,1}} - P_{\mathrm{el,in,1}}}{\left(P_{\mathrm{el,in,1}} + P_{\mathrm{el,in,0,ad}}\right)^2} \end{aligned}$$

The input values and results of the calculation are given in Table D.1.

Example 2: Generator operation
Test machine M4, inverter feeding, rated speed and torque

a) Direct efficiency determination

Efficiency in generator operation:

$$\eta_{\mathrm{gen}} = \frac{P_{\mathrm{el,out}}}{P_{\mathrm{m,in}}}$$

Combined measurement uncertainty:

$$u_{\mathrm{c}}(\eta_{\mathrm{gen}}) = \sqrt{\left(\frac{\partial \eta_{\mathrm{gen}}}{\partial P_{\mathrm{el,out}}}\right)^2 \cdot u^2(P_{\mathrm{el,out}}) + \left(\frac{\partial \eta_{\mathrm{gen}}}{\partial P_{\mathrm{m,in}}}\right)^2 \cdot u^2(P_{\mathrm{m,in}})}\ ,$$

with the partial derivatives:

$$\frac{\partial \eta_{\mathrm{gen}}}{\partial P_{\mathrm{el,out}}} = \frac{1}{P_{\mathrm{m,in}}}\ , \quad \frac{\partial \eta_{\mathrm{gen}}}{\partial P_{\mathrm{m,in}}} = -\frac{P_{\mathrm{el,out}}}{\left(P_{\mathrm{m,in}}\right)^2}$$

b) Indirect efficiency determination

Efficiency in generator operation:

$$\eta_{\mathrm{gen}} = \frac{P_{\mathrm{el,out,1}}}{P_{\mathrm{el,out,1}} + P_{\mathrm{d,1}} + P_{\mathrm{el,in,0,ad}}} = \frac{P_{\mathrm{el,out,1}}}{P_{\mathrm{el,out,1}} + P_{\mathrm{d}}}$$

Combined measurement uncertainty:

$$u_{\mathrm{c}}(\eta_{\mathrm{gen}}) = \sqrt{\left(\frac{\partial \eta_{\mathrm{gen}}}{\partial P_{\mathrm{el,out,1}}}\right)^2 \cdot u^2(P_{\mathrm{el,out,1}}) + \left(\frac{\partial \eta_{\mathrm{gen}}}{\partial P_{\mathrm{d}}}\right)^2 \cdot u^2(P_{\mathrm{d}})}\ ,$$

with the partial derivatives:

$$\frac{\partial \eta_{\mathrm{gen}}}{\partial P_{\mathrm{el,out,1}}} = \frac{P_{\mathrm{d}}}{\left(P_{\mathrm{el,out,1}} + P_{\mathrm{d}}\right)^2}\ , \quad \frac{\partial \eta_{\mathrm{gen}}}{\partial P_{\mathrm{d}}} = -\frac{P_{\mathrm{el,out,1}}}{\left(P_{\mathrm{el,out,1}} + P_{\mathrm{d}}\right)^2}$$

The input values and results of the calculation are given in Table D.2.

Table D.1.: Measurement and uncertainty values for direct and indirect efficiency determination of test machine M4 at rated motor operation at inverter feeding

	Value x_i	Uncertainty $u(x_i)$	Equation
Operation conditions			
Speed n	$2500\,\mathrm{min}^{-1}$	$0.25\,\mathrm{min}^{-1}$	–
Torque M	318.72 Nm	1.00 Nm	–
Mechanical output power $P_{\mathrm{m,out}}$	83 442 W	262 W	–
Stator RMS voltage per phase $U_{\mathrm{s,1}}$	217.76 V	0.26 V	–
Stator RMS current per phase $I_{\mathrm{s,1}}$	146.98 A	0.52 A	–
Power factor $\cos\varphi_{\mathrm{s,1}}$	0.8969	0.0039	–
Stator frequency f_{s}	166.67 Hz	0.017 Hz	–
Electrical input power $P_{\mathrm{el,in}}$	86 886 W	373 W	–
Fundamental el. input power $P_{\mathrm{el,in,1}}$	86 121 W	370 W	–
Indirect loss determination			
Iron losses P_{Fe}	1257 W	16 W	(5.2)
Current-depending losses $P_{\mathrm{Cu}\sim}$	1679 W	14 W	(5.6)
Friction and windage losses $P_{\mathrm{fr+w}}$	16 W	–	(3.22)
Fundamental losses $P_{\mathrm{d,1}}$	2952 W	22 W	(5.9)
Add. losses (inv. feeding) $P_{\mathrm{el,in,0,ad}}$	692 W	9 W	(4.2)
Total losses P_{d}	3644 W	23 W	(5.12)
Efficiency determination			
Direct efficiency η_{mot}	96.04 %	0.5093 %	(4.6)
Indirect efficiency η_{mot}	95.80 %	0.0321 %	(5.10)

Table D.2.: Measurement and uncertainty values for direct and indirect efficiency determination of test machine M4 at rated generator operation at inverter feeding

	Value x_i	Uncertainty $u(x_i)$	Equation
Operation conditions			
Speed n	$2500\,\text{min}^{-1}$	$0.25\,\text{min}^{-1}$	–
Torque M	319.26 Nm	1.00 Nm	–
Mechanical input power $P_{\text{m,in}}$	83 582 W	262 W	–
Stator RMS voltage per phase $U_{\text{s},1}$	191.42 V	0.24 V	–
Stator RMS current per phase $I_{\text{s},1}$	143.84 A	0.51 A	–
Power factor $\cos\varphi_{\text{s},1}$	0.9800	0.0017	–
Stator frequency f_{s}	166.67 Hz	0.017 Hz	–
Electrical output power $P_{\text{el,out}}$	80 284 W	353 W	–
Fundamental el. output power $P_{\text{el,out},1}$	81 115 W	349 W	–
Indirect loss determination			
Iron losses P_{Fe}	1033 W	13 W	(5.2)
Current-depending losses $P_{\text{Cu}\sim}$	1585 W	13 W	(5.6)
Friction and windage losses $P_{\text{fr+w}}$	16 W	–	(3.22)
Fundamental losses $P_{\text{d},1}$	2635 W	19 W	(5.9)
Add. losses (inv. feeding) $P_{\text{el,in,0,ad}}$	784 W	10 W	(4.2)
Total losses P_{d}	3419 W	21 W	(5.12)
Efficiency determination			
Direct efficiency η_{gen}	96.05 %	0.5193 %	(4.7)
Indirect efficiency η_{gen}	95.96 %	0.0349 %	(5.11)

E. Simulation results

Generator no-load operation

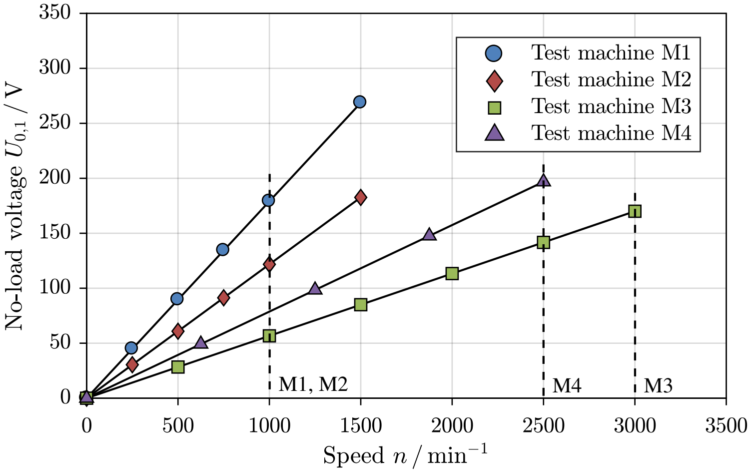

Figure E.1.: Simulated generator no-load voltage U_0 per phase over speed n (rated speed marked)

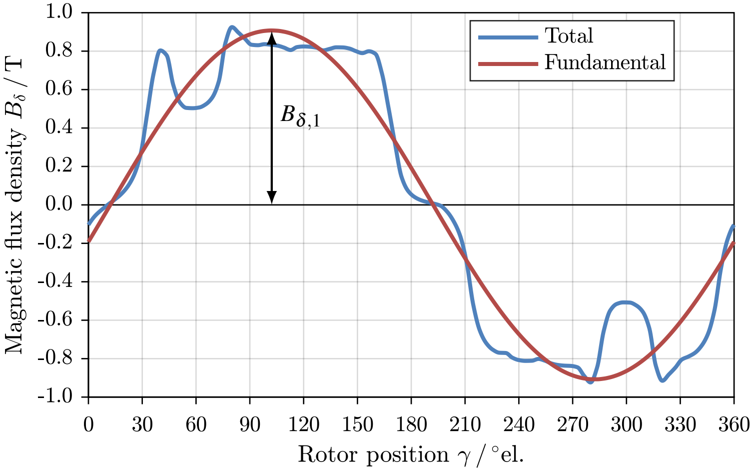

Figure E.2.: Radial component of the simulated magnetic no-load air gap flux density at the center of the air gap of test machine M1 (fundamental amplitude $B_{\delta,1} = 0.91\,\mathrm{T}$)

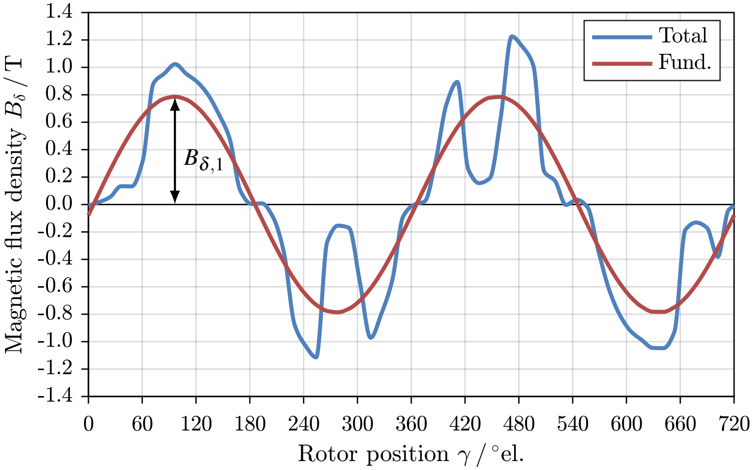

Figure E.3.: Like Figure E.2, but for test machine M2 (fundamental amplitude $B_{\delta,1} = 0.79\,\mathrm{T}$)

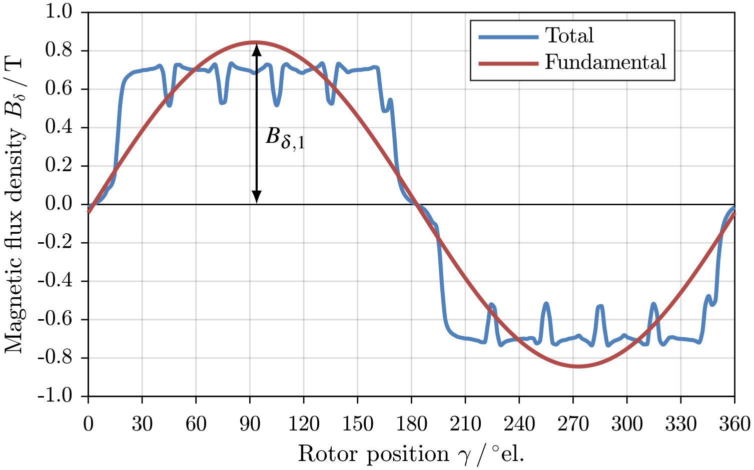

Figure E.4.: Like Figure E.2, but for test machine M3 (fundamental amplitude $B_{\delta,1} = 0.84\,\mathrm{T}$)

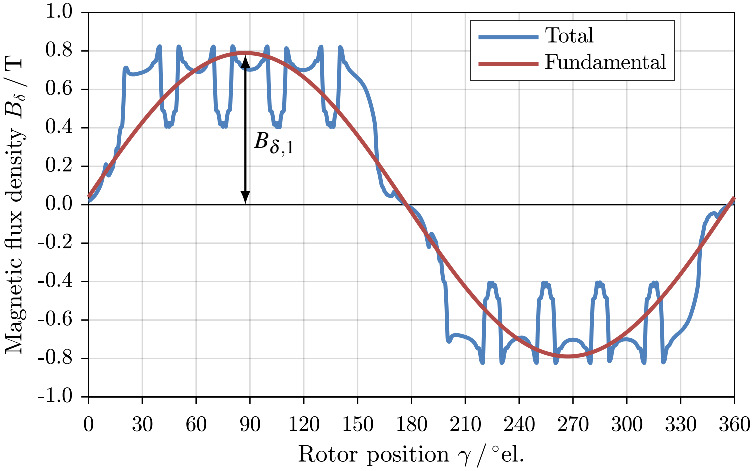

Figure E.5.: Like Figure E.2, but for test machine M4 (fundamental amplitude $B_{\delta,1} = 0.79\,\mathrm{T}$)

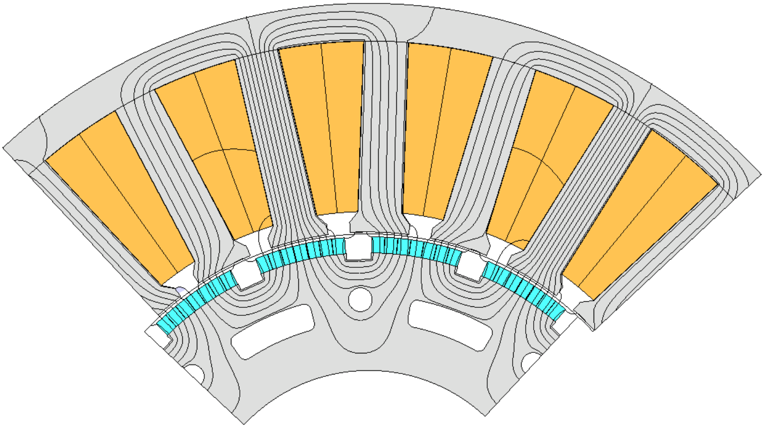

Figure E.6.: Calculated flux lines at generator no-load simulation of test machine M1

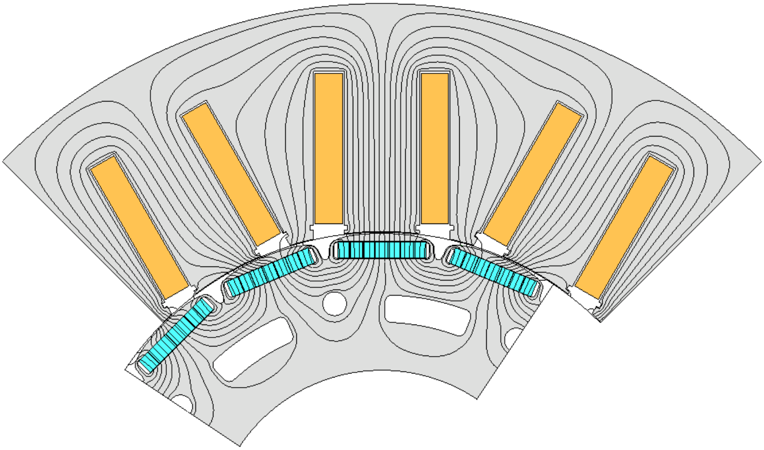

Figure E.7.: Like Figure E.6, but for test machine M2

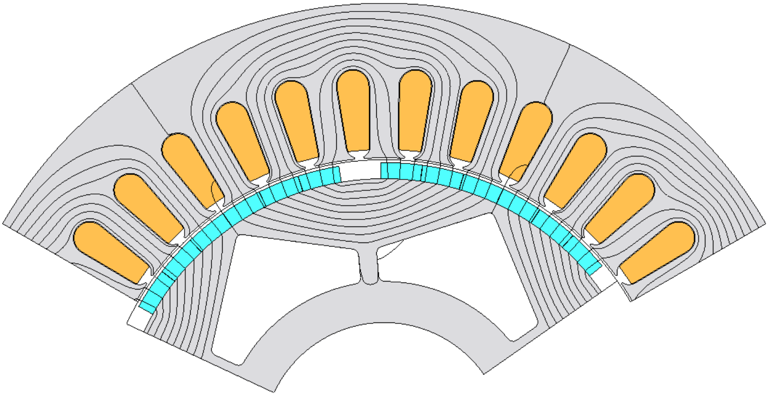

Figure E.8.: Like Figure E.6, but for test machine M3

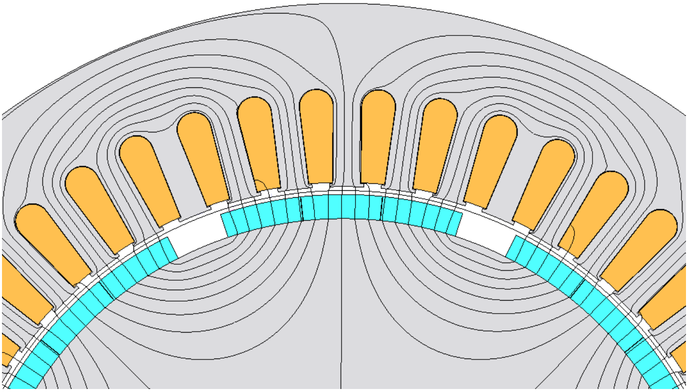

Figure E.9.: Like Figure E.6, but for test machine M4

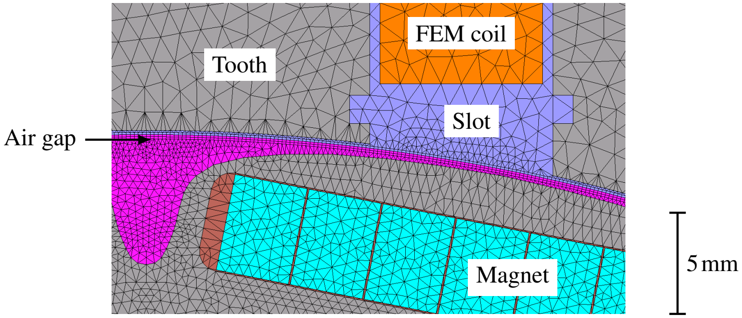

Figure E.10.: Detail of air gap mesh of test machine M2

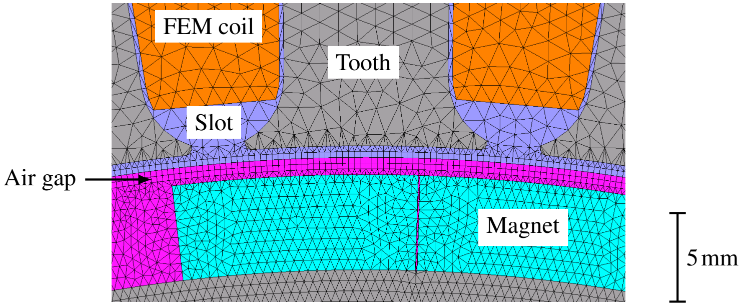

Figure E.11.: Like Figure E.10, but for test machine M3

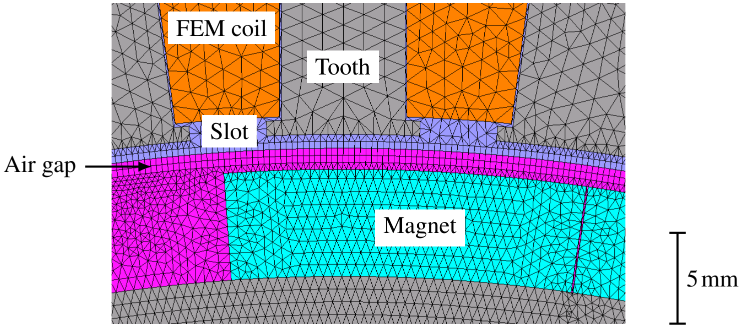

Figure E.12.: Like Figure E.10, but for test machine M4

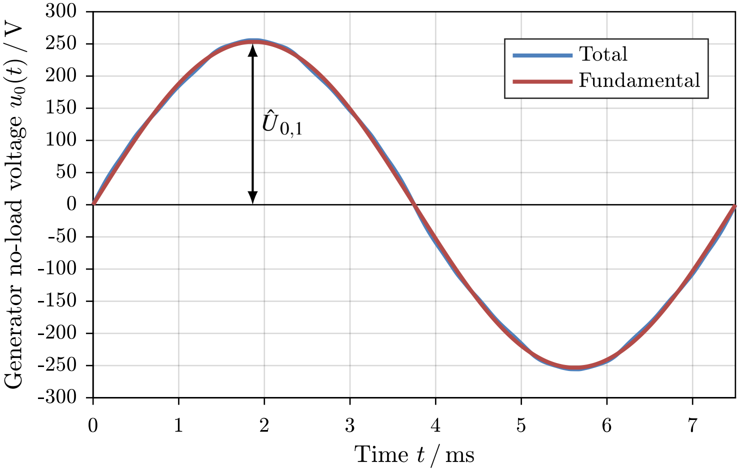

Figure E.13.: Simulated generator no-load phase voltage of test machine M1 and its fundamental ($U_{0,1} = 178.9\,\text{V}$ RMS) over time at rated speed ($n_\text{N} = 1000\,\text{min}^{-1}$)

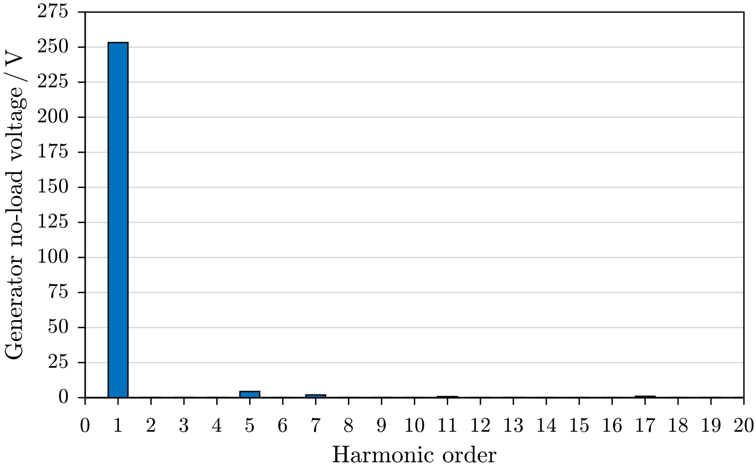

Figure E.14.: Amplitude spectrum of the simulated generator no-load phase voltage of test machine M1 at rated speed ($n_\text{N} = 1000\,\text{min}^{-1}$)

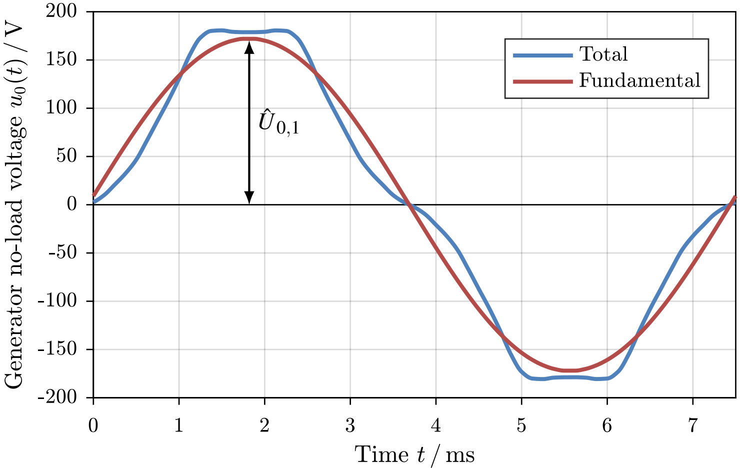

Figure E.15.: Like Figure E.13, but for test machine M2 ($U_{0,1} = 121.6\,\mathrm{V}$ RMS, $n_\mathrm{N} = 1000\,\mathrm{min}^{-1}$)

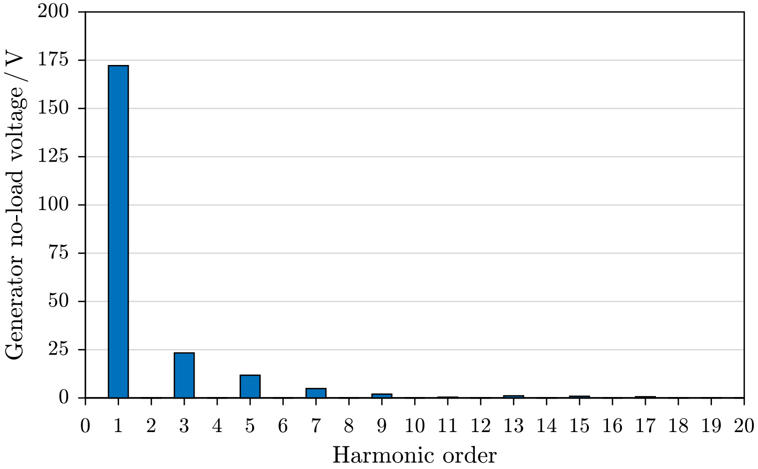

Figure E.16.: Like Figure E.14, but for test machine M2 ($n_\mathrm{N} = 1000\,\mathrm{min}^{-1}$)

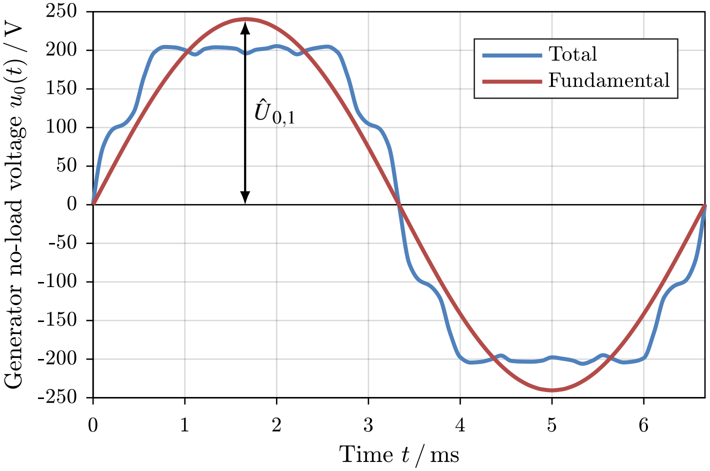

Figure E.17.: Like Figure E.13, but for test machine M3 ($U_{0,1} = 169.9\,\mathrm{V}$ RMS, $n_\mathrm{N} = 3000\,\mathrm{min}^{-1}$)

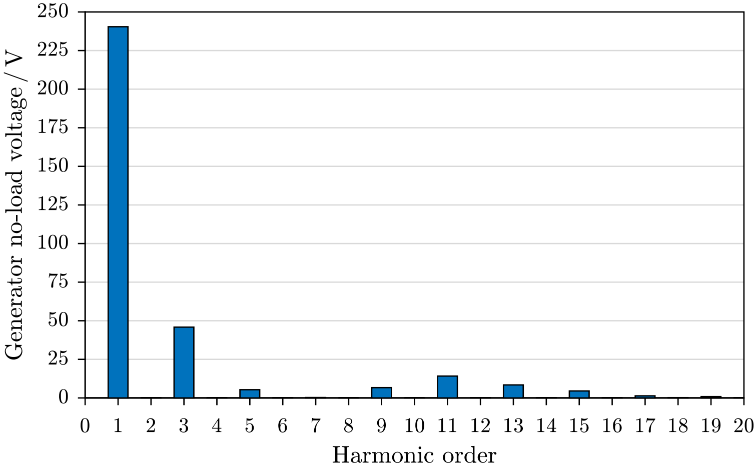

Figure E.18.: Like Figure E.14, but for test machine M3 ($n_\mathrm{N} = 3000\,\mathrm{min}^{-1}$)

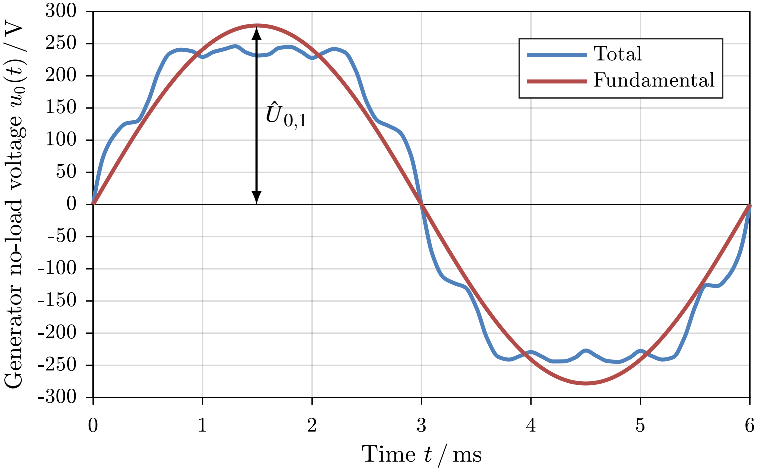

Figure E.19.: Like Figure E.13, but for test machine M4 ($U_{0,1} = 196.7\,\mathrm{V}$ RMS, $n_\mathrm{N} = 2500\,\mathrm{min}^{-1}$)

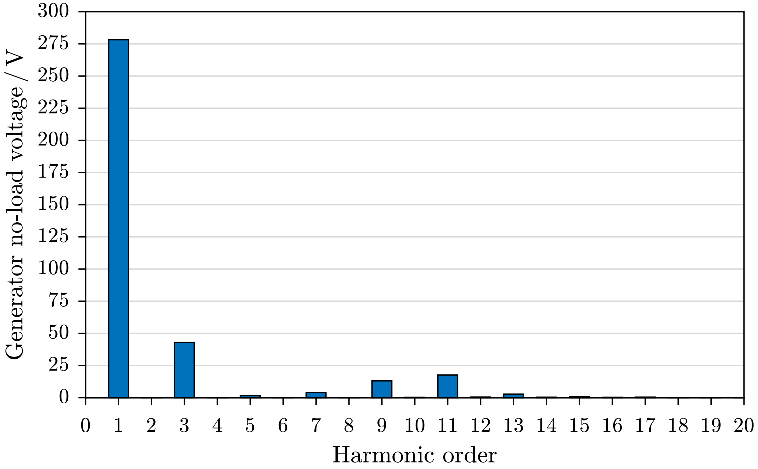

Figure E.20.: Like Figure E.14, but for test machine M4 ($n_\mathrm{N} = 2500\,\mathrm{min}^{-1}$)

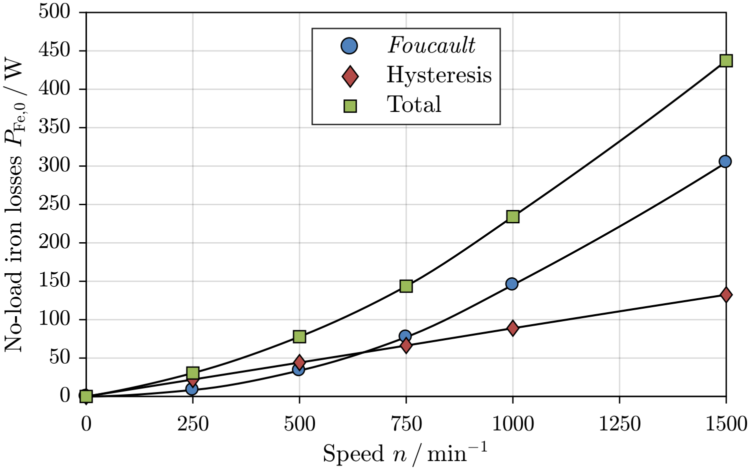

Figure E.21.: Simulated generator no-load iron losses of test machine M2 over speed ($n_\mathrm{N} = 1000\,\mathrm{min}^{-1}, k_\mathrm{V} = 1$)

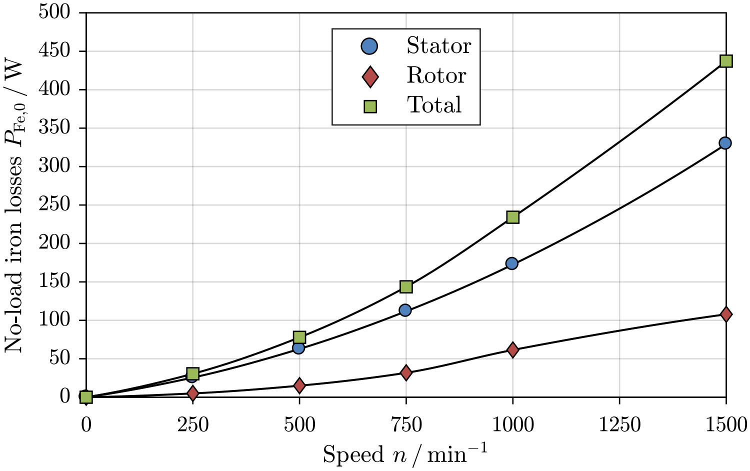

Figure E.22.: Like Figure E.21, but as sum of stator and rotor iron losses

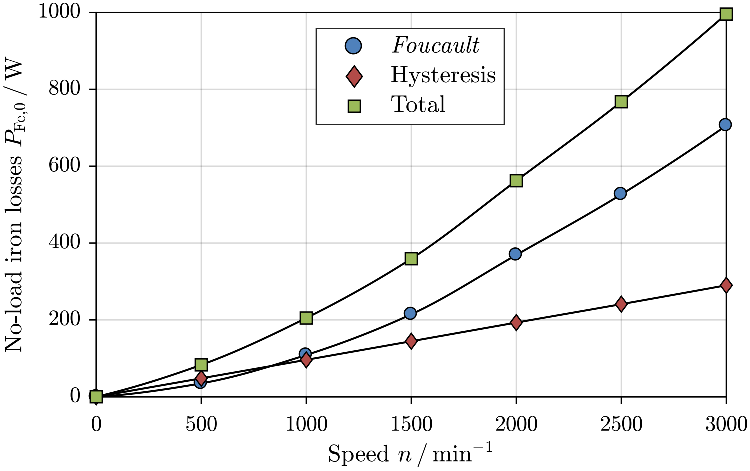

Figure E.23.: Like Figure E.21, but for test machine M3 ($n_{\mathrm{N}} = 3000\,\mathrm{min}^{-1}, k_{\mathrm{V}} = 1$)

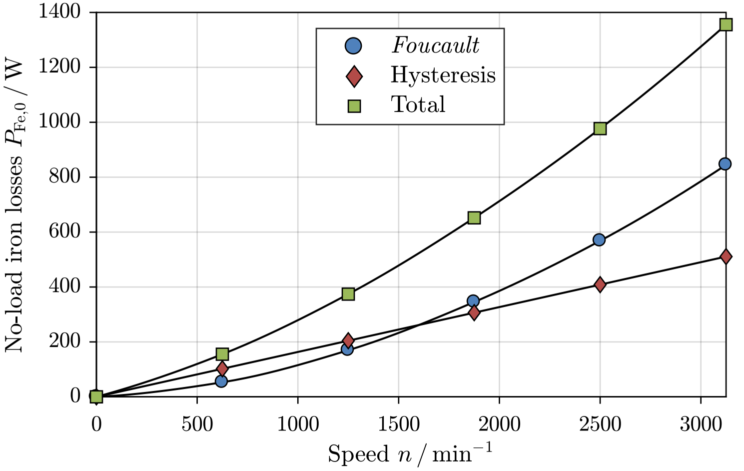

Figure E.24.: Like Figure E.21, but for test machine M4 ($n_{\mathrm{N}} = 2500\,\mathrm{min}^{-1}, k_{\mathrm{V}} = 1$)

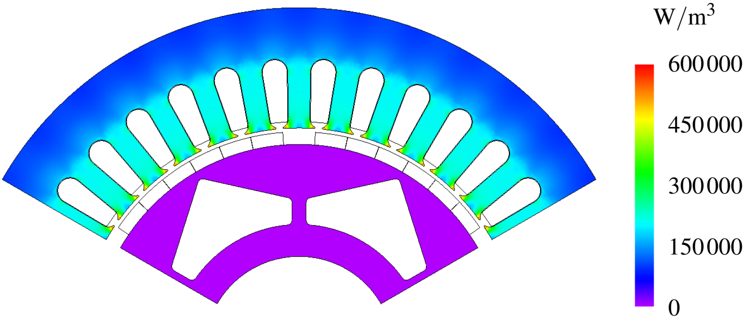

Figure E.25.: Simulated iron loss density at generator no-load operation of test machine M3 at rated speed $n_\mathrm{N} = 3000\,\mathrm{min}^{-1}$

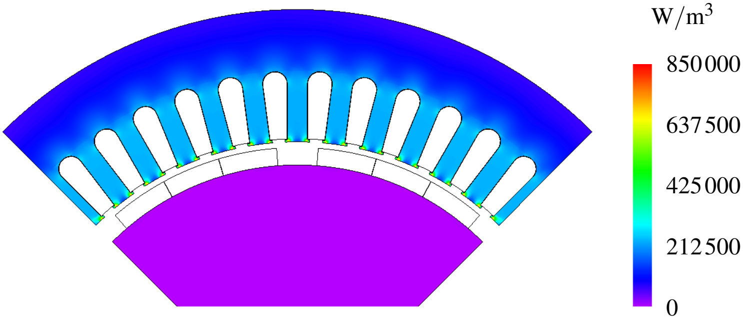

Figure E.26.: Like Figure E.25, but for test machine M4 ($n_\mathrm{N} = 2500\,\mathrm{min}^{-1}$)

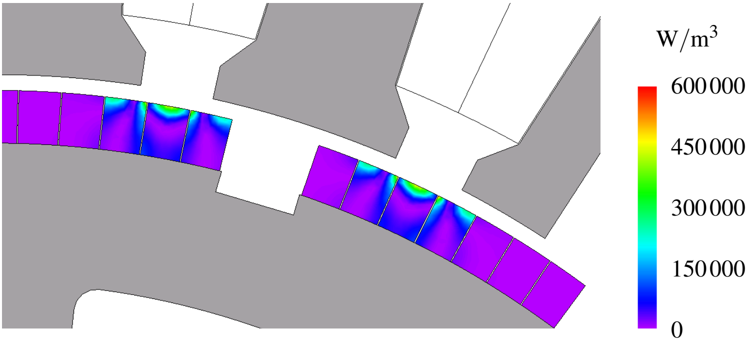

Figure E.27.: Simulated magnet loss density at generator no-load operation of test machine M1 at rated speed $n_\mathrm{N} = 1000\,\mathrm{min}^{-1}$

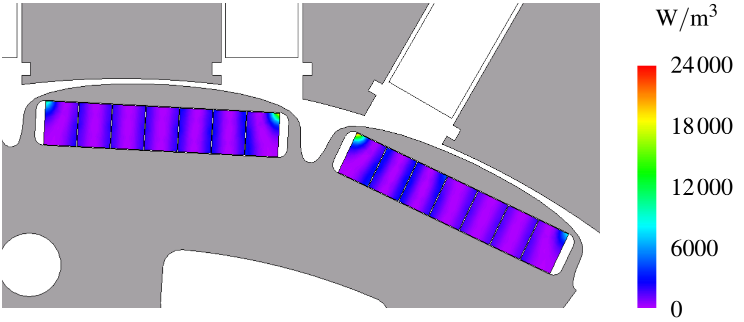

Figure E.28.: Like Figure E.27, but for test machine M2 ($n_\mathrm{N} = 1000\,\mathrm{min}^{-1}$)

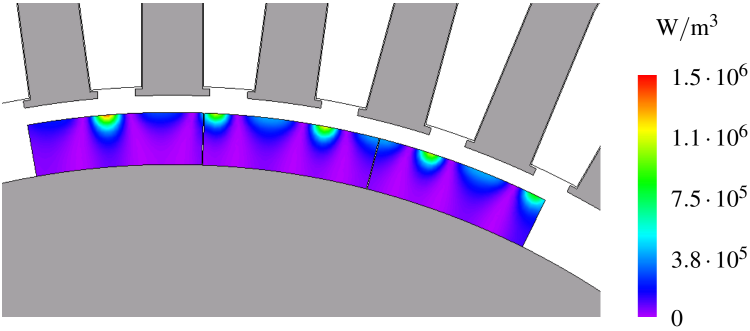

Figure E.29.: Like Figure E.27, but for test machine M4 ($n_\mathrm{N} = 2500\,\mathrm{min}^{-1}$)

Removed rotor operation

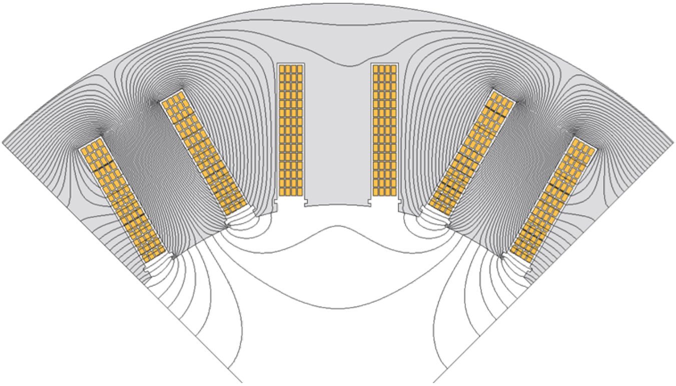

Figure E.30.: Calculated flux lines at the removed rotor simulation of test machine M2

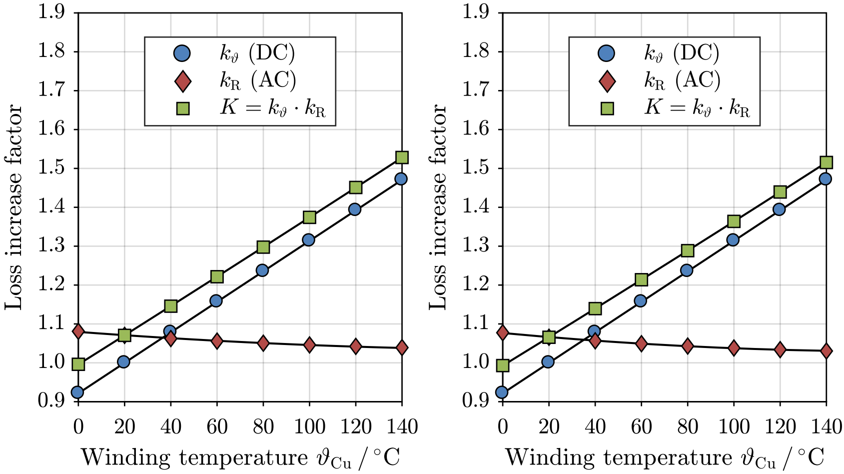

(a) simulated

(b) analytical

Figure E.31.: Calculated resistance increase over conductor temperature at rated frequency $f_\mathrm{sN} = 133.3\,\mathrm{Hz}$ of test machine M1

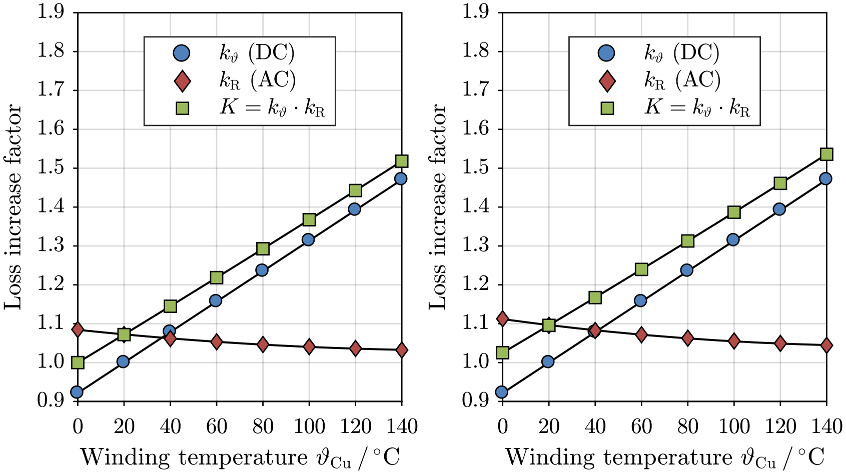

(a) simulated (b) analytical

Figure E.32.: Like Figure E.31, but for test machine M3 ($f_\mathrm{sN} = 150.0\,\mathrm{Hz}$)

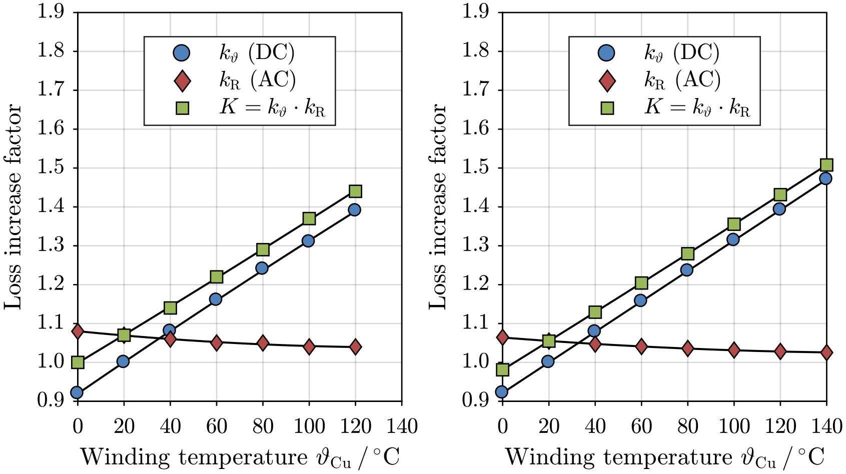

(a) simulated (b) analytical

Figure E.33.: Like Figure E.31, but for test machine M4 ($f_\mathrm{sN} = 166.7\,\mathrm{Hz}$)

Load operation

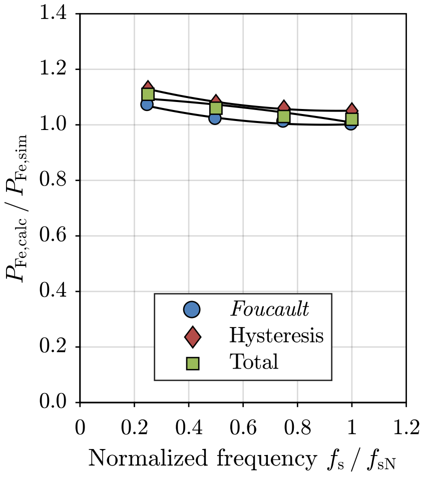

(a) Motor ($\beta^* = 0\,^\circ$el.)

(b) Generator ($\beta^* = 180\,^\circ$el.)

Figure E.34.: Ratio between calculated and simulated iron losses at rated current ($I_{\mathrm{sN}} = 102\,\mathrm{A}$) of test machine M1

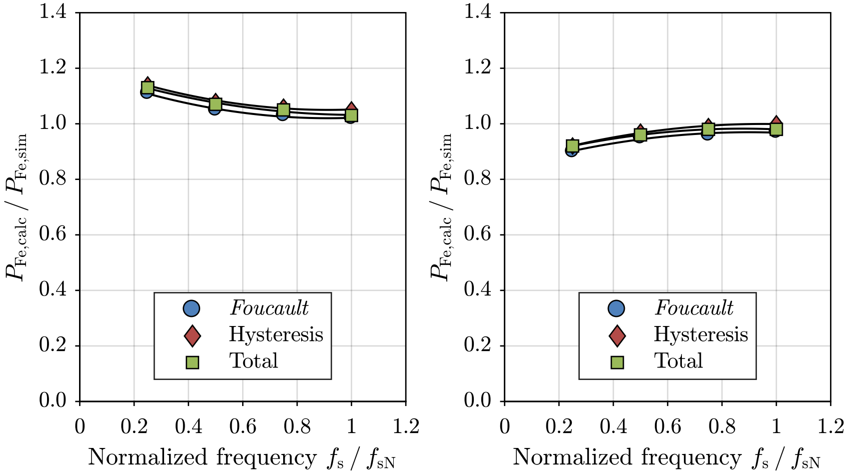

(a) Motor ($\beta^* = 15\,°$el.) (b) Generator ($\beta^* = 165\,°$el.)

Figure E.35.: Like Figure E.34, but at increased current angle β^* by 15 ° el.

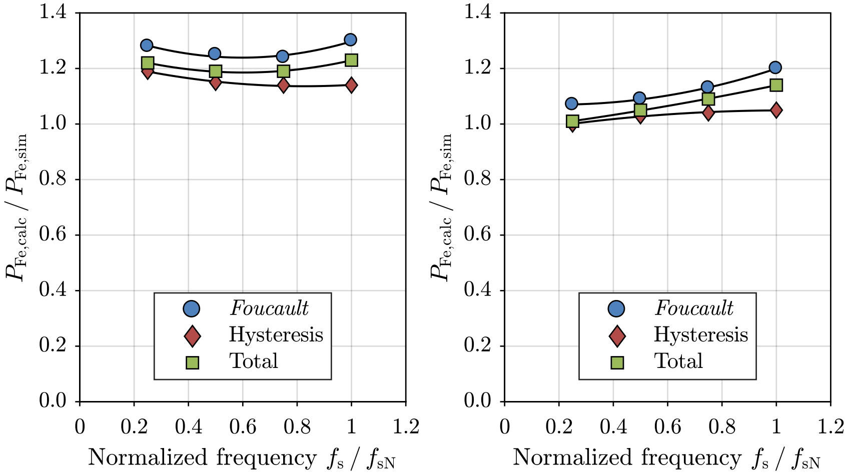

(a) Motor ($\beta^* = 30\,°$el.) (b) Generator ($\beta^* = 150\,°$el.)

Figure E.36.: Like Figure E.34, but for test machine M2 at increased current angle β^* by 30 ° el. ($I_{sN} = 120\,A$)

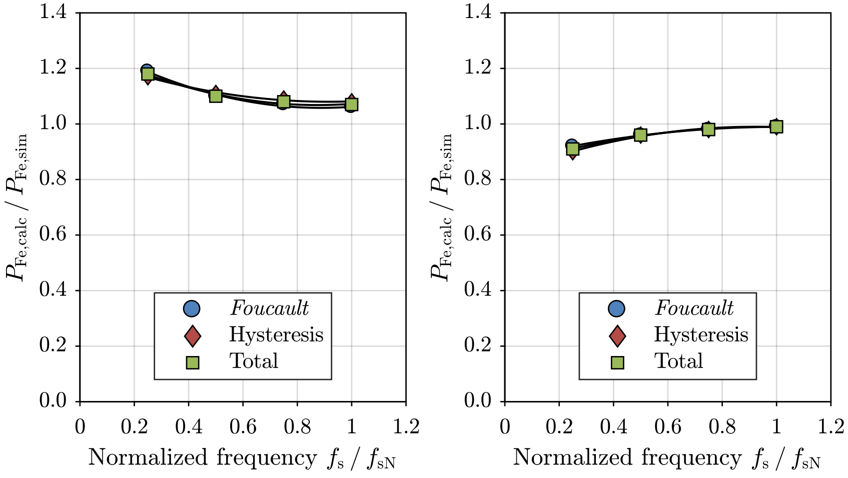

(a) Motor ($\beta^* = 0\,°$el.)

(b) Generator ($\beta^* = 180\,°$el.)

Figure E.37.: Like Figure E.34, but for test machine M4 ($I_{\mathrm{sN}} = 148\,\mathrm{A}$)

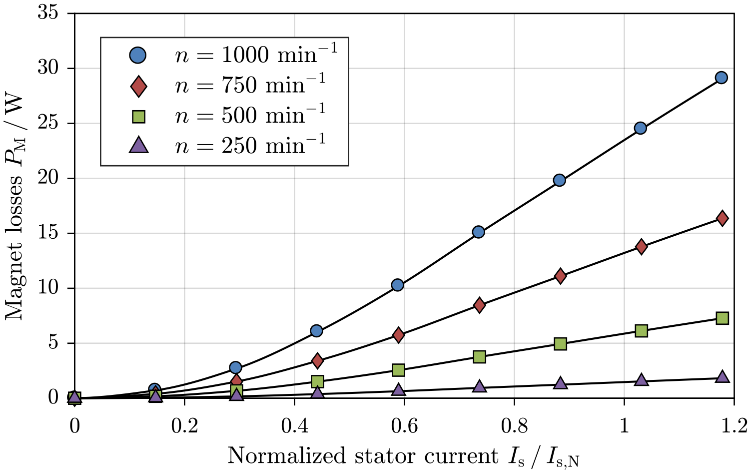

Figure E.38.: Simulated magnet losses P_{M} for different rotor speed n and stator currents I_{s} for test machine M2

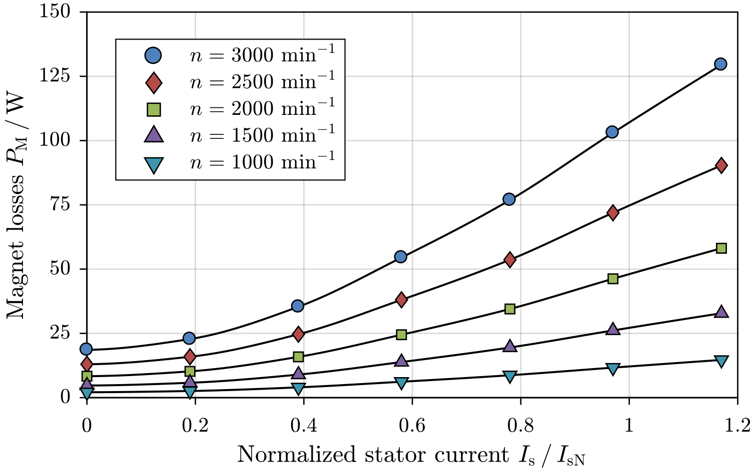

Figure E.39.: Like Figure E.38, but for test machine M3

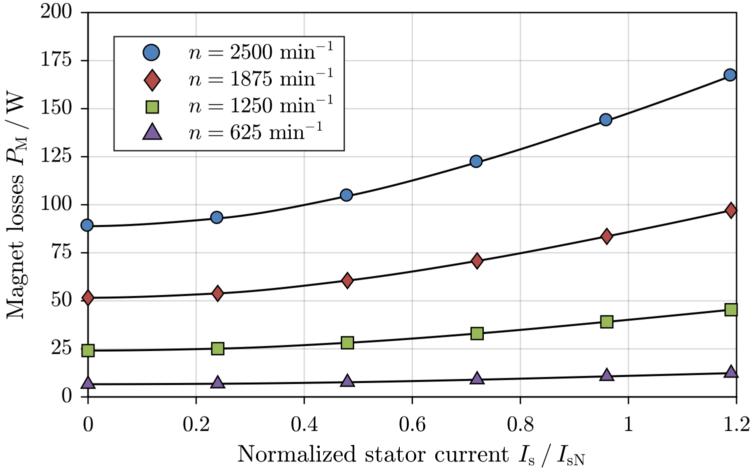

Figure E.40.: Like Figure E.38, but for test machine M4

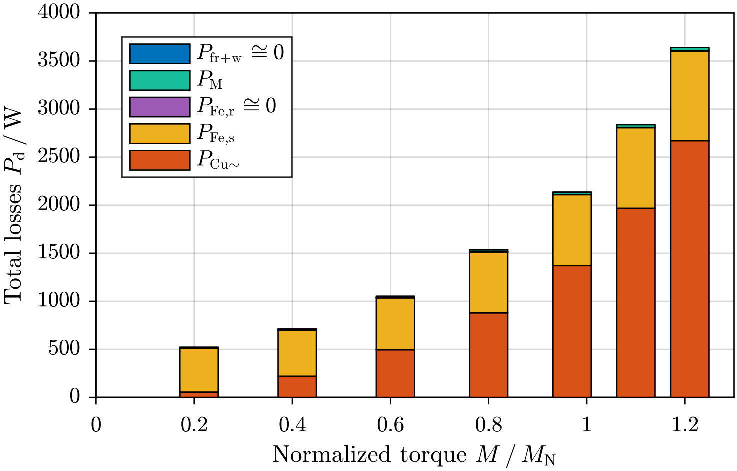

Figure E.41.: Simulated loss distribution of test machine M1 over torque at rated speed ($n_\mathrm{N} = 1000\,\mathrm{min}^{-1}$)

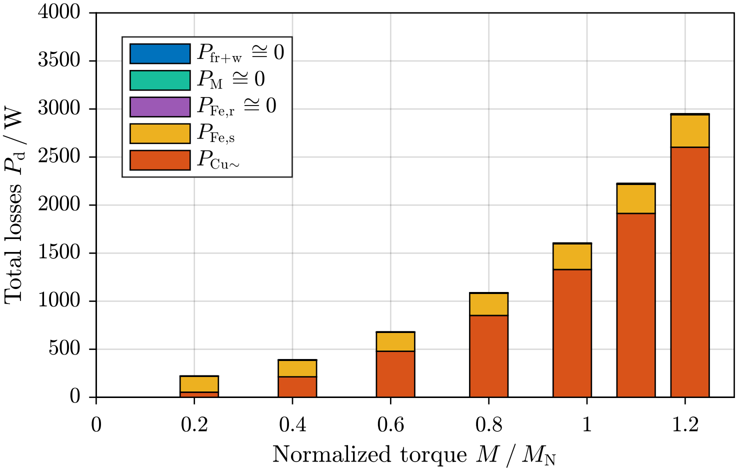

Figure E.42.: Like Figure E.41, but at 50 % of the rated speed ($n = 500\,\mathrm{min}^{-1}$)

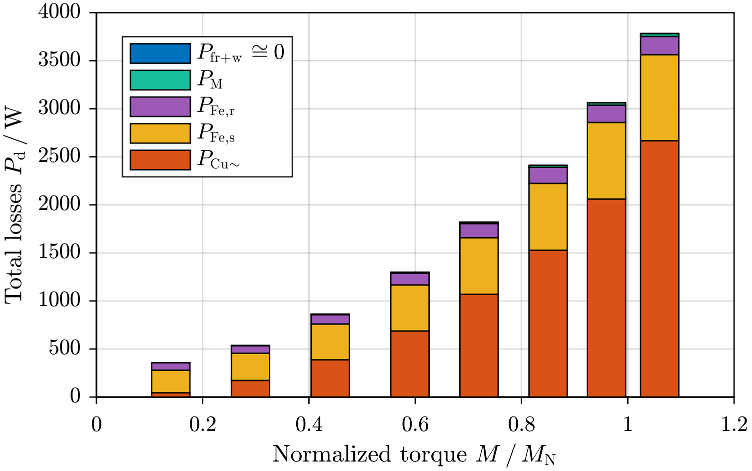

Figure E.43.: Like Figure E.41, but for test machine M2 ($n_N = 1000\,\mathrm{min}^{-1}$)

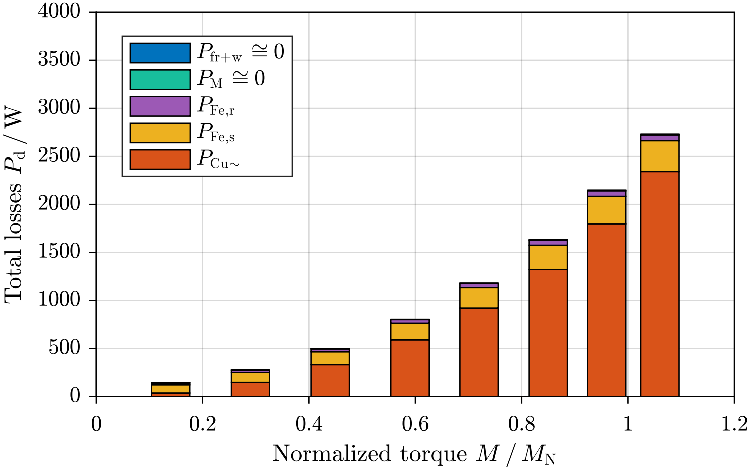

Figure E.44.: Like Figure E.43, but at 50 % of the rated speed ($n = 500\,\mathrm{min}^{-1}$)

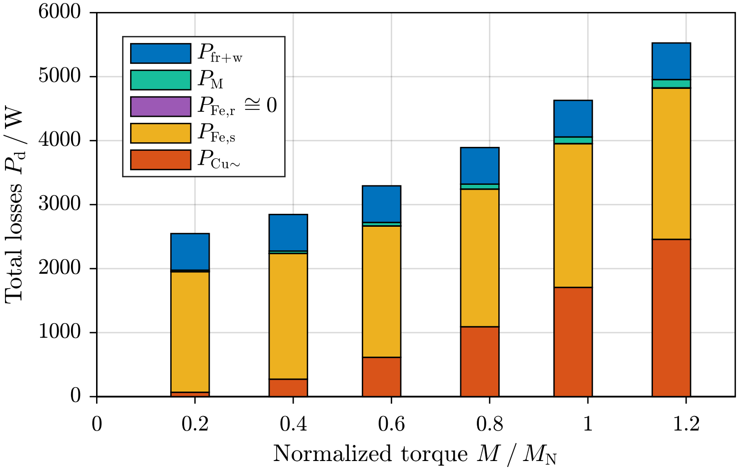

Figure E.45.: Like Figure E.41, but for test machine M3 ($n_{\mathrm{N}} = 3000\,\mathrm{min}^{-1}$)

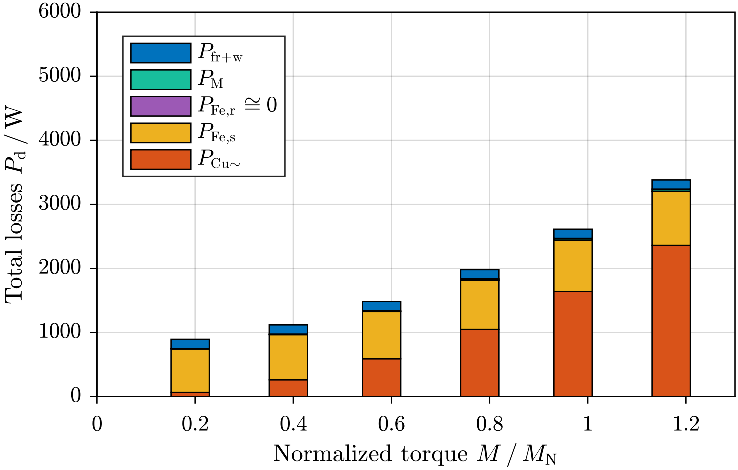

Figure E.46.: Like Figure E.45, but at 50 % of the rated speed ($n = 1500\,\mathrm{min}^{-1}$)

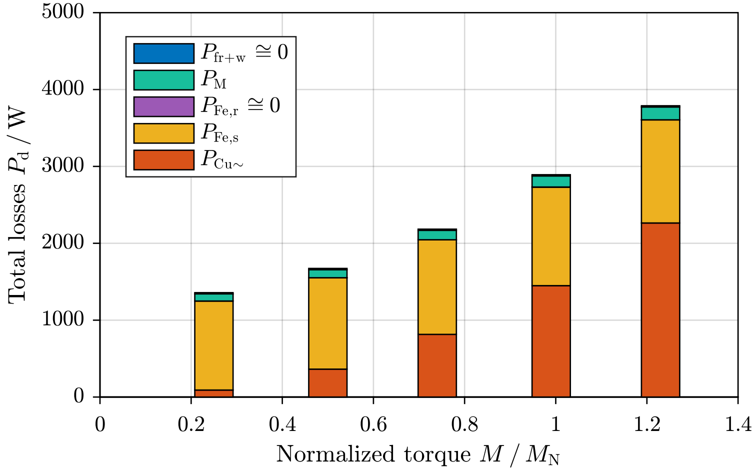

Figure E.47.: Like Figure E.41, but for test machine M4 ($n_N = 2500\,\mathrm{min}^{-1}$)

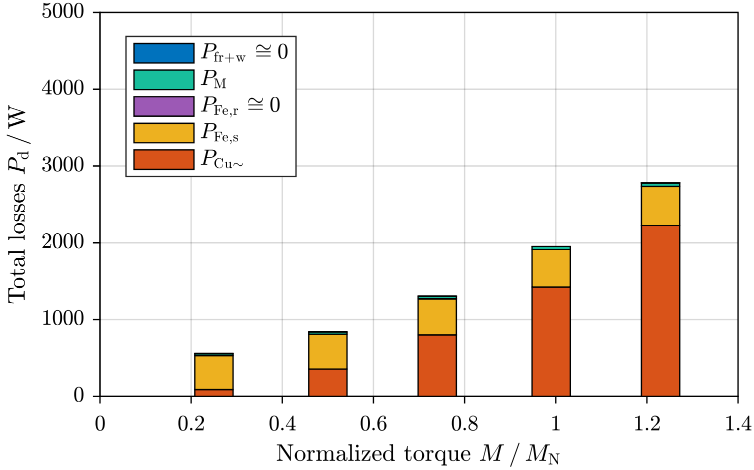

Figure E.48.: Like Figure E.47, but at 50 % of the rated speed ($n = 1250\,\mathrm{min}^{-1}$)

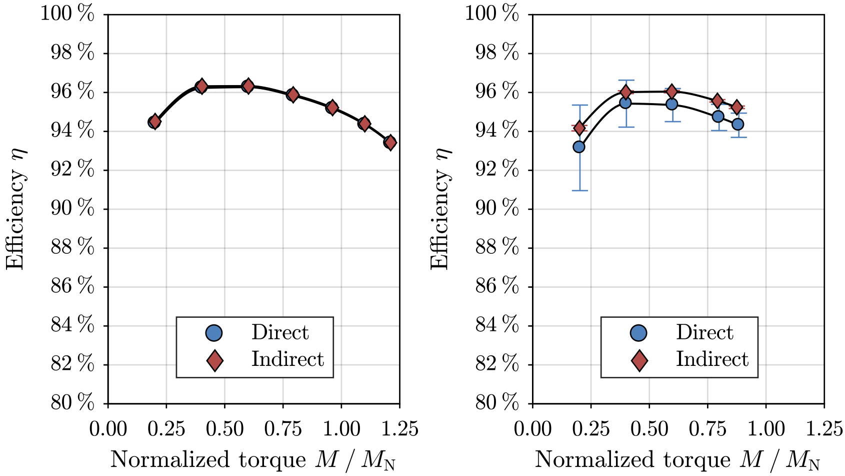

(a) Simulation ($\beta^* = 165\,°\mathrm{el.}$)

(b) Measurement

Figure E.49.: Comparison of the simulated and measured efficiency at sinusoidal current operation of test machine M1 at generator operation and rated speed ($n_\mathrm{N} = 1000\,\mathrm{min}^{-1}$)

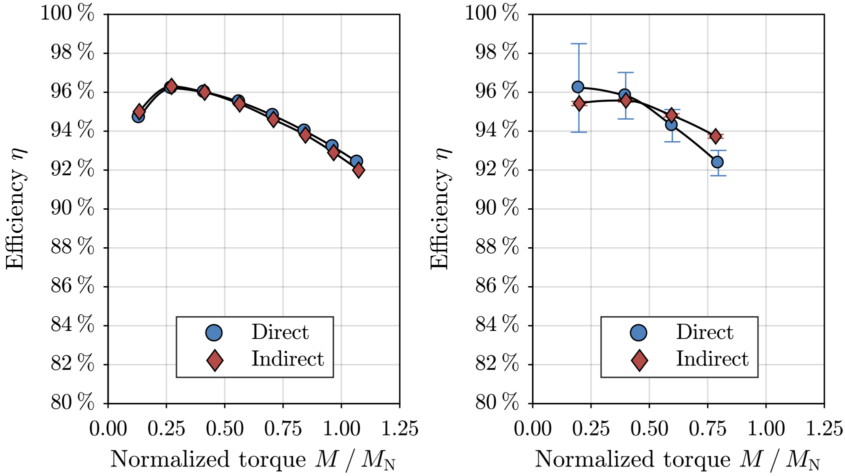

(a) Simulation ($\beta^* = 165\,°\mathrm{el.}$)

(b) Measurement

Figure E.50.: Like Figure E.49, but for test machine M2 ($n_\mathrm{N} = 1000\,\mathrm{min}^{-1}$)

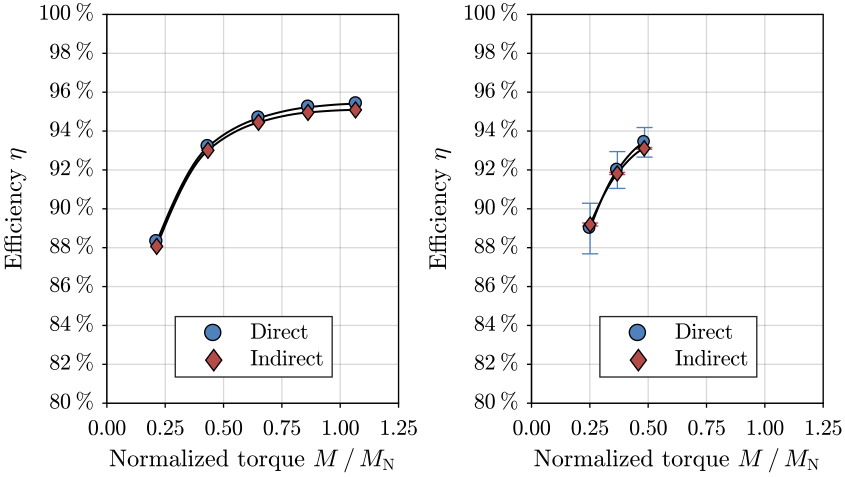

(a) Simulation ($\beta^* = 0\,°$el.)

(b) Measurement

Figure E.51.: Like Figure E.49, but for test machine M3 at motor operation ($n_N = 3000\,\text{min}^{-1}$)

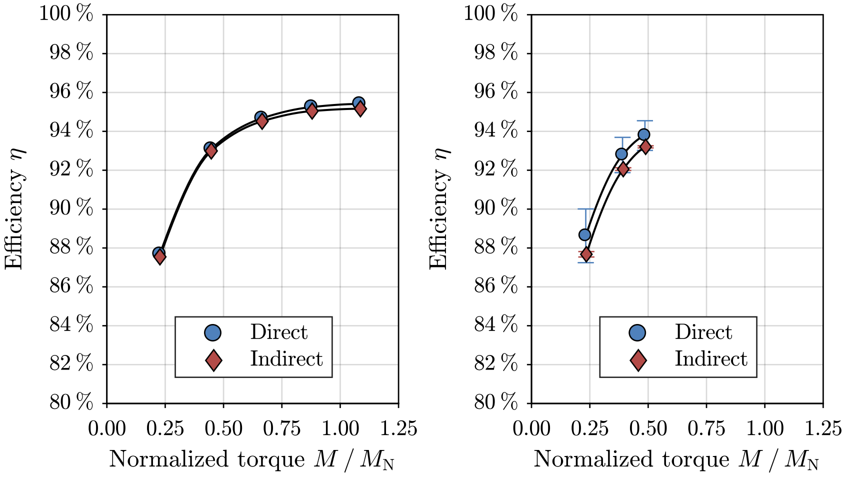

(a) Simulation ($\beta^* = 180\,°$el.)

(b) Measurement

Figure E.52.: Like Figure E.49, but for test machine M3 at generator operation ($n_N = 3000\,\text{min}^{-1}$)

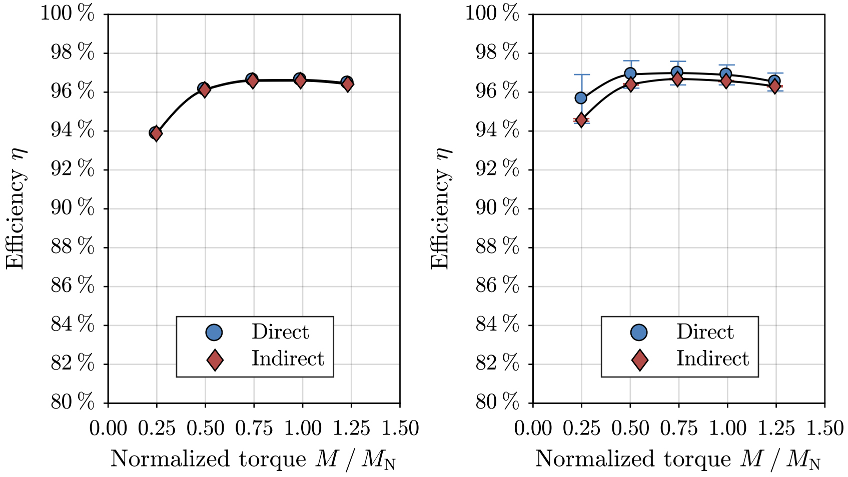

(a) Simulation ($\beta^* = 0\,°$el.)

(b) Measurement

Figure E.53.: Like Figure E.49, but for test machine M4 at motor operation ($n_N = 2500\,\text{min}^{-1}$)

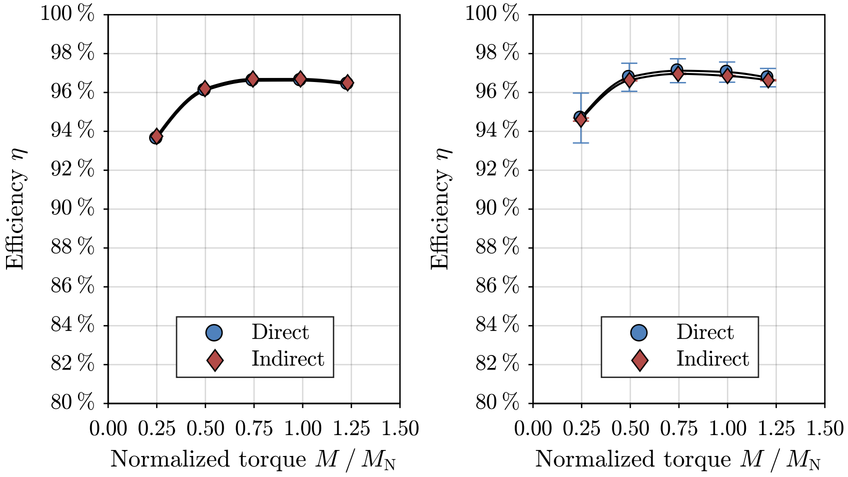

(a) Simulation ($\beta^* = 180\,°$el.)

(b) Measurement

Figure E.54.: Like Figure E.49, but for test machine M4 at generator operation ($n_N = 2500\,\text{min}^{-1}$)

F. Iron loss determination in *JMAG*

The finite element software *JMAG* offers several methods for iron loss determination, e.g. FFT analysis, hysteresis loop evaluation, or user subroutines. Each method requires specific steel sheet material parameters to calculate the iron losses either by analytic loss formulas or pre-calculated specific losses per volume. In this thesis the FFT analysis is used with pre-calculated iron loss tables. The following descriptions are taken from the *JMAG User's Manual* [32]

FFT analysis procedure

1. Magnetic field transient analysis
2. Extraction of time-series data of magnetic flux density B for each material and specification of basic frequency f_1
3. Re-sampling of the time-series data by spline interpolation to get 2^N equally spaced data points, e.g. 24 data points in time-series data lead to 32 data points after re-sampling.
4. FFT analysis gives $2^N/2-1$ frequency components. The lowest frequency is the basic frequency f_1.
5. Hysteresis and *Foucault* losses are calculated for each element and frequency.
6. Output of the loss for each harmonic order and the sum over all frequencies

Frequency separation of loss data

If, like for this thesis, no separate specific loss table for hysteresis and *Foucault* losses is available from the steel sheet data, *JMAG* uses a separation method to split the total losses into hysteresis and *Foucault* losses.

Under the assumption that the hysteresis losses $P_{\mathrm{Fe,Hy}}$ are proportional to the frequency f and the *Foucault* losses $P_{\mathrm{Fe,Ft}}$ depend on the square of the frequency f, the total iron losses P_{Fe} are defined as

$$P_{\text{Fe}} = a(B) \cdot f + b(B,f) \cdot f^2 \ , \tag{F.1}$$

with two arbitrary functions $a(B)$ and $b(B,f)$. By dividing by the frequency f, one gets

$$\frac{P_{\text{Fe}}}{f} = a(B) + b(B,f) \cdot f \ . \tag{F.2}$$

The slope $b(B,f)$ is nearly linear and the constant component $a(B)$ can be extrapolated (Figure F.1).

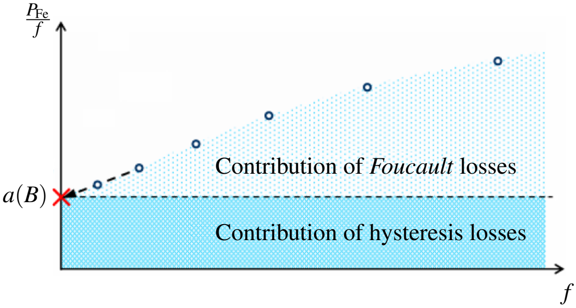

Figure F.1.: Frequency separation of the iron losses in *JMAG* according to [32]

Hysteresis loss calculation

The hysteresis losses $P_{\text{Fe,Hy},j}$ are determined separately for each component (x,y,z) or (ρ,φ,z) of the magnetic flux density according to

$$P_{\text{Fe,Hy},j} = \sum_{i=1}^{n_{\text{elem}}} P_{\text{Fe,Hy},j,i} = \sum_{i=1}^{n_{\text{elem}}} \left(\sum_{k=1}^{N} a(|B_{j,k}|) \cdot f_k \right) \cdot V_i \ , \tag{F.3}$$

with the number of finite elements n_{elem}, the volume of each element V_i, the magnetic flux density $|B_{j,k}|$, and the frequency f_k at the harmonic order $k = 1 \ldots N$. The the magnetic flux density is calculated via

$$|B_{j,k}| = \sqrt{B_{j,k} \cdot \overline{B}_{j,k}} \ , \tag{F.4}$$

with $j = 1 \dots 3$ according to the components (x, y, z) or (ρ, φ, z) of the complex magnetic flux density $B_{j,k}$ and the complex conjugate numbers $\overline{B}_{j,k}$. The coefficient $a(|B_{j,k}|)$ is determined according to the frequency separation method. The total hysteresis losses $P_{\mathrm{Fe,Hy}}$ are determined as the sum of the per-component losses $P_{\mathrm{Fe,Hy},j}$:

$$P_{\mathrm{Fe,Hy}} = \sum_{j=1}^{3} P_{\mathrm{Fe,Hy},j} \ . \tag{F.5}$$

For two-dimensional models the z-component ($j = 3$) of the magnetic flux density and thus the corresponding losses are always zero.

Foucault **loss calculation**

The *Foucault* losses $P_{\mathrm{Fe,Ft}}$ are determined in the same manner as the hysteresis losses (F.3), except for the usage of the coefficient $b(|B_{j,k}|, f_k)$ instead of $a(|B_{j,k}|)$ and the square of the frequency f instead of the linear dependency on f:

$$P_{\mathrm{Fe,Ft},j} = \sum_{i=1}^{n_{\mathrm{elem}}} P_{\mathrm{Fe,Ft},j,i} = \sum_{i=1}^{n_{\mathrm{elem}}} \left(\sum_{k=1}^{N} b(|B_{j,k}|, f_k) \cdot f_k^2 \right) \cdot V_i \ , \tag{F.6}$$

$$P_{\mathrm{Fe,Ft}} = \sum_{j=1}^{3} P_{\mathrm{Fe,Ft},j} \ . \tag{F.7}$$

G. Overestimation of iron losses at load

As shown in Chapter 8, the recalculation of the iron losses $P_{\mathrm{Fe,calc}}$ at load with the reactance voltage U_{x} overestimates the true iron losses $P_{\mathrm{Fe,sim}}$ for test machines M2 and M3. In the following sections the influence of the non-sinusoidal magnetic flux density in the air gap on the stator iron losses and the influence of the rotor iron losses at load are investigated.

Overestimation of the stator iron losses

The no-load air gap flux density (Figure E.4), as well as the no-load phase voltage (Figure E.17), of test machine M3 (surface-mounted magnets) are flat-topped due to a strong third harmonic component (Figure E.18). Each harmonic field wave (order μ) of the rotor field rotate with synchronous speed n_{syn} and induce the stator with the frequency $f = \mu \cdot f_{\mathrm{s}}$, leading to iron losses in the stator iron. During the post processing the frequency components are analyzed by FFT calculation. In this example about 70 % of the iron losses occur at the basic frequency $f_{\mathrm{s}} = 150\,\mathrm{Hz}$, 17 % at the third harmonic $f = 450\,\mathrm{Hz}$, and 4 % at the fifth harmonic $f = 750\,\mathrm{Hz}$ (Figure G.1).

At load, the combined stator and rotor fields lead to a reduction of the air gap flux density at the trailing edge of the permanent magnet pole and an increase of the air gap flux density at the leading edge [5]. This effect is also visible in the stator phase voltage (Figure G.2), for example shown at motor operation with nearly rated current $I_{\mathrm{s}} = 195\,\mathrm{A}$. The third harmonic component is reduced. In the calculated spectrum of the stator iron losses according to Appendix F the fundamental component is increased at load (Figure G.1). If just this component was present, the recalculation with $(U_{\mathrm{x}}/U_0)^2 = 1.39$ would lead to an accurate ratio between $P_{\mathrm{Fe,calc,1}}$ and $P_{\mathrm{Fe,sim,1}}$ of 1.02. For the iron losses also the third harmonic component is reduced to about 9 % of the total iron losses, while the fundamental represents now about 80 %. The third harmonic component is strongly overestimated by the recalculation of the iron losses to a ratio of $P_{\mathrm{Fe,calc,3}}/P_{\mathrm{Fe,sim,3}} = 2.18$. The fifth harmonic component is also calculated slightly higher to $P_{\mathrm{Fe,calc,5}}/P_{\mathrm{Fe,sim,5}} = 1.11$. In total, the stator iron losses are therefore also overestimated by $P_{\mathrm{Fe,calc}}/P_{\mathrm{Fe,sim}} = 1.17$ (Figure 8.18).

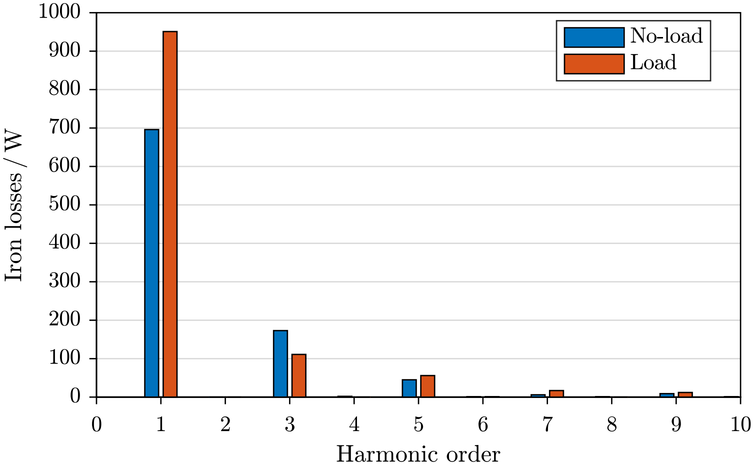

Figure G.1.: Spectrum of the simulated stator iron losses of test machine M3 at rated speed ($n_\mathrm{N} = 3000\,\mathrm{min}^{-1}$, $f_\mathrm{s} = 150\,\mathrm{Hz}$, $k_\mathrm{V} = 1$; Load: $I_\mathrm{s} = 195\,\mathrm{A}$)

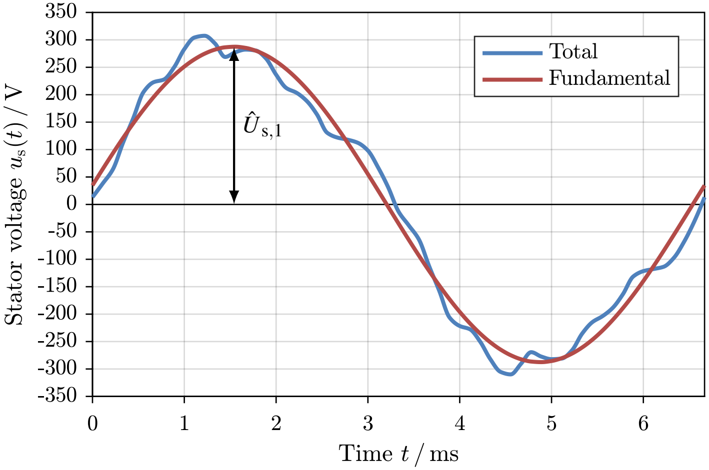

Figure G.2.: Simulated stator phase voltage of test machine M3 at motor operation ($I_\mathrm{s} = 195\,\mathrm{A}$ RMS) and its fundamental ($U_{\mathrm{s},1} = 201$ V RMS) over time at rated speed ($n_\mathrm{N} = 3000\,\mathrm{min}^{-1}$)

Overestimation of the rotor iron losses

Due to the special design of test machine M2 with open stator slots, inter-teeth, buried rotor magnets, and a sub-harmonic stator field wave, the rotor iron losses are not negligible. At generator no-load operation, according to (3.20), the rotor bridges, which cover the magnets and are located close to the stator slots, are induced by the modulation effect of the rotor field due to the stator slot openings with the frequency $f_{\mathrm{Q}} = Q_{\mathrm{s}}/p \cdot f_{\mathrm{s}} = 24/8 \cdot f_{\mathrm{s}} = 3 \cdot f_{\mathrm{s}}$. The inter-teeth lead to additional rotor frequencies $f'_{\mathrm{Q}} = Q'_{\mathrm{s}}/p \cdot f_{\mathrm{s}} = 12/8 \cdot f_{\mathrm{s}} = 1.5 \cdot f_{\mathrm{s}}$ and multiples of f_{Q} and f'_{Q}. In Figure G.3a the modulated magnetic flux density B at the center of the rotor bridges is shown. The stator slot openings lead to periodically decreased flux density. Also the *Fourier* analysis of the first three harmonic components (1.5, 3, 4.5) is shown. At the position of the probe (Figure G.3b) the component $(Q_{\mathrm{s}}/p + Q'_{\mathrm{s}}/p) = 4.5$ has the largest amplitude.

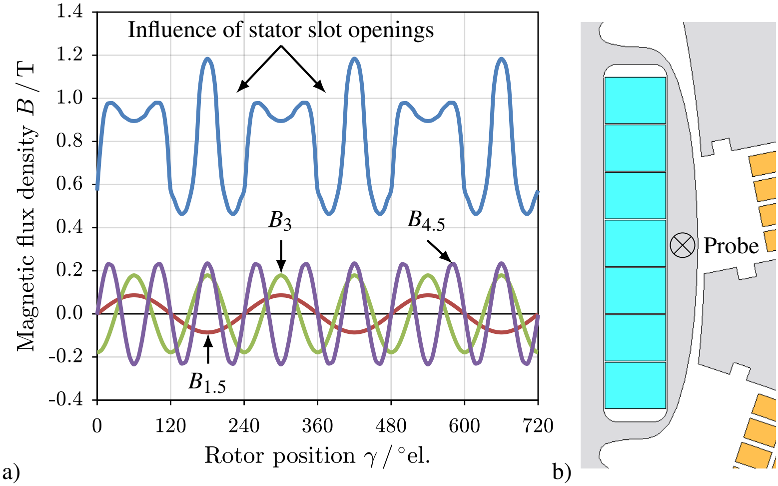

Figure G.3.: a) Simulated magnetic flux density B (absolute value and *Fourier* analysis) in the rotor iron bridge of test machine M2 at generator no-load operation and b) corresponding location of the B-probe in *JMAG*

According to Appendix F the same rotor frequencies are associated to the rotor iron losses (Figure G.4b). The no-load iron losses only occur in the rotor bridges (Figure 8.8), as the flux density pulsations do not enter the rotor yoke.

At load operation the single-layer fractional-slot winding ($q = 1/2$) lead to harmonic stator field waves of the order

$$\nu^* = 1 + m_\mathrm{s} g = 1, -\mathbf{2}, 4, -5, 7, \ldots \quad \text{with} \quad g = 0, \pm 1, \pm 2, \ldots \tag{G.1}$$

The normalized harmonics corresponding to the working field wave ($\nu = -\nu^*/2$) are:

$$\nu = -1/2, \mathbf{1}, -2, 5/2, -7/2, \ldots \tag{G.2}$$

According to (3.21), the stator field wave harmonics $\nu \neq 1$ induce the rotor with the frequencies

$$f_\mathrm{r} = |1 - \nu| \cdot f_\mathrm{s} = 1.5g \cdot f_\mathrm{s} \quad \text{with} \quad g = 1, 2, 3, \ldots$$

The rotor frequencies f_r are identical to the no-load rotor frequencies, as shown before, but at load operation mainly the sub-harmonic field wave with $\nu = -1/2$ leads to iron losses in the rotor bridges *and* the rotor yoke with the frequency $1.5 \cdot f_\mathrm{s}$ (Figure G.4b). The higher harmonic components do not rise significantly at load operation, or are even lower than at generator no-load operation.

In this example the iron losses at q-current operation with $I_\mathrm{sN} = 120\,\mathrm{A}$ are shown. The ratio between the reactance voltage and the no-load voltage $(U_\mathrm{x}/U_0)^2 = 4.09$ is rather high. The stator iron losses at load are therefore also much higher than at generator no-load (Figure G.4a). These losses are already overestimated moderately by the proposed recalculation method to $P_\mathrm{Fe,s,calc}/P_\mathrm{Fe,s,sim} = 1.15$. As the higher harmonic components of the no-load rotor iron losses are not increased in the same manner as the stator iron losses, the rotor iron losses are overestimated by $P_\mathrm{Fe,r,calc}/P_\mathrm{Fe,r,sim} = 1.82$. By taking the absolute distribution of iron losses into account (stator: 82 %, rotor: 18 %), the total iron loss ratio is $P_\mathrm{Fe,calc}/P_\mathrm{Fe,sim} = 1.28$.

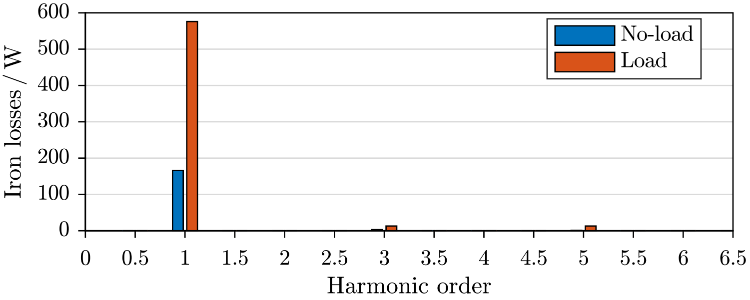

(a) Stator iron losses

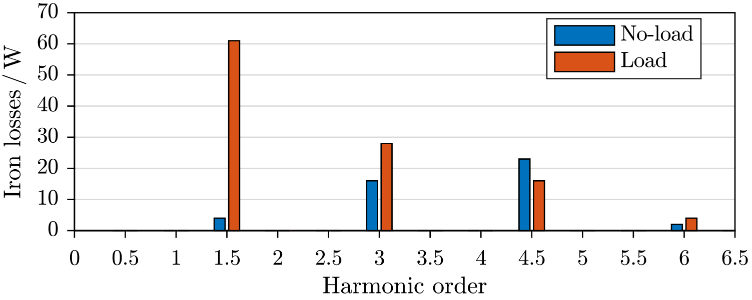

(b) Rotor iron losses

Figure G.4.: Spectrum of the simulated iron losses of test machine M2 at rated speed ($n_{\mathrm{N}} = 1000\,\mathrm{min}^{-1},\ f_{\mathrm{s}} = 133.3\,\mathrm{Hz},\ k_{\mathrm{V}} = 1$; Load: $I_{\mathrm{s}} = 120\,\mathrm{A}, \beta^* = 0\,^{\circ}$el.)

Curriculum Vitae

Persönliche Daten	Björn Deusinger geboren am 28. März 1986 in Frankfurt am Main
Berufliche Praxis	
Seit 04/2013	Technische Universität Darmstadt Institut für Elektrische Energiewandlung Wissenschaftlicher Mitarbeiter
09/2011 – 03/2012	SCHENCK RoTec GmbH, Darmstadt Industriepraktikum und Werkstudent
06/2006 – 09/2006	Siemens VDO Automotive AG, Karben Industriepraktikum
07/2005 – 03/2006	Familienferienstätte Dorfweil, Schmitten Zivildienst
Studium und Schulbildung	
09/2006 – 03/2013	Technische Universität Darmstadt Elektrotechnik und Informationstechnik Studienrichtung Allgemeine Elektrotechnik Abschluss: Diplom-Ingenieur
06/2005	Johann-Philipp-Reis-Schule, Friedberg Berufliches Gymnasium Schwerpunkt Informationstechnik Abschluss: Allgemeine Hochschulreife